

Nanopores with Fluid Walls for Characterizing Proteins and Peptides

by

Erik Christian Yusko

**A dissertation submitted in partial fulfillment
of the requirements for the degree of
Doctor of Philosophy
(Biomedical Engineering)
in The University of Michigan
2012**

Doctoral Committee:

**Associate Professor Michael Mayer, Chair
Professor L. Jay Guo
Associate Professor David Sept
Associate Professor Max Shtein**

© Erik Christian Yusko

All rights reserved

2012

DEDICATION

To my family for fostering my curiosities and for always listening.

and

To Jackie Roessler, my fiancée, for always making me laugh and always, always being
an inspiration.

ACKNOWLEDGMENTS

The research described in this thesis was funded by a National Science Foundation CAREER award and a National Institutes of Health RO1 grant awarded to Michael Mayer. I would like to acknowledge personal funding from the Department of Education in the form a Graduate Assistance in Areas of National Need (GAANN) fellowship as well as a Rackham Pre-Doctoral Fellowship and a Rackham Merit Fellowship from the University of Michigan.

Special thanks are extended to the following people, without whom this work would not have been possible:

My research advisor, Michael Mayer, who has been a constant motivator and inspiration to perform creative and careful science. His guidance, drive, and friendship has proven invaluable, and I will always be grateful for his help. Moreover, Prof. Mayer had the foresight to apply nanopores for protein experiments when almost every other group was interested in DNA studies; without this differentiating vision this thesis would not have been possible.

Jilai Li, Ph.D., and Ryan Rollings, for their amazing willingness to fabricate large nanopores for us to use. The speed at which this work was completed would have been much slower without their help and guidance.

Sheereen Majd, Ph.D., for being an excellent mentor, colleague and friend. Prof. Majd always provided excellent advice and was always willing to listen to my crazy ideas.

Jeff Uram, Ph.D. and Dan Estes, Ph.D. for being excellent mentors and example graduate students. Jeff Uram also laid much of the groundwork that was required to initiate this work.

David Sept, Ph.D. for his biophysical and statistical expertise that ultimately made data that much more exciting to analyze. Prof. Sept, has been an invaluable resource, and I will always appreciate his willingness to teach me about the most robust statistical methods.

Max Shtein, Ph.D., and Jay Guo, Ph.D., who along with Prof. Mayer and Prof. Sept, comprise my thesis committee. I thank all the members of my committee for their helpful suggestions, patience, and support.

Jerry Yang, Ph.D., for his continued advice and support in these projects. Prof. Yang has always provided invaluable insight, particularly for the amyloid- β work and the membrane-active enzyme work.

Alan Hunt, Ph.D., who was always willing to simplify a problem and make it quite clear. My knowledge of biophysics started to develop with the opportunity I had to be a graduate student instructor for his Quantitative Biology course.

Panchika Prangkio, Ph.D., for her amazing tenacity in very carefully developing all of the protocols to prepare properly, and as quantitatively as possible, solutions containing amyloid- β aggregates.

Brandon Bruhn for being a great friend and colleague. Brandon was always willing to help, work hard, and inspire a golfing break.

Jay Johnson, Alex Petti, Janki Patel, and Winston Goan for being patient with me as a graduate student mentor. The experience of mentoring each of them during their undergraduate research and the work they did while in lab was amazingly helpful.

Divya Rao, Ph.D., Haiyan Liu, Ph.D., and Yazan Billeh for always listening and asking thoughtful questions.

Ricardo Capone, Ph.D., for many late night discussions in lab during my early years as a graduate student.

The many friends who inspired and sometimes instigated wonderful dinner parties, especially Sasha Cai Leshner-Perez, Garen Vartanian, Brandon Bruhn, Iverson Bell, and Hillary Welton. They are all food and wine aficionados as well as excellent chefs.

Jackie Roessler for her willingness to correct my sometimes terrible writing habits, her ability to lighten almost any mood, and her clear headedness. Her help and support certainly made this thesis easier to complete.

The Roessler family of Bob, Chris, and Grace for their energy and understanding when my thoughts were elsewhere buried in Science.

And finally, thanks to my grandparents, in particular Ruta Spigers, and my parents, David and Rita Yusko, for always being supportive, understanding, and encouraging of my endeavors. Many thanks to my brother, Adam, for answering my many random math questions and my sister, Larissa, for being hilarious. This thesis would certainly not have been possible without the help and support of my family and friends.

TABLE OF CONTENTS

DEDICATION	ii
ACKNOWLEDGMENTS	iii
LIST OF FIGURES	x
LIST OF TABLES	xiii
LIST OF PUBLICATIONS AND PATENTS	xiv
LIST OF SYMBOLS AND VARIABLES	xvi
ABSTRACT	xix
CHAPTER	
1. Nanopore-based, Single Molecule Biophysics of Proteins.....	1
1.1 Invention and evolution of resistive-pulse sensing	3
1.2 Resistive-pulse sensing of single molecules	6
1.3 Challenges of sensing and a characterizing single proteins with nanopores	9
1.4 Introduction to nanopores with fluid walls inspired by <i>bombyx mori</i>	11
Chapter 1 References	15
2. Controlling the Translocation of Proteins through Nanopores with Bio-Inspired, Fluid Walls.....	21
2.1. Introduction.....	22
2.2. Advantages of fluid coatings	24
2.3. Lipid coating enables time-resolved translocation events	27
2.4. Determining translocation time and charge of proteins	31
2.5. Aggregated A β peptides translocate without clogging	35
2.6. Conclusions.....	36
Chapter 2 Appendix	38
2-App.Methods. Supporting methods	38
2-App.S1. Resistance of nanopores as a function of bilayer thickness	40

2-App.S2. Formation of fluid lipid bilayers on the silicon nitride substrate and determination of translational diffusion constants	45
2-App.S3. Additional evidence for a bilayer coating on the walls of the nanopores	50
2-App.S4. Precise control of the surface chemistry.....	53
2-App.S5. Evidence for the binding of proteins to lipid-anchored ligands in the bilayer and for the translocation of lipid-bound proteins through bilayer-coated nanopores	55
2-App.S6. Translocations of non-spherical proteins generate broad distributions of ΔI	65
2-App.S7. Determining the most probable value of t_d and its error	70
2-App.S8. Calculating the charge of proteins from the translocation time of lipid-anchored proteins	73
2-App.S9. Data acquisition and analysis of resistive pulses for protein detection	81
2-App.S10. Preparation of amyloid-beta samples and gel-electrophoresis	84
Chapter 2 References	87
3. Determining the Shape, Dipole Moment, and Rotational Diffusion Coefficient of Single, Non-Spherical Proteins	92
3.1 Introduction.....	93
3.2 Non-spherical proteins generate bimodal distributions of ΔI values.....	95
3.3. Fitting distributions of ΔI values enables calculation of a protein's shape and volume.....	101
3.4. ΔI values within individual translocation events reveal apparent rotational diffusion coefficients and dipole moments.	103
3.5 Conclusion.	107
Chapter 3 Appendix	108
3-App.Methods	108
3-App.S1. Details regarding equation (3.1).	109
3-App.S2. Broad distributions of IgG ₁ antibodies were not due to impurities, dimers, or simultaneous translocations.	110
3-App.S3. Electrical shape factor and distributions of shape factors.	112
3-App.S4. Using ΔI_{min} and ΔI_{max} to solve for the volume and shape of proteins.	115

3-App.S5. Models for describing mean squared angular displacement and autocorrelation characteristic times.	116
3-App.S6. Derivation of a shape factor distribution that includes the dipole moment of proteins	117
3-App.S7. Chapter 3 appendix figures.....	121
Chapter 3 References	130
4. Using Nanopores with Fluid Walls to Determine the Binding Affinity of Protein Ligand Interactions.....	135
4.1 Introduction.....	136
4.2 Model describing the flux of lipid-anchored proteins across the perimeter of a bilayer-coated nanopore.....	138
4.3 Validation of equation (4.15).....	142
4.4 Affinity constant of a monoclonal anti-biotin IgG ₁ antibody binding to biotin-PE lipids.....	146
4.5 Conclusion	148
Chapter 4 Appendix	150
4-App.Methods	150
4-App.S1 FRAP experiments to measure the diffusion coefficient of lipids	151
4-App.S2 Calibration curve for affinity capillary electrophoresis experiments.	153
Chapter 4 References	156
5. Single Particle Characterization of Aβ Oligomers in Solution	160
5.1 Introduction.....	161
5.2 Results and discussion	164
5.3 Conclusions.....	175
Chapter 5 Appendix	177
5-App.Methods	177
5-App.S1. Nanopores without a fluid, lipid coating clog due to adsorption of A β	179
5-App.S2. Gel electrophoresis experiments.....	180
5-App.S3. Additional characterization of A β preparations by ThT fluorescence assays, circular dichroism spectroscopy and cytotoxicity assays.	184
5-App.S4. Bootstrap resampling statistics of the clustering procedure.	185

5-App.S5. A β aggregate sizes determined by nanopore-based characterization compared to sizes determined by TEM.	187
5-App.S6. Distributions of t_d values in clusters (i) and (ii)	188
5-App.S7. Protofibril diameters as a function of their length determined by TEM analysis.....	191
5-App.S8. Estimation of protofibril lengths	192
5-App.S9. Preparation of transmission electron microcopy samples	196
Chapter 5 References	199
6. Determining the Activity of Membrane-Active Enzymes with Lipid-Coated Nanopores	205
5.1 Introduction.....	206
6.2 Experimental section.....	209
6.3 Results and discussion	210
6.4 Conclusion	215
Chapter 6 Appendix	217
6-App.S1 Control experiment with denatured phospholipase D	217
6-App.S2 Kinetic model for phospholipase D activity.....	217
Chapter 6 References	219
7. Concluding Remarks and Suggestions.....	222
7.1 General strategies to improve the nanopore-with-fluid-walls platform.....	222
7.2 Proposed embodiments of the nanopores-with-fluid-walls platform for simultaneous, multi-parameter characterization of individual proteins.....	227
7.3 Conclusion	229
Chapter 7 References	230
Appendix.....	231

LIST OF FIGURES

FIGURE

1.1 Drawing from Wallace H. Coulter's patent describing the concept of resistive-pulse sensing.	4
1.2 Periodic variations in the magnitude of resistive-pulses due to the rotation of oblate-shaped erythrocytes within a microchannel as predicted and observed by Golibersuch.	5
1.3 Illustration of the experiment performed by Kasianowicz <i>et al.</i> where a single polynucleotide was detected using an α -hemolysin pore embedded in a planar lipid membrane as well as the concept of using synthetic nanopores mounted in a simple microfluidic device.	7
1.4 Lipid-coated nanopores perforate the exoskeleton of olfactory sensilla in the antenna of many insects and serve as a model for synthetic nanopores with fluid walls.	12
2.1 Bioinspired synthetic nanopores with bilayer-coated fluid walls.	23
2.2 Capture, affinity-dependent pre-concentration, and translocation of specific proteins after binding to ligands on mobile lipid anchors.	26
2.3 Controlling the translocation times, t_d , of single lipid-anchored proteins by the viscosity of the bilayer coating and distinguishing proteins by their most probable t_d values.	29
2.4 Distribution of ΔI values and corresponding molecular volumes and shape factors of individual proteins translocating through bilayer-coated nanopores with biotinylated lipids.	30
2.5 Comparison of experimental and theoretical values of charge-dependent translocation times of streptavidin.	33
2.6 Bilayer-coated nanopores resist clogging and enable the monitoring of the aggregation of amyloid-beta ($A\beta$) peptides.	36
3.1 Current recordings through electrolyte-filled, bilayer-coated nanopores during the translocation of the four proteins sensed in this work reveal the corresponding spheroidal shape of proteins (blue shapes) as determined by analysis of resistive pulses.	96
3.2 Current traces showing resistive pulses due to the translocation of monoclonal anti-biotin IgG ₁ antibodies (A-C) through three different bilayer-coated nanopores and the resulting distributions of the maximum ΔI values (D-F).	97
3.3 Current traces showing resistive pulses due to the translocation of streptavidin (A), Fab fragments (B), and GPI-AchE (C) and histograms of the maximum ΔI values	

determined during the translocation of streptavidin (D), Fab fragments (E), and GPI-AchE (F).....	98
3.4 Possible values of shape factors and their probability distribution. (A) Shape factor as a function of m when $\theta = 0$ (solid curves) and when $\theta = \pi/2$ (dashed curves) for prolates (blue curves) and oblates (red curves).....	99
3.5 Resistive pulses due to the translocation of IgG ₁ antibodies and histograms of intra event ΔI values (A-C).....	104
3.6 Intra-event ΔI signals due to the translocation of a single IgG ₁ antibody (A), GPI-AchE (B), and Fab fragment (C) overlaid with the calculated orientation of the protein, $\theta(t)$	105
4.1 Illustration of the cylindrical coordinate system and parameters used to describe the diffusion-limited frequency of translocation events of lipid-anchored proteins.	138
4.2 Frequency of translocation events due to streptavidin-biotin-PE complexes with different fractions of biotin-PE lipids in the bilayer coating as well as kinetic analysis of the binding interaction.....	143
4.3 Frequency of translocation events due to streptavidin bound to biotin-PE lipids immediately after applying the electric potential difference.....	145
4.4 Determination of the equilibrium dissociation constant, K_d , for the binding of monoclonal anti-biotin IgG ₁ antibodies to biotin-PE and biotin-fluorescein.....	147
5.1 Synthetic nanopores with fluid walls make it possible to characterize individual A β aggregates by resistive pulse recordings.	164
5.2 Scatter plots of ΔI values <i>versus</i> t_d values from the translocation of individual A β aggregates reveal clusters of translocation events due to spherical oligomers, protofibrils with lengths shorter than the length of the nanopore, protofibrils with lengths longer than the length of the nanopore, and mature fibers.	166
5.3 Transmission electron microscopy (TEM) analysis of the size of A β ₍₁₋₄₀₎ aggregates.	171
5.4 Distributions of estimated lengths of A β ₍₁₋₄₀₎ protofibrils in clusters (i) and (ii). ...	173
5.5 Frequency of translocation events organized by cluster classification reveals time-dependent aggregation.....	175
6.1 Schematic of PLD-mediated hydrolysis of phosphatidyl choline lipids and illustration of a synthetic, bilayer-coated nanopore for monitoring the activity of phospholipase D.	208
6.2 Increase in the conductance of bilayer-coated nanopores as a function of the mole fraction of PA lipids (X_{PA}).....	211
6.3 Mole fraction of PA in the supported lipid bilayer, X_{PA} , as a function of time after addition of PLD.....	215
7.1 Histogram of 289 proteins that are found in human plasma.	223
7.2 “Polymorphic phases, molecular shapes, and the critical packing parameter for some membrane lipids.”	224

7.3 Concept of a nanopore with fluid walls designed to increase the residence time of lipid-anchored proteins in the pore while not reducing the frequency of translocation events.....	226
7.4 Intraevent ΔI values due to IgG ₁ antibody translocation events have several local maxima (A) and illustration of the multiple conformations of an IgG antibody (B).	227
7.5 Conceptual comparison of a two-dimensional protein characterization obtained by two-dimensional gel electrophoresis and a three-dimensional protein characterization of proteins obtained by nanopore-based single-molecule techniques.	228

LIST OF TABLES

TABLE

2.1	Lipids used in this work to coat nanopore walls.....	25
2.2	Comparison of diffusion coefficients of lipid-anchored proteins within the nanopore, D_P , with diffusion coefficients of lipids, D_L , in coatings of two different lipid bilayers on three different nanopores.	34
3.1	Comparison of the volume and length to diameter ratio, $m = A/B$, of proteins determined by analysis of resistive pulses, the values reported in literature, and the values estimated from the crystal structure of the protein.....	100
5.1	Average values of ΔI , excluded volumes Λ , diameters of spherical $A\beta_{(1-40)}$ aggregates \emptyset_S , and cross-sectional areas A_X as well the corresponding cylindrical diameter \emptyset_C of rod-shaped $A\beta_{(1-40)}$ aggregates in each cluster compared to equivalent values measured <i>via</i> TEM and values reported in literature.	169

List of Publications and Patents

Work presented in this thesis

Source Chapter	Type	Description
2	Publication	Yusko E.C., Johnson J., Majd S., Prangkio P., Rollings R., Li J., Yang J., Mayer M. "Controlling Protein Translocation through Nanopores with Bioinspired, Fluid Walls" <i>Nature Nanotechnology</i> , 2011 , 6, 253 – 260.
3	Publication	Yusko E.C., Bruhn B., Rollings R.C., Li J., Mayer M. "Determining the Shape of Single, Native Proteins" <i>submitted</i> , 2012 .
4	Publication	Yusko E.C., Petti A.M., Rollings R.C., Li J., Mayer M. "Nanopores with Fluid Walls for Determining the Binding Affinity of Protein Ligand Interactions" <i>submitted</i> , 2012 .
5	Publication	Yusko E.C., Prangkio P., Sept D., Rollings R.C., Li J., Mayer M. "Single Particle Characterization of A β Oligomers in Solution" <i>ACS Nano</i> , 2012 , 6, 5909-5919.
6	Publication	Yusko E.C., Majd S., Rollings R.C., Li J., Yang J., Mayer M. "Determining the Activity of Membrane-Active Enzymes with Lipid-Coated Nanopores" <i>submitted</i> , 2012 .
2, 4, 5, & 6	Patent Application	Mayer M., Yusko E.C., Yang J. "Nanopores with Fluid Walls" U.S. Pat. App. No.: 13/400,472. eFiled: February 2, 2012
3	Patent Application	Mayer M., Yusko E.C. "Nanopore-based Determination of Protein Shape, Volume, Rotational Diffusion Coefficient, and Dipole Moment" U.S. Pat. App. No.: <i>in preparation</i>

Additional publications achieved during my Ph.D.

Type	Description
Publication	An R., Uram J.D., Yusko E.C., Ke K., Mayer M., Hunt A. J. "Ultrafast Laser Fabrication of Submicrometer Pores in Glass" <i>Opt. Lett.</i> , 2008, 33, 1153 – 1155.
Publication	Majd S., Yusko E.C., MacBriar A.D., Yang J., Mayer M. "Gramicidin Pores Report the Activity of Membrane-Active Enzymes" <i>J. Am. Chem. Soc.</i> , 2009, 131, 16119 – 16126.
Publication	Yusko E.C., An R., Mayer M. "Electroosmotic Flow can Generate Ion Current Rectification in Nano- and Micropores" <i>ACS Nano</i> , 2010, 4, 477 – 487.
Publication	Majd S., Yusko E.C., Billeh Y.N., Macrae M.X., Yang J., Mayer M. "Applications of Biological Pores in Nanomedicine, Sensing and Nanoelectronics" <i>Curr. Opin. Biotechnol.</i> , 2010, 21, 439 – 476.
Publication	Yusko E.C., Billeh Y.N., Mayer M. "Current Oscillations Generated by Precipitate Formation in the Mixing Zone between Two Solutions inside a Nanopore" <i>J. Phys.-Condes. Matter</i> , 2010, 22, 454127 (9 pgs).
Book Chapter	Yusko E.C., Billeh Y.N., Yang J., Mayer M. "Nanopore Recordings to Quantify Activity-Related Properties of Proteins" <i>Nanopores: Sensing Fundamental Biological Interactions at the Single Molecule Level</i> . Ed. Samir I. and Bashir R., 1 st Edition. 370 pp. (Springer Publishing Company. New York. 2011).
Publication	Majd S., Yusko E.C., Yang J., Mayer M. "Interfacial Kinetic Analysis of Phospholipase D Activity on Long-Chain Lipids in Planar Bilayers" <i>submitted</i> , 2012.

List of Symbols and Variables

roughly in order of appearance

Symbol	Units	Description
ρ	$\Omega \text{ m}$	Resistivity of the electrolyte
ΔI	A	Magnitude of the change in current during a resistive pulse
R	Ω	Resistance
R_A	Ω	Access resistance to one side of a nanopore
R_P	Ω	Resistance of a nanopore
R_C	Ω	Resistance of a channel
t_d	s	Translocation time of the protein (<i>i.e.</i> the time it took the protein to pass through the nanopore).
l_P	m	Length of the nanopore
r_P	m	Radius of the nanopore
d_P	m	Diameter of the nanopore
d	m	Thickness of the lipid bilayer
w_L	m	Thickness of the water layer between a supported lipid bilayer and the synthetic, solid support
l_C	m	Length of the channel in the silicon nitride chips
r_C	m	radius of the cylindrical channel in the silicon nitride chips
θ	rad	Angle between the axis of revolution of a spheroid and the electric field
γ	unitless	Electrical shape factor
γ_{\parallel}	unitless	Electrical shape factor of a spheroid when $\theta = 0$
γ_{\perp}	unitless	Electrical shape factor of a spheroid when $\theta = \pi/2$.
V_A	V	Applied voltage
Λ	m^3	Volume of electrolyte excluded by the protein; generally considered the approximate volume of the protein
d_M	m	Diameter of the molecule or protein
r_M	m	Radius of the molecule or protein

k_B	$1.38 \times 10^{-23} \text{ J K}^{-1}$	Boltzmann constant
T	K	Temperature (here we used 295 K for room temperature)
z	unitless	Net valence of the charge of a molecule or protein
e	$1.60 \times 10^{-19} \text{ C}$	Elementary charge of an electron
V_P	V	Voltage drop across the nanopore
D	$\text{m}^2 \text{ s}^{-1}$	Translational diffusion coefficient
D_r	$\text{rad}^2 \text{ s}^{-1}$	Rotational diffusion coefficient
η	Pa s	Viscosity of a solution
C	M or mol m^{-3}	Concentration of an analyte
A_V	$6.022 \times 10^{23} \text{ mol}^{-1}$	Avagadro's number
λ	nm	Wavelength of light
X	unitless	Mole fraction of a lipid
v	m s^{-1}	Electrophoretic drift velocity
u_e	$\text{m}^2 \text{ v}^{-1} \text{ s}^{-1}$	Electrophoretic mobility
\bar{E}	V m^{-1}	Electric field
ζ	kg s^{-1}	Viscous friction coefficient
L_T	m	Total length of a capillary
L_D	m	Length of a capillary to the detector
t_A	s	Elution time of an analyte
t_{NM}	s	Elution time of the neutral marker
f_C	Hz	Cut-off frequency of an electronic filter
D	$3.336 \times 10^{-30} \text{ C m}$	Debyes, the unit for the magnitude of a dipole moment
$\bar{\mu}$	D	Dipole moment of a protein or molecule
τ_C	s	Characteristic time of the autocorrelation curve of rotational diffusion
U	J	Potential energy

J_L	$\# \text{ m}^{-1}$	Flux across one dimension due to diffusion in two-dimensional plane
Γ_L	$\# \text{ m}^{-2}$	Density of ligand in a two-dimensional plane (e.g. lipid bilayer)
Γ_{PL}	$\# \text{ m}^{-2}$	Density of protein bound to lipid-anchored ligand
f_i	$\# \text{ s}^{-1}$	Frequency of translocation events
[P]	M or $\# \text{ m}^{-3}$	Concentration of protein in solution
K_D	M or $\# \text{ m}^{-3}$	Equilibrium dissociation constant
Θ	unitless	Fraction of total ligand bound to a protein
k_{obs}	h^{-1}	Observed rate-constant for pseudo-first order binding kinetics
k_{on}	$\text{m}^2 \text{ h}^{-1}$	Association rate constant for protein binding to lipid-anchored ligands
k_{off}	h^{-1}	Dissociation rate constant for protein unbinding to lipid-anchored ligands
\emptyset	nm	Diameter of an amyloid- β aggregate
l_M	m	Length of an amyloid- β aggregate
A_x	m^2	Cross-sectional area of an amyloid- β aggregate
κ	Ω^{-1}	Conductance of a nanopore
Q_m	$\text{nM}^{-1} \text{ min}^{-1}$	Interfacial quality constant for an enzyme that catalyzes reactions on a surface

ABSTRACT

Nanopore-based, resistive-pulse sensing is a simple single-molecule technique, is label free, and employs basic electronic recording equipment. This technique shows promise for rapid, multi-parameter characterization of single proteins; however, it is limited by transit times of proteins through nanopores that are too fast to be resolved, non-specific interactions of proteins with the nanopore walls, and poor specificity of nanopores for particular proteins.

This dissertation introduces the concept of nanopores with fluid walls and their applications in sensing and characterization of proteins, disease-relevant aggregates of amyloid- β peptides, and activity of membrane-active enzymes.

Inspired by lipid-coated nanostructures found in the olfactory sensilla of insect antennae, this work demonstrates that coating nanopores with a fluid lipid bilayer confers unprecedented capabilities to a nanopore such as precise control and dynamic actuation of nanopore diameters with sub-nanometer precision, well-defined control of protein transit times, simultaneous multi-parameter characterization of proteins, and an ability to monitor the enzyme phospholipase D.

Using these bilayer-coated nanopores with lipids presenting a ligand, proteins binding to the ligand were captured, concentrated on the surface, and selectively transported to the nanopore, thereby, conferring specificity to a nanopore. These assays enabled the first combined determination of a protein's volume, shape, charge, and affinity for the ligand using a single molecule technique. For non-spherical proteins, the dipole moment and rotational diffusion coefficient could be determined from a single protein.

Additionally, the fluid, biomimetic surface of a bilayer-coated nanopore was non-fouling and enabled characterization of Alzheimer's disease-related amyloid- β aggregates. The presented method and analysis fulfills a previously unmet need in the

amyloid research field: a method capable of determining the size distributions and concentrations of amyloid- β aggregates in solution.

The experiments presented here demonstrate that the concept of a nanopore with fluid walls enables new nanopore-based assays. In particular, it demonstrates the benefits of this concept for simultaneous, multi-parameter characterization of proteins with a single-molecule method. This technique may, therefore, be well-suited for identification of proteins directly in complex biological fluids. Based on these findings, the addition of fluid walls to nanopores holds great promise as a tool for simple, portable single-molecule assays and protein characterization.

Chapter 1

Nanopore-based, Single Molecule Biophysics of Proteins

If you consider the DNA sequences of organisms to be a detailed, architectural layout of a house, then by analogy, proteins are the architects, site managers, wood workers, electricians, plumbers and roofers responsible for erecting that house. The word “protein”, first used by Gerardus Mulder and Jöns Berzelius in 1838, is derived from the Greek word “*proteios*” meaning “primary”, and indeed, proteins are the primary agent of biological function (1). Consequently, abnormal concentrations or functions of a particular protein may reveal medical conditions for which this protein serves as a biomarker (1). To date, however, very few biomarkers have been found and approved by the U.S. Food and Drug Administration for clinical tests (*i.e.* only 10 biomarkers were approved between 1993 and 2002 (2)), in part because current technologies are not capable of performing high throughput, rapid, inexpensive, and simultaneous identification of proteins in complex mixtures (1). Identifying all of the proteins in an organism and their concentrations is a serious technological challenge due to the presence of thousands of different proteins at widely different concentrations (1, 2). For instance, humans have ~10,000 different proteins circulating in the vasculature at concentrations ranging from pM to mM and thousands more proteins are confined within cells and their lipid membranes (3). To overcome these challenges, engineers and scientists would ideally develop technologies capable of determining multiple properties simultaneously of a ***single protein*** within these complex solutions in order to identify each protein in the mixture and its concentration (2). If fast enough and inexpensive enough, this proposed technology could be employed in a clinical setting such that every patient has a historical record of their personal proteome (*i.e.* the protein counterpart to the genome), which would aid diagnoses when biomarkers or abnormalities appear (2, 3). Moreover, these capabilities would enable the construction of a proteome database that also contained

information on every protein's biophysical properties, function, and down-stream effects on organism function. Such a technology and resulting database could be expected to impact human health and scientific understanding as significantly as the sequencing of the human genome (2).

The most popular technologies for characterizing proteins as part of the biomarker search have been two-dimensional gel electrophoresis (invented by Patrick O'Farrell in 1975; ~18,500 citations at press time) (4), mass spectroscopy (Carl-Ove Andersson, 1958 – first use with proteins (5)), and antibody arrays equipped with fluorescent detection (i.e. ELISA, Peter Perlmann and Eva Engvall, 1970 (6, 7)) (2). Analytical centrifugation (Theodor Svedberg, 1924 (8, 9)), capillary electrophoresis (initial work by Tiselius, 1930; realized by Stellan Hjertén, 1983, (10, 11)), surface plasmon resonance (12), nuclear magnetic resonance spectroscopy (Richard R. Ernst and Kurt Wüthrich, 1960's (13)), small angle X-ray scattering (Heinrich Stuhrmann, 1967 (14-18)), and X-ray crystallography (Max Perutz and John Kendrew, 1957 – first use with proteins (19, 20)) are also commonly used to characterize additional properties of proteins such as their size, shape, net electric charge, affinity for a ligand, and atomic structure. While these techniques have been extremely valuable, generally they are capable of determining only one or two properties of a protein and are not well-suited for examining the complex mixtures of proteins that are in biological fluids. Moreover, because these methods are based on ensemble measurements of $10^{15} - 10^{18}$ molecules, they have difficulty resolving dynamic properties and functions of proteins (21). Since the 1970's, however, physicists, biochemists, and engineers have developed extraordinary methods to measure and manipulate individual molecules one at a time *in situ* (21). These methods, called single-molecule methods, are not limited by ensemble averaging and can therefore characterize heterogeneous mixtures, resolve dynamic properties of single molecules, and reveal rare events with unprecedented sensitivity. Moreover, the data obtained from single molecule experiments tends to be more complete and easier to interpret than the data obtained in ensemble and time-averaged techniques, revealing fluctuations in conformation or activity of proteins that can be compared to theoretical models (22). New single molecule methods are currently being developed and advanced at a rapid pace, but

already in the last 30 years they have yielded unprecedented insight into the structure and function of motor proteins, enzymes, receptors, and entire signaling complexes (21, 22).

Here, I will introduce and describe a simple single-molecule method based on an invention by Wallace H. Coulter in 1947. Coulter's invention was re-pioneered in 1996 by Kasianowicz, and over time, the method has become known as "resistive-pulse sensing." It employs a single, electrolyte-filled hole with a length and diameter on the order of 1–100 nm, a so-called nanopore. The work presented here explores recent advancements that I, with the help of many colleagues and advisors, have made toward developing nanopore-based sensors for single-molecule, biophysical investigations and for simultaneous, multi-parameter characterization of proteins. In this introduction, I first describe the principles behind resistive pulse sensing and the challenges associated with sensing and characterizing proteins with nanopore-based sensors. Finally, I briefly introduce the strategies developed in this thesis to overcome these challenges and the resulting advantages of characterizing proteins with nanopore-based sensors.

1.1 Invention and evolution of resistive-pulse sensing

The principles behind resistive-pulse sensing trace their origins to theoretical and experimental work by James Clerk Maxwell and Lord Rayleigh (John William Strutt, 3rd Baron Rayleigh) (23). Lord Rayleigh and Maxwell first described the deformation of an electric field spherical particles in solution, thereby enabling theoretical calculations of the resistivity of solutions containing spherical colloids. The deformation of the electric field around a spherical particle is often considered analogous to the flow of solution around a sphere, described as Hele-Shaw flow. Fricke (1924, 1953), and later Velick and Gorin (1940), extended these models to describe the resistivity of solutions containing non-spherical particles such as prolate and oblates (24-26).

In 1947, Wallace H. Coulter took the innovative step of using a small pore to connect two electrolyte solutions while applying a constant voltage across the pore (Fig. 1.1), thereby inventing the method of resistive-pulse sensing or Coulter counting (27). This innovation enabled rapid identification and counting of blood cells and stimulated the development of automated blood cell counters that were 120 times faster and 10 times more accurate than the best cell counting methods at the time (28). The massive

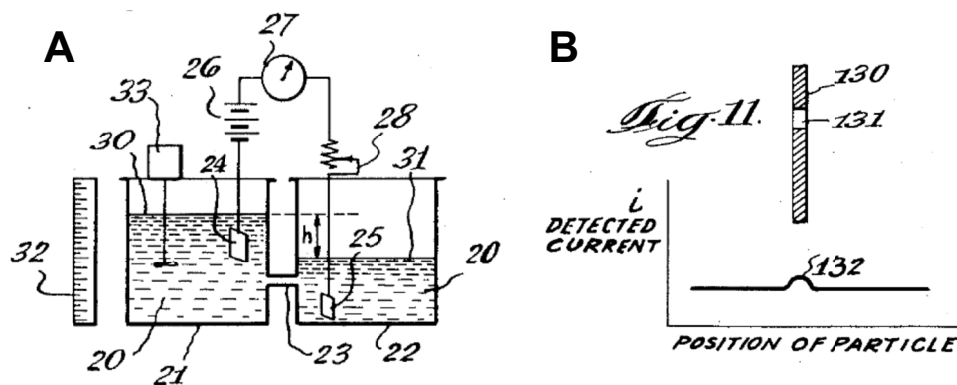


Figure 1.1 | Drawing from Wallace H. Coulter's patent describing the concept of resistive-pulse sensing. (A) Two electrolyte solutions are connected *via* small pore and an electric-field induced current is measured. The magnitude of the current is determined by the applied voltage, the resistivity of the electrolyte, and the dimensions of the pore. In its original embodiment different fluid levels were used to generate a pressure driven flow of electrolyte, and consequently, cells through the pore. (B) As a particle moves from the bulk electrolyte solution and through the nanopore the magnitude of the current decreases while the particle is in the pore. Adapted from (27).

improvement in throughput and accuracy was achieved with the quite simple concept illustrated in Fig. 1.1. Briefly, two electrolyte solutions are connected *via* a small pore, and a constant voltage is applied across the pore resulting in a constant current. The small volume of the pore compared to the bulk solution constitutes the largest electrical resistance between the electrodes, and thus determines the magnitude of the current flow. When an insulating particle, such as a cell in the case of Coulter's demonstrations, passes through the pore it reduces the conducting volume of the pore and temporarily increases the resistance of the pore (*i.e.* causes a resistive pulse) (Fig. 1.1B). This elegant strategy yielded a great consequence: the ability to apply the first principles developed by Maxwell and Lord Rayleigh to determine the volume of *single particles* (*i.e.* cells) as they passed through the pore one-by-one. For instance, by measuring the magnitude of the transient increase in resistance, which is often observed as a reduction in the current, Kubitschek (1960), Gregg and Steidley (1965), and Deblois and Bean (1970) built on these first principles to equate the reduction in current to the volume fraction of the pore that is occupied by an insulating particle (*i.e.* $Vol_{PARTICLE} / Vol_{PORE}$) (29, 30). Additional work demonstrated that the frequency of the resistive-pulses is related to the concentration of the particles in solution and additional experiment factors such as flow rate through the pore, dimensions of the nanopore, and electrostatics. Finally, the duration of the resistive pulse (*i.e.* the time the particle spent in the pore) is related to the

charge and size of the particle and experimental parameters such as the applied voltage, the flow rate and viscosity of the solution in the pore, and the length of the pore.

After Coulter's invention, many studies of μm and sub- μm particles demonstrated that resistive-pulse sensing can reveal the general shape of particles. For instance, Grover *et al.* (1969) considered the effect of a particle's shape and orientation in the pore, which lead to the introduction of an electrical shape factor (31-36) that related the magnitude of the reduction in current to the well-documented depolarization factors of non-spherical particles (in addition to the volume of the particle) (37). Golibersuch elegantly demonstrated the effect of particle shape by sensing oblate-shaped erythrocyte cells (Fig. 1.2) and observing periodic variations in the resistance of the pore as the cells rotated within the pore. Golibersuch took this analysis amazingly far by theoretically describing the expected rotational orbits of the cells (due to the Pouseille flow in the pore) and the expected distribution of resistance values due to the possible values of the electrical shape factor. Other spheroid particles that have been detected include oblate shaped objects such as erythrocytes (Golibersuch 1973), T-Cells (Carbonaro 2008) and Rochelle salt (Berge, Feder, Jossang 1989) as well as prolate shaped objects such as fused polystyrene spheres (Golibersuch 1973), bacteriophages (Deblois *et al.* 1977).

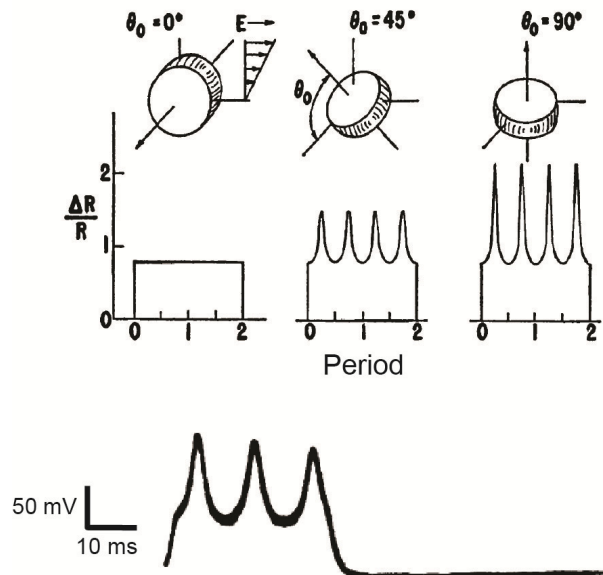


Figure 1.2 | Periodic variations in the magnitude of resistive-pulses due to the rotation of oblate-shaped erythrocytes within a microchannel as predicted and observed by Golibersuch. The volume of each cell remains constant, but the resistance varies with time as a consequence of the orientation-dependent shape factor. Adapted from (32).

It soon became apparent in theory and experiment that the sensitivity of resistive-pulse sensors (*i.e.* the smallest particles that can be detected) was primarily limited by the size of the pore. For instance, smaller pores could detect smaller particles than larger pores. Hence, there was a push to develop methods of fabricating pores with smaller diameters and shorter lengths than the micrometer-sized holes in use at the time (38-42). During this time period, methods of fabricating pores in the sub-micrometer range (diameters of several hundred nanometers and lengths less than 1 μm) enabled exciting assays where smaller and smaller particles and the assembly of particles could be characterized including bacterial cells (30), nanoparticles (30, 42, 43), virus particles (34, 38, 44), assembly of nanoparticles (45), and antibodies binding to synthetic particles (40, 46).

1.2 Resistive-pulse sensing of single molecules

In the 1980's and early 1990's, many investigators were examining the interaction between soluble polymers and ion channels that were embedded in planar lipid bilayers. From these first reports, the idea emerged to take advantage of the "incredibly" small dimensions of biological ion channels to sense individual molecules (47). The first report describing this concept was published by Bezrukov *et al.* in *Nature* in 1994 (48), and it was first realized in the seminal paper by Kasianowicz *et al.* in the *Proceedings of the National Academy of Sciences* in 1996 (49). The landmark publication by Kasianowicz *et al.* used the resistive-pulse sensing technique to detect individual polynucleotide strands passing through the lumen of the membrane protein α -hemolysin (Fig. 1.3A). This work led the groups of Daniel Branton, David Deamer, and George Church (1996) to the hypothesis that single strands of DNA may be sequenced by detecting nucleobase-dependent changes in the current through the pore (50). If it would be possible to achieve this nucleobase-specific signal, nanopore-based sequencing would potentially be able to sequence long strands of DNA (10's of kilo-bases or longer) without any modifications or amplification steps, and therefore, reduce the cost and experiment time by an order of magnitude or more. Consequently the work by Kasianowicz *et al.* energized a large community of scientists to pursue nanopore-based nucleotide sequencing and formed the foundation of a new research field: nanopore-based, single molecule biophysics.

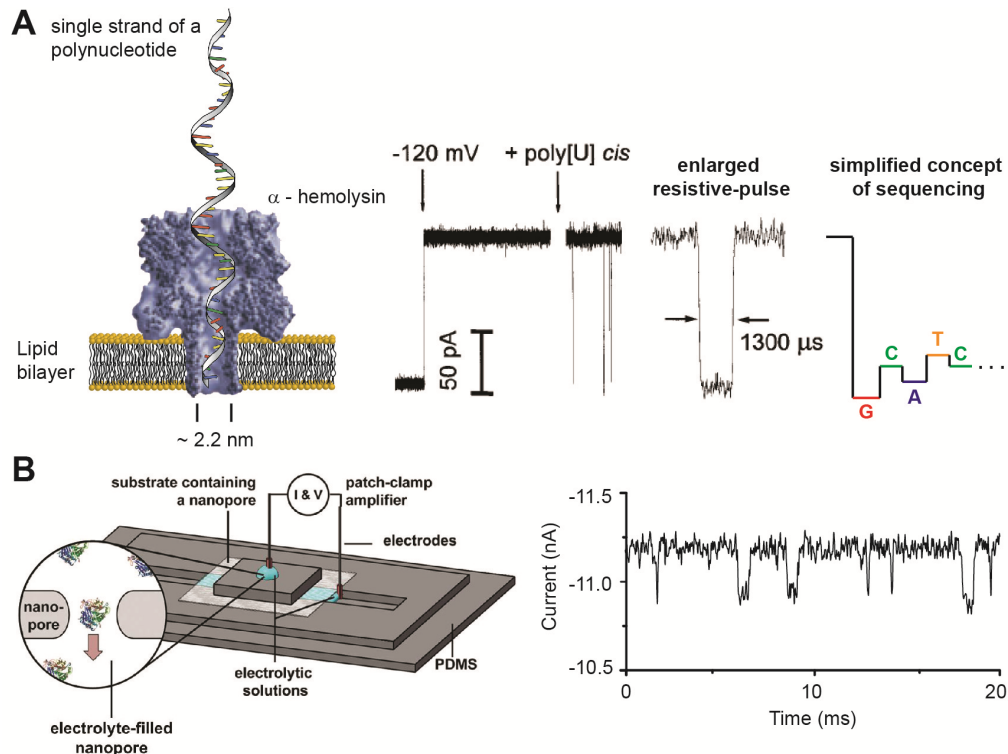


Figure 1.3 | Illustration of the experiment performed by Kasianowicz *et al.* where a single polynucleotide was detected using an α -hemolysin pore embedded in a planar lipid membrane as well as the concept of using synthetic nanopores mounted in a simple microfluidic device. (A) Illustration of α -hemolysin embedded in a planar lipid membrane and the translocation of a single-stranded polynucleotide translocating through the lumen. Each polynucleotide passing through the lumen causes a reduction in the current through pore as shown in the current trace on the right. This result led Branton, Church, and Deamer to hypothesize that single polynucleotide strands (10's of kilobases long) could be sequenced by detecting nucleobase-dependent changes in current (*i.e.* Adenine, Thymine, Guanine, and Cytosine; far right illustration). Adapted from (49). (B) Illustration of a chip that contains a nanopore fabricated in a synthetic material, typically silicon nitride. These synthetic nanopores have larger diameters than biological pores and enable the detection of folded, native proteins. The passage of each protein through the nanopore also leads to a transient decrease in the current through the pore as seen in the current trace on the right.

NOTE: In spring of this year (February and April 2012), sixteen years after the initial hypothesis by Branton, Church, and Deamer, nanopore-based sequencing of DNA was realized. The group of Jens Gundlach published the first report in *Nature Biotechnology* in which Manrao *et al.* used an engineered pore, *mycobacterium smegmatis* porin A (MspA), in combination with a motor protein, phi29 DNA polymerase, to sequence approximately 100 bases from individual polynucleotide strands (51). The company Oxford Nanopore technologies presented a similar method at the

Advances in Genome Biology and Technology Conference (February 15 – 18, Marco Island, FL, U.S.) and reported the ability of its nanopore-based products (expected release in early 2013) to sequence single stranded DNA with read lengths up to ~10 kilo-bases. Their products are reported to contain more than 2,000 nanopores, each individually addressable, on devices the size of a USB stick or portable hard drive, and by combining approximately 20 of these devices together are reported to sequence an entire human genome in ~15 minutes for ~\$1,000 USD (52). These capabilities met the stated goal of the \$1,000 genome proposed by the National Human Genome Research Institute and approach economics where personalized medicine for the population based on an individual's genomic data is feasible.

Since the initial work by Kasianowicz *et al.*, various ion channels were engineered to be optimal resistive-pulse sensors (53) and nanofabrication methods were developed in order to fabricate robust, synthetic nanopores in silicon-based materials commonly used by the semi-conductor industry (54-56). There were two advantages of fabricating nanopore-based sensors in synthetic materials. First, biological pores derived from membrane porins or ion channels require the use of a fragile lipid bilayer that is susceptible to thermodynamic and mechanical instabilities that limits its use to less than ~30 min. Second, the “incredibly” small dimensions of biological pores were too small to allow native, folded proteins to pass through the interior of the pore. While many elegant studies were performed with biological nanopores that characterized properties of proteins such as enzymatic activity (57-60), binding affinities (61-63), and polymerization (64), nanopores with diameters between ~5 nm and ~50 nm and short lengths less than 50 nm would be required to perform resistive-pulse sensing experiments on folded, native proteins (Fig. 1.3B) (65).

These ideal synthetic nanopores became available with new a fabrication method reported by Li *et al.* in the journal *Nature* in 2001 (66). Briefly, a silicon chip is used to support a thin (~ 200 nm) membrane of silicon nitride. In the free-standing silicon nitride membrane a focused ion beam (*i.e.* Ar⁺ or Ne⁺ etc.) is used to machine a nanopore with diameters on the order of 1 to 50 nm and lengths ranging from ~10 nm to 20 nm. In 2006, Han *et al.* used these types of nanopores to detect, for the first time, individual, folded proteins passing through a nanopore one-by-one, opening a new door for

nanopore-based resistive pulse sensing. Han *et al.* employed the same principles of earlier resistive-pulse sensors to measure accurately the diameter of the protein bovine serum albumin directly in solution and without labels. This report marked the beginning of many future studies aimed at sensing single, native proteins with nanopore-based resistive pulse sensors.

1.3 Challenges of sensing and a characterizing single proteins with nanopores

The first reports of protein translocation by Han *et al.* and several later reports demonstrated that the magnitude of the change in current due to individual translocation events could be used to determine the volume of the protein and identify different proteins, if their differences in volume were significant (67-71). From 2006 until the work described in this thesis, however, nanopore-based resistive pulse sensing of single proteins, in particular the work with synthetic nanopores, faced many challenges that limited the first reports primarily to detecting the presence of a protein. One of the primary challenges involved the fast translocation speeds of proteins through the pores due the short length of the pore and the electrophoretic force (*i.e.* the electric field interacting with the charge of the protein) pushing charged proteins through the pore (41, 72, 73). For instance, by diffusion alone a typical protein would be expected to pass through a 20 nm long pore in $\sim 10 \mu\text{s}$, approximately five times faster than the translocation time required to determine the magnitude of the current change accurately due the required electronic filtering of the noise (41, 73). Consequently, the inherently fast translocation speeds of proteins led to large errors in measuring the magnitude of resistive pulses and inaccurate determination of the volume of proteins. A time-averaged signal of $\sim 250 \mu\text{s}$ or longer, however, would enable very accurate determination of protein volume and therefore better differentiate proteins of different volume.

Based on the expected time for proteins to go through the pore it was surprising they could be seen at all in the first reports; this serendipitous result was the consequence of another major challenge specific to protein sensing experiments: non-specific interactions of proteins with the pore walls. These interactions reduced the average transit speed through the pore and increased their total translocation time. This effect

caused two problems: 1) it frequently lead to clogging of nanopores (74) and 2) it made translocation times unpredictable (56). Even the best non-stick coatings such as monolayers of polyethylene glycol could not prevent protein adsorption to the synthetic pore walls (72). This challenge was particularly limiting because Talaga and Li demonstrated that, in the absence of additional effects, the distribution of translocation times of proteins is related the electrophoretic force on the protein and the diffusion coefficient of the protein (67, 75). Consequently, if the distribution of translocation times could be experimentally determined in the absence of non-specific adsorption, nanopore-based resistive pulse sensing might be able to characterize the volume, charge, and diffusion coefficient of proteins. Recently, Wei *et al.* and Ding *et al.* circumvented the issue of translocation times by immobilizing a single or very few ligand within a nanopore to detect the binding and unbinding of individual proteins; in the work by Wei *et al.* this enabled detection and differentiation of immunoglobulin G subtypes based on their affinity constants (76, 77).

Another major issue with nanopore-based resistive pulse sensing of proteins pertains to specificity. Any protein that is small enough to pass through the nanopore has the potential to pass through the pore and be detected. In many cases, however, the ideal nanopore would be specific to a protein of interest and, therefore, enable detection and characterization of that particular protein. Immobilizing a ligand within the nanopore as described above was the state-of-the-art strategy for imparting specificity to a nanopore. Several nanopore based assays used thousands of immobilized ligands to bind thousands of proteins and monitor the resulting change in bulk current flow; these studies were primarily aimed at biosensing, however, Siwy's research group determined the isoelectric point of streptavidin from these types of assays, but not the volume of the protein (78-83).

Despite these challenges, synthetic nanopore-based resistive pulse sensors enabled several very nice biophysical studies of proteins and their function including the interactions between DNA and DNA-binding proteins (55, 84-89), Fab-fragments binding to bovine serum albumin (90), and the folding and unfolding of proteins (67, 91). Many of these studies are reviewed in these works (92-94). Though not yet realized, the

results from these first reports suggested that it should be possible to characterize proteins of interest by three parameters in a single assay: size, charge, and conformation.

1.4 Introduction to nanopores with fluid walls inspired by bombyx mori

In order to address the challenges of sensing single proteins with nanopores, we pursued the concept of nanopores with fluid walls. As it turns out, Nature already developed a nanopore structure with fluid walls that was also involved in sensing with exquisite detection limits (95, 96) (Fig. 1.4A). These nanopores are less sophisticated and more stable than ion channel proteins, and they evolved in organisms that can survive in some of the harshest habitats on the planet: insects (95).

Sensing of odorants by many insects involves the translocation of these molecules through lipid-coated nanopores (diameter 6-65 nm) that span the exoskeleton of the insect (Fig. 1.3) (97-100). These lipid coatings are thought to participate in capture, pre-concentration, and subsequent translocation of odorants to specific receptors on dendrites of olfactory neurons in the antennae of insects (95, 98, 100). Inspired by this natural design, we explored whether coating synthetic nanopores of comparable diameters with fluid lipid bilayers could provide benefits for nanopore-based, single-molecule studies of proteins while addressing associated challenges. Previous reports on coating synthetic nanopores with organic molecules focused on strategies that generated coatings of molecules that were fixed on the surface of the pore (101-103); here, we introduce the concept of fluid coatings.

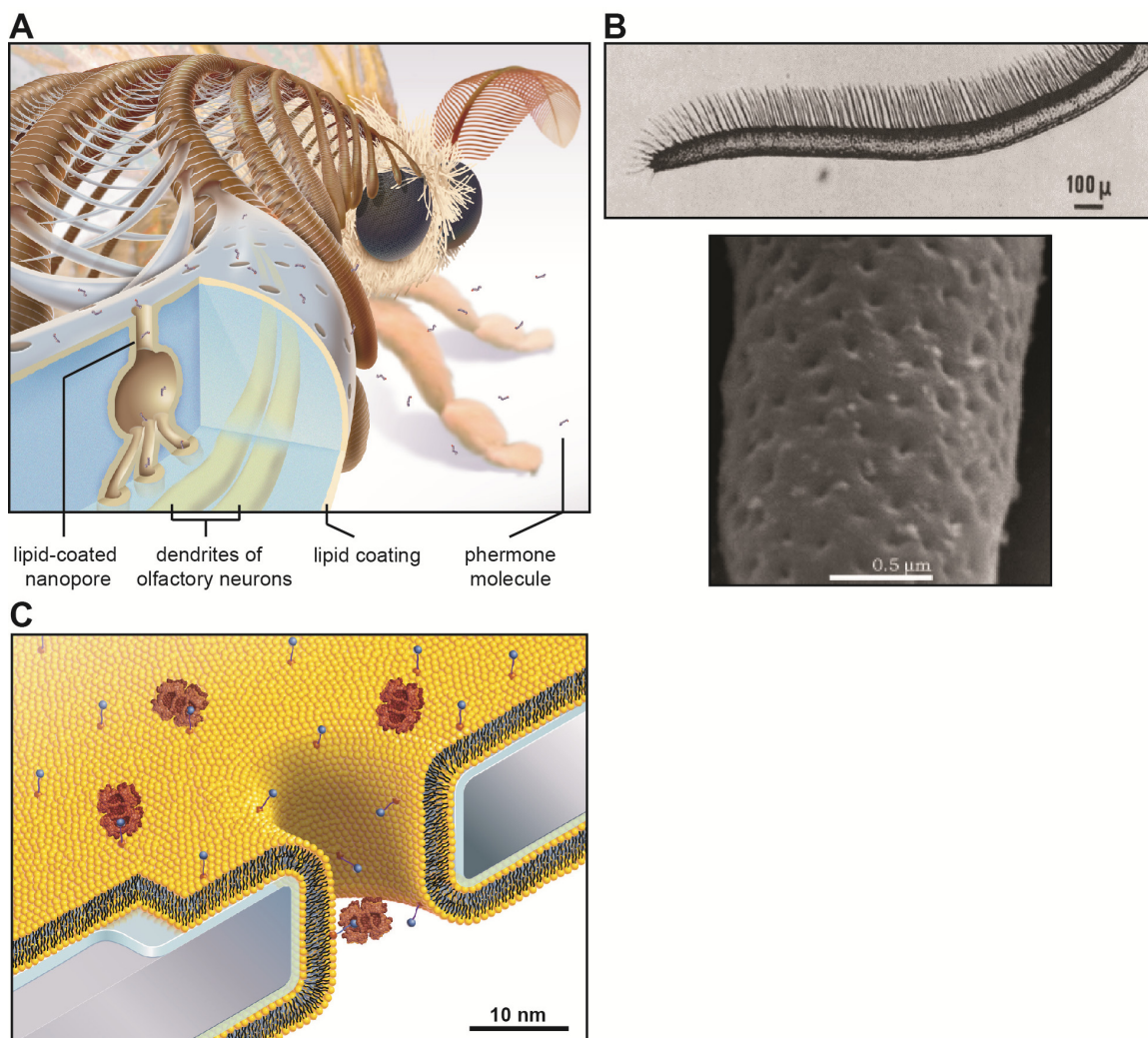


Figure 1.4 | Lipid-coated nanopores perforate the exoskeleton of olfactory sensilla in the antenna of many insects and serve as a model for synthetic nanopores with fluid walls. (A) Illustration of a magnified cross-section through one sensillum in the antenna of the silk moth *Bombyx mori*. Capture, pre-concentration, and subsequent translocation of pheromones to dendrites of olfactory neurons in these sensilla is thought to occur through lipid-coated nanopores and pore tubules (95, 97-100). (B) Electron micrographs of an antenna hair with thousands of sensilla and a close-up micrograph of a sensillum perforated with nanopores. Adopted from (95, 97-100). (C) Cross-section illustration of a synthetic nanopore (grey) and the concept of a nanopore with fluid walls for capturing specific proteins by using fluid lipid bilayers (yellow and black). Adopted from (104).

In Chapter 2, we describe the process of creating nanopores with fluid walls and many of the advantages associated with this coating. Briefly, the fluid wall structure is achieved *via* formation of a supported lipid bilayer on the synthetic substrate and interior walls of the nanopore (Fig. 1.4B). This simple strategy enabled various chemically reactive groups to be on the surface by including different lipids in the coating, permitted inclusion of mobile ligands in the fluid bilayer coating, and minimized non-specific

interactions between proteins and the pore walls. Chapter 2 demonstrates that lipid-anchored ligands could be used to concentrate proteins on the fluid surface and move these proteins through the nanopore in a controlled and predictable speed based on the viscosity of the bilayer coating. Moreover, the frequency of translocation events was related to the affinity of the protein for the mobile ligand. Chapter 2 demonstrates the ability of nanopores with fluid walls for determining the size, charge, and affinity for a ligand of a protein in a single experiment.

In Chapter 3, we demonstrate the use of nanopores with fluid walls for determining a protein's shape as spherical, prolate, or oblate. For non-spherical proteins, we demonstrate that the fluctuations in the current through the pore due to the rotation of a single protein in the nanopore enabled determination of that individual protein's volume, shape, dipole moment and rotational diffusion coefficient. Consequently, this chapter demonstrates the possibility of nanopores to perform the multiparameter characterization of an individual protein that would be required to differentiate proteins in a mixture.

In Chapter 4, we present a model to describe the frequency of protein translocations quantitatively based on their affinity for a mobile ligand in the fluid bilayer coating and the two-dimensional diffusion of these lipid-anchored proteins on the bilayer coating. Kinetic and equilibrium binding parameters are determined. The chapter confirms the ability of nanopores with fluid walls for determining the size, charge, shape, and affinity for a ligand of a protein in a single experiment.

In Chapter 5, we show that nanopores with fluid walls are resistant to clogging and take advantage of this fact to analyze single aggregates of amyloid- β peptide. Amyloid- β aggregates are implicated in Alzheimer's disease, and in order to determine how amyloid- β contributes to Alzheimer's disease pathology, characterization of the size distributions of amyloid- β aggregates in solution is required. This chapter demonstrates the first nanopore-based assay, to the knowledge of the author, that analyzes such heterogeneous and biologically relevant aggregates of peptides. We report accurate determination of the size of amyloid- β aggregates and demonstrate the ability to track the size distribution of aggregates in solution over time.

In Chapter 6, we demonstrate the capability of nanopore-based assays to determine quantitatively the activity of membrane-active enzymes. Since most membrane-active enzymes modify the charge of lipid head groups, we measured the change in the bulk current through the pore as the enzyme phospholipase D catalyzed the hydrolysis of zwitterionic, neutral lipids to negatively charged lipids. We were able to determine kinetic parameters of phospholipase D and demonstrate the utility of lipid-bilayer coated nanopores for monitoring the activity of this unique class of membrane-active enzymes.

In chapter 7, I summarize the major results and impacts of this work and provide suggestions for future research, and in the Appendix, I provide a discussion of the electrical noise in these experiments and a list of the equations that govern these experiments.

Chapter 1 References

1. Perrett D (2007) From 'protein' to the beginnings of clinical proteomics. *PROTEOMICS – Clinical Applications* 1(8):720-738.
2. Anderson NL, Anderson NG (2002) The human plasma proteome - history, character, and diagnostic prospects. *Molecular & Cellular Proteomics* 1(11):845-867.
3. Rifai N, Gillette MA, Carr SA (2006) Protein biomarker discovery and validation: The long and uncertain path to clinical utility. *Nat Biotechnol* 24(8):971-983.
4. Ofarrell PH (1975) High-resolution 2-dimensional electrophoresis of proteins. *J Biol Chem* 250(10):4007-4021.
5. Andersson CO (1958) Mass spectrometric studies on amino acid and peptide derivatives. *Acta Chemica Scandinavica* 12(6):1353-1353.
6. Lequin RM (2005) Enzyme immunoassay (eia)/enzyme-linked immunosorbent assay (elisa). *Clinical Chemistry* 51(12):2415-2418.
7. Engvall E (2005) Perspective on the historical note on EIA/ELISA by Dr. R.M. Lequin. *Clinical Chemistry* 51(12):2225.
8. Svedberg T, Hedenius A (1934) The sedimentation constants of the respiratory proteins. *Biological Bulletin* 66(2):191-223.
9. Svedberg T, Rinde H (1924) The ultra-centrifuge, a new instrument for the determination of size and distribution of size of particle in amicroscopic colloids. *J Am Chem Soc* 46:2677-2693.
10. Tiselius A, Hjerten S, Levin O (1956) Protein chromatography on calcium phosphate columns. *Archives of Biochemistry and Biophysics* 65(1):132-155.
11. Hjerten S (1985) High-performance electrophoresis - elimination of electroendosmosis and solute adsorption. *Journal of Chromatography* 347(2):191-198.
12. Nelson RW, Krone JR, Granzow R, Jansson O, Sjolander S (1996) PTO US 5,955,729 (September 21, 1999).
13. Wüthrick K (Nobel Lecture, December 8, 2002) NMR studies of structure and function of biological macromolecules. (http://www.nobelprize.org/nobel_prizes/chemistry/laureates/2002/wutrich-lecture.pdf).
14. Stuhrmann HB (2008) Small-angle scattering and its interplay with crystallography, contrast variation in SAXS and SANS. *Acta Crystallographica Section A* 64:181-191.
15. Stuhrmann HB (1983) Applications of synchrotron radiation in molecular biology. *Acta radiologica Supplementum* 365:16-18.
16. Stuhrmann HB, Gabriel A (1983) A small-angle camera for resonant scattering experiments at the storage ring doris. *Journal of Applied Crystallography* 16(OCT):563-571.
17. Nierhaus KH, *et al.* (1983) Shapes of and distances between components within the large (50s) subunit of escherichia-coli ribosomes. *Physica B & C* 120(1-3):426-435.
18. Nierhaus KH, *et al.* (1983) Shape determinations of ribosomal-proteins insitu. *Proceedings of the National Academy of Sciences of the United States of America-Biological Sciences* 80(10):2889-2893.

19. Crick FHC, Kendrew JC (1957) X-ray analysis and protein structure. *Advances in Protein Chemistry* 12:133-214.
20. Kendrew JC, Perutz MF (1957) X-ray studies of compounds of biological interest. *Annu Rev Biochem* 26:327-372.
21. Serdyuk IN, Zaccai NR, Zaccai J (2007) *Methods in molecular biophysics: Structure, dynamics, and function* (Cambridge University Press, Cambridge, UK).
22. Rigler R, Vogel H eds (2008) *Single molecules and nanotechnology* (Springer-Verlag, Berlin).
23. Maxwell JC (1904) *A treatise on electricity and magnetism* (Clarendon Press, Oxford) 3rd Ed.
24. Fricke H (1953) The electric permittivity of a dilute suspension of membrane-covered ellipsoids. *J Appl Phys* 24(5):644-646.
25. Fricke H (1924) A mathematical treatment of the electrical conductivity of colloids and cell suspensions. *Journal of General Physiology* 6(4):375-384.
26. Velick S, Gorin M (1940) The electrical conductance of suspensions of ellipsoids and its relation to the study of avian erythrocytes. *Journal of General Physiology* 23(6):753-771.
27. Coulter WH (1953) Office USP 2,656,508.
28. (October 9, 2012) <http://www.whcf.org/about/wallace-h-coulter>
29. Gregg EC, Steidley KD (1965) Electrical counting and sizing of mammalian cells in suspension. *Biophys J* 5(4):393-&.
30. Deblois RW, Bean CP (1970) Counting and sizing of submicron particles by resistive pulse technique. *Rev Sci Instrum* 41(7):909-915.
31. Hurley J (1970) Sizing particles with a Coulter counter. *Biophys J* 10(1):74-79.
32. Golibersuch DC (1973) Observation of aspherical particle rotation in Poiseuille flow via the resistance pulse technique. Part 1. Application to human erythrocytes. *Biophys J* 13(3):265-280.
33. Golibersuch DC (1973) Observation of aspherical particle rotation in Poiseuille flow via the resistance pulse technique. Part 2. Application to fused sphere dumbbells. *J Appl Phys* 44(6):2580-2584.
34. Deblois RW, Wesley RKA (1976) Viral sizes, concentrations, and electrophoretic mobilities by nanopar analyzer. *Biophys J* 16(2):A178-A178.
35. Grover NB, Naaman J, Ben-sasson S, Doljansk F, Nadav E (1969) Electrical sizing of particles in suspensions. 2. Experiments with rigid spheres. *Biophys J* 9(11):1415-1425.
36. Grover NB, Naaman J, Ben-sasson S, Doljansk F (1969) Electrical sizing of particles in suspensions. I. Theory. *Biophys J* 9(11):1398-1414.
37. Osborn JA (1945) Demagnetizing factors of the general ellipsoid. *Physical Review* 67(11-1):351-357.
38. Uram JD, Ke K, Hunt AJ, Mayer M (2006) Submicrometer pore-based characterization and quantification of antibody-virus interactions. *Small* 2(8-9):967-972.
39. Uram JD, Ke K, Hunt AJ, Mayer M (2006) Label-free affinity assays by rapid detection of immune complexes in submicrometer pores. *Angew Chem-Int Edit* 45:2281-2285.

40. Uram JD, Mayer M (2007) Estimation of solid phase affinity constants using resistive-pulses from functionalized nanoparticles. *Biosensors and Bioelectronics* 22(7):1556-1560.
41. Uram JD, Ke K, Mayer M (2008) Noise and bandwidth of current recordings from submicrometer pores and nanopores. *ACS Nano* 2(5):857-872.
42. An R, *et al.* (2008) Ultrafast laser fabrication of submicrometer pores in borosilicate glass. *Opt Lett* 33(10):1153-1155.
43. Ito T, Sun L, Crooks RM (2003) Simultaneous determination of the size and surface charge of individual nanoparticles using a carbon nanotube-based Coulter counter. *Anal Chem* 75(10):2399-2406.
44. DeBlois RW, Uzgiris EE, Cluxton DH, Mazzone HM (1978) Comparative measurements of size and polydispersity of several insect viruses. *Anal Biochem* 90(1):273-288.
45. Vonschulthess GK, Benedek GB, DeBlois RW (1980) Measurement of the cluster size distributions for high functionality antigens cross-linked by antibody. *Macromolecules* 13(4):939-945.
46. Saleh BEA, Teich MC eds (2007) *Fundamentals of photonics* (John Wiley & Sons, Inc.), 2nd Ed, p pg. 80.
47. Bezrukov SM, Kasianowicz JJ (2002) *Dynamic partitioning of neutral polymers into a single ion channel* pp 117-130.
48. Bezrukov SM, Vodyanoy I, Parsegian VA (1994) Counting polymers moving through a single-ion channel. *Nature* 370(6487):279-281.
49. Kasianowicz JJ, Brandin E, Branton D, Deamer DW (1996) Characterization of individual polynucleotide molecules using a membrane channel. *Proc Natl Acad Sci U S A* 93(24):13770-13773.
50. Branton D, *et al.* (2008) The potential and challenges of nanopore sequencing. *Nat Biotechnol* 26(10):1146-1153.
51. Manrao EA, *et al.* (2012) Reading DNA at single-nucleotide resolution with a mutant MspA nanopore and phi29 DNA polymerase. *Nat Biotechnol* 30(4):349-U174.
52. Oxford nanopore introduces DNA 'strand sequencing' on the high-throughput gridion platform and presents minion, a sequencer the size of a USB memory stick. (May 18, 2012) <http://www.nanoporetech.com/news/press-releases/view/39>
53. Majd S, *et al.* (2010) Applications of biological pores in nanomedicine, sensing, and nanoelectronics. *Curr Opin Biotech* 21(4):439-476.
54. Healy K, Schiedt B, Morrison AP (2007) Solid-state nanopore technologies for nanopore-based DNA analysis. *Nanomedicine* 2(6):875-897.
55. Dekker C (2007) Solid-state nanopores. *Nat Nanotechnol* 2(4):209-215.
56. Howorka S, Siwy Z (2009) Nanopore analytics: Sensing of single molecules. *Chem Soc Rev* 38(8):2360-2384.
57. Majd S, Yusko EC, MacBriar AD, Yang J, Mayer M (2009) Gramicidin pores report the activity of membrane-active enzymes. *J Am Chem Soc* 131(44):16119-16126.
58. Raillon C, *et al.* (2012) Nanopore detection of single molecule RNAP-DNA transcription complex. *Nano Lett* 12(3):1157-1164.

59. Zhao QT, de Zoysa RSS, Wang DQ, Jayawardhana DA, Guan XY (2009) Real-time monitoring of peptide cleavage using a nanopore probe. *J Am Chem Soc* 131(18):6324-6235.
60. Macrae MX, *et al.* (2009) A semi-synthetic ion channel platform for detection of phosphatase and protease activity. *ACS Nano* 3(11):3567-3580.
61. Mayer M, Semetey V, Gitlin I, Yang J, Whitesides GM (2008) Using ion channel-forming peptides to quantify protein-ligand interactions. *J Am Chem Soc* 130(4):1453-1465.
62. Howorka S, Nam J, Bayley H, Kahne D (2004) Stochastic detection of monovalent and bivalent protein-ligand interactions. *Angew Chem-Int Edit* 43(7):842-846.
63. Movileanu L, Howorka S, Braha O, Bayley H (2000) Detecting protein analytes that modulate transmembrane movement of a polymer chain within a single protein pore. *Nat Biotechnol* 18(10):1091-1095.
64. Kasianowicz JJ, Robertson JWF, Chan ER, Reiner JE, Stanford VM (2008) Nanoscopic porous sensors. *Annual review of analytical chemistry*, Annual review of analytical chemistry, Vol 1, pp 737-766.
65. Yusko EC, Billeh YN, Yang J, Mayer M (2011) Nanopore recordings to quantify activity-related properties of proteins. *Nanopores: Sensing and fundamental biological interactions*, eds Iqbal SM & Bashir R (Springer Publishing Co., New York), pp 203-225.
66. Li J, *et al.* (2001) Ion-beam sculpting at nanometre length scales. *Nature* 412(6843):166-169.
67. Talaga DS, Li JL (2009) Single-molecule protein unfolding in solid state nanopores. *J Am Chem Soc* 131(26):9287-9297.
68. Saleh OA, Sohn LL (2003) Direct detection of antibody-antigen binding using an on-chip artificial pore. *Proc Natl Acad Sci U S A* 100(3):820-824.
69. Han A, *et al.* (2008) Label-free detection of single protein molecules and protein-protein interactions using synthetic nanopores. *Analytical Chemistry* 80(12):4651-4658.
70. Han AP, *et al.* (2006) Sensing protein molecules using nanofabricated pores. *Appl Phys Lett* 88(9): 093901
71. Fologea D, Ledden B, David SM, Li J (2007) Electrical characterization of protein molecules by a solid-state nanopore. *Appl Phys Lett* 91(5):053901.
72. Sexton LT, *et al.* (2010) An adsorption-based model for pulse duration in resistive-pulse protein sensing. *J Am Chem Soc* 132(19):6755-6763.
73. Pedone D, Firnkes M, Rant U (2009) Data analysis of translocation events in nanopore experiments. *Anal Chem* 81(23):9689-9694.
74. Yusko EC, *et al.* (2012) Single-particle characterization of A β oligomers in solution. *ACS Nano* 6(7):5909-5919.
75. Li JL, Talaga DS (2010) The distribution of DNA translocation times in solid-state nanopores. *J Phys-Condens Matter* 22(45).
76. Ding S, Gao CL, Gu LQ (2009) Capturing single molecules of immunoglobulin and ricin with an aptamer-encoded glass nanopore. *Anal Chem* 81(16):6649-6655.

77. Wei R, Gatterdam V, Wieneke R, Tampe R, Rant U (2012) Stochastic sensing of proteins with receptor-modified solid-state nanopores. *Nat Nanotechnol* 7(4):257-263.
78. Vlassiouk I, Kozel TR, Siwy ZS (2009) Biosensing with nanofluidic diodes. *J Am Chem Soc* 131(23):8211-8220.
79. Siwy Z, *et al.* (2002) Rectification and voltage gating of ion currents in a nanofabricated pore. *Europhys Lett* 60(3):349-355.
80. Siwy Z, Heins E, Harrell CC, Kohli P, Martin CR (2004) Conical-nanotube ion-current rectifiers: The role of surface charge. *J Am Chem Soc* 126(35):10850-10851.
81. Siwy ZS (2006) Ion-current rectification in nanopores and nanotubes with broken symmetry. *Advanced Functional Materials* 16(6):735-746.
82. Ali M, *et al.* (2008) Biosensing and supramolecular bioconjugation in single conical polymer nanochannels. Facile incorporation of biorecognition elements into nanoconfined geometries. *J Am Chem Soc* 130(48):16351-16357.
83. Ali M, Schiedt B, Healy K, Neumann R, Ensinger A (2008) Modifying the surface charge of single track-etched conical nanopores in polyimide. *Nanotechnology* 19(8):085713.
84. Hall AR, van Dorp S, Lemay SG, Dekker C (2009) Electrophoretic force on a protein-coated DNA molecule in a solid-state nanopore. *Nano Lett* 9(12):4441-4445.
85. Kowalczyk SW, Hall AR, Dekker C (2010) Detection of local protein structures along DNA using solid-state nanopores. *Nano Lett* 10(1):324-328.
86. Smeets RMM, Kowalczyk SW, Hall AR, Dekker NH, Dekker C (2009) Translocation of RecA-coated double-stranded DNA through solid-state nanopores. *Nano Lett* 9(9):3089-3095.
87. Soni GV, Dekker C (2012) Detection of nucleosomal substructures using solid-state nanopores. *Nano Lett* 12(6):3180-3186.
88. Hall AR, Dekker C (2011) *Molecular detection and force spectroscopy in solid-state nanopores with integrated optical tweezers* pp 35-49.
89. Hornblower B, *et al.* (2007) Single-molecule analysis of DNA-protein complexes using nanopores. *Nature Methods* 4(4):315-317.
90. Sexton LT, *et al.* (2007) Resistive-pulse studies of proteins and protein/antibody complexes using a conical nanotube sensor. *J Am Chem Soc* 129(43):13144-13152.
91. Oukhaled G, *et al.* (2007) Unfolding of proteins and long transient conformations detected by single nanopore recording. *Physical Review Letters* 98(15):158101.
92. Movileanu L (2009) Interrogating single proteins through nanopores: Challenges and opportunities. *Trends in Biotechnology* 27(6):333-341.
93. Griffiths J (2008) The realm of the nanopore. *Anal Chem* 80(1):23-27.
94. Ma L, Cockroft SL (2010) Biological nanopores for single-molecule biophysics. *ChemBiochem* 11(1):25-34.
95. Gullan PJ, Cranston PS (2005) *The insects an outline of entomology* (Blackwell Publishing Ltd, Malden) 3 Ed.

96. Adam G, Delbrueck M (1968) Reduction of dimensionality in biological diffusion processes. *Structural chemistry and molecular biology*, eds Rich A & Davidson N (W. H. Freeman and Company, San Francisco), pp 198-215.
97. Steinbrecht RA (1992) Experimental morphology of insect olfaction - tracer studies, x-ray-microanalysis, autoradiography, and immunocytochemistry with silkworm antennae. *Microsc Res Tech* 22(4):336-350.
98. Steinbrecht RA (1997) Pore structures in insect olfactory sensilla: A review of data and concepts. *International Journal of Insect Morphology & Embryology* 26(3-4):229-245.
99. Zacharuk RY (1985) Antennae and sensilla. *Comparative insect physiology chemistry and pharmacology*, eds Kerkut GA & Gilbert LI (Pergamon Press, Oxford), Vol 6.
100. Locke M (1965) Permeability of insect cuticle to water and lipids. *Science* 147(3655):295-298.
101. Nilsson J, Lee JRI, Ratto TV, Letant SE (2006) Localized functionalization of single nanopores. *Adv Mater* 18(4):427-431.
102. Wang GL, Zhang B, Waymunt JR, Harris JM, White HS (2006) Electrostatic-gated transport in chemically modified glass nanopore electrodes. *J Am Chem Soc* 128(23):7679-7686.
103. Wanunu M, Meller A (2007) Chemically modified solid-state nanopores. *Nano Lett* 7(6):1580-1585.
104. Yusko EC, *et al.* (2011) Controlling protein translocation through nanopores with bio-inspired fluid walls. *Nat Nanotechnol* 6(4):253-260.

Chapter 2

Controlling the Translocation of Proteins through Nanopores with Bio-Inspired, Fluid Walls

Synthetic nanopores have been used to study individual biomolecules in high throughput, but their performance as sensors does not match biological ion channels. Controlling the translocation times of single-molecule analytes and their non-specific interaction with pore walls remain a challenge. Inspired by the olfactory sensilla of the insect antenna, here we show that coating nanopores with fluid bilayer lipids allows the pore diameters to be fine-tuned in sub-nanometre increments. Incorporation of mobile ligands in the lipid conferred specificity and slowed down the translocation of targeted proteins sufficiently to time-resolve translocation events of individual proteins. The lipid coatings also prevented pores from clogging, eliminated non-specific binding and enabled the translocation of amyloid-beta ($A\beta$) oligomers and fibrils. Through combined analysis of their translocation time, volume, charge, shape and ligand affinity, different proteins were identified.

2.1. Introduction

Nanopores hold tremendous promise for applications such as single-molecule binding assays (1-3), portable detection of (bio)warfare agents (4-6), and ultra-fast sequencing of DNA or RNA(7, 8). Nanopore-based experiments provide sub-molecular detail on the composition of individual molecules (9) and on the formation of molecular complexes or aggregates (1, 10). Recording of resistive current pulses during the translocation of single molecules through electrolyte-filled nanopores makes it possible to study their size (1, 4, 6, 11-13), conformation (14, 15), and activity (16, 17) *in situ* (3, 18-23). This technique can characterize hundreds of unlabeled single molecules per second in physiological solutions and yields distributions of measured parameters from these single-molecule investigations (3, 9). However, several challenges should be addressed. First, there is a need for methods that can reliably fabricate synthetic nanopores on the sub-nanometre scale (24) and adjust or actuate pore diameters *in situ* (24, 25). Second, better control of translocation times of single-molecule analytes are still needed to achieve complete time resolution of translocation signals and more accurate determination of the amplitude and duration of resistive pulses (26-28). Third, methods to control the surface chemistry inside synthetic pores (16) may reduce non-specific interactions of analytes with the pore walls (1, 3, 29) and prevent pore clogging (3). Finally, low frequency of translocation events at low analyte concentrations (30) and the poor specificity of the nanopores for analytes (3) need to be improved.

Nature solved most of these challenges in the design of biological nanopores (23). Ion channel proteins, for instance, fold into three-dimensional structures with predetermined locations of individual atoms and precisely defined internal diameters that can be actuated by ligand binding or by changes in the environment of the pore (31). Many ion channel proteins are specific towards ligands and permeants, have minimal non-specific interactions, and irreversible clogging is rare. However, instability of these proteins limits their sensing applications (23).

Insects detect pheromones by translocating odorant molecules through lipid-coated nanopores (diameter 6-65 nm) that span their exoskeleton (Fig. 2.1A) (32-34). These lipid coatings are thought to participate in capture, pre-concentration, and subsequent translocation of odorants to specific receptors on dendrites of olfactory neurons in the

antennae of insects (32, 34). Inspired by this design, we explored whether coating synthetic nanopores of comparable diameters with fluid lipid bilayers could provide benefits for nanopore-based, resistive pulse sensing of single proteins while addressing the associated challenges. Coating synthetic nanopores with organic molecules has been shown but these coatings were fixed on the surface of the pore (35-37). Here we introduce the concept of fluid coatings.

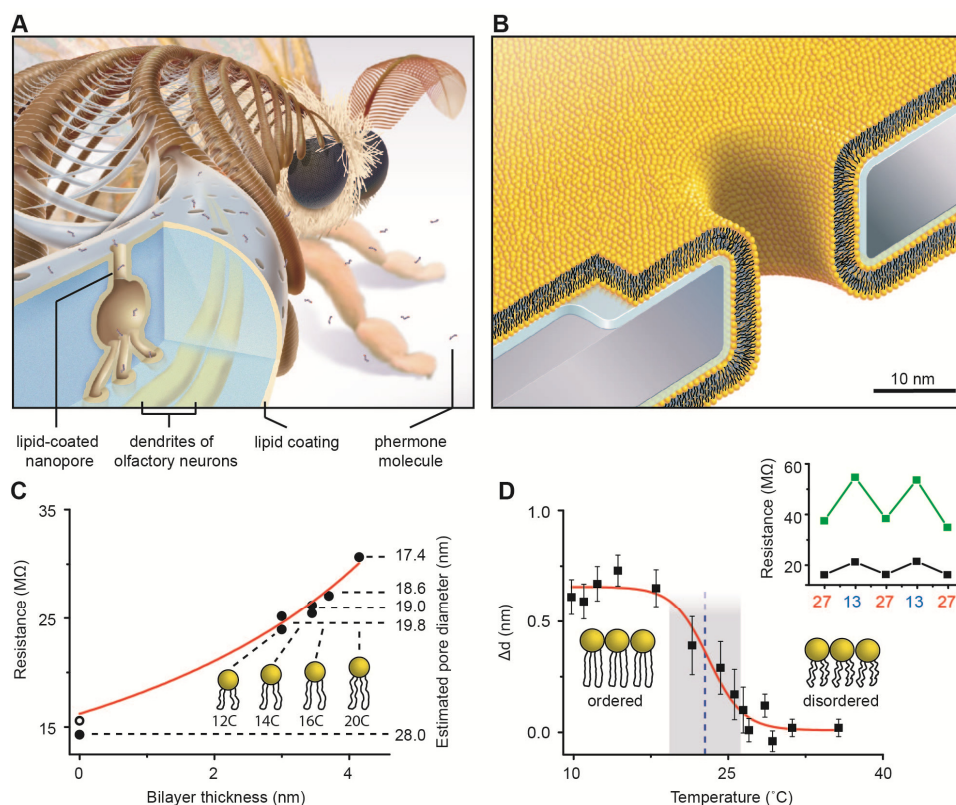


Figure 2.1 | Bioinspired synthetic nanopores with bilayer-coated fluid walls. (A) Drawing showing a cross-section through one sensillum in the antenna of the silk moth *Bombyx mori*. Capture, pre-concentration, and translocation of pheromones through the exoskeleton of these sensilla towards dendrites of olfactory neurons is thought to occur *via* lipid-coated nanopores and pore tubules (32-34). (B) Drawing, to scale, showing a synthetic, lipid-coated (yellow) nanopore in a silicon nitride substrate (grey) and the interstitial water layer (blue). (C) Nanopore resistance and corresponding open pore diameter as a function of the thickness of the bilayer coating (38). Red curve is a best fit of the data to equation (2.1). Numbers underneath the lipid cartoons refer to the number of carbons in their acyl chains (see Table 2.1). (D) Actuation of nanopore diameters by a change in the thickness of the bilayer coating, Δd , in response to a thermal phase transition of DMPC lipids (see Section 2-App.S1). Blue dotted line and grey shaded region represent the mean value and range of phase transition temperatures reported for DMPC lipids (39). Inset: cycling the temperature between 13° and 27° C actuated the pore diameter dynamically as indicated by the larger changes in electrical resistance through a pore with (green squares) than without (back squares) a bilayer.

2.2. Advantages of fluid coatings

To create lipid bilayer-coated nanopores (Fig. 2.1B), we exposed silicon chips that contained a single pore through a silicon nitride window to an aqueous suspension of small unilamellar liposomes (40-43). Spreading of these liposomes on the Si_3N_4 window and on the walls of the nanopore (see Sections 2-App.S1 – 2-App.S3) created a bilayer coating and reduced the nanopore diameter. The thickness and surface chemistry of this coating can be accurately controlled by the choice of lipids in the liposome preparation. For instance, the bilayer thickness is fine-tuned by the length and the number of double bonds in the hydrocarbon tails of the lipids (Fig. 2.1C), whereas the surface chemistry is controlled by the nature of their polar head groups (see Section 2-App.S4).

The capability of fine-tuning the diameter of nanopores is illustrated by the red curve in Fig. 2.1C. This curve resulted from a best fit of the data to a simple physical model that described the electrical resistance through the nanopore, R (Ω), as the sum of four terms: 1) the resistance of the cylindrical nanopore, 2) the access resistance to and from the nanopore (31), 3) the resistance of the cylindrical channel through the silicon nitride window that led to the pore (see Section 2-App.S1 for a schematic drawing), and 4) the access resistance to this cylindrical channel. These four resistances in series are represented in sequence by the terms in equation (1) (see Section 2-App.S1 for a derivation):

$$R = \frac{\rho(l_P + 2d + 2w_L)}{\pi(r_P - d - w_L)^2} + \frac{\rho}{2(r_P - d - w_L)} + \frac{\rho(l_C + 2d + 2w_L)}{\pi(r_C - d - w_L)^2} + \frac{\rho}{4(r_C - d - w_L)}, \quad (2.1)$$

where ρ (Ω m) represents the resistivity of the electrolyte, l_P (m) the length of the cylindrical nanopore, d (m) the thickness of the lipid bilayer (see Table 2.1), w_L (m) the thickness of the interstitial water layer between the bilayer and the silicon nitride wall of the pore (44, 45), r_P (m) the radius of the nanopore, l_C (m) the length of the cylindrical channel through the silicon nitride that led to the pore, and r_C (m) the radius of this cylindrical channel (see Section 2-App.S1 for values of ρ , l_P , r_P , l_C , and r_C).

Table 2.1. Lipids used in this work to coat nanopore walls.

Chemical name	Abbreviation	Acyl chains ^a	Bilayer thickness ^b (nm)
1,2-dilauroyl- <i>sn</i> -glycero-3-phosphocholine	DLPC	(12:0)	3.0 ± 0.1
1,2-dimyristoyl- <i>sn</i> -glycero-3-phosphocholine	DMPC	(14:0)	3.4 ± 0.1
1,2-dipalmitoleoyl- <i>sn</i> -glycero-3-phosphocholine	DΔPPC	(16:1)	3.6 ± 0.1
1,2-dieicosenoyl- <i>sn</i> -glycero-3-phosphocholine	DEPC	(20:1)	4.2 ± 0.1
1-palmitoyl-2-oleoyl- <i>sn</i> -glycero-3-phosphocholine	POPC	(18:1–16:0)	3.7 ± 0.1
1,2-dipalmitoyl- <i>sn</i> -glycero-3-phosphoethanolamine- <i>N</i> -(cap biotinyl)	Biotin-PE	(16:0)	-

^aFor lipids with two identical acyl chains, (c:db) indicates the number of carbons (c) and the number of double bonds (db); for lipids with two different acyl chains, (c1:db1–c2:db2) refer to acyl chains 1 and 2.
^bThickness according to Lewis *et al.* (38).

Equation (2.1) shows that this model estimated the effective, open radius of a pore by taking into account the reduction of its radius and increase of its length as a function of the thickness of the bilayer coating and the thickness of the interstitial water layer between the bilayer and the silicon nitride wall of the pore. A fit of the data in Fig. 2.1C to this model returned a thickness of the water layer of $w_L = 1.2 \pm 0.1$ nm (literature values: 0.5 – 1.7 nm) (44, 45) as the only fitting parameter. The excellent fit of the data to equation (1) ($R^2 = 0.97$, $N = 7$) and the realistic value for the thickness of the water layer, suggest that self-assembled bilayer coatings make it possible to fine-tune and predict the radius of a cylindrical nanopore in increments of two carbon atoms (albeit in a range limited to lipids that can generate stable supported lipid bilayers).

Since the sensitivity and information content of nanopore-based single-molecule experiments depend strongly on the size of the pore, one particularly desirable feature for nanopore sensing would be the ability to adjust the diameter of a nanopore dynamically to the size of various analytes, *in situ*. Fig. 2.1D demonstrates that a thermal phase transition of a coating of DMPC lipids (Table 1) from the ordered gel phase (L_β) to the disordered liquid crystalline phase (L_α) decreased the estimated thickness of the bilayer coating by $\Delta d \approx 0.7$ nm (lit.: 0.9 – 1.1 nm) (39, 46, 47) and made it possible to actuate the diameter of the nanopores dynamically by 1.4 ± 0.1 nm. Fig. 2.1D also shows that the midpoint (dashed blue line) and range (grey area) of the phase transition in the nanopore

coating occurred precisely at the reported temperature for DMPC lipids of $23.5 \pm 2.3^\circ \text{C}$ (39). Changing the diameter of nanopores by a phase transition of lipids may be a relevant mechanism by which insects regulate their water uptake and evaporative loss through lipid-coated nanopores in their exoskeleton (34, 48). In the context of synthetic nanopores, this bio-inspired capability of changing pore diameters constitutes a novel approach to determine thermal phase transition temperatures of lipid bilayers, *in situ*.

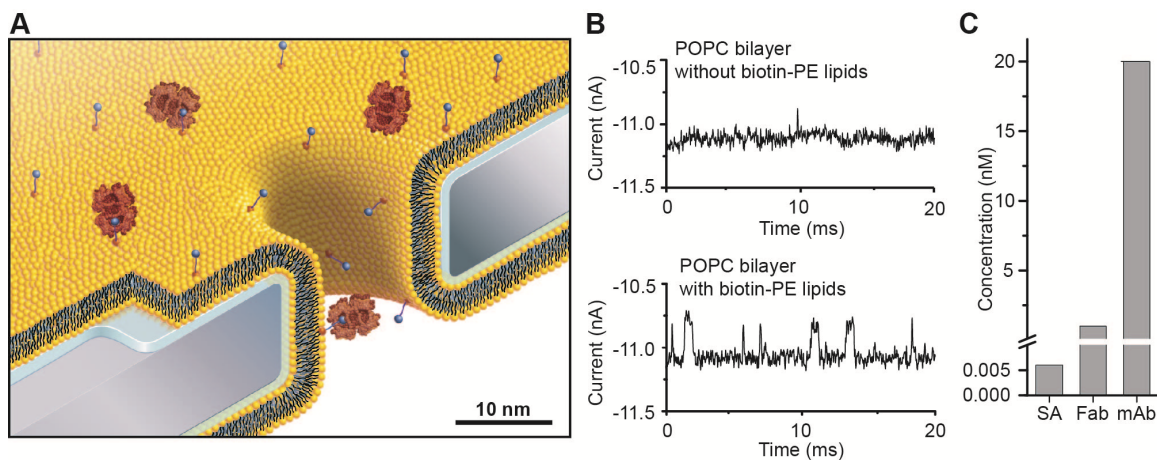


Figure 2.2 | Capture, affinity-dependent pre-concentration, and translocation of specific proteins after binding to ligands on mobile lipid anchors. (A) Cartoon, drawn to scale, illustrating binding of streptavidin (large red) to specific lipid-anchored biotin-PE (blue circles) followed by single molecule translocation of the anchored complex through the nanopore. (B) Current *versus* time traces illustrating capture, pre-concentration, and reduced translocation speed of streptavidin. In the absence of biotin groups, only rare translocation events with short translocation times, t_d , could be detected in electrolytes containing 6 pM streptavidin (top current trace). In contrast, 0.4 mol% of biotinylated lipids in the lipid coating strongly increased the event frequency and slowed down the translocation speed sufficiently to enable complete time resolution of translocation events (bottom current trace). (C) Minimum bulk concentrations of streptavidin, polyclonal anti-biotin Fab fragments, and monoclonal anti-biotin IgG antibodies required to observe at least 30 – 100 translocation events per second.

In addition to fine-tuning and actuating the diameters of nanopores, bilayer coatings provide a straightforward strategy to render nanopore recordings specific for certain analytes by functionalizing the bilayer surface with ligands or receptors. Fig. 2.2 illustrates that adding defined mole fractions of lipids with desired functional groups (here, biotinylated lipids) during the formulation of liposomes and the subsequent formation of a bilayer coating (42) can control the surface density of ligands in and

around the pore. These lipid-anchored ligands, which were mobile within the fluid sheet of the lipid bilayer, could concentrate dilute analytes from the bulk solution to specific ligands on the bilayer surface and deliver these analytes to the pore by two-dimensional diffusion (Fig. 2.2A,B). This same basic principle is thought to occur on the lipid coating of olfactory sensilla in insect antenna, which contributes to the extremely sensitive detection of lipophilic pheromones by insects (32, 34, 49).

Pre-concentrating and translocating analytes that are bound to a fluid surface also made it possible to distinguish between different analytes based on their affinity to the displayed ligand (Fig. 2.2C). For instance, proteins present at picomolar concentrations in the bulk electrolyte solution concentrated at the surface and induced frequent translocation events if they bound with high affinity to lipid-anchored ligands in the bilayer. In contrast, proteins with low affinity to these ligands required more than 300-fold increased bulk concentrations to reach comparable frequencies of time-resolved translocation events (Fig. 2.2C). In the case of streptavidin, polyclonal anti-biotin Fab fragments and monoclonal anti-biotin IgG antibodies, we found that to reach a frequency of 30 - 100 translocation events per second, a concentration of only 0.006 nM streptavidin was required compared to 1 nM of Fab fragment and 20 nM monoclonal antibody. Control experiments revealed that in the absence of biotinylated lipids in the bilayer coating, or in the presence of excess biotin in solution, the frequency of detectable translocation events for each protein was up to 500-fold lower than in the presence of specific capture sites in the bilayer (Fig. 2.2B and Section 2-App.S5).

2.3. Lipid coating enables time-resolved translocation events

The capability of moving captured analytes through pores with fluid walls made it possible to obtain the translocation time, t_d , through the pore as well as the corresponding amplitude of the resistive pulses, ΔI . This information is unique to the fluid nanopore coatings introduced here; previous reports on nanopore recordings with specific, surface-attached binding groups captured analytes on permanently fixed positions (4, 5) and did not allow translocation of bound analytes thereby excluding the possibility to determine t_d or to relate ΔI to the molecular volume of the bound analyte. An additional benefit of translocating analytes that are bound to a lipid anchor emerges if the intrinsic

translocation speed of the unbound analyte through a pore is too fast to resolve t_d and ΔI completely in time – a problem encountered previously by other groups (26-28).

Fig. 2.2B and Section 2-App.S5 show that translocation events of individual proteins could not be fully resolved without lipid-anchored capture sites. In contrast, anchoring analytes to lipids during their passage through the pore had the advantage that the translocation speed was dominated by the high viscosity of the bilayer coating rather than the low viscosity of the aqueous electrolyte in the pore (50). The resulting, prolonged translocation times enabled time-resolved detection of t_d (Fig. 2.3) and ΔI (Fig. 2.4) combined with accurate, quantitative characterization of individual proteins. Alternative strategies for prolonging the translocation time by increasing the length of the pore or the viscosity of the electrolyte or by reducing the applied voltage have been associated with a reduction of the amplitude of translocation events and reduced the signal to noise ratio (28). In contrast, bilayer coatings with fluid capture sites can fine-tune the viscosity of the bilayer and prolong the translocation times of lipid-anchored analytes while the conductivity of the aqueous electrolyte remains unchanged.

Fig. 2.3A demonstrates that acyl chains with increasing length and saturation could slow down translocation speeds. For instance, POPC lipids with one monounsaturated acyl chain of 18 carbon atoms and a second saturated acyl chain of 16 carbons generated approximately 1.4 times more viscous bilayers than D Δ PPC lipids with two monounsaturated acyl chains of 16 carbons. These two bilayer coatings resulted in most frequently observed translocation times for streptavidin of $114 \pm 15 \mu\text{s}$ in the POPC coating compared to $81 \pm 10 \mu\text{s}$ in the D Δ PPC coating (Fig. 2.3A). Translocation speeds could be slowed down even further by adding 50 mol% cholesterol to a POPC bilayer; in this case the most frequently observed translocation time of Fab fragments doubled from $78 \pm 5 \mu\text{s}$ to $175 \pm 4 \mu\text{s}$ (Fig. 2.3B).

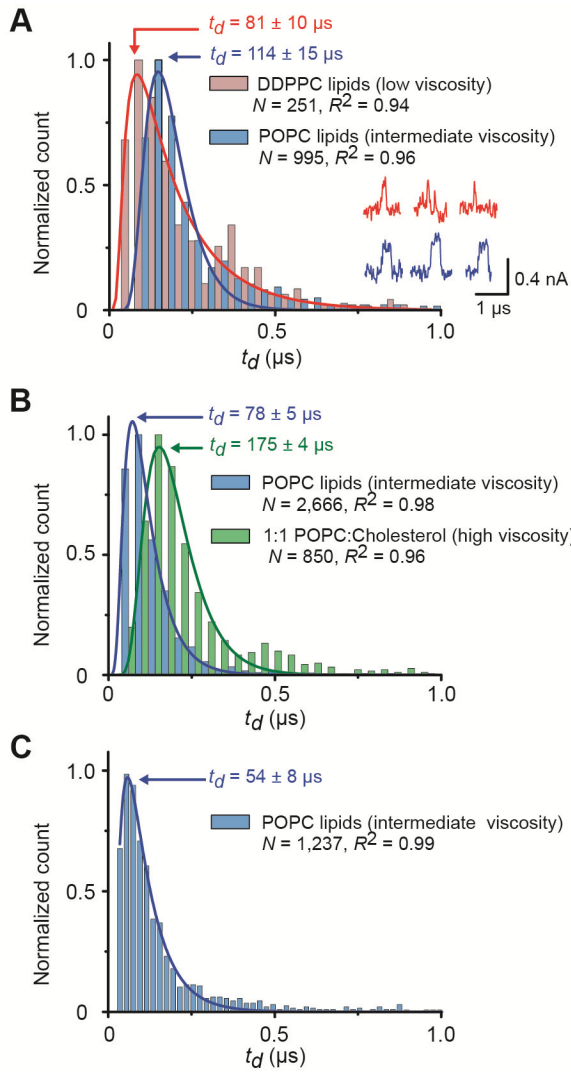


Figure 2.3 | Controlling the translocation times, t_d , of single lipid-anchored proteins by the viscosity of the bilayer coating and distinguishing proteins by their most probable t_d values. (A) Distribution of translocation times of streptavidin. Insets: current *versus* time traces illustrating that t_d could be prolonged more with intermediate viscosity POPC bilayers (blue current traces) than with low viscosity DDPPC bilayers (red current traces). (B) Translocation of anti-biotin Fab fragments through nanopores with bilayers of intermediate viscosity (POPC) or high viscosity (~49 mol% cholesterol and 50 mol% POPC). (C) Translocation of anti-biotin antibodies through a pore with a coating of intermediate viscosity (POPC). Red, blue, and green curves represent a best fit of the corresponding data to a biased diffusion first passage time model (14) (equation 10-App.2 in Section 2-App.S5). All bilayers contained 0.15 - 0.4 mol% biotin-PE. See Sections 2-App.S7 and 2.App.S9 for binning methods, errors of t_d , and measurement errors.

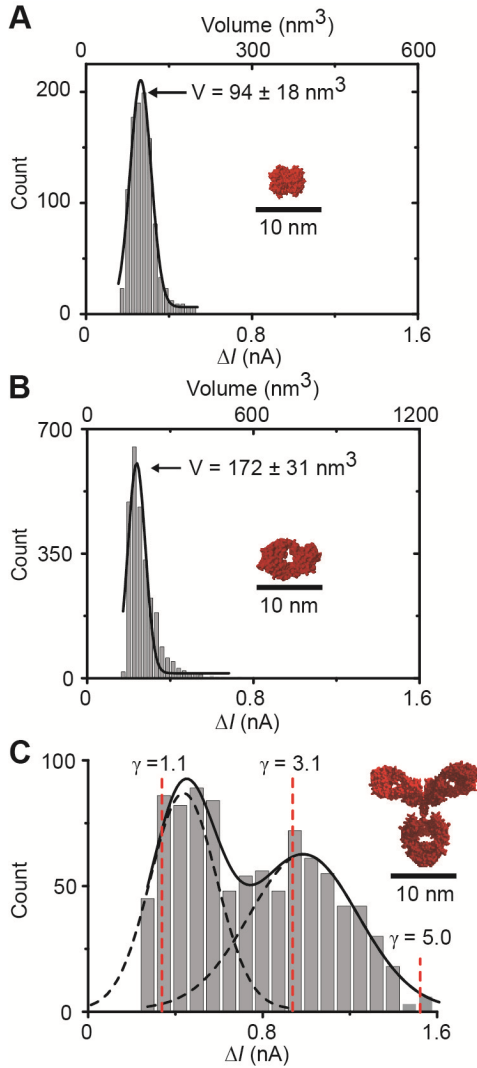


Figure 2.4 | Distribution of ΔI values and corresponding molecular volumes and shape factors of individual proteins translocating through bilayer-coated nanopores with biotinylated lipids. (A-C) Translocation of streptavidin (A), anti-biotin Fab fragments (B) and anti-biotin antibodies (C); the dashed red lines indicate ΔI values that would be expected for IgG antibodies with a volume of 347 nm^3 and different shape factors γ ; see Section 2-App.S6 for a schematic illustration and discussion of shape factors (51, 52).

Complete time resolution of translocation events of lipid-anchored proteins allowed us to determine the volume of individual translocating proteins based on accurate acquisition of the amplitude of resistive pulses, $\Delta I(t)$. Fig. 2.4 shows amplitude distributions of the resistive pulses for three different biotin-binding proteins. We used equation (2.2) to estimate the transiently excluded volume of electrolyte, $\Lambda(t)$ (m^3) during the translocation of these three proteins (12, 13, 53).

$$\Delta I(t) = \frac{\gamma V_a \Lambda(t)}{\rho(l_p + 1.6r_p)^2} S\left(\frac{r_p}{d_M}\right) \quad (2.2)$$

In equation 2.2, γ (unitless) represents a shape factor (52) with a value of 1.5 for spheres, V_a (V) is the total applied voltage, and $S(r_p/d_M)$ is a correction factor that depends on the

relative values of r_P and the diameter of the molecule, d_M . Like most groups, we used a value of 1 for $S(r_P, d_M)$ for all calculations (12, 13). Since $\Lambda(t)$ from the translocation of spheroidal particles is approximately equal to the molecular volume of the particles(14, 29), we were able to estimate the molecular volumes of streptavidin ($94 \pm 18 \text{ nm}^3$; lit. value: $105 \pm 3 \text{ nm}^3$)(54), Fab fragments ($172 \pm 31 \text{ nm}^3$; lit. value: $\sim 140 \text{ nm}^3$)(55), and antibodies ($308 - 696 \text{ nm}^3$; lit. value: $347 \pm 15 \text{ nm}^3$)(51). The distributions of ΔI values for streptavidin (Fig. 4a) and Fab fragments (Fig. 2.4B) were significantly narrower than the distribution for the antibodies (Fig. 2.4C). Since control experiments revealed that the broad distribution was not caused by contamination of the antibody sample with other proteins (see Section 2-App.S6), we attribute the broad distribution of ΔI values in Fig. 2.4C primarily to the complex molecular shape of IgG antibodies ($\gamma \neq 1.5$) compared to the approximately spherical shape ($\gamma \approx 1.5$) of streptavidin and Fab fragments (for a detailed discussion on the proposed effect of molecular shape on ΔI , see Section 2-App.S6).

2.4. Determining translocation time and charge of proteins

Fig. 2.3 shows that different proteins moved through the nanopores at different distributed speeds as expected for biased diffusion first passage time processes (14). Because we performed the experiments with streptavidin using a different pore (see Table 1-App.2 for dimensions of pores used for all experiments), a direct comparison of the most frequently observed t_d values was only possible between Fab fragments ($78 \pm 5 \mu\text{s}$, blue bars in Fig. 2.3B) and monoclonal antibodies ($54 \pm 8 \mu\text{s}$; Fig. 2.3C). The observed differences in t_d values added a third dimension for distinguishing between different proteins in addition to comparing their affinity to specific ligands based on the frequency of translocation events (Fig. 2.2C) and quantifying their molecular volumes based on ΔI values (Fig. 2.4A-C).

Since the translocation speed of different lipid-anchored proteins varied, we hypothesized that the fluid nature of the pore walls may minimize non-specific adsorption processes and open the door to determining the net charge of proteins. To test this hypothesis, we developed the simplest possible model that yields a relationship between t_d of a lipid-anchored protein and the net charge of this protein, $|z| \times e$, based on a model

introduced recently by Sexton *et al.* (26). Here z (unitless) is the net valency of the overall charge on the protein and e (C) is the elementary charge of an electron. This model assumed that a charged protein experiences an electrophoretic force that is opposed by the viscous drag inside the pore and leads to a constant drift velocity (l_p/t_d) through the pore. It also assumed that the viscous drag of lipid-anchored proteins is determined by the diffusion constant of the lipid anchor, D_L ($\text{m}^2 \text{s}^{-1}$) in the lipid bilayer rather than by the diffusion constant of the protein in the aqueous electrolyte inside the pore lumen (50). Based on these assumptions, we derived equation (2.3) to predict t_d values theoretically (for a detailed derivation and additional assumptions made, see Section 2-App.S8):

$$t_d = \frac{l_p^2 k_B T}{|z| e V_p D_L} \quad (2.3)$$

Here k_B (J K^{-1}) is the Boltzmann constant, T (K) is temperature and V_p (V) refers to the part of the total applied voltage that drops inside the pore; it does not include the voltage drop due to the access resistance to and from the pore (see Section 2-App.S8).

Equation (2.3) made it possible to compare theoretically predicted t_d values with experimentally determined values for proteins with known net charge. Fig. 2.5 shows this comparison for translocation events of streptavidin at five different pH values in the recording electrolyte and therefore five different values of $|z|$. The excellent agreement between the data (black squares) and the predicted t_d values (red curve) supports the simple model used for the derivation of equation (2.3).

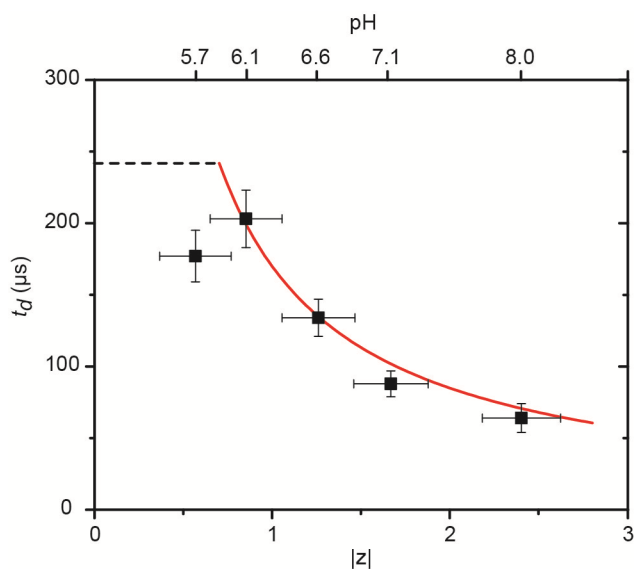


Figure 2.5 | Comparison of experimental and theoretical values of charge-dependent translocation times of streptavidin. Experimental values are shown in black squares and the red curve represents the theoretical prediction by equation (2.3). Dashed black line corresponds to the expected translocation time for streptavidin assuming a translocation event due purely to diffusion in one dimension ($t_d = \langle l_p \rangle^2 / (2D_L)$), i.e. without an electrophoretic effect. The valance $|z|$ of the net charge of streptavidin was varied by the pH of the electrolyte (56). The length of the pore with the bilayer coating was 28 ± 0.2 nm. Note that the red curve is not a best fit to the data; it is the prediction of t_d as a function of $|z|$ according to equation (2.3) when all parameters were fixed to their known values.

Additional support for this model stems from a comparison between two bilayer coatings of different viscosity. In one experiment we coated the nanopore with a POPC bilayer and in the other experiment with a DΔPPC bilayer. Before adding streptavidin to the top compartment of the chips, we determined the lateral diffusion coefficient of lipids in the POPC bilayer ($D_L = 1.13 \pm 0.11 \text{ nm}^2 \mu\text{s}^{-1}$) and in the DΔPPC bilayer ($D_L = 1.56 \pm 0.16 \text{ nm}^2 \mu\text{s}^{-1}$) by fluorescence recovery after photobleaching (FRAP) experiments on the silicon nitride support (see Section 2-App.S2) (57). With these D_L values and a valence of net charge of $|z| = |-1.9 \pm 0.4|$ at pH 7.4 (56), equation (2.3) predicted a translocation time for streptavidin of $126 \pm 29 \mu\text{s}$ in POPC-coated pores and of $91 \pm 21 \mu\text{s}$ in DΔPPC-coated pores. Experimentally, the most frequently observed translocation time of streptavidin (Fig. 2.3A) was $114 \pm 15 \mu\text{s}$ through pores with a POPC coating (deviation from the predicted value: -10%) and $81 \pm 10 \mu\text{s}$ through pores with a DΔPPC coating (deviation from the predicted value: -11%). The excellent agreement between the theoretically predicted values of t_d and the experimentally measured t_d values as well as the data in Table 2 confirm that translocation times of lipid-anchored analytes were indeed dominated by the viscosity of the bilayer (50) and were hence independent of the shape of the proteins (Fig. 2.3B,C).

These observations raise the possibility to use t_d values, in analogy to migration times in electrophoresis, for distinguishing between, and possibly identifying, specific

proteins. The agreement between theory and experiment also suggests that determining translocation times of lipid-anchored proteins through a bilayer-coated nanopore makes it possible to determine the net charge of proteins. For instance, at pH 7.4, the measured t_d values suggest a net charge between -2.9 and -5.3 for the polyclonal anti-biotin Fab fragments and a net charge of -4.2 ± 0.5 for the monoclonal anti-biotin antibodies (see Section 2-App.S8). These values agree well with results from capillary electrophoresis experiments (see Section 2-App.S8). Moreover, for a protein with known charge, translocation experiments combined with equation (2.3), make it possible to determine – non-optically – the lateral diffusion constants of lipids and therefore the fluidity of bilayers within seconds (Table 2.2). This attribute might be useful to test therapeutic compounds for their propensity to change membrane fluidity (57).

Table 2.2. Comparison of diffusion coefficients of lipid-anchored proteins within the nanopore, D_p , with diffusion coefficients of lipids, D_L , in coatings of two different lipid bilayers on three different nanopores.

Protein	Lipid bilayer ^a	D_L ^b	D_p ^c	ΔD
		($\text{nm}^2 \mu\text{s}^{-1}$)	($\text{nm}^2 \mu\text{s}^{-1}$)	%
SA ^d	D Δ PPC	1.56 ± 0.16	1.7 ± 0.4	+9
SA ^d	POPC	1.13 ± 0.11	1.2 ± 0.3	+6
SA ^e	POPC	1.65 ± 0.17	1.9 ± 0.5	+15
mAb ^f	POPC	1.29 ± 0.13	2.6 ± 0.7	+100
Fab ^f	POPC	1.27 ± 0.13	1.5 ± 0.2	+18

^aAll lipid bilayers also contained 0.15 – 0.4 mol% of biotin-PE. ^bValues for D_L were determined by FRAP as described in Section 2-App.S2. ^cValues for D_p were determined with equation (2.3) based on the most frequently measured values of t_d and values of $|z|$ for SA from Sivasankar *et al.* (56) and values of $|z|$ for mAb and Fab as determined by capillary electrophoresis (see Section 2-App.S8). ^dNanopore dimensions: $r_p = 10.0$ nm, $l_p = 18$ nm. ^eNanopore dimensions: $r_p = 10.5$ nm, $l_p = 18$ nm. ^fNanopore dimensions: $r_p = 16.5$ nm, $l_p = 22$ nm

Finally, the agreement between predicted and experimental t_d values suggests that the measured t_d values are close to the “true” electrophoretic translocation times. In other words, these measured translocation times represent translocation in the absence of non-specific adsorption of proteins to the bilayer coating or to the silicon nitride substrates. This point is important because all single-molecule translocation experiments with proteins reported so far were hampered by non-specific adsorption of proteins to the nanopore walls with regard to accurate determination of t_d values (1, 14, 26). In some

cases, these interactions increased the translocation times of proteins by several orders of magnitude (26).

2.5. Aggregated A β peptides translocate without clogging

Due to the unique capability of fluid bilayer coatings to eliminate non-specific interactions, these pores made it possible to analyze translocation events of molecules that aggregate and have a tendency to clog nanopores. Amyloidogenic peptides, such as Alzheimer's disease-related amyloid- β (A β) peptides (58), belong to this category of molecules. The current *versus* time trace in Fig. 2.6A shows that a nanopore without a bilayer coating clogged within minutes after addition of A β peptides. Despite several attempts, we were never able to detect translocation events from samples of A β peptides with uncoated pores. In contrast, Fig. 2.6B illustrates that coating nanopores with bio-inspired, fluid lipid bilayers incurred non-fouling properties to these pores and made it possible to detect numerous large amplitude translocation events due to the passage of individual A β oligomers and fibrils.

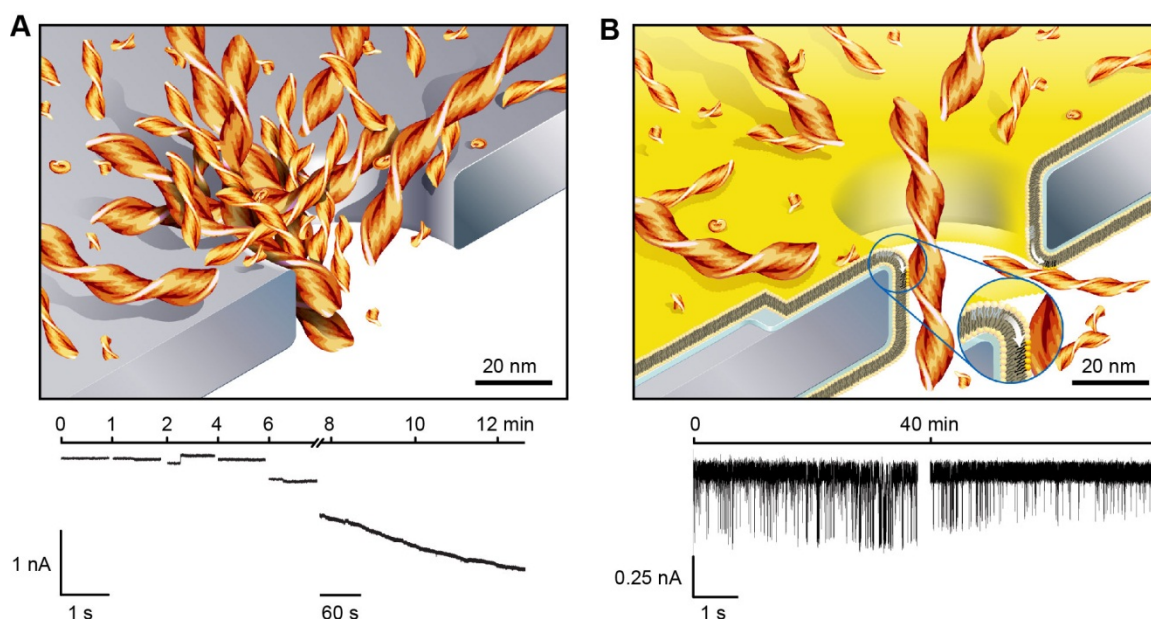


Figure 2.6 | Bilayer-coated nanopores resist clogging and enable the monitoring of the aggregation of amyloid-beta ($A\beta$) peptides. (A) Cartoon illustrating clogging of uncoated nanopores and a typical current *versus* time trace during clogging of a nanopore by $A\beta$ aggregates. This concatenated current trace shows several 1 s recordings and one 5 min recording. (B) Cartoon illustrating translocation of individual $A\beta$ aggregates through a bilayer-coated nanopore with a fluid wall (white arrow in the inset) and a typical current *versus* time trace of translocation events. The bilayer coating conferred non-fouling properties to these pores and enabled resistive pulse recordings over at least 40 min without clogging. Both recordings are 5 s long, one was taken immediately after addition of the $A\beta$ sample and the other one 40 min later. $A\beta$ (1-40) samples were aggregated for 72 h.

2.6. Conclusions

In conclusion, the crucial novelty of lipid-coated, synthetic nanopores is the multifunctional and fluid nature of the self-assembled coating. This singular, bio-inspired strategy addresses many of the unmet challenges in nanopore sensing and is particularly beneficial in the context of single-molecule studies of native proteins. For example, the fluidity of the coating enables capture and concentration of proteins from dilute solutions and permits translocation of lipid-anchored proteins at frequencies that reveal information about their affinity to ligands on these lipid anchors. Fluid coatings also eliminate non-specific adsorption of proteins to the synthetic walls of the pore by translocating captured proteins on top of a fluid, biocompatible lipid bilayer and establish a predictable, quantitative relationship between translocation times and the charge of individual proteins. The viscous character of the fluid coating slows the translocation

speed of lipid-anchored proteins and makes it possible to introduce selectivity while resolving translocation events completely in time. These viscous coatings therefore enable accurate quantitative analyses of the molecular volume and qualitative analyses of the shape of individual proteins. The anti-fouling character of fluid coatings made it possible to translocate aggregated forms of disease-relevant A β peptides through the pore without clogging. This capability may open the door for analyses of the diameter, length, and volume from a large number of individual A β oligomers and fibrils during their aggregation *in situ*.

Chapter 2 Appendix

2-App.Methods. Supporting methods

Lipids and proteins. We obtained all phospholipids from Avanti Polar Lipids, Inc. We purchased the proteins streptavidin (SA) and monoclonal anti-biotin antibody (mAb, B7653) from Sigma Aldrich and polyclonal anti-biotin Fab fragments (Fab, 20938) from Rockland Inc.

Nanopores. We used a focused ion beam to fabricate nanopores in a silicon nitride membrane that was supported by a silicon chip (see Section 2-App.S1 for information on the pores) (59). Prior to experiments, we cleaned the pore-containing chips for at least 30 min with a fresh mixture of 3:1 (v/v) concentrated sulfuric acid and 30% (v/v) aqueous hydrogen peroxide solution at a temperature of 60 – 70 °C followed by rinsing with deionized water and drying with argon gas. To create separate fluid compartments on either side of the nanopore, we mounted the chip between two pieces of cured polydimethylsiloxane (PDMS) (10). After each experiment, we rinsed the silicon chips for 2 – 3 min successively with the following solvents: water, ethanol, methanol, and chloroform. We stored chips in chloroform between experiments.

Formation of supported lipid bilayers. We formed supported lipid bilayers by fusion of small unilamellar vesicles (SUVs) (40-43). We prepared these SUVs as described in Section 2-App.S2. To form the supported lipid bilayer on silicon nitride membranes, we filled the top compartment of the PDMS fluidic setup with 10 – 30 μ L of the aqueous solution with the SUVs and the bottom compartment with a 150 mM KCl solution without liposomes. After 5-10 min, we removed excess SUVs by immersing the entire fluidic setup for 5 – 10 min in a large (500 mL) beaker containing deionized water. Before recordings, the fluidic compartments were filled with the desired electrolyte. Each liposome preparation contained 0.8 mol% of the fluorescently-labeled lipid, 1,2-dipalmitoyl-*sn*-glycero-3-phosphoethanolamine-N-(lissamine rhodamine B sulfonyl) (Rh-PE), for measuring the fluidity of lipid bilayers by fluorescence recovery after photobleaching (FRAP, see Section 2-App.S2).

Electrical resistance as a function of bilayer thickness. We used Ag/AgCl pellet electrodes (Warner Instruments) to monitor ionic currents through electrolyte-filled

nanopores with a patch-clamp amplifier (Axopatch 200B, Molecular Devices Inc.) in voltage clamp mode (i.e., at constant applied voltage). See Section 2-App.S9 for a description of data acquisition methods. We determined the resistance between the electrodes by measuring the current at various applied voltages in the range of ± 0.5 V; the slope of the corresponding current *versus* voltage plots equaled the inverse of the resistance. To measure the resistance as a function of the bilayer thickness, we formed different lipid bilayers on the same chip by using SUVs composed of DLPC, DMPC, D Δ PPC, or DEPC lipids. We cleaned this chip before the formation of each lipid bilayer as described above. The chip used for these experiments contained a nanopore with a diameter of 28 nm and a length of 12 nm (see Section 2-App.S1 for a TEM image) and the recording buffer contained 500 mM KCl and 10 mM HEPES at a pH value of 7.4 ± 0.1 . To measure the resistance of nanopores as a function of temperature, we used a feedback-controlled Peltier Cooler from Warner Instruments (see Section 2-App.S1).

Sensing proteins with biotinylated lipids in the bilayer. We formed supported lipid bilayers on the silicon chip from SUVs containing 0.15 – 0.4 mol% of biotin-PE, 0.8 mol% Rh-PE, and ~ 99 mol% POPC. We used an electrolyte containing 2.0 M KCl and 10 mM HEPES with a pH of 7.4 ± 0.1 and performed all current recordings at -0.1 V. To detect SA, we used a nanopore with an area-equivalent diameter of 19.2 nm (see Section 2-App.S1) and a length of 18 nm (before formation of the bilayer), and we added SA to the top compartment at concentrations of 3.2 - 6.2 pM. To detect mAb and Fab, we used a nanopore with an area equivalent diameter of 33.0 nm and a length of 22 nm; we added mAb or Fab to the top compartment at concentrations of mAb or Fab of 0.1 – 50 nM. See Section 2-App.S9 for a description of the resistive-pulse analysis.

Detection of aggregates of amyloid-beta (A β) peptides. See Section 2-App.S10 for a description of A β sample preparation. We used a nanopore with a diameter of 96 nm and a length of ~ 275 nm (before bilayer coating), which was either uncoated or coated with a POPC bilayer. We added solutions containing A β peptides (residues 1-40) to the top compartment at concentrations of A β of 0.1 to 0.2 mg \times mL $^{-1}$. We used an electrolyte containing 70 mM KCl and 10 mM HEPES with a pH of 7.4 ± 0.1 and recorded resistive pulses at $+0.2$ V.

2-App.S1. Resistance of nanopores as a function of bilayer thickness

S1.1 Model of electrical resistance in electrolyte-filled nanopores. We

explored the simplest possible model for the relationship between the electrical resistance and the geometry of the nanopore. Based on previous work, this model assumes that the smallest constriction of a nanopore and the resistivity of the electrolyte solution in the nanopore determine the total resistance, while the electrical resistance through the bulk electrolyte solution from the electrodes to the chip with the nanopore is negligible (52, 53). In the work presented here, the cylindrical nanopore and channel leading to the pore were the narrowest constrictions (Fig. 1-App.2).

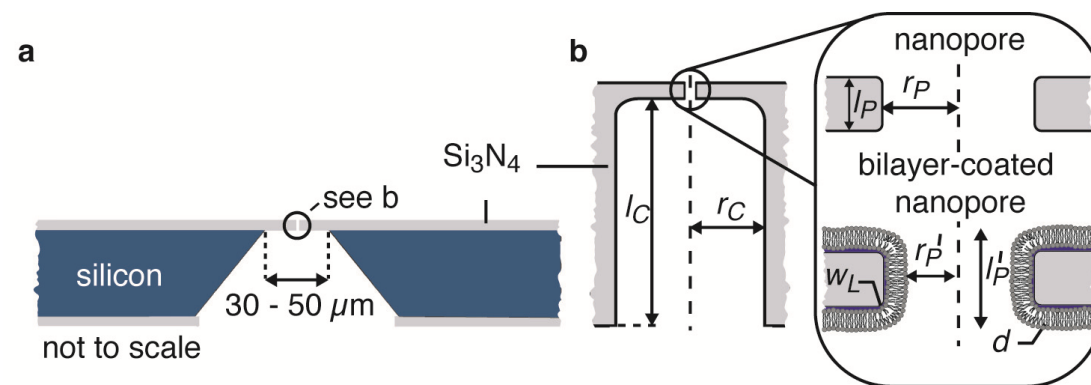


Figure 1-App.2 | Schematic cross-section of the silicon chip and of the nanopore with the channel leading to the pore. (A) Silicon chip (blue) with a silicon nitride layer (grey) on the top; the free-standing part of this Si₃N₄ layer constitutes a window with a nanopore and with a channel through the silicon nitride that leads to the pore. (B) Schematic illustration of this channel with a length l_C of 258 ± 9 nm and a radius r_C of 50 ± 7.5 nm, which led to a nanopore with radii r_P of 16 – 50 nm and lengths l_P of 12 – 22 nm, depending on the chip. Schematic illustration of a lipid bilayer coating with a thickness d and a water layer between the bilayer and the chip with a thickness w_L ; this bilayer coating increases the effective length of the nanopore to $l_P' = l_P + 2(w_L + d)$ and reduces the effective radius to $r_P' = r_P - w_L - d$.

We described the nanopore, and the channel leading to the nanopore, as cylinders, each with a radius r (m) and length l (m) that were filled with an electrolyte with resistivity, ρ ($\Omega \times \text{m}$). Due to the nanoscale diameter of the pore, the electric field lines converge from the bulk solution to the entrance of the nanopore, resulting in an additional resistive component called the access resistance, R_A (31). Equation (1-App.2) quantifies R_A for *one entrance* to a nanopore (31).

$$R_A = \frac{\rho}{4r} \quad (1\text{-App.2})$$

Thus, the total resistance is a function of the resistance of the nanopore, R_P , the access resistance at each side of the pore, R_{AP} , the resistance due to the channel, R_C , and the access resistance from the bulk solution below the chip to the channel, R_{AC} . We treated these resistive components as resistors in series such that equations (2-App.2) and (3-App.2) describe the total resistance between two electrodes on opposite sides of a nanopore:

$$R = R_P + 2R_{AP} + R_C + R_{AC}, \quad (2\text{-App.2})$$

$$R = \frac{\overbrace{\rho l_P}^{\rho l_P}}{\pi r_P^2} + \frac{\overbrace{\rho}^{\rho}}{2r_P} + \frac{\overbrace{\rho l_C}^{\rho l_C}}{\pi r_C^2} + \frac{\overbrace{\rho}^{\rho}}{4r_C}, \quad (3\text{-App.2})$$

where l_P is the length of the nanopore, r_P is the radius of the nanopore, l_C is the length of the channel, and r_C is the radius of the channel (Fig. 1B-App.2).

S1.2 Dimensions of nanopores. We determined the radius of the nanopores, r_P , and of the channels leading to these pores, r_C , from transmission electron microscopy images (Fig. S2). To determine the total resistance of a pore for a given electrolyte, we measured the current through a pore at various applied voltages. For these measurements, we used an electrolyte solution containing 500 mM KCl and 10 mM HEPES at pH 7.4 with a resistivity ρ of $0.1517 \Omega \times \text{m}$ (measured with a calibrated conductance meter). Finally, we determined the length of the pore, l_P , by solving equation (S3) with the measured value of resistance R , the values of r_P and r_C determined from the TEM images, and *the known value for the thickness of the silicon nitride membrane ($275 \pm 15 \text{ nm}$ (59, 60))*. Fig. 2-App.2 shows TEM micrographs of several pores used in this work; the caption lists the dimensions of these pores and specifies for which experiments they were used.

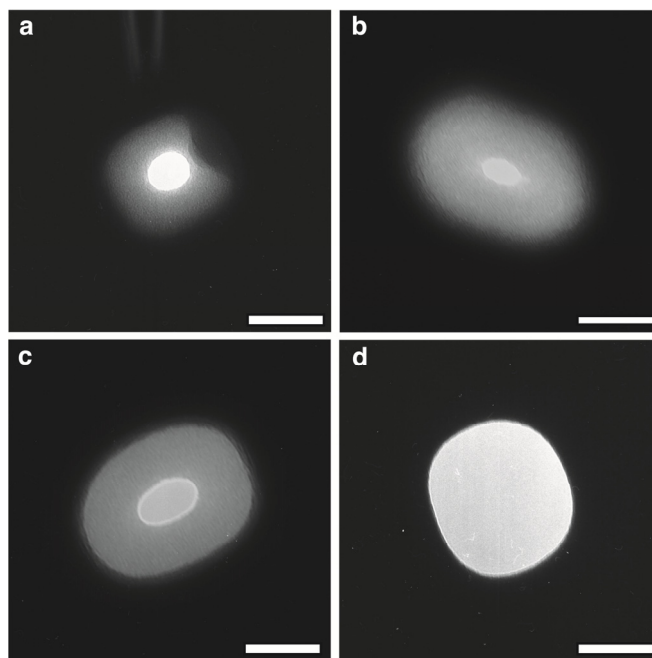


Figure 2-App.2 | Transmission electron micrographs of several nanopores used in this work. The brightest part in the center of each image depicts the shape and size of the nanopore and the surrounding circle with reduced brightness reflects the channel leading to the nanopore. All scale bars are 50 nm. **(A)** Pore used for experiments with bilayers that contained lipids with different acyl-chain lengths ($\langle r_p \rangle = 14$ nm, $l_p = 12$ nm, $r_c = 48$ nm, and $l_c = 264$ nm). **(B)** Pore used for sensing streptavidin ($\langle r_p \rangle = 9.6$ nm, $l_p = 18$ nm, $\langle r_c \rangle = 49$ nm, and $l_c = 258$ nm). **(C)** Pore used for sensing monoclonal anti-biotin antibody and anti-biotin antibody Fab fragment ($\langle r_p \rangle = 16.5$ nm, $l_p = 22$ nm, $\langle r_c \rangle = 53$ nm, and $l_c = 255$ nm). **(D)** Pore used for sensing aggregates of A β peptides. For these experiments, the channel created by a focused ion beam without sculpting was used as the pore ($\langle r_p \rangle = 48$ nm and $l_p = 275$ nm; $r_c = 0$ and $l_c = 0$). Notation of a radius as $\langle r \rangle$ indicates an area-equivalent radius calculated with equations (4-App.2) or (5-App.2). All dimensions refer to the pores before bilayer coating.

For cases in which the cross-section through the nanopore was ellipsoid rather than circular, we calculated an “area-equivalent” radius of the pore, $\langle r_p \rangle$, in such a way that the area of a perfect circle with radius r_p would be equal to the area of the ellipse with x corresponding to the major axis and y corresponding to the minor axis of the elliptical cross-section:

$$\langle r_p \rangle = \sqrt{xy} . \quad (4\text{-App.2})$$

Similarly, we calculated an area-equivalent radius for channels, $\langle r_c \rangle$, through the silicon nitride with an ellipsoid cross-section by:

$$\langle r_c \rangle = \sqrt{xy} . \quad (5\text{-App.2})$$

Table 1-App.2 lists the dimensions of nanopores used for experiments in the main chapter and the corresponding experiments.

Table 1-App.2. Dimensions of all nanopores used for experiments and corresponding experiment and figure. All dimensions refer to the pores before bilayer coating.

Figure	Description of experiment	Pore dimensions (nm)	Notes
2.1C	Resistance as a function of bilayer thickness	$r_p = 14; l_p = 12$	TEM image in Fig. 2A-App.2
2.1D	Resistance during a phase transition of DMPC lipids	$r_p = 13; l_p = 28$	-
2.2B, 2.3A, 2.4A	Sensing streptavidin	$\langle r_p \rangle = 9.6; l_p = 18$	TEM image in Fig. 2B-App.2
2.3B, 2.3C, 2.4B, 2.4C	Sensing anti-biotin Fab fragments and anti-biotin monoclonal antibodies (IgG)	$\langle r_p \rangle = 16.5; l_p = 22$	TEM image in Fig. 2C-App.2
2.5	Sensing streptavidin as a function of charge and pH	$r_p = 10.5; l_p = 18$	-
2.6	Sensing aggregated of amyloid-beta (A β) peptides	$\langle r_p \rangle = 48; l_p = 275$	TEM image in Fig. 2D-App.2

S1.3 Dimensions of nanopores after the formation of a lipid bilayer coating.

To determine the dimensions of a nanopore after forming a lipid bilayer coating, we used the cylindrical pore shown in Fig. 2A-App.2 and added parameters for the thickness of the lipid bilayer, d , and for the thickness of the water layer between the silicon nitride and the lipid bilayer, w_L , to equation (3-App.2) to obtain equation (6-App.2), which is the same as equation (2.1):

$$R = \frac{\rho(l_p + 2d + 2w_L)}{\pi(r_p - d - w_L)^2} + \frac{\rho}{2(r_p - d - w_L)} + \frac{\rho(l_c + 2d + 2w_L)}{\pi(r_c - d - w_L)^2} + \frac{\rho}{4(r_c - d - w_L)}. \quad (6-App.2)$$

Equation (6-App.2) implies that the lipid bilayer and water layer did not conduct ionic current through the nanopore. These two layers, hence, reduced the effective radius of the nanopore by $(d + w_L)$ and increased the effective length of the pore by $2 \times (d + w_L)$ (Fig. 1B-App.2).

Note that we measured currents over tens of seconds in order to determine the resistance of the nanopore, R . As a result, fluctuations in the water layer or in the thickness of the supported lipid bilayer due to possible membrane undulations were averaged. We attribute the excellent agreement between the resistance of the nanopore and the thickness of the lipid bilayers (shown in Fig. 2.2C) to the use of the same chip and lipids with the same chemical head group (phosphatidylcholine) in these

experiments. These conditions resulted in similar interactions between the bilayer, substrate, and water. In addition, we used the same cleaning procedure, same methods of preparing liposomes, and same electrolyte in each experiment.

S1.4 Thermal actuation of the diameter of bilayer-coated nanopores. To calculate the thickness of a lipid bilayer, and hence, the effective open radius of a nanopore as a consequence of a thermal phase transition of the lipids, we described the resistivity, ρ , of the electrolyte as a function of temperature with equation (7-App.2) (61):

$$\rho = \frac{6 \pi \eta}{C A_V e^2 \left(\frac{1}{r_+} + \frac{1}{r_-} \right)}, \quad (7\text{-App.2})$$

where the viscosity of water, η (Pa \times s), as a function of the temperature, T (K), is given by (62):

$$\eta = \left(2.414 \times 10^{-5} \text{ Pa} \cdot \text{s} \right) \times 10^{\left(\frac{247.8\text{K}}{T-140\text{K}} \right)}, \quad (8\text{-App.2})$$

and C (mol \times m⁻³) is the concentration of a monovalent salt, A_V is Avogadro's constant (mol⁻¹), e (C) is the elementary charge of an electron, r_+ (m) is the radius of the hydrated cation, and r_- (m) is the radius of the hydrated anion in the electrolyte. To validate this model, we measured the resistance of a nanopore without a bilayer coating as a function of temperature. We used an electrolyte containing 500 mM KCl and controlled the temperature of the device and electrolyte with a Peltier cooler (Warner Instruments, Hamden CT). Fig. 3-App.2 shows the measured resistance as a function of temperature (squares). Note that the green curve is not a fit to the data; instead it reflects the calculated resistance as a function of temperature based on equations (3-App.2), (7-App.2) and (8-App.2). In equation (8-App.2), we used values for r_+ of 133×10^{-12} (m) for K⁺ ions and for r_- of 181×10^{-12} (m) for Cl⁻ ions (31).

To change the diameter of the nanopore, we coated the pore with a lipid bilayer of DMPC lipids (both acyl chains of DMPC are saturated and contain 14 carbons) and varied the temperature while measuring the resistance (Fig. 3-App.2, circles). We fit the data in Fig. 3-App.2 with equations (6-App.2) – (8-App.2) using the thickness of the bilayer, d , as the only fitting parameter. This fit in the temperature range of 300 – 310 K

returned the red curve ($N = 5$, $R^2 = 0.97$), and in the temperature range of 280 – 290 K, it returned the blue curve ($N = 5$, $R^2 = 0.95$) (Fig. 3-App.2). To calculate the change in d as a function of the thermal phase transition of the lipid bilayer, we used Maple™ 13 to solve equations (6-App.2) – (8-App.2) for d , with all parameters except temperature held constant (Fig. 2.2C). These calculations revealed a change in bilayer thickness, Δd , between the disorderd liquid crystalline phase ($T > 296$ K) and the ordered gel phase ($T < 296$ K) of 0.7 ± 0.04 nm (fit in Fig. 2.2C). This value of Δd is similar to reported values for Δd of DMPC bilayers of 0.9 - 1.1 nm (46, 47).

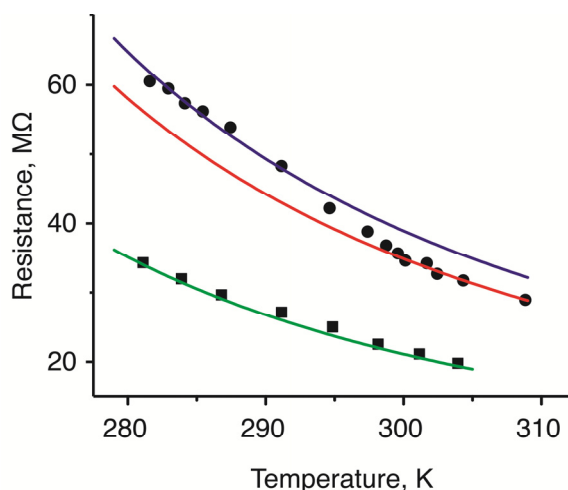


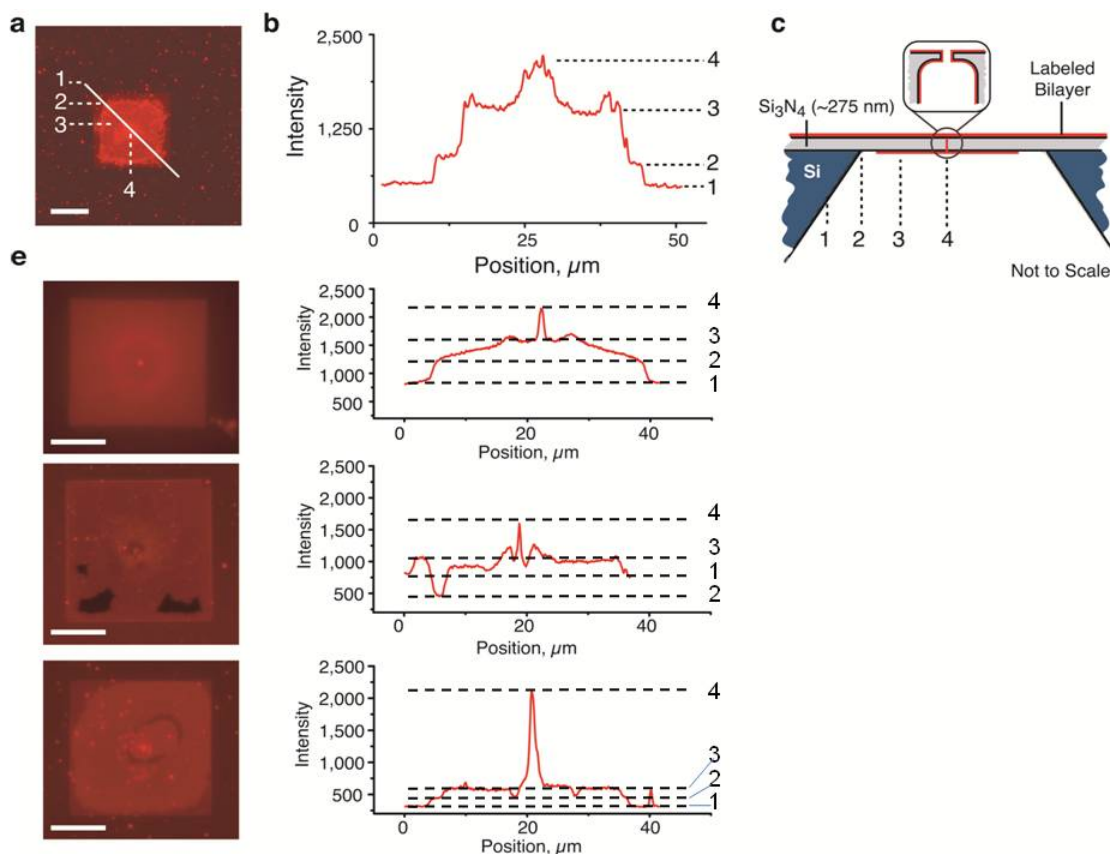
Figure 3-App.2 | Shrinking and actuating the diameter of bilayer-coated nanopores with temperature. Resistance as a function of temperature in a nanopore coated with a bilayer of DMPC lipids, (●), and in a pore without a bilayer coating, (■). The green curve (–) represents a physical model based on equations (3-App.2), (7-App.2), and (8-App.2) and described the resistance through the uncoated nanopore. Inclusion of the bilayer thickness, d , as a fitting parameter by employing equations (6-App.2) – (8-App.2) described the resistance through a bilayer coated-nanopore in the temperature range from 280 K to 290 K (–, $R^2 = 0.95$, $N = 5$) and in the temperature range from 300 K to 310 K (–, $R^2 = 0.97$, $N = 5$). The dimensions of the nanopore before bilayer formation were $r_P = 13$ nm, $l_P = 28$ nm, $r_C = 50$ nm, and $l_C = 247$ nm. The recording buffer contained 500 mM KCl and 10 mM HEPES (pH 7.4 ± 0.1), and the applied potential difference was ± 0.1 V.

2-App.S2. Formation of fluid lipid bilayers on the silicon nitride substrate and determination of translational diffusion constants

Reimhult *et al.* demonstrated that liposome fusion on a silicon nitride surface forms a single supported lipid bilayer (42). To prepare small unilamellar vesicles (SUVs), we dissolved the desired lipids in 100 μ L chloroform to a lipid concentration of

10 mM. We evaporated the solvent under vacuum using a rotary evaporator to form a lipid film in a round bottom glass flask with a volume of 10 mL. We resuspended this lipid film in an aqueous solution containing 150 mM KCl and 10 mM HEPES at pH 7.5 such that the lipid concentration was 2 mM. Finally, we formed SUVs via tip sonication (Branson Sonifier 150) of the solution with a power of 3 – 4 W for ~ 10 min and stored these solutions at 4 °C for up to 4 days. We formed the supported lipid bilayer on the chips as described in 2-App.Methods.

We used epifluorescence microscopy to confirm the formation of a fluid lipid bilayer for experiments with bilayer-coated nanopores. To visualize the lipid bilayer, we prepared all liposomes with 0.8 mol% of lipids labeled with the fluorophore rhodamine B (1,2-dipalmitoyl-*sn*-glycero-3-phosphoethanolamine-N-(lissamine rhodamine B sulfonyl)) (Rh-PE, Avanti Polar Lipids). To form the lipid bilayer, we incubated the top side of the chip in a solution containing Rh-PE labeled liposomes for 5 – 10 min followed by rinsing with pure water for 5 – 10 min. We used a Nikon E600FN upright microscope equipped with an Evolution MP (Media Cybernetics, Canada) camera and a 60× water-dipping objective (NA = 1.00) to image the bilayers. Fig. 4A-App.2 shows a fluorescent micrograph (false-colored in red) that confirmed the presence of a supported lipid bilayer on the silicon nitride substrate. The sharply defined square in the middle of the image is the free-standing silicon nitride membrane. A line scan across the silicon nitride membrane (solid white line) quantified the fluorescence intensity as a function of the position along this line (Fig. 4A-App.2).



Figur 4-App.2 | Fluorescence micrographs of Si-Si₃N₄ chips with a supported lipid bilayer containing Rh-PE lipids and corresponding line scans. (A) Epifluorescence micrograph with a line scan to quantify the fluorescence intensity along the path shown by the solid white line. This pore had an area-equivalent diameter of 33.5 nm and a length of 22 nm without the bilayer coating. (B) Plot of fluorescence intensity as a function of position along the line scan. The numbers 1-4 correspond to the numbers in (A) to the location on the chip indicated in the schematic illustration (C). (D) Additional epifluorescence micrographs showing the diffraction limited spot at the location of the nanopore. Line scans were measured from the opposite corners of the silicon nitride window similar to that in panel (A). From top to bottom these pores had area-equivalent diameters of 31 nm, 33.5 nm, and 20 nm; and lengths of 20 nm, 22 nm, and 18 nm. All bilayers were labeled with 0.8 mol% Rh-PE. All scale bars correspond to 10 μ m.

Interestingly, we observed four values of fluorescence intensity along this path. The lowest intensity occurred in area 1 ($I = 528 \pm 15$); a location in which the bulk silicon chip supported the silicon nitride membrane. Moving along the line scan to an area over part of the free-standing silicon nitride membrane, indicated as area 2, we observed a slightly greater intensity ($I = 873 \pm 31$) than in area 1. We attribute the reduced intensity in area 1 compared to area 2 to destructive interference from light reflected by the bulk silicon chip below area 1 (63). Moving further along the line scan toward the center of the free-standing, silicon nitride membrane (area 3), we observed a fluorescence intensity

approximately twice the intensity ($I = 1,542 \pm 29$) of area 2. This result indicates that area 3 contained approximately twice the amount of fluorescent Rh-PE lipids than area 2 and is consistent with a supported bilayer on both sides of the free-standing, silicon nitride membrane. Finally, area 4, in the center of the free-standing, silicon nitride membrane and at the location of the nanopore, had the greatest fluorescence intensity ($I = 2,222$). We attribute this high intensity to the presence of a lipid bilayer on the vertical walls of the nanopore and channel (see Fig. 1-App.2), and hence, to an increased number of Rh-PE lipids in the optical path. Fig. 4E-App.2 shows three additional fluorescence micrographs with a spot of high intensity in the center of the free standing, silicon nitride membrane at the precise location of the nanopores. The width of these spots at $1/e^2$ of their maximum intensity, $w_{(1/e^2)}$, ranged from 0.8 μm to 1.8 μm . These values are 2-5 times larger than the theoretical diffraction-limited spot size of 0.33 μm that we calculated for this objective with equation (9-App.2) (64):

$$w_{(1/e^2)} = \frac{2\lambda}{n \pi NA}, \quad (9\text{-App.2})$$

where, λ is the wavelength of light (here ~ 700 nm), n is the index of refraction of the medium (here 1.33), and NA is the numerical aperture of the objective (here 1.00). The larger than expected values for the size of the diffraction-limited spot could be due to reflection or refraction occurring at the interface between the aqueous solution and the transparent silicon nitride structure of the nanopore. Furthermore, equation (9-App.2) predicts the size of the smallest spot that can be obtained theoretically given all of the optics were perfect – real microscopes typically cannot reach this theoretical limit.

Regardless of deviations from the theoretically expected spot size, the images in Fig. 4E-App.2 confirm the observations in Fig. 4A,B-App.2 with regard to the fluorescence intensity from bilayers on the chips. These results, in combination with the well-defined shrinkage of the pore diameter by bilayer coatings of various lipids (Fig. 2.2B) and the results from Fig. 2.3 and 2.4, suggest that a supported lipid bilayer formed on the silicon nitride, on the inner walls of the nanopore and channel, and on the underside of the free-standing, silicon nitride membrane.

To confirm the fluidity of the supported lipid bilayers and to determine lateral diffusion constants of the lipids, we performed fluorescence recovery after

photobleaching (FRAP) experiments (Fig. 4A,B-App.2) on the bilayer at a location outside, but near, the free-standing, silicon nitride membrane (*i.e.*, in area 1 of Fig. 4A-App.2) (57). We analyzed these images by calculating the difference between the mean fluorescence intensity of the photobleached spot and a second spot on the same bilayer that was not photobleached. We normalized to the maximum difference between these two intensities and determined the diffusion coefficients by the equation, D_L ($\text{nm}^2 \times \mu\text{s}^{-1}$) = $0.224 \times \omega^2$ (nm^2) / $t_{1/2}$ (μs), where ω is the radius of the bleached spot and $t_{1/2}$ is the half time of the fluorescence recovery (65, 66). We obtained the value of $t_{1/2}$ from an exponential curve fit through the data (Fig. 5B-App.2). On the chip used in Fig. 5-App.2 and shown in Fig. 2-App.2, the diffusion coefficient for bilayers containing POPC lipids was $1.13 \pm 0.13 \text{ nm}^2 \times \mu\text{s}^{-1}$ and for bilayers containing D Δ PPC lipids it was $1.56 \pm 0.16 \text{ nm}^2 \times \mu\text{s}^{-1}$. These values are close to reported values of diffusion coefficients of supported bilayers, which range from $2 \text{ nm}^2 \times \mu\text{s}^{-1}$ to $5 \text{ nm}^2 \times \mu\text{s}^{-1}$ and are typically obtained on glass or SiO_2 surfaces instead of Si_3N_4 surfaces (67, 68).

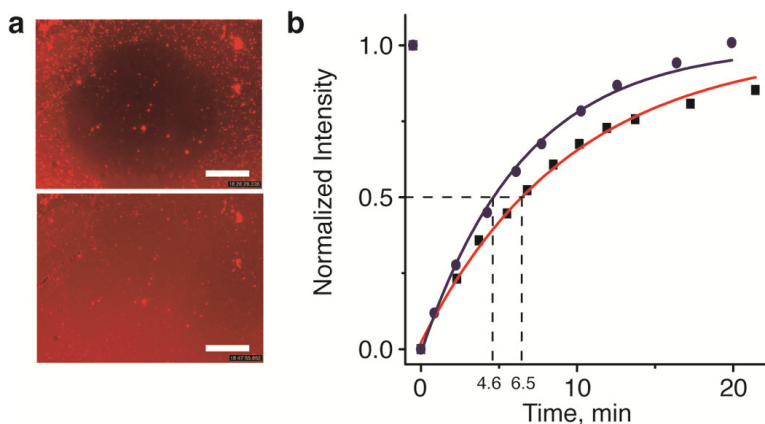


Figure 5-App.2 | Fluorescence micrographs for determining bilayer fluidity by fluorescence recovery after photobleaching (FRAP) experiments. (A) Epifluorescence micrographs indicating the recovery of fluorescence in a photobleached spot of the lipid bilayer on the Si-Si₃N₄ chip. (B) Plot of intensity *versus* time from two separate FRAP experiments on a chip that was coated with a bilayer containing 98.8 mol% POPC (■) or with 98.8 mol% D Δ PPC (●). The larger $t_{1/2}$ value for POPC lipids compared to D Δ PPC lipids indicated the increased viscosity of POPC bilayers compared to D Δ PPC bilayers. All bilayers were labeled with 0.8 mol% Rh-PE and contained 0.4 mol% of 1,2-dipalmitoyl-*sn*-glycero-3-phosphoethanolamine-N-(cap biotinyl) (biotin-PE) because the same chips were later used to sense the translocation of streptavidin (Fig. 2.3A and 2.4A). Images in (A) were both contrast enhanced to the same extent to increase clarity. The scale bars correspond to 25 μm .

2-App.S3. Additional evidence for a bilayer coating on the walls of the nanopores

S3.1 Bilayer coatings prevented physisorption of fluorescently-labeled streptavidin. To provide additional evidence that a supported lipid bilayer formed on the walls inside the nanopores, we incubated a chip containing a nanopore with rhodamine-labeled streptavidin (SA-TRITC). We incubated the same piranha-cleaned chip with SA-TRITC in one experiment after forming a supported lipid bilayer on the chip (and in the pore) and in the other experiment before forming the bilayer. Fig. 6-App.2 shows that in the absence of a bilayer coating, SA-TRITC physisorbed to the silicon nitride surface including in the center of the silicon nitride window where a bright spot of fluorescence indicates that SA-TRITC also physisorbed onto the walls inside the uncoated nanopore. Similar to the line scans shown in Fig. 4-App.2, the width of the diffusion limited high intensity spot in Fig. 6A-App.2 was 0.9 μm . In contrast, Fig. 6B-App.2 shows that the same chip, after being cleaned and subsequently coated with a lipid bilayer, did not physisorb a detectable amount of rhodamine-labeled streptavidin. Additionally, at the center of the silicon nitride window and the location of the nanopore, we did not detect an increase in the intensity of fluorescence. This result suggests that the vertical walls inside the nanopore were also coated with a lipid bilayer that prevented the physisorption of SA-TRITC.

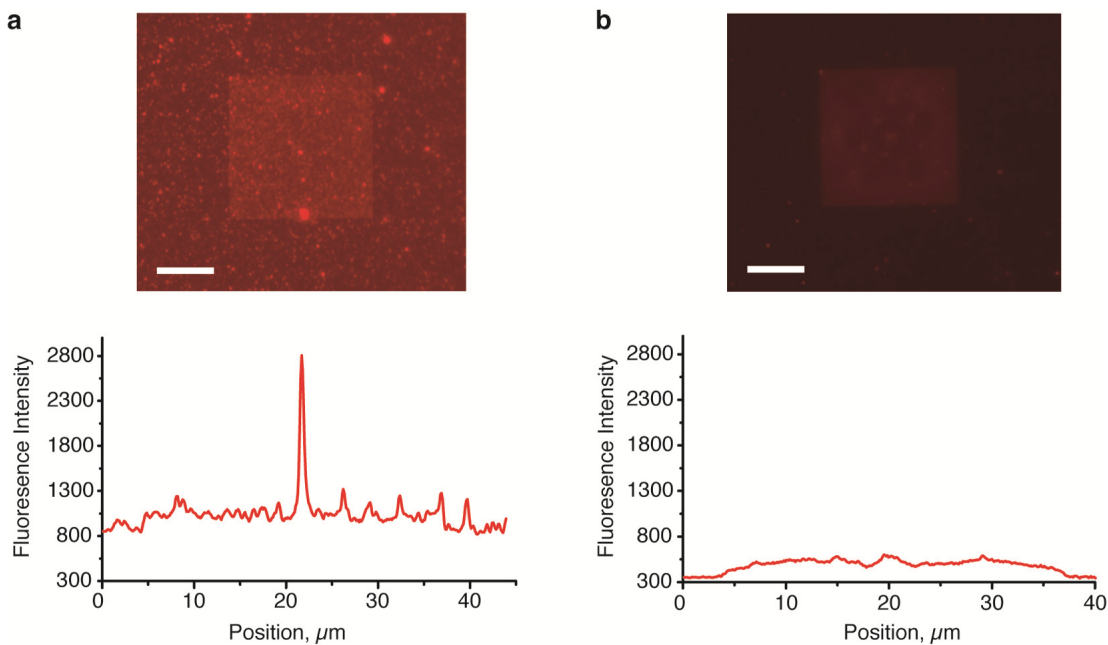


Figure 6-App.2 | Fluorescence micrographs of silicon-nitride windows with a nanopore after exposure to fluorescently labeled-streptavidin. (A) Fluorescence micrograph taken of the silicon nitride window after physisorption of streptavidin-TRITC onto a chip that was cleaned with a fresh 3:1 mixture of concentrated sulfuric acid and a 30% (v/v) hydrogen peroxide solution (Piranha solution). The line scan beneath the image corresponds to the intensity of fluorescence along a diagonal path across the silicon nitride window through the location of the nanopore at its center. (B) Fluorescence micrograph taken of the same silicon nitride window but after formation of a supported lipid bilayer of POPC lipids followed by incubation with streptavidin-TRITC. The line scan beneath the image corresponds to the intensity of fluorescence along a diagonal path across the silicon nitride window through the location of the nanopore at its center. The nanopore for these experiments had an area-equivalent diameter of 110 nm and a length of 275 nm. Scale bars correspond to 10 μm . The same camera and exposure settings were used to acquire both images.

S3.2 Analysis of the electrical current noise provides additional evidence for the formation of a bilayer inside the pore. Since supported lipid bilayers are fluid sheets, lipid molecules within the bilayer are in dynamic motion. In addition, the water layer between the lipid bilayer and the silicon nitride substrate fluctuates around an average value. We hypothesized that the resulting bilayer undulations may influence the electrical noise in current recordings. Fig. 7A,B-App.2 compares the power spectra of the noise as a function of frequency for two chips with nanopores before and after generating a supported lipid bilayer. As expected, when the pore was coated with a fluid lipid bilayer, the noise increased at low frequencies (< 2 kHz) compared to the uncoated pore. Since this increased noise was likely due to dynamic motions consistent with a supported lipid bilayer inside the nanopores, it provides additional evidence for the formation of a lipid bilayer on the walls inside the nanopores. To test this hypothesis, we obtained power spectra of the noise with a chip that contained a very small nanopore with area-equivalent diameter of 9 nm. The diameter of this nanopore was too small for a supported lipid bilayer to form on the interior walls of the pore. In this case, spreading of fluorescently-labeled liposomes on the top side of the chip coated only this top side while no increased fluorescence could be detected at the location of the pore and no doubled fluorescence intensity could be detected from creeping of fluorescent bilayers through the pore to the other side of the silicon nitride window. Fig. 7C,D-App.2 shows that in this case, the electrical noise in the system remained relatively unchanged compared to the nanopores with a diameter large enough to accommodate a bilayer coating inside the pore. In both experiments, we confirmed by FRAP experiments that the bilayer near the pore was fluid. Together these results provide additional evidence for the formation of a fluid lipid bilayer on the walls inside the nanopore.

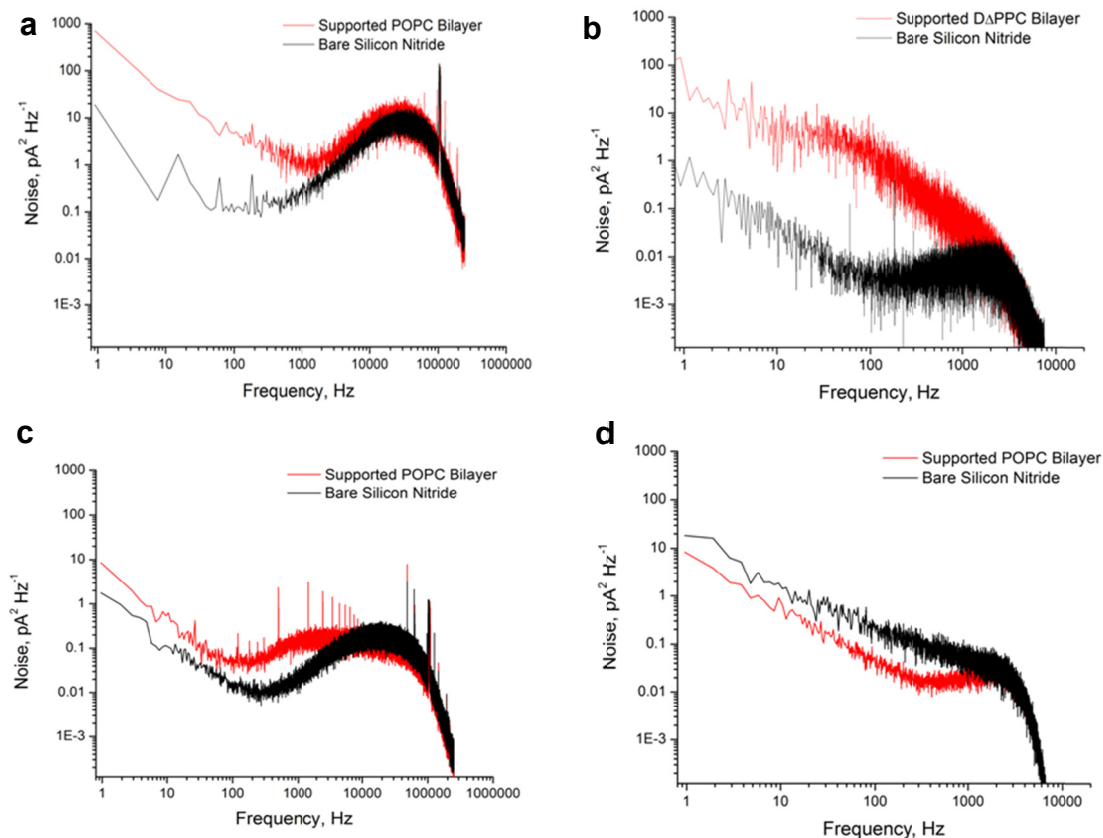


Figure 7-App.2 | Power spectra of the electrical current noise from chips with a bilayer coating and from chips without a bilayer coating. (A, B) Power spectra of the noise before and after formation of supported lipid bilayers from two different lipids on the same chip while a voltage of -0.1 V was applied. The nanopore had a diameter of 28 nm before formation of the supported lipid bilayer (A, POPC lipids; B, D Δ PPC lipids). In (B) the current recording was recorded with the hardware filter of the amplifier set to a cut-off frequency of 2 kHz. (C, D) Power spectra of the noise from two independent experiments with a chip containing a very small area-equivalent diameter of 9 nm, which was too small for the formation of a lipid bilayer inside the nanopore. In (D) the current recording was recorded with the hardware filter of the amplifier set to a cut-off frequency of 2 kHz. The electrolyte for all recordings contained 500 mM KCl and 10 mM HEPES with a pH of 7.4 ± 0.1 .

2-App.S4. Precise control of the surface chemistry

The surface chemistry of bilayer-coated nanopores can be precisely controlled by the nature of the polar head groups of the lipids used in the bilayer coating. To demonstrate this capability, we formed several liposome preparations from POPC lipids that contained different mole fractions of 1,2-dioleoyl-*sn*-glycero-3-phosphate (DOPA), a lipid with a negatively charged head group. After vesicle fusion of these liposomes onto

Si/Si₃N₄ chips with a nanopore to generate the bilayer coating, we measured the electrical resistance through the nanopore. Since under conditions of low ionic strength, positively charged ions accumulate near the surface of a negatively charged bilayer, we expected to observe a decrease in the resistance of the pore with increasing mole fractions of DOPA (69). Fig. 8-App.2 confirms that the resistance of the bilayer coated nanopore decreased with increasing mole fractions of DOPA lipids inside the nanopore walls.

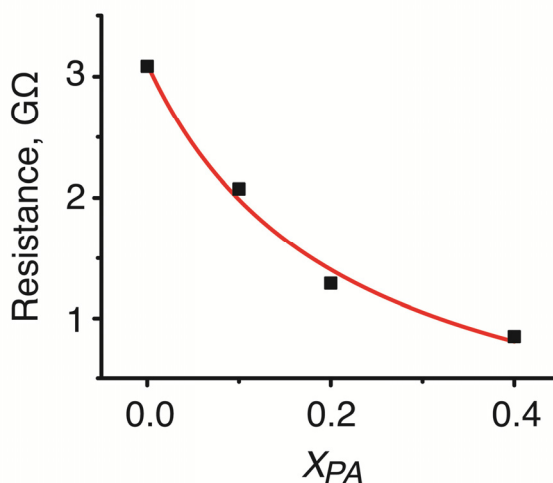


Figure 8-App.2 | Nanopore coatings with increasing mole fractions of negatively charged lipids reduce the resistance of the nanopore in electrolytes with low ionic strength. The supported lipid bilayers were formed from liposomes with the indicated mole fractions, X_{PA} , of DOPA lipids with a background of POPC lipids. The pore used for these experiments had a diameter of 28 nm before the bilayer coating. The electrolyte had an ionic strength of ~2.5 mM and contained 750 μ M CaCl₂ and 250 μ M KCl with a pH of ~ 7.

To demonstrate that this decrease in the resistance was a nanoscopic effect, as predicted by the Gouy-Chapman theory, we compared the resistance of a conical pore (tip diameter 500 nm) whose walls were coated by an electrically neutral bilayer (~99 mol% POPC) to the resistance of the same pore with a negatively charged bilayer coating (~40 mol% DOPA and ~59 mol% POPC). Using the same electrolyte as in Fig. 8-App.2, the resistance of this large pore remained independent of the presence of a neutral or negatively charged bilayer coating (Fig. 9-App.2). This result confirms that the observations in Fig. 8-App.2 were due to nanoscopic phenomena in pores with diameters that are significantly smaller than 500 nm; it also provides additional evidence for the formation of a negatively charged bilayer on the walls inside the nanopore.

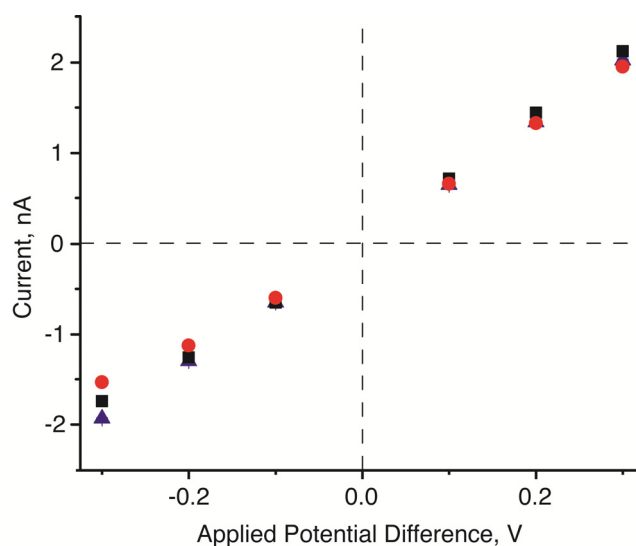


Figure 9-App.2 | Charges on the surface of a pore with a diameter of 0.5 μm did not significantly affect the permeation of ions, and hence resistance, through the pore. Currents were measured as a function of applied potential difference through a conical pore (tip diameter 500 nm) without a bilayer (■), through the same pore with an electrically neutral bilayer coating of POPC lipids (▲), and through the same pore with a bilayer coating containing 40 mol% of negatively charged lipids (●). The recording electrolyte was the same as in Fig. 8-App.2.

2-App.S5. Evidence for the binding of proteins to lipid-anchored ligands in the bilayer and for the translocation of lipid-bound proteins through bilayer-coated nanopores

We used the amplitude of resistive pulses, ΔI , to distinguish the translocation of streptavidin (SA), monoclonal anti-biotin antibody (mAb), and anti-biotin Fab fragments (Fab) through nanopores. These pores were coated with a bilayer that contained biotinylated lipids (biotin-PE) at the specified mole fractions. To confirm that resistive pulses were due to proteins that were bound to biotin-PE, we performed several control experiments that entailed: 1) replacing the electrolyte in the top compartment with a solution that did not contain SA to investigate if the frequency of events would be reduced (as expected for unbound SA) or remain the same (as expected for lipid-anchored SA); 2) presenting an excess of soluble biotin in solution in the presence of mAb on a chip that contained a bilayer-coated nanopore with biotin-PE lipids; and 3) detecting the translocation of SA, mAb, and Fab with bilayer-coated nanopores that did

not contain biotin-PE lipids. We describe these experiments in detail in the following paragraphs, but briefly, when the protein could bind to biotin-PE in the bilayer coating, we observed 20-500 times more frequent translocation events than under conditions in which the protein could not bind to biotin-PE. Furthermore, we observed significantly prolonged translocation times when proteins could bind to biotin-PE; these increased t_d values permitted time-resolved measurements of ΔI (and therefore quantitative estimation of protein volume). Finally, the viscosity of the bilayer coating influenced the translocation time of proteins passing through the nanopore only when proteins could bind to biotin-PE. We show that the diffusion coefficients of the proteins in the nanopore under these conditions were similar to the diffusion coefficients of the lipids in the bilayer coating, and we present a simple model for predicting the translocation times for proteins through a nanopore. We conclude from these results that bilayer-coated nanopores with biotin-PE lipids detected specifically proteins that bound to these lipid anchored biotin groups. Moreover, resistive pulses were due to the translocation of protein-(biotin-PE) complexes through the nanopore because biotin-PE remained mobile within the fluid bilayer coating of the nanopore. The unique ability of bilayer-coated nanopores to exploit the viscosity of a fluid bilayer coating in order to reduce the translocation speed of proteins made it possible to determine the volume of proteins accurately and, consequently, to distinguish anti-biotin Fab fragments from anti-biotin mAbs.

S5.1 Control experiments with streptavidin. We hypothesized that SA would remain bound to biotin-PE for extended periods of time due to the very slow off-rate of the SA to biotin interaction ($k_{off} \sim 10^{-6} \text{ s}^{-1}$) (70). Consequently, after washing the liquid compartments to remove unbound SA from solution, we expected to observe a continuation of frequent resistive pulses with a nanopore coated with a bilayer containing biotin-PE. To start this experiment, we generated a bilayer-coated nanopore that contained 0.15 mol% biotin-PE lipids. After adding 6 pM SA to the electrolyte on top of the fluidic setup, we applied a voltage of -0.1 V and observed resistive pulses at a frequency of $\sim 45 \text{ s}^{-1}$ (Fig. 10A-App.2). Consistent with resistive pulses due to proteins with a net negative charge, we observed a 28-fold decrease in the frequency of resistive pulses after changing the polarity of the applied voltage to +0.1 V (frequency of $\sim 1.6 \text{ s}^{-1}$). After rinsing the

fluidic channels periodically for 3 h, we again applied a voltage of -0.1 V and observed resistive pulses at a frequency similar to the frequency before washing (41 s^{-1} versus 45 s^{-1} , Fig. 10A-App.2). When we repeated this experiment with a bilayer-coated nanopore that did not contain biotin-PE lipids, we observed almost no resistive pulses (frequency of $\sim 0.09 \text{ s}^{-1}$, Fig. 2.2B and Fig. 10A-App.2). Together these results confirm that the observed resistive pulses were due to translocation of SA bound to lipid-anchored biotin through the nanopore while biotin-PE remained mobile within the fluid bilayer coating.

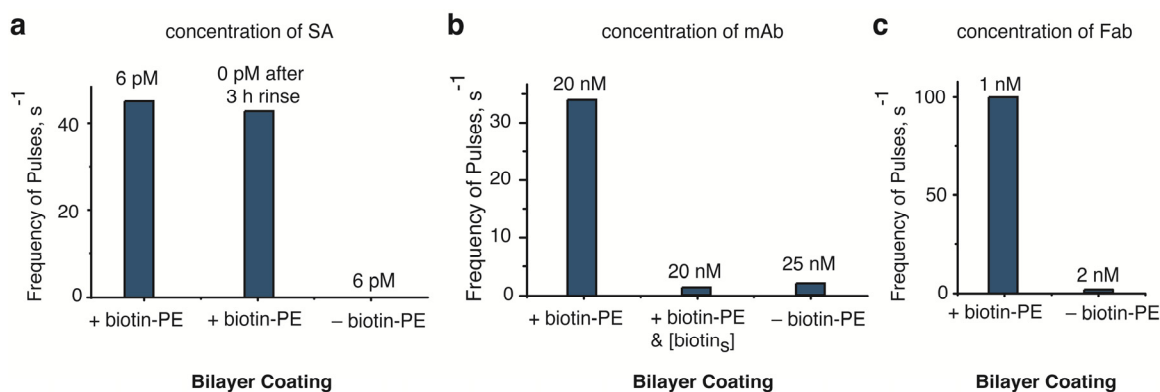


Figure 10-App.2 | Bar graphs comparing the frequency of resistive pulses due to the translocation of streptavidin, anti-biotin mAb, and anti-biotin Fab fragments through bilayer-coated nanopores with biotin-PE lipids and respective control experiments. (A) Frequency of resistive pulses due to translocation of SA through a nanopore with a bilayer coating that contained biotin-PE lipids and after exchanging the electrolyte for 3 h to remove SA from solution compared to a coating without biotin-PE lipids (in this case the frequency of events was 0.09 s^{-1} and is too low to be seen as a bar). **(B)** Frequency of resistive pulses due to the translocation of anti-biotin mAb through a nanopore with a bilayer coating that contained biotin-PE lipids compared to the same experiment after adding $10 \mu\text{M}$ of soluble biotin to the solution and compared to an experiment with a nanopore coating that did not contain biotin-PE lipids. **(C)** Frequency of resistive pulses due to the translocation of anti-biotin Fab through a nanopore with a bilayer coating that contained biotin-PE lipids compared to a coating without biotin-PE lipids. The concentrations of the proteins are shown above the bars. Bilayers were formed from $\sim 99 \text{ mol}\%$ POPC, $0.8 \text{ mol}\%$ Rh-PE, and if indicated, $0.15 \text{ mol}\%$ biotin-PE.

S5.2 Excess free biotin in solution abolished resistive pulses due to anti-biotin mAb. To provide additional evidence for the specificity of detection of proteins that were targeted by lipid-anchored biotin (i.e. streptavidin, anti-biotin mAb, or anti-biotin Fab fragments) with bilayer-coated nanopores, we performed a control experiment by adding a high concentration of soluble biotin ($10 \mu\text{M}$) to an ongoing experiment with a bilayer-coated nanopore that contained biotin-PE. We hypothesized that the excess biotin

in solution would compete for biotin binding sites on these proteins, and consequently, the frequency of resistive pulses after the addition of biotin would decrease. To start this experiment, we coated a nanopore with a bilayer that contained biotin-PE lipids. After adding 20 nM anti-biotin mAb to the solution in the top fluid compartment, we observed resistive pulses at a frequency of 34 s^{-1} (Fig. 10B-App.2 and 11A-App.2). After adding 10 μM soluble biotin to the solution, we observed significantly fewer resistive pulses (frequency of 1.3 s^{-1}) demonstrating that approximately 96% of the resistive pulses in Fig. 11A-App.2 were due to mAb that was bound to biotin-PE (Fig. 10B-App.2 and Fig. 11B-App.2). This result indicates that the detection of the proteins (i.e. streptavidin, mAb, or Fab) required binding of the proteins to biotin-PE lipids and that the proteins moved through the nanopore while bound to mobile biotin-PE lipids in the fluid, lipid bilayer coating.

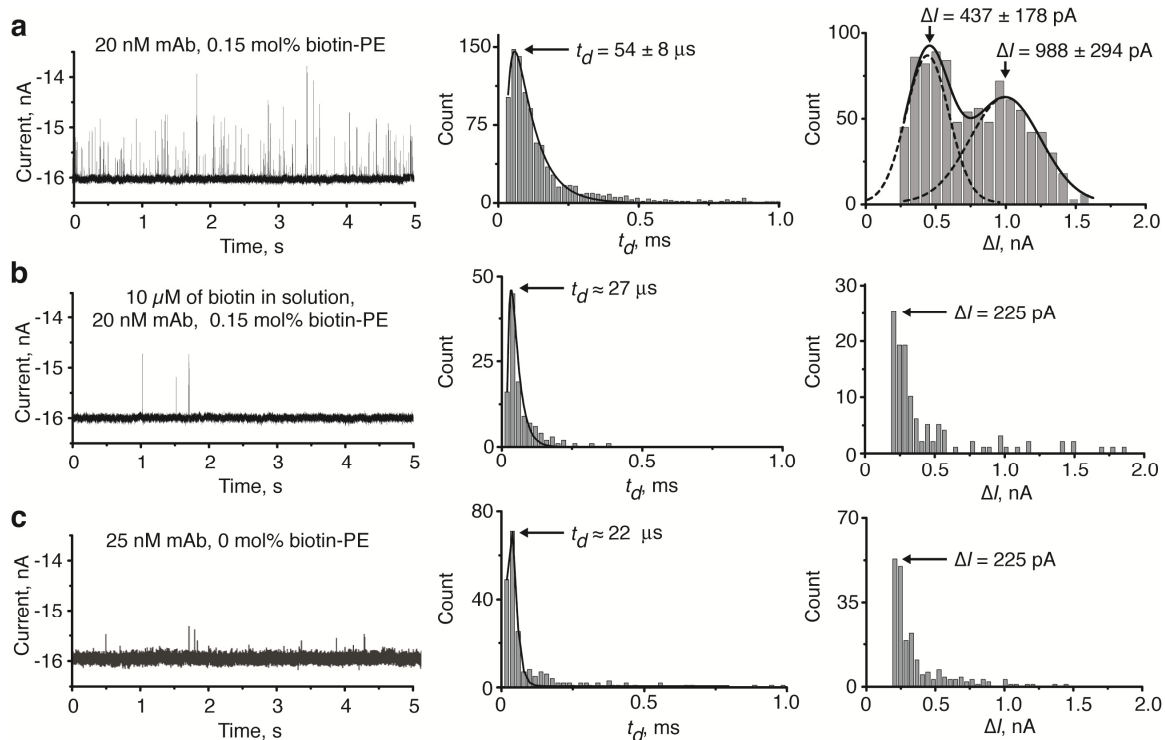


Figure 11-App.2 | Detection of monoclonal anti-biotin IgG₁ antibody (mAb) with a bilayer-coated nanopore. (A) Current *versus* time trace showing resistive pulses due to translocation of mAbs that were bound to biotin-PE lipids in the bilayer coating and analysis of t_d and ΔI of the corresponding resistive pulses. Resistive pulses occurred at a frequency of 34 s^{-1} . (B) Current *versus* time trace recorded after the addition of excess biotin ($10 \mu\text{M}$) to the solution, illustrating the reduced frequency of resistive pulses (1.3 s^{-1}) and analysis of t_d and ΔI of the corresponding resistive pulses. (C) Current *versus* time trace recorded using the same nanopore as (A) and (B) but with a bilayer coating that did not contain biotin-PE lipids, illustrating the reduced frequency (2 s^{-1}) of resistive pulses even at a concentration of mAb of 25 nM and analysis of t_d and ΔI of the corresponding resistive pulses. Distributions of t_d values were fit with equation (10-App.2) as described in Sections 2-App.S5.4 and 2-App.S7.1. Bilayers were formed from $\sim 99 \text{ mol}\%$ POPC, $0.8 \text{ mol}\%$ Rh-PE, and if indicated, $0.15 \text{ mol}\%$ biotin-PE. The experiments were performed with the nanopore shown in Fig. 2C-App.2. The recording buffer contained 2.0 M KCl and 10 mM HEPES buffered at a pH of 7.4 ± 0.1 , and currents were recorded at an applied potential difference of -0.1 V .

We hypothesized that in this control experiment, the excess biotin in solution would occupy the majority of the binding sites of anti-biotin mAb and would therefore prevent the mAb from binding to biotin-PE lipids. Consequently, we expected the translocation of mAb through the nanopore to occur faster than before the addition of excess biotin (*i.e.* when the mAb moved through the nanopore as a lipid-anchored mAb-biotin-PE complex). The histograms of t_d and ΔI values in Fig. 11A,B-App.2 confirmed this expectation by illustrating that the most frequently observed translocation time

decreased from $54 \pm 8 \mu\text{s}$ to $\sim 27 \mu\text{s}$ after adding excess biotin in solution. This result indicates that the viscosity of the bilayer coating reduced the translocation speed (*i.e.* increased the value of t_d) of mAbs that were bound to biotin-PE lipids in the bilayer by at least a factor of two compared to translocation of unbound mAbs. Furthermore, in contrast to the translocation times for mAb that was bound to biotin-PE ($t_d = 54 \pm 8 \mu\text{s}$), translocation times for unbound mAb ($t_d \approx 27 \mu\text{s}$) were shorter than the bandwidth of the recording setup (Section 2-App.S9), and consequently, the values for ΔI were attenuated because they were not time resolved (Fig. 11B-App.2).

S5.3 Resistive-pulses in the absence of biotinylated lipids could not be time-resolved. To confirm that time-resolved detection of streptavidin, anti-biotin mAb, and anti-biotin Fab fragments with bilayer-coated nanopores required biotin-PE lipids in the bilayer coating, we generated bilayer-coated nanopores that did not contain biotin-PE and added SA, mAb, or Fab fragments. We analyzed the current recordings to determine the frequency of resistive pulses, the values of t_d , and the magnitudes of ΔI . Fig. 10-App.2 shows that bilayers without biotin-PE resulted in resistive pulses at 20-500-fold lower frequencies than bilayers with biotin-PE (see also Fig. 11-App.2 and 12A-App.2 for original current traces). These results suggest that biotin-PE in the supported lipid bilayer concentrated the proteins from solution onto the surface of the fluid bilayer via protein-ligand binding and that these surface bound proteins translocated through the pores at a higher frequency than proteins from the bulk electrolyte. Furthermore, it suggests that the resistive pulses we observed with bilayer-coated nanopores containing biotin-PE were mostly (> 90%) due to the movement of protein-biotin-PE complexes within the bilayer coating of the nanopore.

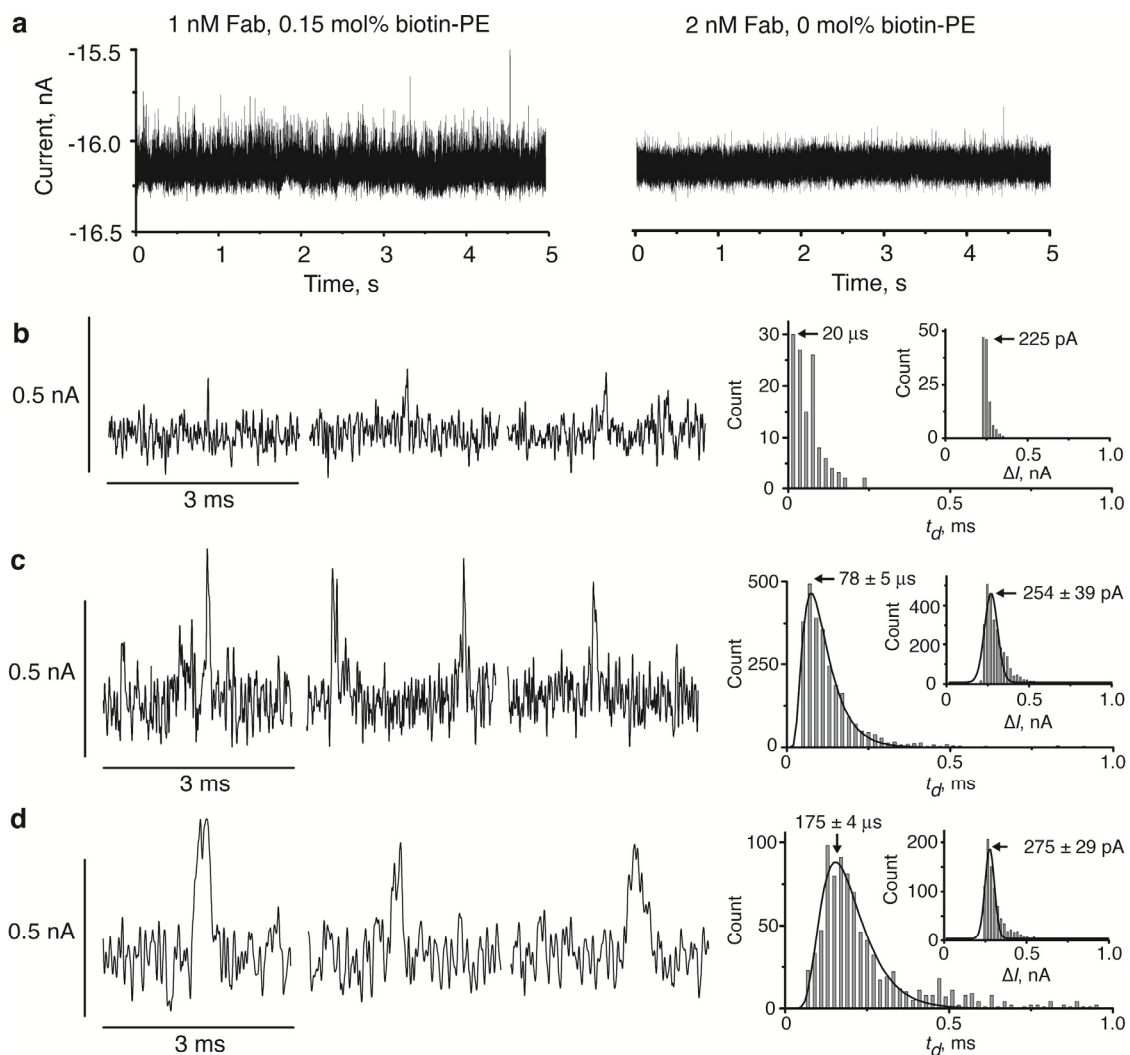


Figure 12-App.2 | Viscosity of bilayers can slow the translocation of anti-biotin Fab fragments that are bound to biotin-PE lipids permitting time-resolved determination of the peak amplitude of resistive pulses. (A) Current traces showing resistive pulses due to the translocation of Fab fragments through the nanopore. Resistive pulses were observed at a frequency of $\sim 100 \text{ s}^{-1}$ with bilayer coatings that contained biotin-PE, whereas bilayer coatings without biotin-PE resulted in resistive pulses at a frequency of 2 s^{-1} . (B) Individual resistive pulses from translocation of Fab fragments through a bilayer-coated nanopore containing 99.2 mol% POPC and 0.8 mol% Rh-PE in the bilayer coating (but no biotin-PE) and analysis of t_d and ΔI of these resistive-pulses. (C) Individual resistive pulses from translocation of Fab fragments through a bilayer-coated nanopore containing 0.15 mol% biotin-PE, ~ 99 mol% POPC, and 0.8 mol% Rh-PE and analysis of t_d and ΔI of these resistive-pulses. (D) Individual resistive-pulses from translocation of Fab fragments through a nanopore coated with a bilayer of increased viscosity (containing 0.15 mol% biotin-PE, 49.5 mol% POPC, 49.5 mol% cholesterol, and 0.8 mol% Rh-PE) and analysis of t_d and ΔI of these resistive-pulses. Distributions of t_d , except the incomplete distribution in (B) were fit with equation (10-App.2) as described in Section 2-App.S5.4 and 2-App.S7.1. The experiments were performed with the nanopore shown in Fig. 2C-App.2. The recording buffer contained 2.0 M KCl and 10 mM HEPES buffered at a pH of 7.4 ± 0.1 . Currents were recorded at an applied potential difference of -0.1 V .

In the absence of biotin-PE in the bilayer coating, we expected the translocation of proteins through the pore to occur faster than in pores that were coated with a bilayer containing biotin-PE since in the latter case the viscosity of the bilayer can reduce the translocation speed of proteins bound to lipids. As a result, we expected to observe reduced values of t_d and attenuated values of ΔI compared when biotin-PE was not used in the bilayer coating. Due to the non-Gaussian distributions of t_d , we compared the values of translocation times, t_d , that we observed most frequently in each distribution of t_d values (*i.e.* the most probable value). For instance, the translocation of anti-biotin mAb through a bilayer-coated pore without biotin-PE lipids was significantly faster ($t_d \approx 22 \mu\text{s}$) than the translocation through the same pore with a bilayer coating that contained biotin-PE ($t_d = 54 \pm 8 \mu\text{s}$) (Fig. 11-App.2). The translocation time of $22 \mu\text{s}$ was below the lower limit of accurate quantification of t_d , and consequently, we obtained reduced values of ΔI when the bilayer coating did not contain biotin-PE (Fig. 11C-App.2). Thus, we did not resolve a complete distribution of ΔI , and we observed few values of ΔI (<10%) larger than 500 pA (Fig. 11C-App.2).

We obtained similar results from analyzing resistive pulses due to the translocation of Fab fragments; the translocation of Fab fragments through a bilayer-coated pore without biotin-PE lipids was faster ($t_d \approx 20 \mu\text{s}$, Fig. 12B-App.2) than the translocation through the same pore with a bilayer coating that contained biotin-PE ($t_d = 78 \pm 5 \mu\text{s}$, Fig. 12C-App.2). Again, we observed reduced values of ΔI and an incomplete distribution of ΔI (Fig. 12B-App.2) when the bilayer did not contain biotin-PE lipids. In contrast, when the bilayer coating contained biotin-PE, the increased translocation time of Fab through the nanopore resulted in a fully resolved distribution of ΔI with an average value of $254 \pm 39 \text{ pA}$ (Fig. 12C-App.2). Using equation (2.2), we estimated a volume of $172 \pm 31 \text{ nm}^3$ for the Fab fragments; the expected volume from literature is $\sim 140 \text{ nm}^3$ (55). Together, these results provide evidence that the local viscosity of the bilayer coating in combination with lipids presenting ligands provides an effective novel strategy for increasing the translocation time of specific proteins that are bound to lipid-anchored ligands.

To further increase the translocation time of Fab fragments, we generated a bilayer coated nanopore that contained biotin-PE and cholesterol. The presence of cholesterol in a lipid bilayer can increase its viscosity significantly (57). We hypothesized that the translocation of Fab through this bilayer-coated nanopore would be slower than with a bilayer coating of purely POPC and biotin-PE. For these experiments, we formed the bilayer coating from liposomes prepared with 0.15 mol% biotin-PE, 0.8 mol% Rh-PE, 49.5 mol% POPC, and 49.5 mol% cholesterol. As expected, in the presence of anti-biotin Fab fragments, we observed translocation times ($t_d = 175 \pm 4 \mu\text{s}$, Fig. 12D-App.2) approximately twice as long as with bilayers that did not contain cholesterol ($t_d = 78 \pm 5 \mu\text{s}$, Fig. 12C-App.2). We obtained a value of ΔI of $275 \pm 29 \text{ pA}$, which corresponds to a volume of $178 \pm 19 \text{ nm}^3$ (Fig. 12D-App.2). Given that the reported volume of Fab fragments are $\sim 140 \text{ nm}^3$, these results suggest, once again, that a bilayer coating with increased viscosity made it possible to resolve translocation events of individual proteins completely in time and that this capability makes it possible to determine the volume of Fab fragments accurately.

S5.4 Comparison of diffusion coefficients of lipids and diffusion coefficients of proteins in the nanopore. We expected the diffusion coefficient of the lipids in the bilayer, D_L , and the diffusion coefficient of the proteins in the nanopore, D_P , to have similar values since diffusion coefficients of lipid-anchored proteins are determined by the diffusion coefficients of their lipid anchor in a lipid bilayer (50, 71, 72). Table 2.2 compares D_L to D_P using equation (2.3) to calculate D_P based on measured t_d values. For this comparison, we used the most probable value of t_d and the known charge of the protein to calculate the diffusion coefficient, D_P . Recent work by Talaga and Li enables an additional method for determination of D_P by fitting individual distributions of t_d values to a biased diffusion first passage time model developed by these authors (14). Here, we compare diffusion coefficients obtained by these fits to the entire distribution of t_d values with diffusion coefficients of the lipids, D_L , determined by FRAP.

The model developed by Talaga and Li is shown in equation (10-App.2); this function describes the distribution of values of t_d that result from the translocation of charged proteins through a nanopore in the presence of an electric field (14):

$$P(t_d) = \frac{(vt_d + l_p) \times e^{-\frac{(l_p - vt_d)^2}{4Dt_d}}}{t_d \times \sqrt{4Dt_d} \pi} \quad (10\text{-App.2})$$

Here, v ($\text{m} \times \text{s}^{-1}$) is the electrophoretic drift velocity and D ($\text{m}^2 \times \text{s}^{-1}$) is the diffusion coefficient of the protein *within the nanopore*. Briefly, this equation assumes that a particle (or protein) moves in one dimension with an electrophoretic mobility u_e ($\text{m}^2 \times \text{V}^{-1} \times \text{s}^{-1}$) and that its motion is driven by a linear electric field, \bar{E} ($\text{V} \times \text{m}^{-1}$), which results in the electrophoretic drift velocity, $v = \bar{E} \times u_e$. It also assumes that the protein moves from a starting point (signified in time by the beginning of the resistive pulse) to an infinite sink that is a distance l_p away (signified in time by the end of the resistive pulse). Further details on the derivation can be found in the article by Talaga and Li (14, 73, 74).

Since the values of t_d result from the translocation of a protein, a best-fit analysis of the distribution of t_d values from protein translocation experiments with equation (10-App.2) provides the diffusion coefficient of the proteins in the nanopore (i.e. $D = D_P$). As shown in Table 2-App.2, the values of D_P were similar to values of D_L when the bilayer coating contained biotin-PE lipids and when the proteins were able to bind to the lipid-anchored biotin moiety. Typically we observed values of D_P that were within $\pm 31\%$ of the value for D_L , with a maximum deviation of $+117\%$. When the bilayer coating did not contain biotin-PE or when the protein did not bind to the lipid-anchored biotin moiety (i.e. in the presence of excess biotin free in solution), this analysis determined values of D_P that were at least 3-fold greater than the value of D_L . Although these D_P values were only semi-quantitative due to the incomplete distribution of such short t_d values, they indicate that the diffusion coefficient of unbound proteins through the nanopore did not depend on the viscosity of the bilayer coating. Moreover, the agreement between D_P of proteins bound to a lipid-anchored ligand and D_L supports the hypothesis that the fluidity of the bilayer coating determined the translocation time of lipid-anchored proteins through the nanopores. These results provide further evidence for the formation of a fluid, bilayer coating within the nanopore.

Table 2-App.2. Comparison of diffusion coefficients of lipid-anchored proteins within the nanopore, D_p , determined by equation (10-App.2) with diffusion coefficients of lipids in the bilayer coating, D_L .

Protein	Lipid Bilayer	D_L^a ($\text{nm}^2 \mu\text{s}^{-1}$)	D_p^b ($\text{nm}^2 \mu\text{s}^{-1}$)	Δ_D^c %
SA ^d	POPC + biotin-PE	1.13 ± 0.13	1.4 ± 0.1	+24
SA ^d	DΔPPC + biotin-PE	1.56 ± 0.16	1.7 ± 0.1	+9
mAb ^e	POPC + biotin-PE	1.29 ± 0.13	2.8 ± 0.2	+117
Fab ^e	POPC + biotin-PE	1.27 ± 0.13	1.7 ± 0.1	+31
Fab ^e	50 mol% POPC and 50 mol% cholesterol + biotin-PE	0.31 ± 0.03	0.6 ± 0.05	+100

^a D_L was calculated based from the FRAP method as described in Section 2-App.S2. ^b Diffusion coefficient of the protein, D_p , in the nanopore as obtained from the best-fit of equation (13-App.2), the integrated form of equation (10-App.2), to the cumulative distributions of t_d values (see Section 2-App.S7.1). ^c Delta (Δ_D) was calculated by: $100 \times (D_p - D_L) / D_L$. ^d Experiments were performed with the nanopore shown in Fig. 2B-App.2. ^e Experiments were performed with the nanopore shown in Fig. 2C-App.2.

2-App.S6. Translocations of non-spherical proteins generate broad distributions of ΔI

Fig 2.4 shows that the distributions of ΔI values for streptavidin and Fab fragments were significantly narrower than the distribution for the IgG antibodies. On first sight, the two maxima in Fig. 2.4C might be attributed to a contamination by other proteins in the solution of anti-biotin IgG antibodies. Closer inspection of the data reveals, however, that these contaminants would have to bind specifically to biotin, since neither of the two peaks in Fig. 2.4C were present in control experiments with pores that were coated with the same bilayer but without biotinylated lipids (Fig. 11-App.2). The broad distribution in Fig. 2.4C was, however, not caused by a contamination of anti-biotin Fab fragments in the solution of anti-biotin IgG antibodies because Fab fragments would result in a narrow peak in the distribution with a most frequently observed ΔI value ~ 0.25 nA (Fig. 2.4B), while the two maxima in Fig. 2.4C were located at ΔI values of ~ 0.4 nA and ~ 1.0 nA. Therefore, we attribute the broad distribution of ΔI values in Fig. 2.4B primarily to the complex molecular shape of IgG antibodies ($\gamma \neq 1.5$) compared to the approximately spherical shape ($\gamma \approx 1.5$) of streptavidin and Fab fragments. In order to provide an estimate for the shape factor of IgG antibodies, we considered their thickness of 2.4 nm and volume of 347 nm³ (51) and approximated their shape by an oblate spheroid (*i.e.*, by a lentil-shaped particle) with a volume equal to IgG antibodies

and a pole-to-pole diameter, A , equal to the thickness of IgG antibodies ($A = 2.4$ nm). This approximation yields an oblate spheroid with an equatorial diameter, B , of 16.6 nm. The shape factor, γ , of an oblate spheroid with diameters A and B depends on the orientation in which it translocates through the pore (52). Fig. 13-App.2 illustrates this orientation dependence of γ graphically. For the two extremes of translocation with the pole-to-pole axis of the spheroid oriented perpendicular to the length axis of the pore, Grover *et al.* predicted $\gamma = 1.1$, and for translocation with the equatorial axis oriented perpendicular to the length axis of the pore they predicted $\gamma \approx 5.0$ (52). The two dashed red lines in Fig. 2.4C indicate ΔI values for these two values of γ as predicted theoretically by equation (2.2) for oblate spheroids with diameters A and B and a volume of 347 nm^3 . Since these two values of ΔI represent the extremes with regard to the orientation during translocation, the majority of the experimentally observed values of ΔI would be expected to lie between these extremes. Fig. 2.4C confirms this expectation and provides the first experimental support that resistive pulse analysis may yield information about the shape (based on the distribution of ΔI values) and orientation (based on the individual ΔI value) of proteins with known volumes during their translocation, as predicted theoretically by Grover *et al.* in 1969 (52). Previously, Mathe *et al.* observed orientation dependent translocation in nanopore-based DNA experiments through α -hemolysin pores (75) and Akesson *et al.* observed large variations in ΔI for the same population of nucleic acids due to various physical processes (76).

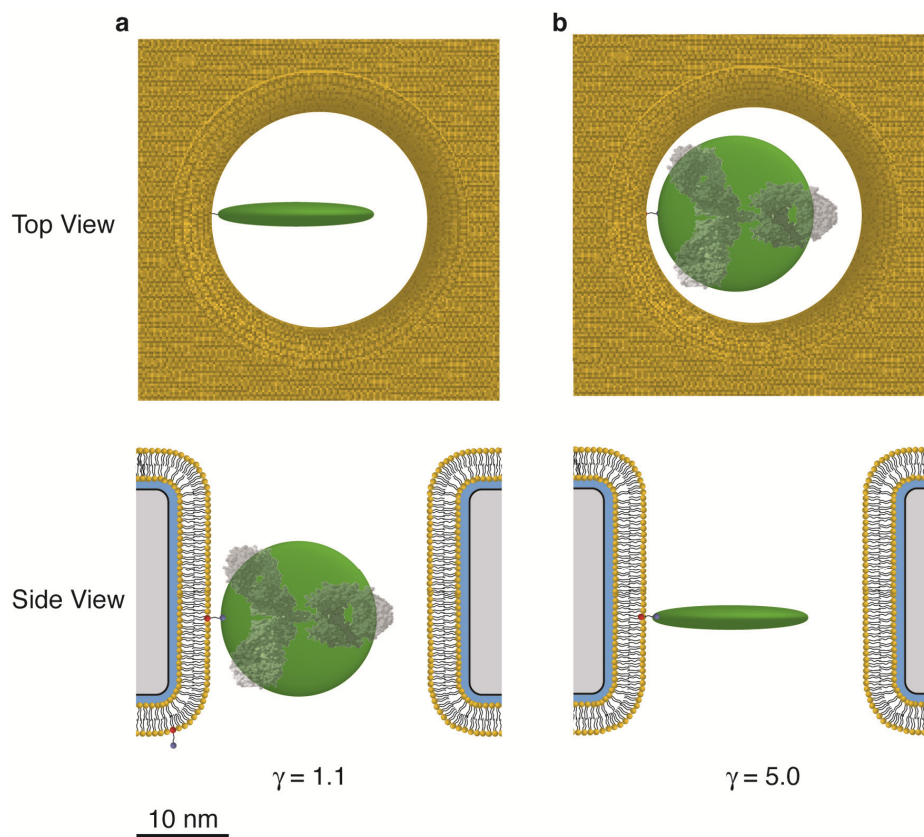


Figure 13-App.2 | Two extremes of possible orientations of an IgG antibody, approximated by an oblate spheroid, during its translocation through a nanopore. (A) Cartoon illustrating the translocation of an oblate spheroid with its pole-to-pole axis oriented perpendicular to the length axis of the pore; this orientation would result in a shape factor, γ , of 1.1. (B) Illustration of the same oblate spheroid as in (A) but translocating through the pore with its equatorial axis oriented perpendicular to the length axis of the pore; this orientation would result in a shape factor, γ , of 5.0. Note that the illustration is drawn to scale and that the nanopore was drawn to match the dimensions of the pore used for the experiments in Fig. 2.4C. A scaled space-filling model of an IgG antibody (77) with a volume of 347 nm^3 overlays the oblate spheroid with the same volume.

As mentioned before, the two orientations in Fig. 13-App.2 represent the two extremes, realistically a lipid-anchored protein will probably not move through the pore in only one orientation but in many orientations as it rotates around its lipid anchor. To examine the possibility of rotation, we estimated the time it would take an antibody to rotate 2π radians (360°) around one axis based on equations (11-App.2) and (12-App.2) (78):

$$\langle \theta^2 \rangle = 2D_r t, \quad (11\text{-App.2})$$

where θ (rad) is the degrees of rotation, D_r ($\text{rad}^2 \text{ s}^{-1}$) is the rotational diffusion coefficient and, t is (s) the time. Using the effective radius of an IgG antibody determined from

diffusion coefficient measurements (79) ($r_{eff} = 5.5$ nm), we estimated D_r for an IgG antibody from equation 12-App.2 (78):

$$D_r = \frac{k_B T}{f_r} = \frac{k_B T}{8\pi\eta r_M^3}, \quad (12\text{-App.2})$$

where k_B (J K⁻¹) is the Boltzmann constant, T (K) is the temperature, and f_r is the rotational friction coefficient. Based on these calculations, which were derived for spherical particles, we estimated that the average time for an antibody to complete one rotation would be ~ 18 μ s. We also calculated the time for one rotation of a disk with a similar size to an IgG antibody and obtained a value of ~ 26 μ s (78). These times are approximately one third of the translocation time of the antibody through the nanopore (Fig. 2.3C). Consequently, the rotation of the antibody while inside the nanopore may result in a value of γ that is the average of the two extreme values, which would yield $\langle\gamma\rangle = 3.1$. This hypothesis is consistent with the peak at $\Delta I \sim 1.0$ nA in the distribution of ΔI values for the mAb as indicated by the red dashed line in Fig. 2.4C. The additional peak in Fig. 2.4C at $\Delta I \sim 0.4$ nA might be due to factors that are not considered in equations (11-App.2) and (12-App.2). For instance, the rotational diffusion coefficient predicted by equation (12-App.2) assumes a spherical protein that is free in solution. Here, the protein was not spherical and attached to a surface inside the confined volume of a nanopore. All three effects likely increase the average time it takes for the antibody to complete a full rotation. This increased time in combination with steric effects inside the confined volume of the nanopore may result in a preferred orientation of the antibody in the nanopore (i.e. Fig. 13A-App.2) that is maintained throughout most of the translocation time. Another possibility is the alignment of the antibody within the electric field due to a dipole moment within the molecule. Due to the shape of the IgG antibody, such an alignment would be most likely along its length axis and result in the orientation of the mAb shown in Fig. 13A-App.2 and a peak in the ΔI distributions at a value of γ of approximately 1.1. In addition, hydrodynamic effects as a result of rotation may drive antibodies towards the wall of the pore, which would also favor the orientation shown in Fig. 13A-App.2.

To provide a second example of a broad distribution of ΔI obtained with a non-spherical protein, we employed a bilayer coated nanopore containing biotin-PE lipids in

the bilayer coating, streptavidin, and a biotinylated IgG antibody (anti-catalase antibody, AbCam[®]). In this experiment, streptavidin bound to the biotin-PE lipids and translocated through the pore resulting in resistive pulses with small values of ΔI (Fig. 14A-App.2). Subsequent addition of the biotinylated-IgG antibody and the translocation of the lipid-anchored, streptavidin-IgG complex returned large values of ΔI and an even broader distribution of values for ΔI (Fig. 14B-App.2) than those from the translocation of the anti-biotin mAb (Fig. 11A-App.2 and Fig. 2.4C). We expected this result since the shape of the streptavidin-IgG complex deviates even further from a spherical shape than an IgG antibody. We approximated the streptavidin-IgG complex as an oblate spheroid with a pole-to-pole diameter of 2.4 nm and an equatorial diameter of 18.8 nm; the shape factor of such an oblate spheroid would be $\gamma = 1.1$ when the pole-to-pole axis is oriented perpendicular to the length axis of the pore and $\gamma = 5.5$ when the equatorial axis is oriented perpendicular to the length axis of the pore. Figure 14-App.2 shows that approximately 95% of the values for ΔI were between the expected ΔI for the protein complex given the molecular volume of the complex and these values for γ .

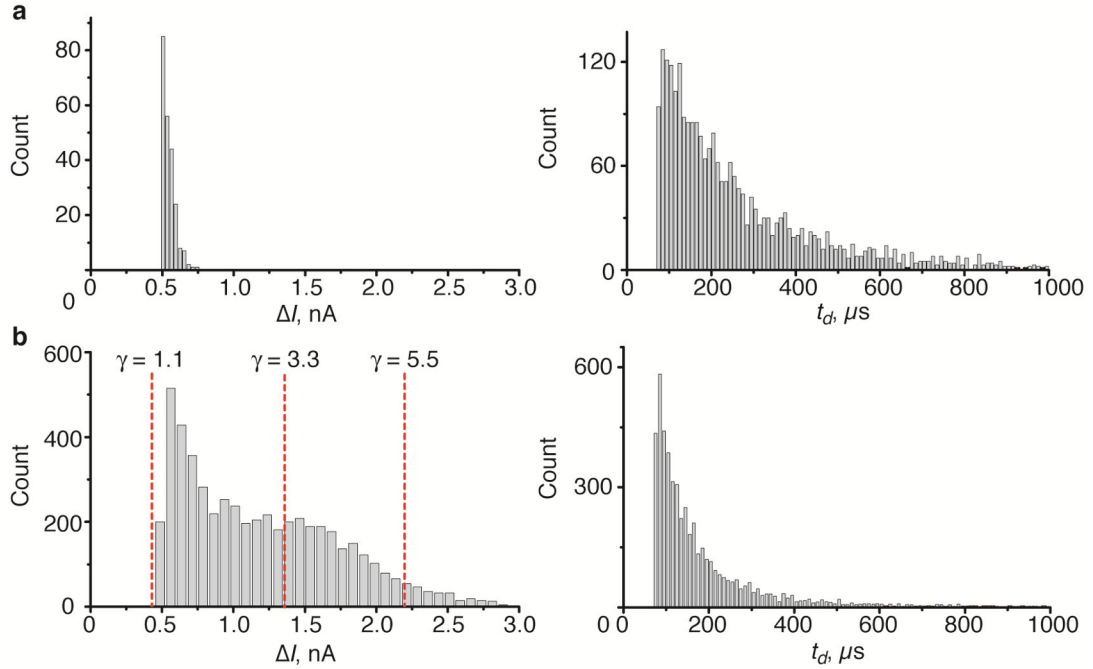


Figure 14-App.2 | Translocation of non-spherical lipid-anchored streptavidin-IgG complexes resulted in broad distributions of ΔI due to the various orientations the complex could assume inside the nanopore. (A) Distributions of ΔI and t_d resulting from the translocation of streptavidin while bound to biotin-PE lipids in the bilayer coating of a nanopore. (B) Distributions of ΔI and t_d after the addition of a biotinylated polyclonal, IgG antibody against catalase. Note that before recording resistive pulses, the electrolyte solutions were thoroughly rinsed to remove unbound proteins from the solution. The bilayer coating in this experiment contained 0.15 % biotin-PE, 0.8% Rh-PE, and ~99% POPC. The nanopore had a diameter of 36 nm and a length of 26 nm with the bilayer coating.

2-App.S7. Determining the most probable value of t_d and its error

S7.1 Determining the most probable t_d value and its error by fitting cumulative distributions of t_d values. In the main chapter, we report the most frequently observed value of t_d , located at the absolute maximum of each distribution of measured t_d values. We quantified these most probable values of t_d by generating cumulative distributions of t_d values. To generate cumulative distributions we summed the relative number of observations that occurred at or below a specified t_d value (x-axis), effectively integrating the data (80). Cumulative distributions are advantageous compared to the histograms shown in Fig. 2.3 because they are generated from all t_d values without binning the data (80). To fit these cumulative distributions we integrated equation (10-App.2) to obtain equation (13-App.2) and fit the data to this equation:

$$A(t_d) = \frac{1}{2} \operatorname{erfc} \left[\frac{(l_p - vt_d)}{2\sqrt{Dt_d}} \right]. \quad (13\text{-App.2})$$

Fig. 15-App.2 shows several cumulative distributions of t_d values that we obtained from translocation events of mAb through the pore while we applied different voltages across the pore. Fig. 15-App.2 also shows the corresponding best fits of equation (13-App.2) to the data in these distributions.

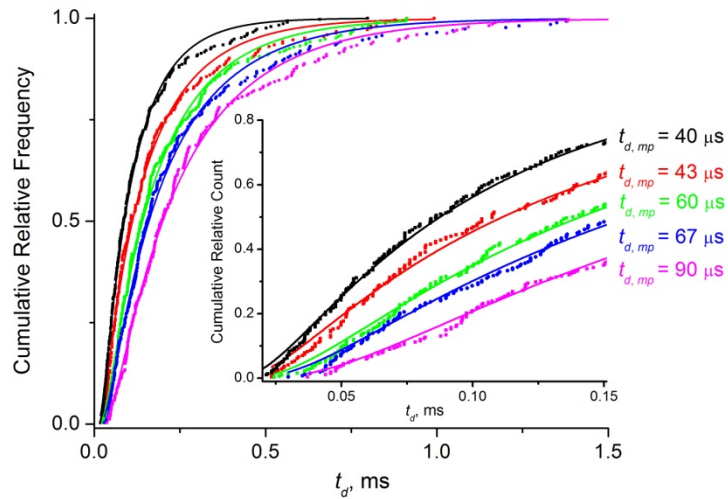


Figure 15-App.2 | Cumulative distributions of t_d obtained from translocation events of mAb at different applied voltages. Distributions of t_d values were determined from recording translocation events of mAb while applying potential differences of 120 mV (—), 100 mV (—), 80 mV (—), 70 mV (—), and 60 mV (—) across the chip. The inset shows the distributions over the range of t_d values of 20 μ s to 150 μ s. Best curve fits of this data to equation (13-App.2) determined the most probable values of t_d in order of decreasing applied potential difference: 40 μ s, 43 μ s, 60 μ s, 67 μ s, and 90 μ s.

To determine the most probable t_d value for a given distribution, we set the second derivative of the fitted equation (13-App.2) equal to 0 and solved for t_d . The most probable t_d values determined from the cumulative distributions shown in Figure 15-App.2 are plotted in Figure 16-App.2 in Section 2-App.S8.1. To report an error for each most probable t_d value, we varied the fitting parameters, the length of the nanopore (l_p) and the diffusion coefficient (D_L), by their measured error and reported the maximum deviation in t_d . The maximum error in l_p , as estimated from the data in Fig. 2.1C, was ± 1 nm while the maximum error of diffusion coefficients of lipids in supported lipid

bilayers as determined by FRAP was $\pm 10\%$ (57). This method resulted in most probable t_d values with errors that ranged from $\pm 5\%$ to $\pm 15\%$ of the most probable value of t_d .

Figure 15-App.2 shows that occasionally cumulative distributions whose most probable t_d values differed by only $3\ \mu\text{s}$ could be resolved (see the black and red data) if the experiment was performed on the same chip, with the same bilayer, and under the same experimental conditions. This resolution occurred because any error in l_p would be nearly the same systematic error for all recordings and would therefore be expected to be significantly smaller than $\pm 1\ \text{nm}$. The errors of $\pm 5\%$ to $\pm 15\%$ of the most probable t_d values reported above refer to separate experiments, possibly with different chips, when the chips were cleaned and fresh bilayers were formed between each experiment.

S7.2 Determining the most probable t_d value by fitting histograms of t_d . In the experiments for determining the most probable values of t_d for the translocation of streptavidin at different pH values of the electrolyte (Fig. 2.5), we found that a few of the cumulative t_d distributions could not be fit very well with equation (13-App.2). Therefore we determined the most probable value of t_d from these distributions with equation (14-App.2), which returns the location of the maximum in the histograms:

$$y = y_o + A e^{\left(-e^{\frac{(x_c+x)}{w}} - \frac{(x-x_c)}{w} + 1 \right)} \quad (14\text{-App.2})$$

In this equation y_o is the baseline, A is the amplitude of the peak, x_c is the x -value at the center of the peak (i.e. the most probable value of t_d), and w is the width of the distributions. Based on the results of this fit to the distributions of t_d , we reported the value of x_c and its error from the fit as the most probable t_d value with its associated error. To determine if the value of x_c was sensitive to the size of the bins in the t_d histograms, we generated histograms with different bin-widths from t_d values obtained streptavidin. In all cases the first bin began at $25\ \mu\text{s}$ since this value represents the lower limit for accurate detection and quantification of t_d (see Section 2-App.S9). Fig. 16-App.2 shows the resulting histograms from bin widths of $15\ \mu\text{s}$, $30\ \mu\text{s}$, and $50\ \mu\text{s}$. In all three cases, the most probable t_d values (i.e. the value of x_c) determined by the best curve fits of equation (14-App.2) to the distributions were within error of each other (with maximum deviations of $6\ \mu\text{s}$), demonstrating that this method of fitting distributions of t_d values for

determining the most probable t_d value was not sensitive to the binning method in a range of bin widths from 15 to 50 μs .

One of the advantages of using the most probable value of t_d for quantitative analysis compared to using, for instance, the average value of t_d , is that the absolute maximum in each distribution can be determined with high accuracy and small errors (smaller than 15% of the most probable value of t_d) from fits to histograms of t_d . This approach of determining the location of the absolute maximum is not sensitive to the possible presence of small sub-peaks in t_d histograms such as those present in some t_d distributions in Fig. 2.3.

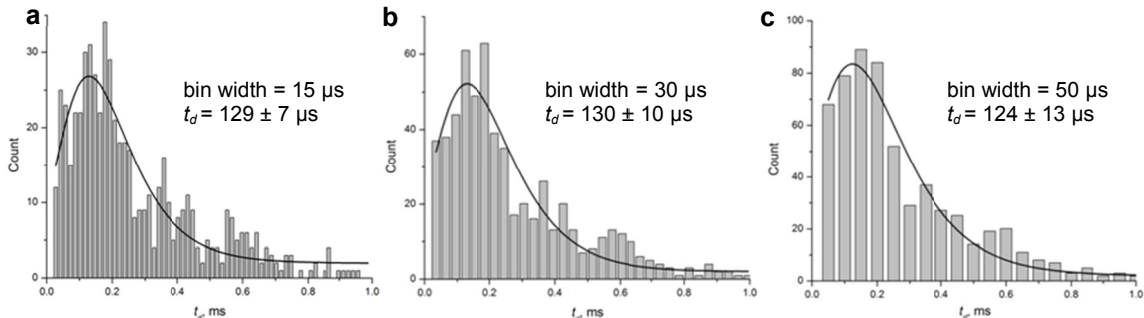


Figure 16-App.2 | Effect of different bin-widths for determining the most frequently observed value of t_d based on best curve fits of t_d data in histograms to equation (14-App.2). Different bin-widths of (A) 15 μs , (B) 30 μs , and (C) 50 μs were used to produce these histograms from t_d values that were measured from translocation events of streptavidin in an electrolyte with pH = 6.6. These t_d histograms were fit with equation (14-App.2) using the non-linear curve fitting function of the software OriginPro 8 with its so called “Extreme Function”.

2-App.S8. Calculating the charge of proteins from the translocation time of lipid-anchored proteins

S8.1 Derivation of equation (2.3). Based on recent work by Sexton *et al*, we developed the simplest possible model that yields a relationship between t_d , the lateral diffusion coefficient of the lipids in the bilayer coating, D_L , and the net charge of a protein, $|z| \times e$, where z (unitless) is the net valency of the charge on the protein and e (C) is the elementary charge of an electron (26). This model assumed that the only driving force, $f(N)$, acting on a charged, translocating protein is exerted by the electric field that

drops inside the pore; it also assumed that inside of cylindrical nanopores the voltage V_p (V) drops linearly along the length of the pore, l_p (m):

$$f = |z|e \frac{V_p}{l_p}. \quad (15\text{-App.2})$$

Note that V_p refers only to the part of the total applied voltage, V_a , that drops inside the pore, and it can be calculated by $V_p = V_a \times R_p / R_{total}$ (see equations (3-App.2) and (6-App.2)). Based on these assumptions, the charged protein experiences a constant force opposed by a viscous drag inside the pore, leading to a constant net electrophoretic drift velocity, v (m s⁻¹):

$$v = \frac{l_p}{t_d} = \frac{f}{\zeta}, \quad (16\text{-App.2})$$

where ζ (kg s⁻¹) represents the viscous friction coefficient. Assuming that, for lipid-anchored proteins, ζ is dominated by the lipid anchor in the bilayer (50, 71, 72), it can be expressed by the Stokes-Einstein relationship:

$$\zeta = \frac{k_B T}{D_L}, \quad (17\text{-App.2})$$

where k_B (J K⁻¹) is the Boltzmann constant, T (K) is temperature, and D_L (m² s⁻¹) represents the lateral diffusion coefficient of lipids in the bilayer. Combining equations (15-App.2)-(17-App.2) yields the desired functional relationship between t_d , the diffusion coefficients of the lipids in the bilayer coating, and the net charge of a translocating protein:

$$t_d = \frac{l_p^2 k_B T}{|z|eV_p D_L}. \quad (18\text{-App.2})$$

This equation is the same as equation (2.3).

In order to validate this model and the resulting equation (18-App.2), we analyzed translocation events of streptavidin molecules through bilayer-coated pores with biotin-PE lipids while employing electrolyte solutions of various pH to vary the value of $|z|$ according to Sivasankar *et al.* (56). Fig. 2.5 shows that equation (18-App.2) accurately predicted t_d as a function of $|z|$ and could be used to determine parameters such as D_L , l_p , or $|z|$.

We further validated equation (18-App.2), which is the same as equation (2.3), by determining the most probable t_d values from translocation events of the IgG antibody as a function of the voltage drop inside the nanopore, V_p . Fig. 17-App.2 illustrates that t_d was indeed inversely proportional to V_p as predicted by equation (18-App.2). Moreover, fitting equation (18-App.2) to the data in Fig. 16-App.2 revealed a net charge of the antibody of $z = -4.2 \pm 0.5$ with z as the only fitting parameter. This value compares well to the value of $z = -3.6 \pm 2.3$ determined by capillary electrophoresis (Section 2-App.S8.2). We also used equation 18-App.2 to calculate a net average charge for the Fab fragment of -5.4 ± 0.6 based on the most frequently observed t_d value in Fig. 2.3B. This value is comparable to the charge that we determined by capillary electrophoresis ($z = -4.3 \pm 0.4$) or by fits to the distributions of t_d ($z = -2.9 \pm 0.6$) (see Sections 2-App.S8.2 and 2-App.S8.3). As a result, we reported a range for the values of z in the main chapter.

Note that in all experiments, we assumed that the pH value inside the nanopore was the same as the pH value in the bulk electrolyte solution. Since we carried out all protein translocation experiments in nanopores that were coated with electrically neutral phosphatidylcholine bilayers and since the KCl concentration of the electrolyte in these experiments was 2.0 M, we did not expect significant differences between the pH value inside the pore and the value in the bulk solution.

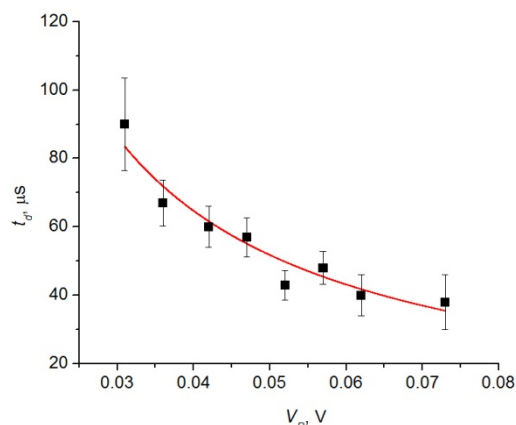


Figure 17-App.2 | Most probable t_d values for the monoclonal anti-biotin IgG₁ antibody (mAb) as a function of the voltage drop, V_p , across a bilayer-coated nanopore containing biotin-PE. The red curve was obtained by a best fit of equation (18-App.2) to the data with z as the only fitting parameter. The fit returned a value for z of -4.2 ± 0.5 with $R^2 = 0.94$ ($N = 8$). The error bars of the most probable t_d values in this plot are overestimates that are based on an l_p of ± 1 nm since all of these recordings were performed on the same chip with the same bilayer and the variations in l_p between current recordings are more likely to be ± 0.2 nm due to fluctuations in the thickness of the water layer and lipid bilayer. The bilayer coating in this experiment contained 0.15% biotin-PE, 0.8% Rh-PE, and \sim 99% POPC. After the bilayer coating, the nanopore had a diameter of 36 nm and a length of 24 nm.

S8.2 Capillary electrophoresis for determining the net charge of proteins.

To provide independent evidence that values of t_d can be used to calculate the net charge of proteins used in this work, we determined the net charge of streptavidin (SA), anti-biotin antibody Fab fragments, and monoclonal anti-biotin IgG antibodies (mAb) from capillary electrophoresis (CE) experiments. Fig. 18A,B-App.2 shows electropherograms for SA and Fab that we obtained using a CE instrument from Hewlett-Packard equipped with a UV absorbance detector. In each electropherogram, two peaks were present due to a transient increase in the absorbance within the light-path of the detector near the end of the capillary. The first peak was due to the so-called neutral marker (a small molecule with a net charge of zero), 4-methoxybenzyl alcohol, and the second peak was attributed to the protein. The difference between the elution time for the neutral marker, t_{NM} (s), and the elution time, t_A (s), for a spherical protein is given by equation (19-App.2) (81):

$$z = \frac{L_T L_D 6 \pi \eta r_M \left(\frac{1}{t_A} - \frac{1}{t_{NM}} \right)}{V_A e}, \quad (19\text{-App.2})$$

where L_T (m) is the total length of the capillary, L_D (m) is the length of the capillary to the detector, η (Pa \times s) is the viscosity of the electrolyte (calculated in this work from equation (8-App.2)), r_M (m) is the effective radius of the protein, V_A (V) is the applied potential difference across the capillary, and e (C) is the elementary charge of an electron. Based on the volume of the proteins, we estimated an effective radius for SA of 2.9 nm (corresponding to 105 nm³) and for Fab of 3.2 nm (corresponding to 140 nm³). For the mAb, we used an effective radius of 5.5 nm that Jossang *et al.* determined from the diffusion coefficient of IgG antibodies (79). Table 3-App.2 lists the calculated charge of SA and Fab that we determined from these CE experiments and compares these values to the ones determined from fits to the distributions of t_d values obtained during the nanopore translocation experiments.

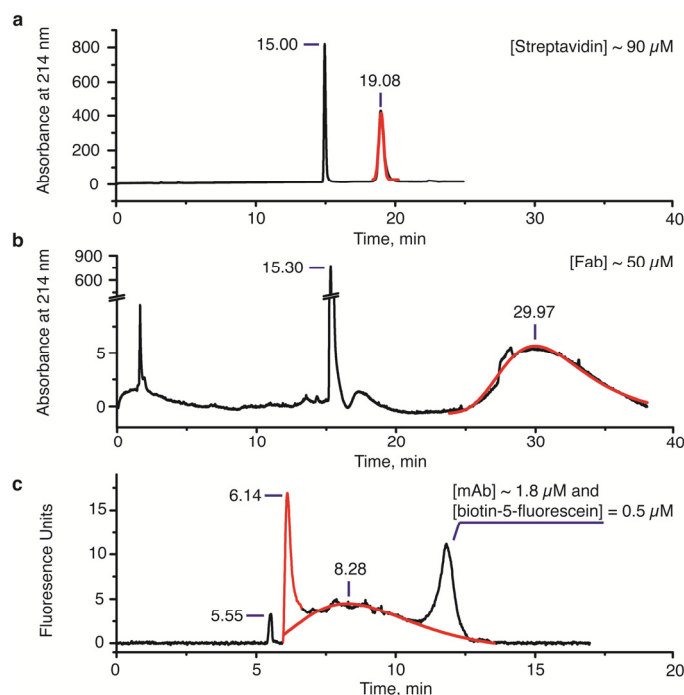


Figure 18-App.2 | Capillary electropherograms for determining the charge of the proteins used in this work. (A,B) Electropherograms obtained with a CE instrument equipped with UV detection. Protein samples were prepared in PBS at pH 7.4 and included the neutral marker, 4-methoxybenzyl alcohol. The neutral marker appeared at 15-15.5 min and is labeled in the figure. Peaks due to the protein are shown in red and the time of each peak's maxima is indicated in the figure. The capillary was a fused silica capillary with a total length of 64.5 cm and an internal diameter of 50 μm. The length of the capillary to the detector was 56 cm and the total applied voltage was 15 kV. The temperature of the capillary was maintained at 25 °C (C) Electropherogram obtained with a CE instrument equipped with fluorescence excitation at 490 nm and detection at 540 nm. The protein sample was prepared in PBS at pH 7.4 and included the zwitterionic fluorophore, rhodamine B, which served as the neutral fluorescent marker. The sample contained 1.8 μM of the anti-biotin IgG mAb and 0.5 μM of biotin-5-fluorescein, with a net charge of $z = -1$. The capillary was a fused silica capillary with a total length of 30 cm and an internal diameter of 50 μm. The length of the capillary to the detector was 20 cm and the total applied voltage was 7.0 kV. The temperature of the capillary in (C) was maintained at 28 °C. Note that in all cases, the baseline of the electropherograms were adjusted.

Based on CE experiments, we measured slightly different values for the charge of SA than those reported by Sivasankar *et al*; these deviations increased as the pH decreased. These discrepancies are likely due to the difference in the charge of SA in solution compared the charge of SA bound to a surface by a biotin anchor. The reported pI of SA in solution is 6.3 (56) while Sivasankar *et al*. reported a pI of SA bound to biotinylated lipids of 5-5.5 and Vlassiounk *et al*. reported a pI of SA bound to immobilized biotin on a surface of ~5.5 (56, 82). Since, the experimental conditions used by Sivasankar *et al*. were very similar to those used here (i.e. SA bound to biotinylated lipids

in a lipid bilayer composed of lipids with a head group of phosphatidylcholine), we plotted t_d values in Fig. 2.5 versus the values reported by Sivasankar *et al.*

Table 3-App.2. Net valence, $|z|$, of the charge of proteins, diffusion coefficients of proteins within the nanopore, D_p , and diffusion coefficients of lipids in the bilayer coating, D_L .

Protein	Lipid Bilayer ^a	pH	$z_{\text{LITERATURE}}^{(56)}$	z_{CE}^b	z_{Td}^c	D_L^d ($\text{nm}^2 \mu\text{s}^{-1}$)	D_p^e ($\text{nm}^2 \mu\text{s}^{-1}$)	Δ_p %
SA	POPC	7.4	-1.9 ± 0.4	-1.8 ± 0.1	-0.8 ± 0.2	1.13 ± 0.13	1.4 ± 0.1	+24
SA	DΔPPC	7.4	-1.9 ± 0.4	-1.8 ± 0.1	-1.1 ± 0.2	1.56 ± 0.16	1.7 ± 0.1	+9
SA	POPC	8.0	-2.4 ± 0.4	-2.8 ± 0.3	-2.3 ± 0.2^f	1.65 ± 0.17	1.8 ± 0.1^f	+6
SA	POPC	7.1	-1.7 ± 0.4	-0.9 ± 0.2	-1.6 ± 0.1^f	1.65 ± 0.17	1.7 ± 0.1^f	+6
SA	POPC	6.6	-1.2 ± 0.4	-0.7 ± 0.2	-1.0 ± 0.1^f	1.65 ± 0.17	1.4 ± 0.1^f	-15
SA	POPC	6.1	-0.8 ± 0.4	-0.3 ± 0.1	-0.9 ± 0.1^f	1.65 ± 0.17	1.0 ± 0.1^f	-39
SA	POPC	5.7	-0.5 ± 0.4	—	-0.9 ± 0.1^f	1.65 ± 0.17	1.2 ± 0.1^f	-21
Fab	POPC	7.4	—	-4.3 ± 0.4	-2.9 ± 0.6	1.27 ± 0.13	1.7 ± 0.1	+31
mAb	POPC	7.4	—	Peak 1: -0.3 ± 0.3 Peak 2: -3.6 ± 2.3	-4.2 ± 0.5^e	1.29 ± 0.13	1.8 ± 0.5	+38

^a All lipid bilayers also contained 0.15 – 0.4 mol% of Biotin-PE. ^b Value of z_{CE} determined by capillary electrophoresis from equation (18-App.2). ^c Value of z_{Td} and D_p determined by fitting the cumulative distributions of t_d with equation (13-App.2), in which v was described by equation (20-App.2), with both z_{Td} and D_p as fitting parameters. ^d Values for D_L determined by FRAP as described in Section 2-App.S2. ^e Value of z determined from the fit in Fig. 17-App.2. ^f Values were determined by fitting equation 21-App.2 to histograms.

We performed a second set of CE experiments with a CE instrument from Beckman equipped with fluorescence detection. To detect proteins with this instrument, we incubated the anti-biotin IgG antibody with biotin-5-fluorescein prior to performing the CE experiment. Fig. 16C-App.2 shows the resulting electropherogram, which we used to calculate the net charge of the mAb. Since biotin-5-fluorescein presumably has a net charge of approximately -1 at pH 7.4, we subtracted 1 charge from the value of z determined with equation (19-App.2) to calculate a net charge of the mAb. We observed two peaks in the presence of mAb, both of which grew in size with increasing concentrations of biotin-5-fluorescein. These two peaks did not overlap with the peak of unbound biotin-5-fluorescein and could therefore both represent the antibody-ligand

complex. These two peaks after the neutral marker in Fig. 18C-App.2 correspond to z values of -0.3 ± 0.3 and -3.6 ± 2.3 (Table 3-App.2).

S8.3 Fitting individual distributions of t_d with both z and D as fitting parameters. To determine if parameters such as $|z|$ and D_L could be extracted from distributions of t_d such as those shown in Fig. 2.3, we incorporated the net valence of the charge, $|z|$, of a protein into equation (10-App.2) by combining it with equation (20-App.2), which describes the electrophoretic drift velocity, v , based on equations (15-App.2)-(17-App.2):

$$v = \frac{|z|eV_p D}{l_p k_B T}. \quad (20\text{-App.2})$$

Substituting equation (20-App.2) into equation (10-App.2) resulted in equation (21-App.2), which permitted the determination of the diffusion coefficient of lipid anchored proteins, D_p , and the net valence of the charge of the proteins, $|z|$, in the nanopore based on best curve fits to individual distributions of t_d .

$$P(t_d) = \frac{\left[\left(\frac{|z|eV_p D}{l_p k_B T} \right) t_d + l_p \right] \times e^{-\left[l_p - \left(\frac{|z|eV_p D}{l_p k_B T} \right) t_d \right]^2 / 4Dt_d}}{t_d \times \sqrt{4Dt_d \pi}}. \quad (21\text{-App.2})$$

Table 3-App.2 compares the values of $|z|$ obtained with this method to the literature values of $|z|$ for SA, the values of $|z|$ obtained with CE, the values of D_p , and the values of D_L for SA, mAb, and Fab. For Fab, values of $|z|$ and D_p determined with equation (21-App.2) from nanopore-based t_d distributions were in good agreement ($\pm 35\%$) with the expected values as obtained from CE and from FRAP experiments.

For streptavidin, values of $|z|$ determined by Sivasankar *et al.* agreed well with the values determined by fitting t_d distributions from translocation experiments with SA with equation (21-App.2). The only exception was the experiment with streptavidin in an electrolyte with a pH of 5.7. The difference in the value of $|z|$ of $\Delta z = 0.4$ in the electrolyte with a pH of 5.7, is likely due to the reduced charge of SA at this pH ($|z| = 0.5 \pm 0.2$) (56). This charge, which is close to neutral, presumably led to a shift from an electrophoretically dominated movement through the nanopore to a diffusion-dominated movement of SA. Consequently, a fraction of the recorded resistive pulses may have

been due to partial translocation events (i.e. diffusion of SA into and out of the same side of the nanopore). Such events could be associated with shorter than expected values for t_d .

For the mAb, we observed two peaks in the CE data which corresponded to two different charges for the mAb. One of the peaks corresponds to a $z = -3.6 \pm 2.3$, which agrees well with the value of $z = -4.2 \pm 0.5$ determined from the fit in Fig. 17-App.2. The second peak in the CE data corresponds to a $z = -0.3 \pm 0.3$. If the charge of the mAb would indeed be -0.3 ± 0.3 , then some proteins may only partially move through the nanopore (as discussed for SA at pH 5.7), which may result in shorter than expected values for t_d . Consequently, the predictions of the charge of the mAb based on t_d values would calculate values for z that are larger than the true value. However, based on the results in Fig. 17-App.2, the charge of the mAb is likely to be $z = -3.6$ rather than -0.3 .

2-App.S9. Data acquisition and analysis of resistive pulses for protein detection

We used Ag/AgCl pellet electrodes (Warner Instruments) to monitor ionic currents through electrolyte-filled nanopores with a patch-clamp amplifier (Axopatch 200B, Molecular Devices Inc.) in voltage clamp mode (i.e., at constant applied voltage). We set the analog low-pass filter of the amplifier to a cutoff frequency of 100 kHz. We used a digitizer (Digidata 1322) with a sampling frequency of 500 kHz in combination with a program written in LabView to acquire and store data.

To detect resistive pulses caused by the translocation of proteins through the nanopore, we applied a potential difference of ± 0.1 V across the nanopore. The polarity refers to the top fluid compartment that contained the protein while the other fluid compartment was always connected to ground. We recorded the resulting current with the maximum bandwidth of the recording setup (cut-off frequency, $f_c \sim 50$ kHz) (28) and with a sampling frequency of 500 kHz using a custom program written in LabVIEW. To distinguish resistive pulses reliably from the electrical noise, we used the software PClamp (Molecular Devices Inc.) to determine the baseline of the current and to filter current recordings with a digital, Gaussian low-pass filter ($f_c = 15$ kHz).

Using PClamp software, we performed a threshold-search for resistive pulses within the current recordings. We defined the start of a resistive pulse by a resistive decrease in the magnitude of the current past a threshold value that we set to $5\times$ the standard deviation of the noise of the baseline current. Based on this definition, typical threshold values ranged from 150 to 250 pA depending on the nanopore dimensions and the bilayer coating. The subsequent return of the current past a second threshold, which we set to one standard deviation of the noise in the baseline current, and toward the baseline value, marked the end of the resistive pulse. We confirmed that for the analysis of translocation events from streptavidin and Fab, this procedure returned the same t_d values as a method based on half-widths of resistive pulse recently reported by Talaga and Li (14). Due to the large magnitude and magnitude variability of resistive pulses in the antibody experiments, we determined t_d values based on the half-width of resistive pulses from antibodies in a method similar to the approach described by Talaga and Li (14). We defined ΔI as the maximum deviation from the baseline current within the time, t_d .

To determine the time-response of the recording and analysis methods experimentally, we used a waveform generator (Agilent 33220A) to input current pulses in a method similar to Talaga and Li (14). These current pulses had a ΔI of 650 pA with a rise time of 5 ns and durations ranging from 10 μs to 200 μs . Analyzing the data based on the half-width of the current pulses, Fig. 19A-App.2 shows that we could accurately measure the magnitude (ΔI) of resistive pulses if these pulses had t_d values larger than 50 μs and Fig. 19B-App.2 shows that we could accurately determine t_d values that were larger than 25 μs . In all quantitative analyses of resistive pulses reported in this work, we constructed t_d histograms only from translocation events that lasted at least 25 μs and ΔI histograms only from translocation events that lasted at least 50 μs (typically 70 μs).

To characterize the inherent measurement error of t_d , σ_t , of the recording and analysis methods, we added a current trace containing experimentally recorded electrical noise from a resistive-pulse experiment to current traces containing current pulses generated by a waveform generator. Thus, these current traces contained current pulses with a precisely defined duration and contained a realistic representation of the electrical noise in a resistive pulses experiment. Using the resulting current traces we determined t_d

based on the half-width of the current pulses as described above. For current pulses with a precisely defined duration, we measured a range of t_d values and Fig. 20-App.2 plots these values in histograms. We fit these histograms with Gaussian distributions, and from the fit we determined that the inherent measurement error of t_d ranged from 2 to 4 μs and was not affected by the magnitude of t_d .

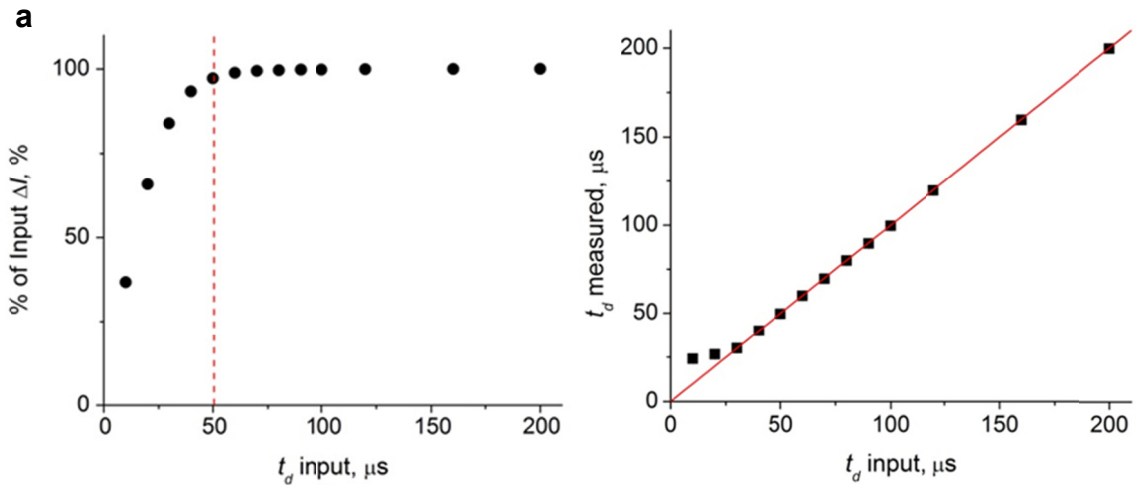


Figure 19-App.2 | Characterization of t_d and ΔI for pulses of various simulated translocation times resulting from an input from a waveform generator. (A) Measured values for the pulse magnitude, ΔI , of pulses input into the headstage with a waveform generator. The dotted red line denotes the value of t_d at which ΔI was attenuated by 3% ($\sim 50 \mu\text{s}$). (B) Measured values for the pulse duration of pulses input into the headstage with a waveform generator show that t_d could be accurately determined if it exceeded a threshold value of $\sim 25 \mu\text{s}$. Therefore the lower limit of accurate quantification of t_d values was $25 \mu\text{s}$. The red line is plotted with a slope equal to 1.

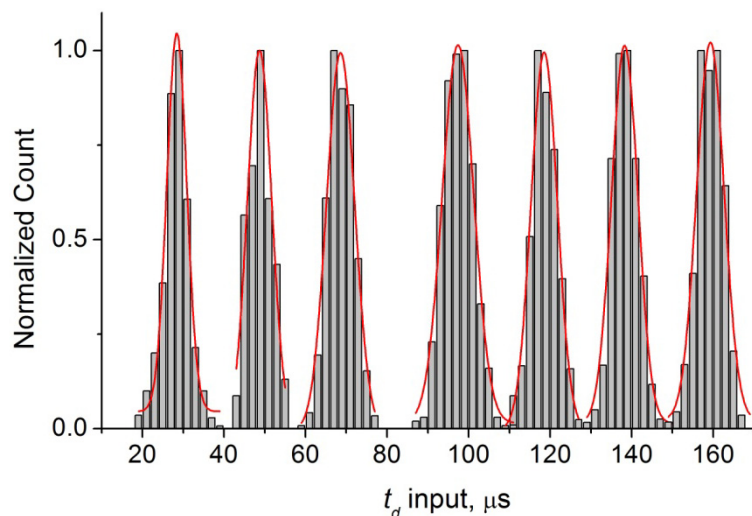


Figure 20-App.2 | Histograms of t_d

values measured from current pulses with defined duration and added electrical noise from resistive pulse experiments. Current pulses with precisely defined durations of 30, 50, 70, 100, 120, 140, and 160 μs were combined with electrical noise from a resistive-pulse experiment and the duration of these pulses was determined by their half-width. The red lines were obtained by fitting the histograms with a Gaussian distribution. From these fits, the measurement error of t_d , σ_t , was determined to be 2.3, 4.0, 3.4, 3.9, 3.2, 3.2, and 3.4 μs (listed in order of increasing pulse duration).

2-App.S10. Preparation of amyloid-beta samples and gel-electrophoresis

We received A β peptides (residues 1-40, A β 1-40) in powder form from GL Biochem (Shanghai) Ltd with a purity above 98%. To remove aggregates of A β 1-40, we dissolved the powder in hexafluoroisopropanol (HFIP) to a concentration of 1 mM of A β 1-40. After 24 h incubation in HFIP, we diluted this solution with cold (4 °C) deionized water at a 2:1 (v/v) ratio (H₂O:HFIP). We then rapidly aliquoted the solution, immediately froze it in a CO₂/acetone bath, and lyophilized the frozen aliquots for two days to remove HFIP (58). To start the aggregation process of A β (1-40) peptides, we dissolved the lyophilized powder in deionized water to a concentration of 1 mg \times mL⁻¹. We incubated these samples in siliconized plastic microcentrifuge tubes on a temperature-controlled shaker at a temperature of 22 °C. To detect aggregates of A β 1-40, we formed a supported lipid bilayer of POPC lipids on a chip containing a nanopore with a diameter of 96 nm and a length of \sim 275 nm (dimensions are before the lipid bilayer coating). We added solutions containing A β (1-40) to the top solution compartment of the fluidic setup such that the final concentration of A β (1-40) ranged from 0.1 to 0.2 mg \times mL⁻¹. We used a recording buffer containing 70 mM KCl and 10

mM HEPES with a pH of 7.4 ± 0.1 and recorded resistive pulses at an applied potential difference of +0.2 V.

To confirm the presence of large aggregates of A β peptides in these samples independently, we performed a Western blot with solutions containing A β (1-40) that were allowed to aggregate for 0, 24, 48, and 72 h. Prior to performing the electrophoresis, we followed a standard protocol (83) and cross-linked A β (1-40) samples (1 mg mL^{-1}) with 0.04% glutaraldehyde for 20 min at room temperature and stopped the reaction by adding 200 mM of Tris. We diluted the cross-linked samples to $0.01 \text{ } \mu\text{g } \mu\text{L}^{-1}$ in native sample buffer (Bio-Rad), containing 10% (v/v) sodium dodecyl sulfate. To resolve aggregates of A β (1-40) of different molecular weights we used a polyacrylamide gel: 18% Tris-HCl Ready Gel (Bio-Rad) in Tris-Glycine buffer. After running the gel, we transferred proteins to a polyvinylidene fluoride (PVDF) membrane (PerkinElmer Life Science) and blocked the membrane for 1 h with TBS buffer containing 5% (w/v) nonfat dry milk and 0.0625% (w/v) Tween20. We incubated the membrane with a primary antibody against A β (1-40) (6E10 from Covance) for 1.5 h. An IgG anti-goat antibody served as the secondary antibody and was incubated with the membrane for 1 h. We developed the membrane onto film using enhanced chemiluminescence (ECL, PerkinElmer Life Sciences). Fig. 21-App.2 shows the resulting Western blot and the increasing molecular weights of A β (1-40) aggregates with increasing incubation time. Note the presence of fibrillar aggregates with molecular weights greater than 250 kDa that remained in the wells of the polyacrylamide gel. Also note that the amount of these fibrillar A β (1-40) aggregates in the wells of the gel increased with increasing time of aggregation.

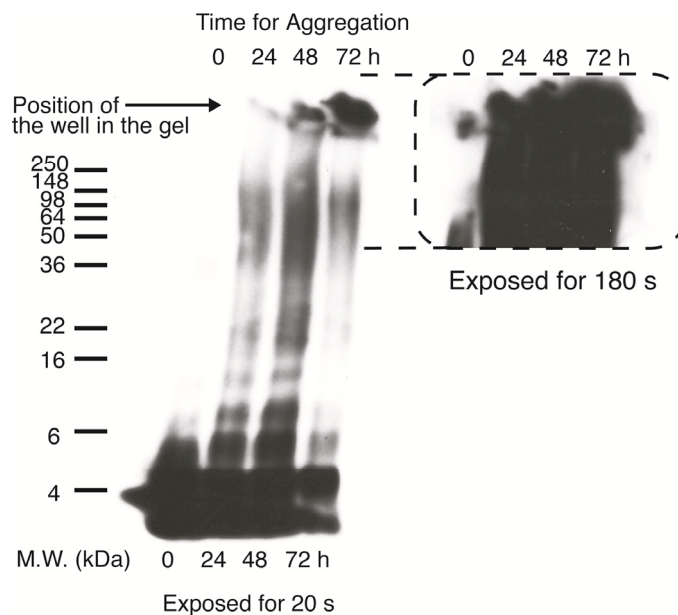


Figure 21-App.2 | Gel electrophoresis results showing aggregation of amyloid-beta (residues 1-40) as a function of incubation time in water. Lane 1 (0 h), containing a solution of freshly prepared A β (1-40), shows that initially most of the A β peptides in solution were monomers with a molecular weight of ~4 kDa. Lanes 2 (24 h), 3 (48 h), and 4 (72 h) show that as A β aggregated in solution for increasing times, it formed aggregates of large molecular weight (6 – 250 kDa). Furthermore, lanes 2 and 3 show a population with a very large molecular weight (greater than 250 kDa) that remained in the wells of the polyacrylamide gel as it would be expected for fibrillar aggregates. The inset shows the same gel but exposed for 180 s and reveals that aggregates of large molecular weight (greater than 250 kDa), which remained in the well of the gel, were already present after 24 h of aggregation (lane 2). The molecular weight markers were SeeBlue Plus2 Stained Standard Markers from Invitrogen.

Chapter 2 References

1. Sexton LT, *et al.* (2007) Resistive-pulse studies of proteins and protein/antibody complexes using a conical nanotube sensor. *J Am Chem Soc* 129(43):13144-13152.
2. Movileanu L, Howorka S, Braha O, Bayley H (2000) Detecting protein analytes that modulate transmembrane movement of a polymer chain within a single protein pore. *Nat Biotechnol* 18(10):1091-1095.
3. Howorka S, Siwy Z (2009) Nanopore analytics: Sensing of single molecules. *Chem Soc Rev* 38(8):2360-2384.
4. Siwy Z, *et al.* (2005) Protein biosensors based on biofunctionalized conical gold nanotubes. *J Am Chem Soc* 127(14):5000-5001.
5. Ding S, Gao CL, Gu LQ (2009) Capturing single molecules of immunoglobulin and ricin with an aptamer-encoded glass nanopore. *Anal Chem* 81(16):6649-6655.
6. Uram JD, Ke K, Hunt AJ, Mayer M (2006) Submicrometer pore-based characterization and quantification of antibody-virus interactions. *Small* 2(8-9):967-972.
7. Branton D, *et al.* (2008) The potential and challenges of nanopore sequencing. *Nat Biotechnol* 26(10):1146-1153.
8. Iqbal SM, Akin D, Bashir R (2007) Solid-state nanopore channels with DNA selectivity. *Nat Nanotechnol* 2(4):243-248.
9. Wanunu M, Morrison W, Rabin Y, Grosberg AY, Meller A (2010) Electrostatic focusing of unlabelled DNA into nanoscale pores using a salt gradient. *Nat Nanotechnol* 5(2):160-165.
10. Uram JD, Ke K, Hunt AJ, Mayer M (2006) Label-free affinity assays by rapid detection of immune complexes in submicrometer pores. *Angew Chem-Int Edit* 45:2281-2285.
11. Robertson JWF, *et al.* (2007) Single-molecule mass spectrometry in solution using a solitary nanopore. *Proc Natl Acad Sci U S A* 104(20):8207-8211.
12. Han AP, *et al.* (2008) Label-free detection of single protein molecules and protein-protein interactions using synthetic nanopores. *Anal Chem* 80(12):4651-4658.
13. Ito T, Sun L, Crooks RM (2003) Simultaneous determination of the size and surface charge of individual nanoparticles using a carbon nanotube-based Coulter counter. *Anal Chem* 75(10):2399-2406.
14. Talaga DS, Li JL (2009) Single-molecule protein unfolding in solid state nanopores. *J Am Chem Soc* 131(26):9287-9297.
15. Oukhaled G, *et al.* (2007) Unfolding of proteins and long transient conformations detected by single nanopore recording. *Physical Review Letters* 98(15):158101.
16. Benner S, *et al.* (2007) Sequence-specific detection of individual DNA polymerase complexes in real time using a nanopore. *Nat Nanotechnol* 2(11):718-724.
17. Clarke J, *et al.* (2009) Continuous base identification for single-molecule nanopore DNA sequencing. *Nat Nanotechnol* 4(4):265-270.
18. Bayley H, Cremer PS (2001) Stochastic sensors inspired by biology. *Nature* 413(6852):226-230.

19. Nakane JJ, Akeson M, Marziali A (2003) Nanopore sensors for nucleic acid analysis. *Journal of Physics: Condensed Matter* 15(32):R1365-R1393.
20. Dekker C (2007) Solid-state nanopores. *Nat Nanotechnol* 2(4):209-215.
21. Martin CR, Siwy ZS (2007) Learning nature's way: Biosensing with synthetic nanopores. *Science* 317(5836):331-332.
22. Movileanu L (2009) Interrogating single proteins through nanopores: Challenges and opportunities. *Trends in Biotechnology* 27(6):333-341.
23. Majd S, *et al.* (2010) Applications of biological pores in nanomedicine, sensing, and nanoelectronics. *Curr Opin Biotech* 21(4):439-476.
24. Hou X, *et al.* (2009) A biomimetic potassium responsive nanochannel: G-quadruplex DNA conformational switching in a synthetic nanopore. *J Am Chem Soc* 131(22):7800-7805.
25. Yameen B, *et al.* (2009) Single conical nanopores displaying pH-tunable rectifying characteristics. Manipulating ionic transport with zwitterionic polymer brushes. *J Am Chem Soc* 131(6):2070-2071.
26. Sexton LT, *et al.* (2010) An adsorption-based model for pulse duration in resistive-pulse protein sensing. *J Am Chem Soc* 132(19):6755-6763.
27. Pedone D, Firnkes M, Rant U (2009) Data analysis of translocation events in nanopore experiments. *Anal Chem* 81(23):9689-9694.
28. Uram JD, Ke K, Mayer M (2008) Noise and bandwidth of current recordings from submicrometer pores and nanopores. *ACS Nano* 2(5):857-872.
29. Fologea D, Ledden B, David SM, Li J (2007) Electrical characterization of protein molecules by a solid-state nanopore. *Appl Phys Lett* 91(5):053901.
30. Chun KY, Mafe S, Ramirez P, Stroeve P (2006) Protein transport through gold-coated, charged nanopores: Effects of applied voltage. *Chem Phys Lett* 418(4-6):561-564.
31. Hille B (2001) *Ion channels of excitable membranes* (Sinauer Associates, Inc., Sunderland) pp 347-349.
32. Steinbrecht RA (1997) Pore structures in insect olfactory sensilla: A review of data and concepts. *International Journal of Insect Morphology & Embryology* 26(3-4):229-245.
33. Zacharuk RY (1985) Antennae and sensilla. *Comparative insect physiology chemistry and pharmacology*, eds Kerkut GA & Gilbert LI (Pergamon Press, Oxford), Vol 6.
34. Locke M (1965) Permeability of insect cuticle to water and lipids. *Science* 147(3655):295-298.
35. Nilsson J, Lee JRI, Ratto TV, Letant SE (2006) Localized functionalization of single nanopores. *Adv Mater* 18(4):427-431.
36. Wang GL, Zhang B, Wayment JR, Harris JM, White HS (2006) Electrostatic-gated transport in chemically modified glass nanopore electrodes. *J Am Chem Soc* 128(23):7679-7686.
37. Wanunu M, Meller A (2007) Chemically modified solid-state nanopores. *Nano Lett* 7(6):1580-1585.
38. Lewis BA, Engelman DM (1983) Lipid bilayer thickness varies linearly with acyl chain-length in fluid phosphatidylcholine vesicles. *J Mol Biol* 166(2):211-217.

39. Caffrey M, Hogan J (1992) Lipidat: A database of lipid phase transition temperatures and enthalpy changes. Dmpc data subset analysis. *Chem Phys Lipids* 61(1):1-109.
40. Watts TH, Brian AA, Kappler JW, Marrack P, McConnell HM (1984) Antigen presentation by supported planar membranes containing affinity-purified i-a^d. *Proc Natl Acad Sci U S A* 81(23):7564-7568.
41. Cremer PS, Boxer SG (1999) Formation and spreading of lipid bilayers on planar glass supports. *Journal of Physical Chemistry B* 103(13):2554-2559.
42. Reimhult E, Hook F, Kasemo B (2003) Intact vesicle adsorption and supported biomembrane formation from vesicles in solution: Influence of surface chemistry, vesicle size, temperature, and osmotic pressure. *Langmuir* 19(5):1681-1691.
43. Sackmann E (1996) Supported membranes: Scientific and practical applications. *Science* 271(5245):43-48.
44. Miller CE, Majewski J, Gog T, Kuhl TL (2005) Characterization of biological thin films at the solid-liquid interface by x-ray reflectivity. *Physical Review Letters* 94(23).
45. Bayerl TM, Bloom M (1990) Physical-properties of single phospholipid-bilayers adsorbed to micro glass-beads - a new vesicular model system studied by h-2-nuclear magnetic-resonance. *Biophys J* 58(2):357-362.
46. Tokumasu F, Jin AJ, Dvorak JA (2002) Lipid membrane phase behaviour elucidated in real time by controlled environment atomic force microscopy. *J Electron Microsc* 51(1):1-9.
47. Schuy S, Janshoff A (2006) Thermal expansion of microstructured dmpc bilayers quantified by temperature-controlled atomic force microscopy. *ChemPhysChem* 7(6):1207-1210.
48. Gibbs AG (2002) Lipid melting and cuticular permeability: New insights into an old problem. *J Insect Physiol* 48(4):391-400.
49. Adam G, Delbrueck M (1968) Reduction of dimensionality in biological diffusion processes. *Structural chemistry and molecular biology*, eds Rich A & Davidson N (W. H. Freeman and Company, San Francisco), pp 198-215.
50. Gambin Y, *et al.* (2006) Lateral mobility of proteins in liquid membranes revisited. *Proc Natl Acad Sci U S A* 103(7):2098-2102.
51. Schneider SW, Larmer J, Henderson RM, Oberleithner H (1998) Molecular weights of individual proteins correlate with molecular volumes measured by atomic force microscopy. *Pflugers Arch* 435(3):362-367.
52. Grover NB, Naaman J, Ben-sasson S, Doljansk F (1969) Electrical sizing of particles in suspensions. I.Theory. *Biophys J* 9(11):1398-1414.
53. Grover NB, Naaman J, Ben-sasson S, Doljansk F, Nadav E (1969) Electrical sizing of particles in suspensions. 2. Experiments with rigid spheres. *Biophys J* 9(11):1415-1425.
54. Neish CS, Martin IL, Henderson RM, Edwardson JM (2002) Direct visualization of ligand-protein interactions using atomic force microscopy. *Br J Pharmacol* 135(8):1943-1950.
55. Janeway CA (2001) *Immunobiology: The immune system in health and disease* (Garland Publishing, New York) 5th Ed.

56. Sivasankar S, Subramaniam S, Leckband D (1998) Direct molecular level measurements of the electrostatic properties of a protein surface. *Proc Natl Acad Sci U S A* 95(22):12961-12966.
57. Majd S, Mayer M (2005) Hydrogel stamping of arrays of supported lipid bilayers with various lipid compositions for the screening of drug-membrane and protein-membrane interactions. *Angew Chem-Int Edit* 44(41):6697-6700.
58. Capone R, *et al.* (2009) Amyloid-beta-induced ion flux in artificial lipid bilayers and neuronal cells: Resolving a controversy. *Neurotox Res* 16(1):1-13.
59. Li J, *et al.* (2001) Ion-beam sculpting at nanometre length scales. *Nature* 412(6843):166-169.
60. Cai Q, Ledden B, Krueger E, Golovchenko JA, Li JL (2006) Nanopore sculpting with noble gas ions. *J Appl Phys* 100(2):024914.
61. Hamann CH, Hamnett A, Vielstich W (1998) *Electrochemistry* (Wiley-VCH, New York).
62. Fox RW, McDonald AT, Pritchard PJ (2004) *Introduction to fluid mechanics 6th edition* (Wiley, New York, NY) p 724.
63. Lambacher A, Fromherz P (1996) Fluorescence interference-contrast microscopy on oxidized silicon using a monomolecular dye layer. *Appl Phys A-Mater Sci Process* 63(3):207-216.
64. Saleh BEA, Teich MC eds (2007) *Fundamentals of photonics* (John Wiley & Sons, Inc.), 2nd Ed, p pg. 80.
65. Axelrod D, Koppel DE, Schlessinger J, Elson E, Webb WW (1976) Mobility measurement by analysis of fluorescence photobleaching recovery kinetics. *Biophys J* 16(9):1055-1069.
66. Soumpasis DM (1983) Theoretical-analysis of fluorescence photobleaching recovery experiments. *Biophys J* 41(1):95-97.
67. Kalb E, Frey S, Tamm LK (1992) Formation of supported planar bilayers by fusion of vesicles to supported phospholipid monolayers. *Biochimica Et Biophysica Acta* 1103(2):307-316.
68. Starr TE, Thompson NL (2000) Formation and characterization of planar phospholipid bilayers supported on tio2 and strtio3 single crystals. *Langmuir* 16(26):10301-10308.
69. Majd S, Yusko EC, MacBriar AD, Yang J, Mayer M (2009) Gramicidin pores report the activity of membrane-active enzymes. *J Am Chem Soc* 131(44):16119-16126.
70. Hamblett KJ, *et al.* (2002) A streptavidin-biotin binding system that minimizes blocking by endogenous biotin. *Bioconjugate Chem* 13(3):588-598.
71. Fein M, *et al.* (1993) Lateral mobility of lipid analogs and gpi-anchored proteins in supported bilayers determined by fluorescent bead tracking. *J Membr Biol* 135(1):83-92.
72. Knight JD, Falke JJ (2009) Single-molecule fluorescence studies of a ph domain: New insights into the membrane docking reaction. *Biophys J* 96(2):566-582.
73. Redner S (2001) *A guide to first-passage processes* (Cambridge University Press, New York) p 312.
74. Wasan MT (1969) *First passage time distribution of brownian motion with positive drift* (Queen's University).

75. Mathé J, Aksimentiev A, Nelson DR, Schulten K, Meller A (2005) Orientation discrimination of single-stranded DNA inside the alpha-hemolysin membrane channel. *Proc Natl Acad Sci U S A* 102(35):12377-12382.
76. Akeson M, Branton D, Kasianowicz JJ, Brandin E, Deamer DW (1999) Microsecond time-scale discrimination among polycytidylic acid, polyadenylic acid, and polyuridylic acid as homopolymers or as segments within single rna molecules. *Biophys J* 77:3227-3223.
77. Yang J, Mayer M, Kriebel JK, Garstecki P, Whitesides GM (2004) Self-assembled aggregates of iggs as templates for the growth of clusters of gold nanoparticles. *Angew Chem-Int Edit* 43(12):1555-1558.
78. Berg HC (1993) *Random walks in biology* (Princeton University Press, Princeton, NJ).
79. Jossang T, Feder J, Rosenqvist E (1988) Photon-correlation spectroscopy of human-IgG. *J Protein Chem* 7(2):165-171.
80. M.C. W, D. S (2009) *The analysis of biological data* (Roberts and Company, Greenwood Village, CO) 1 Ed.
81. Gitlin I, Carbeck JD, Whitesides GM (2006) Why are proteins charged? Networks of charge-charge interactions in proteins measured by charge ladders and capillary electrophoresis. *Angew Chem-Int Edit* 45(19):3022-3060.
82. Vlassiuk I, Kozel TR, Siwy ZS (2009) Biosensing with nanofluidic diodes. *J Am Chem Soc* 131(23):8211-8220.
83. Stine WB, Dahlgren KN, Krafft GA, LaDu MJ (2003) In vitro characterization of conditions for amyloid-beta peptide oligomerization and fibrillogenesis. *J Biol Chem* 278(13):11612-11622.

Chapter 3

Determining the Shape, Dipole Moment, and Rotational Diffusion Coefficient of Single, Non-Spherical Proteins

Recording ionic current through electrolyte-filled nanopores during the passage of proteins is an emerging technique for characterizing unmodified proteins in their native, aqueous environment. Here, we demonstrate the use of lipid-bilayer coated nanopores for determining the shape and volume of single, spherical and non-spherical proteins that are anchored to mobile lipids in the coating. This work shows that individual resistive-pulses can also be used to determine the rotational diffusion coefficient and dipole moment of non-spherical proteins while in the nanopore. Moreover, this method has the potential to detect transient changes in the conformation of flexible proteins (*e.g.* an IgG antibody). This work extends the power of nanopores for characterizing proteins by adding the parameters of shape, volume, rotational diffusion coefficient, and dipole moment of non-spherical proteins to those that can already be determined in a single experiment such as the volume of spherical proteins, charge, and affinity for a ligand.

3.1 Introduction

Proteins orchestrate cell behavior, serve as functional biomarkers, and are the targets of almost all drugs; consequently, methods for rapid analysis of proteins are necessary to reduce health care costs and continue the advancement of personalized medicine (1). Arguably, the best techniques available for identifying proteins (i.e. two-dimensional polyacrylamide gel electrophoresis and mass spectroscopy) are time consuming and require biochemical steps that modify, denature, or enzymatically digest proteins (1). Few techniques characterize proteins in their native environment. Here, we describe the use of electrolyte-filled nanopores for determining the shape and volume of single native proteins *in situ*, and for non-spherical proteins, we describe methods for determining their apparent rotational diffusion coefficients and dipole moments while in the nanopore.

Electrolyte-filled nanopores through an insulating membrane are an emerging technology for characterizing macromolecules in their native environment (2-13). For instance, recordings of ionic current through individual nanopores can be used in applications such as single-molecule folding and binding assays (6, 14-18), portable detection of biowarfare agents (19-21), and ultrafast sequencing of nucleic acids (22-25). These single-molecule experiments involve measuring the electric field-induced flow of ions through a single nanopore and the changes in this current (i.e. resistive pulses) when single macromolecules pass through the nanopore. Measuring the magnitude and duration of these transient changes in current (ΔI and t_d) during the translocation of thousands of single proteins enables construction of distributions that can reveal dynamic heterogeneities in size (4, 12, 18, 19, 21, 26-29), conformation (6, 14, 15, 30), and activity of biomolecules *in situ* (8, 10, 16, 31-33).

Established methods for measuring the shape and rotational diffusion coefficients of native proteins in solution include depolarized dynamic light scattering (34), sedimentation by ultracentrifugation (35), small-angle X-ray scattering (36), and neutron scattering after modification of the proteins with deuterium (37). These techniques employ ensemble-based measurements and, therefore, have difficulty characterizing heterogeneous populations and resolving dynamic structures (33). For example, Gambin *et al.* recently used single-molecule FRET methods to observe transient intermediates

during the folding of a single protein that would have been masked using traditional ensemble-based methods (38, 39). As another example, we previously translocated IgG₁ antibodies through bilayer-coated nanopores and observed broad distributions of ΔI values that appeared to be bimodal (16). We hypothesized that this unexpected result was related to the shape and time-dependent orientation of IgG proteins in the nanopore (16). A few months later, Raillon *et al.* also observed what appeared to be bimodal distributions of ΔI values due to the translocation of a non-spherical RNA polymerase through a nanopore and attributed this result to different orientations of the RNA polymerase (26). Additional indications that the shape and orientation of macromolecules can affect the ΔI signal have been reported by Mathé *et al.* who observed orientation-dependent translocation signals of DNA through α -hemolysin pores (40) and Fologea *et al.* who observed unimodal, skewed distribution of ΔI values due to the translocation of nodular fibrinogen proteins through nanopores (5). Despite these first reports, a detailed understanding and quantitative analysis of the effect of molecular shape and orientation on single protein translocation events has not been described. Furthermore, single-molecule methods capable of resolving the shape and volume of single, unlabeled proteins in aqueous environments have yet to be reported.

Here, we use bilayer-coated nanopores to sense four proteins with different shapes: IgG₁ antibody, GPI-anchored acetylcholinesterase (GPI-AchE), IgG-Fab fragment, and streptavidin. We demonstrate that the resulting distributions of maximum ΔI values as well as the time-dependent ΔI signals during the translocation of single proteins are bimodal for non-spherical proteins and thus can be used to calculate the shape and volume of these proteins *in situ*. The time-dependent ΔI signals also reflect the time-dependent orientation of non-spherical proteins in the nanopore and make it possible to determine the apparent rotational diffusion coefficient and dipole moment of a single, unlabeled protein.

3.2 Non-spherical proteins generate bimodal distributions of ΔI values.

To sense the four proteins used in this work (Fig. 3.1), we mounted nanopores between two fluidic channels and coated nanopores with a lipid bilayer comprised of 1-palmitoyl-2-oleoyl-*sn*-glycero-3-phosphocholine (POPC) lipids and 0.15 mol% 1,2-dipalmitoyl-*sn*-glycero-3-phosphoethanolamine-N-capbiotinyl (biotin-PE) lipids (Fig. 3.1A) (16). The biotin-PE lipids served as a ligand to bind and effectively lipid-anchor monoclonal anti-biotin IgG₁ antibodies, polyclonal anti-biotin IgG fab fragments, and streptavidin on the fluid bilayer surface. In contrast, GPI-AchE self-associated with the lipid bilayer coating *via* its glycosylphosphatidylinositol (GPI) anchor. The lipid anchor serves to reduce the translocation speed of the proteins, and the fluid bilayer coating minimizes non-specific interactions with the nanopore surface (16). After recording the baseline current, we added the desired protein to the solution on one side of the nanopore and recorded the resulting current pulses. The magnitudes of resistive pulses, ΔI , due to the translocation of monoclonal anti-biotin IgG₁ antibodies (Fig. 3.2) were markedly more distributed than the ΔI values due to the translocations of the other proteins (Fig. 3.3). In fact, the resistive pulses due to IgG₁ translocations contained multiple current levels within single translocation events, and we observed these types of distributed ΔI values in three different nanopores. These results were interesting because researchers in the field have traditionally considered proteins to be globular spheres for which the ΔI value is proportional to the volume of the protein according to equation (3.1) (4, 5, 12, 16, 29, 31, 41).

$$\Delta I = -\frac{\Lambda V_A \gamma}{\rho(l_p + 0.8d_p)^2} S\left(\frac{d_M}{d_p}\right) \quad (3.1)$$

In this equation, Λ (m³) is the excluded volume of the protein, V_A (V) is the applied voltage, γ (unitless) is an electrical shape factor set to a value of 1.5 for spherical particles, l_p (m) is the length of the pore, d_p (m) is the radius of the cylindrical pore, and ρ (Ω m) is the resistivity of the electrolyte. $S\left(\frac{d_M}{d_p}\right)$ is a correction factor that we set to a value of 1 (Section 3-App.S1) (4, 5, 16, 29, 41-43). Only recently has the shape of non-spherical proteins, determined from crystal structures, been used to estimate values of γ and, subsequently, to calculate the volume of proteins using equation (3.1) (16, 26, 27).

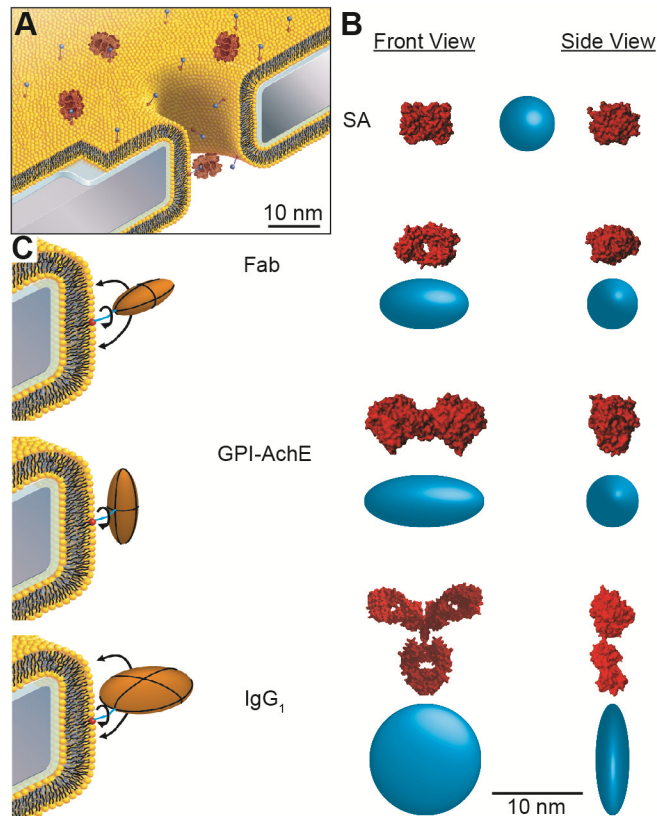


Figure 3.1 | Current recordings through electrolyte-filled, bilayer-coated nanopores during the translocation of the four proteins sensed in this work reveal the corresponding spheroidal shape of proteins (blue shapes) as determined by analysis of resistive pulses. (A) Cross-sectional view of a nanopore fabricated in silicon nitride (grey), the lipid bilayer coating (yellow and black), and the water layer between the lipid bilayer and silicon nitride (blue). In this illustration, streptavidin binds to the biotin group of the biotin-PE lipid (blue and red). (B) Crystal structures were obtained from the protein database bank (IgG₁: 1HZH, GPI-AchE: 3LII, Fab: 1F8T, and streptavidin: 3RY1). Blue spheroids show the volume and shape of the proteins as estimated by analysis of resistive pulses (Table 3.1). (C) Possible orientations of lipid-anchored Fab fragments, GPI-AchE, and IgG₁ antibodies.

In agreement with the treatment of proteins as spherical particles, the ΔI values of resistive pulses due to the translocation of spherical streptavidin proteins were not widely distributed (Fig. 3.3A). We confirmed that the distribution of maximum ΔI values due to streptavidin was Normal (44) by generating empirical cumulative distributions* and performing a Kolmogorov-Smirnov (KS) test (Fig. 3.3D). The resulting p -value of

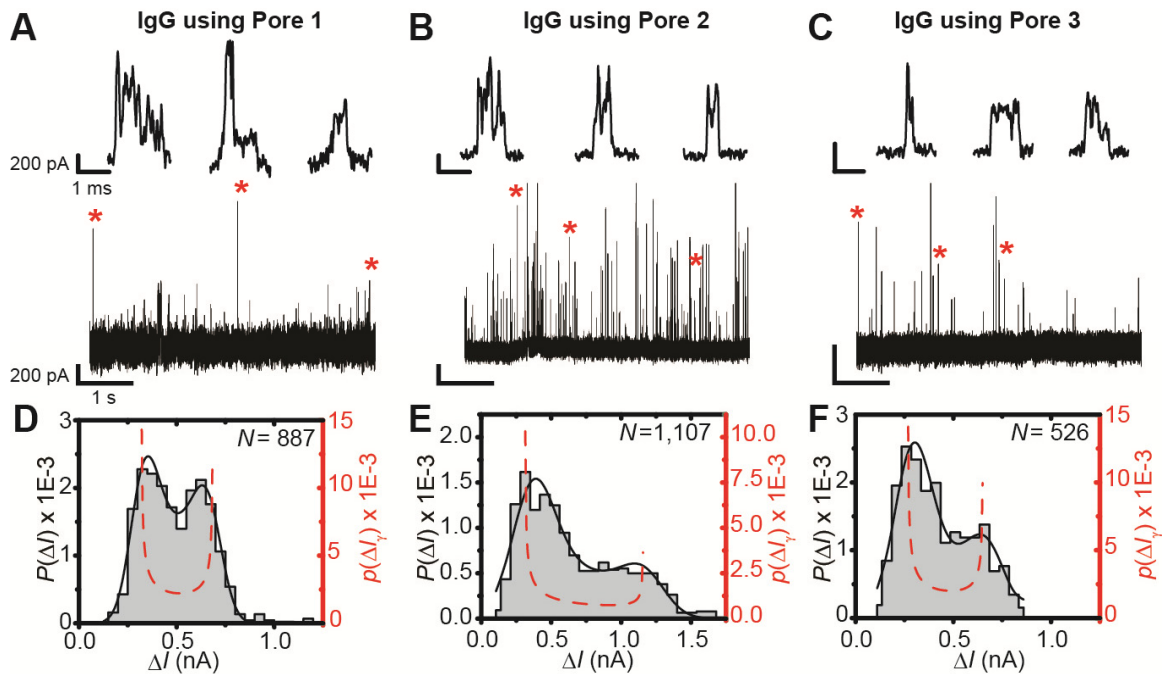


Figure 3.2 | Current traces showing resistive pulses due to the translocation of monoclonal anti-biotin IgG₁ antibodies (A-C) through three different bilayer-coated nanopores and the resulting distributions of the maximum ΔI values (D-F). The volumes of the three nanopores were different resulting in different ΔI values in each pore. Stars (*) indicate the three pulses shown enlarged above the 5 s current traces. (D-F) Histograms of maximum ΔI values show empirical distributions of ΔI values, $P(\Delta I)$. Black curves show the solution of the convolution model, $p(\Delta I)$, after a non-linear least squares fitting procedure, and red dashed curves show the estimated distribution of ΔI values due to the distribution of shape factors, $p(\Delta I_\gamma)$. Dimensions of all nanopores are shown in Fig. 4-App.3, and Table 1-App.3 shows the values for all fitting parameters.

$p = 0.23$ indicated that the difference between these two distributions was not significant. Thus, for streptavidin, the mean ΔI value corresponds to the molecular volume of 110 nm³ according to equation (3.1), and the width of the Normal distribution reflects measurement errors, $\sigma = 70$ pA or 25 nm³ (Table 3.1). In contrast to streptavidin, the distributions of maximum ΔI values due to the translocation of the non-spherical proteins (IgG antibody, Fab fragment, and GPI-AchE) were not Normal (p -values < 0.002, Fig. 1-App.3). Furthermore, control experiments confirmed that the widely distributed ΔI values during IgG₁ translocations were not due to impurities in the solutions, dimers of IgG₁, or translocation of multiple IgG₁ proteins simultaneously (Fig. 2-App.3 and Section 3-App.S2). We also confirmed that the large molecular weight of an IgG protein (152 kDa) (45) did not cause the large variations in ΔI , since the translocation of GPI-AchE (160 kDa) (46) through the same nanopore resulted in a significantly narrower

distribution of ΔI values than the IgG antibodies (Fig. 3-App.3). Consequently, we hypothesized that the non-spherical shape of these three proteins and their orientations in the nanopore relative to the electric field were responsible for the non-Normal distributions of ΔI values and the large variations in ΔI values for IgG antibodies.

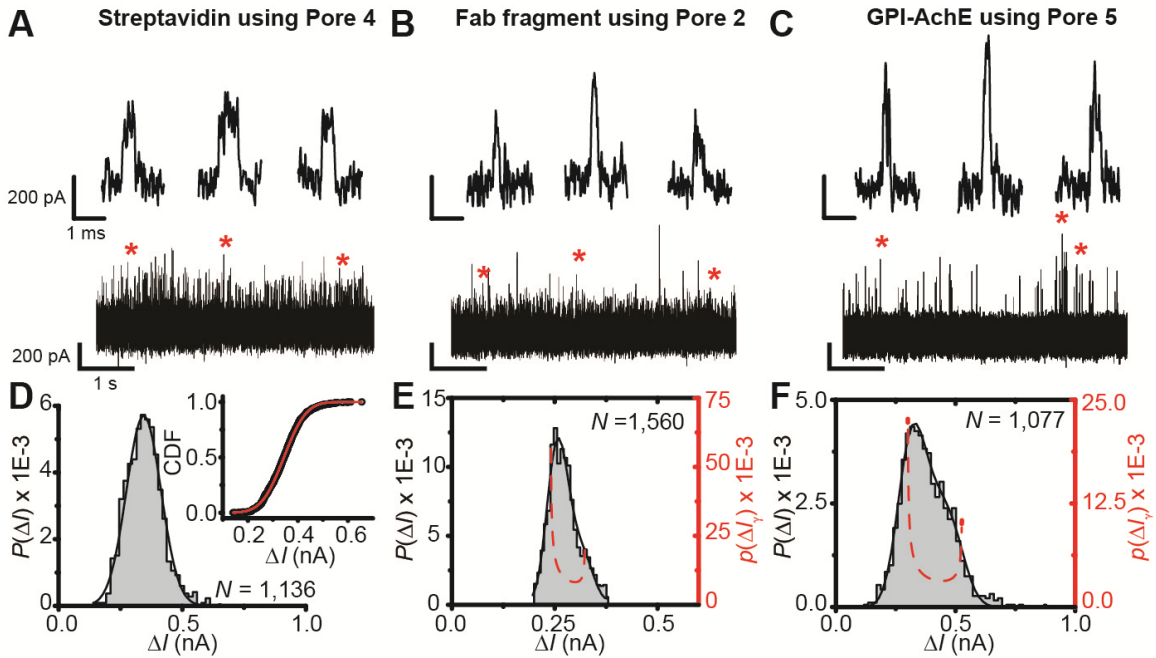


Figure 3.3 | Current traces showing resistive pulses due to the translocation of streptavidin (A), Fab fragments (B), and GPI-AchE (C) and histograms of the maximum ΔI values determined during the translocation of streptavidin (D), Fab fragments (E), and GPI-AchE (F). (D inset) Empirical cumulative distribution (black circles) fit with a Normal cumulative distribution function (CDF) (red line). The derivative of the CDF shows the probability density function (PDF) and is plotted in black with the histogram in D. (E-F) Black curves show the solution of the convolution model, $p(\Delta I)$, after a non-linear least squares fitting procedure, and red dashed curves show the estimated distribution of ΔI values due to the distribution of shape factors, $p(\Delta I_\gamma)$. Stars (*) indicate the three pulses shown enlarged above the 5 s current traces. Table 1-App.3 lists the values of all fitting parameters.

Consistent with this hypothesis, Golibersuch first described the effect of particle shape and orientation on the *distribution* of ΔI values due to cell-sized objects in 1973 (47). Golibersuch observed periodic variations in the values of ΔI during the translocation of rotating, oblate-shaped erythrocytes through microchannels and attributed this periodic signal to the orientation- and shape-dependent values of the electrical shape factor, γ , which is a function of the length to diameter ratio, m , of a spheroid and the angle between

the spheroid's axis of revolution and the electric field, θ , (Fig. 3.4A and 3.4B, Section 3-App.S3) (47-55). Assuming the erythrocytes were randomly oriented at the time the maximum value of ΔI was determined, Golibersuch derived a bimodal probability distribution of shape factors, $p(\gamma)$, (Figure 3.4C black line), which is a function of the minimum and maximum possible values of γ for a given shape, γ_{\min} and γ_{\max} . The two modes of $p(\gamma)$ occur at γ_{\min} and γ_{\max} and correspond to orientations of the particle of $\theta = 0$ and $\theta = \pi/2$. Bimodal distributions of shape factors would lead to bimodal distributions of maximum ΔI values according to equation (3.1) and, therefore, would explain the broad, bimodal distributions of ΔI values due to IgG₁ antibodies (Fig. 3.2D-F). This effect may also explain the non-Normal distributions of ΔI values due to Fab fragments and GPI-AchE (Fig. 3.3E-F).

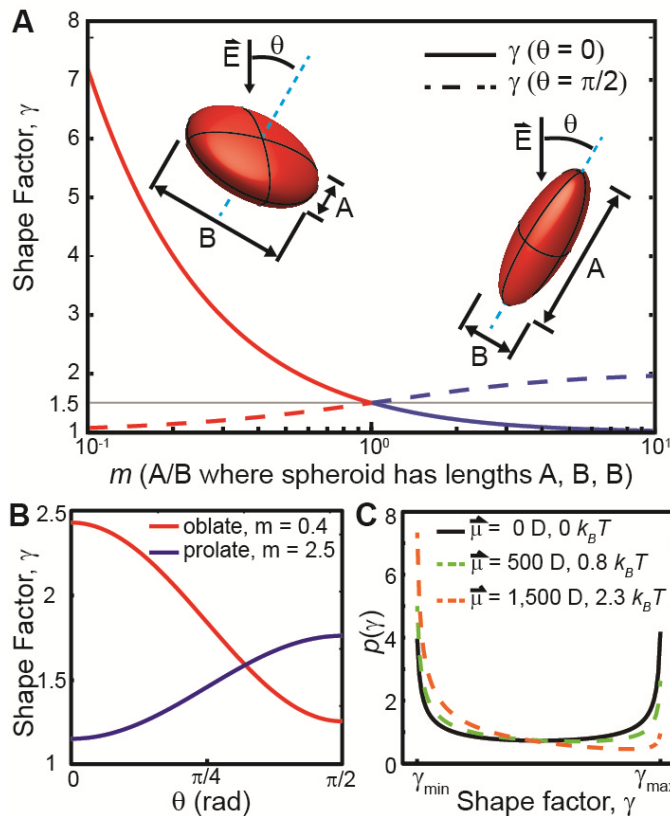


Figure 3.4 | Possible values of shape factors and their probability distribution. (A) Shape factor as a function of m when $\theta = 0$ (solid curves) and when $\theta = \pi/2$ (dashed curves) for prolates (blue curves) and oblates (red curves). For a sphere, m equals 1, and the shape factor is 1.5 (grey line). (B) Shape factor as a function of θ for prolates and oblates with a defined m . For a sphere, m equals 1, and the shape factor is 1.5 (grey line). (C) Probability distribution of shape factors, $p(\gamma)$, predicted by Golibersuch (black curve) and for proteins with a dipole moment pointed parallel to the longest axis of the protein (dashed curves). For the different magnitudes of the dipole moment, the energy difference between $\theta = 0$ and $\theta = \pi/2$ is listed when the electric field equals $2 \times 10^6 \text{ V m}^{-1}$. Section 3-App.S3 describes the electrical shape factor in detail.

Table 3.1. Comparison of the volume and length to diameter ratio, $m = A/B$, of proteins determined by analysis of resistive pulses, the values reported in literature, and the values estimated from the crystal structure of the protein.

Protein	Measured Λ (nm^3)	Literature Λ (nm^3)	Measured m	Literature m
IgG ₁	292±12	347±15 ⁽⁴⁵⁾	0.30±0.05	0.2–0.5 ^(57, 58)
GPI-AchE ^a	216±24	250 ^b	0.53 or 2.6	2.9 ^b
Fab	160±8	125 ^b 140 ⁽⁶⁹⁾ 170±31 ⁽¹⁶⁾	0.65 or 1.8	1.7 ^b 1.8 ⁽⁷⁰⁾
Streptavidin	120±25 ^c	94±18 ⁽¹⁶⁾ 105±3 ⁽⁷¹⁾	1 ^c	1.1 ^b

^aValues were calculated from two experiments (Table 1-App.3). ^bValues were estimated from the crystal structures of the protein shown in Figure 1B. ^c Since the distribution of ΔI values due to streptavidin translocations was unimodal and Normal, we assumed that streptavidin had a spherical shape, and therefore $m = 1$; to calculate the excluded volume of streptavidin, we solved equation (1) with γ set to a value of 1.5.

Before attempting to describe the non-Normal distributions of ΔI values as a consequence of $p(\gamma)$, we considered whether the three non-spherical proteins could sample various orientations, and therefore shape factors, in these experiments. We first examined whether the dipole moment of a protein may align completely in the large electric field in the nanopore ($\sim 10^6 \text{ V m}^{-1}$). Combining the potential energy, ΔU , of a dipole moment in an electric field and the Boltzmann distribution of energies while assuming that the dipole moment was pointed parallel to the longest axis of the protein, we expanded on Golibersuch's probability distribution of shape factors to develop a $p(\gamma)$ for proteins with dipole moments (Fig. 3.4C, Sections 3-App.S3 and 3-App.S6). This simple model predicts a bimodal distribution of shape factors in these experiments when the dipole moment ranged from 0 to 1,500 Debyes. Since the average dipole moment of proteins is approximately 550 Debyes (<http://bioinfo.weizmann.ac.il/dipol/aves2.html>), this model implies that most non-spherical proteins would not be biased by the electric field sufficiently to prevent their rotation. This prediction is supported by our recent discovery of bimodal distributions of ΔI values from translocation of a single, pure protein (16) and subsequent observations made by Raillon *et al.* (26). We next considered potential steric limitations on the orientations of the proteins in the nanopore. Fig. 3.1C shows the expected lipid anchoring locations on spheroids approximately the

shape of a Fab fragment, GPI-AchE (46), and an IgG antibody. Since the chemical linker between the lipid head group and the ligand for the IgG₁ and Fab fragments was approximately 1.5 nm in length, we expect the anchoring positions shown in Fig. 3.1C to permit rotation of the proteins in orientations that could generate the minimum and maximum shape factors. Consequently, we propose that the underlying distribution of shape factors for non-spherical proteins explains the non-Normal distributions of ΔI values and enables the calculation of each protein's volume and shape.

3.3. Fitting distributions of ΔI values enables calculation of a protein's shape and volume.

To determine the excluded volume, Λ , and length to diameter ratio, m , of the proteins from the non-Normal distributions of maximum ΔI values, we first considered that γ is directly proportional to ΔI according to equation (3.1). Consequently, γ_{\min} and γ_{\max} for a given shape correspond to the minimum and maximum ΔI values, ΔI_{\min} and ΔI_{\max} , of a given particle, where ΔI_{\min} is a function of $\gamma_{\min}(m)$ and Λ , and ΔI_{\max} is a function of $\gamma_{\max}(m)$ and Λ (Section 3-App.S4). By determining ΔI_{\min} and ΔI_{\max} from the measured distributions of ΔI values, we can solve for the values of Λ and m of each non-spherical protein.

To describe the non-Normal distributions of ΔI values quantitatively based on the distribution of shape factors, $p(\gamma)$, and to determine ΔI_{\min} and ΔI_{\max} , we converted the distribution of shape factors into a corresponding distribution of ΔI values, $p(\Delta I_{\gamma})$ (Section 3-App.S3). Complicating the analysis is the fact that $p(\Delta I_{\gamma})$ is convolved with experimental and analytical noise in determining individual ΔI values, which we describe as a Normal distribution, $p(\Delta I_{\sigma})$. Thus, the empirical distributions of ΔI values, $P(\Delta I)$, should be described by the theoretical model $p(\Delta I) = p(\Delta I_{\gamma}) \otimes p(\Delta I_{\sigma})$, where \otimes is the convolution operator (Fig. 5-App.3). We fit this model to the empirical distributions of ΔI values using the Levenberg-Marquardt nonlinear-least-squares fitting algorithm in the software Origin Pro 8. The procedure compared the experimental distribution of ΔI values, $P(\Delta I)$, to estimates of $p(\Delta I)$, and generated new values for the four fitting parameters ΔI_{\min} , ΔI_{\max} , ΔU , and σ after each iteration (56). The black curves in Fig. 3.2D-F and Fig. 3.3E-F show the resulting estimate of $p(\Delta I)$ and the red dashed curves

show the estimate of $p(\Delta I)$, which was bimodal with modes at ΔI_{\min} and ΔI_{\max} . The estimates of $p(\Delta I)$ described the empirical distributions of ΔI values well ($R^2 > 0.92$), and we confirmed by KS-tests that the differences between each empirical $P(\Delta I)$ and each estimated $p(\Delta I)$ were not statistically significant ($p\text{-values} > 0.31$). Fig. 1-App.3 shows results from KS tests and compares plots of cumulative distributions of $P(\Delta I)$ and $p(\Delta I)$. Using the resulting estimates of ΔI_{\min} and ΔI_{\max} , we solved for the excluded volume of the proteins, Λ , and the length to diameter ratio, m , (Table 3.1). The calculated values of Λ and m agree well with the expected values for all four proteins. For instance, from the three experiments with the IgG₁ antibodies, we calculated the excluded volume of an IgG₁ to be 290 nm³, 281 nm³, and 305nm³ with an average of 292 ± 19 nm³, and the reported volume of IgG antibodies is 347 nm³ (45). Corresponding values of m were 0.35, 0.26, and 0.29 with an average of 0.30 ± 0.05 (a diameter to length ratio of 3.33); reported estimates of m when an antibody is approximated as an oblate shape range from 0.2 to 0.5 (57, 58). For the prolate-shaped Fab fragments and GPI-AchE, we found two solutions to the system of equations, indicating that either an oblate or prolate shaped protein could have generated these non-normal distributions of ΔI values (Fig. 6-App.3). In both cases, the value of m that corresponds to a prolate shape ($m > 1$) was close to the value we estimated from the crystal structure of the protein (Table 3.1), suggesting this solution was correct. Fig. 3.1B shows the crystal structure of each protein next to the corresponding spheroid and illustrates the close agreement between the shape of the proteins calculated from the analysis presented here and the expected shape based on crystal structures. This result and the good fits of $p(\Delta I)$ to the empirical distributions of ΔI values demonstrates that non-Normal distributions of ΔI can be used to determine the volume and shape of proteins in solution.

As additional evidence that the orientation and shape of non-spherical proteins affects the distribution of ΔI values, we biased the orientation of IgG₁ antibodies and GPI-AchE proteins in the nanopore by increasing the electric field (Fig. 7-App.3). For both proteins, increasing the strength of the electric field skewed the distribution of ΔI values toward their respective ΔI_{\min} values (i.e. $\theta = \pi/2$ for an oblate and $\theta = 0$ for a prolate) and reduced the proportion of events with magnitudes close to the value ΔI_{\max} . Furthermore, the ratio between the number of events with magnitudes near ΔI_{\max}

compared to ΔI_{\min} declined exponentially with increasing electric field strength, suggesting that the potential energy of proteins in the orientation corresponding to ΔI_{\min} was lower than the energy of those in the orientation corresponding to ΔI_{\max} . Considering that the orientations of the two proteins were biased due to the energy of a dipole moment in an electric field, we fit these curves (Fig. S7-App.3) with a two-state Boltzmann model and estimated a dipole moment of 996 ± 32 Debyes for the IgG₁ antibody and 360 ± 30 Debyes for GPI-AchE. These values for the dipole moment are in the expected range for the dipole moments of proteins. Many factors could bias the alignment of the proteins and the accuracy of these values, however, including alignment of the slender proteins in the electric field gradient prior to entering the nanopore (59, 60), entropic barriers affecting orientation inside the nanopore, and dipole moments that are not aligned perpendicular or parallel to the axis of symmetry of these non-spherical proteins.

3.4. ΔI values within individual translocation events reveal apparent rotational diffusion coefficients and dipole moments.

So far, we have discussed distributions of maximum ΔI values; however, the ionic current signal during an individual translocation event (intra event- ΔI) can also reveal the shape and time-dependent orientation of a single protein in the nanopore. For instance, Fig. 3.5 shows individual translocation events and distributions of intra event- ΔI values during three long translocation events of single IgG₁ antibodies. Again, the convolution model, $p(\Delta I) = p(\Delta I_{\gamma}) \otimes p(\Delta I_{\sigma})$, described the empirical distributions of ΔI values well and returned estimates of the excluded volume and the value of m ($\Lambda = 300, 240, \text{ and } 335 \text{ nm}^3$; $m = 0.33, 0.23, \text{ and } 0.44$) that were similar to those determined earlier by analyzing distributions of the maximum ΔI values from thousands of events (Table 3.1).

Since γ is a function of the orientation of the proteins (Fig. 3.4B), we calculated $\theta(t)$ from a intra event ΔI signal due to a single IgG₁ antibody, GPI-AchE, and Fab fragment protein and generated plots of the mean-squared-angular-displacement, $\langle \Delta \theta^2(t) \rangle$ (Fig. 3.6). We fit these curves with a model based on the Langevin torque

equation in which we neglected inertia and included terms for the thermal driven torque (*i.e.* $\sim k_B T$) viscous drag (*i.e.* $\sim k_B T/D_R \times d\theta/dt$), and electric-field induced restoring torque

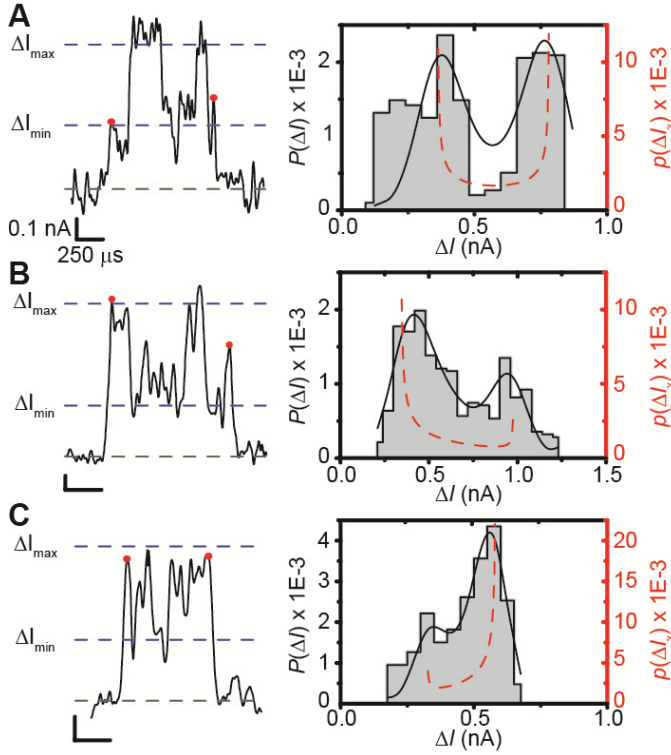


Figure 3.5 | Resistive pulses due to the translocation of IgG₁ antibodies and histograms of intra event ΔI values (A-C). Experiments were performed in three different nanopores as in Fig. 3.2, and the dotted blue lines indicate the values of ΔI_{\min} and ΔI_{\max} expected from fitting the convolution model to the distributions in Fig. 3.2D-F. The current signal between the red dots was considered the intra event- ΔI signal. Black curves show the solution of the convolution model, $p(\Delta I)$, after a non-linear least squares fitting procedure, and red dashed curves show the estimated distribution of ΔI values due to the distribution of shape factors, $p(\Delta I_\gamma)$.

due to the dipole moment (*i.e.* $\sim \bar{E} \bar{\mu} \sin(\theta)$) (Section 3-App.S5) (61), where D_R ($\text{rad}^2 \text{s}^{-1}$) is the rotational diffusion coefficient, \bar{E} (V m^{-1}) is the electric field, and $\bar{\mu}$ (Debyes) is the dipole moment of the protein. This model describes the Brownian rotational motion about one axis of a particle in a harmonic energy well; it is analogous to translational motion of a Brownian, harmonically bound particle (62). With D_R and $\bar{\mu}$ as fitting parameters, this model described $\langle \Delta \theta^2(t) \rangle$ very well ($R^2 > 0.97$) and returned values of the apparent rotational diffusion constant and dipole moment of: for the IgG₁ $D_R = 3,700$ (3000, 4500) rad s^{-2} , $\bar{\mu} = 1,220$ (1190, 1230) D; for GPI-AchE $D_R = 6,000$ (5200, 7000) rad s^{-2} , $\bar{\mu} = 730$ (670, 790) D; and for Fab $D_R = 7,200$ (6400, 7900) rad s^{-2} , $\bar{\mu} = 1,749$ (1580, 1960) D. The 95% confidence interval of the values is listed in the parenthesis. The resulting values of D_R were in the expected range for lipid-anchored proteins; for instance, Axelrod reported that the rotational diffusion coefficient of membrane-

associated, monomeric GPI-AchE is on the order of $D_R = 10,000 \pm 4,000 \text{ rad}^2 \text{ s}^{-1}$ (63). Moreover, the values of D_R for the different proteins exhibit the expected trend of the smallest D_R for the largest protein, IgG₁ antibody, and the greatest D_R for the smallest protein, Fab fragment. The estimates of $\bar{\mu}$ ranged from ~ 700 to 2000 Debyes for the

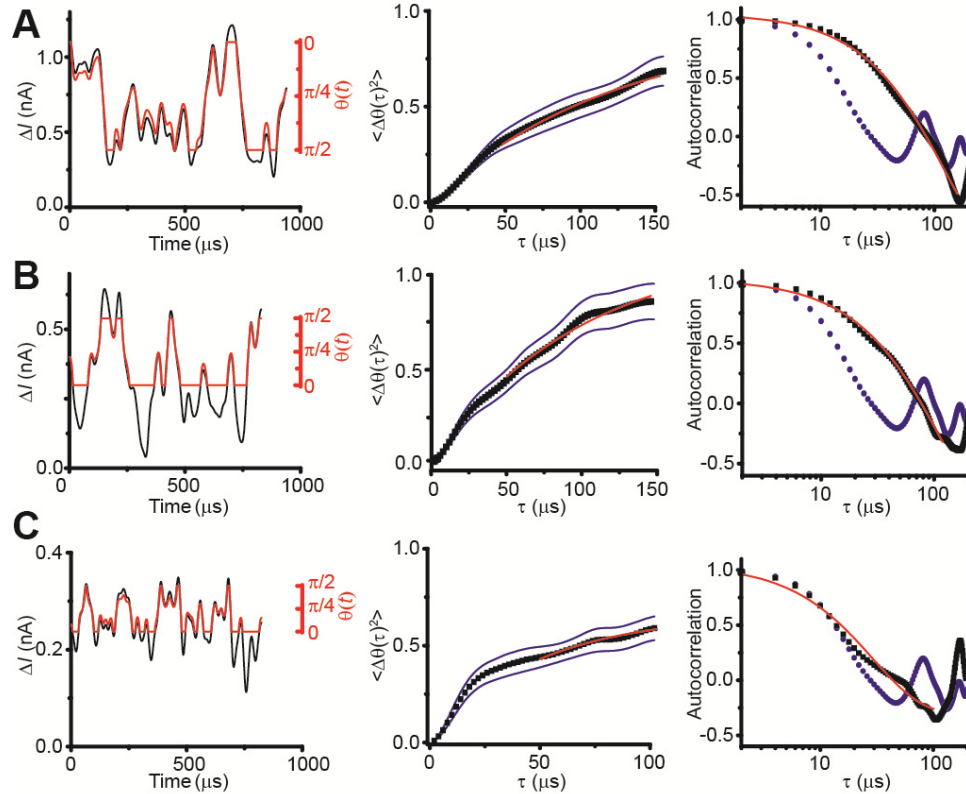


Figure 3.6 | Intra-event ΔI signals due to the translocation of a single IgG₁ antibody (A), GPI-AchE (B), and Fab fragment (C) overlaid with the calculated orientation of the protein, $\theta(t)$. Values of $\theta(t)$ were calculated based on the function $\gamma(\theta)$ (Section 3-App.S3) and using the values of ΔI_{\min} and ΔI_{\max} that are listed in Table 1. The $\theta(t)$ signal enabled construction of mean squared angular displacement curves, $\langle \Delta\theta(\tau)^2 \rangle$, and temporal autocorrelation curves. In the $\langle \Delta\theta(\tau)^2 \rangle$ plots, blue lines indicate the 95% confidence interval of the mean; red lines are the best-fit of the data with a model based on the Langevin torque equation (Section 3-App.S5). We only fit the data with $\tau > 50 \mu\text{s}$ because the signal for $\tau < 50 \mu\text{s}$ was dominated by the electrical noise. In the autocorrelation plots, red lines show an exponential decay with a characteristic time τ_C that is inversely proportional to the rotational diffusion constant, D_R , and the effective rotational spring constant, k_θ , by $\tau_C = k_B T / (D_R \times k_\theta)$ (66). Blue circles show temporal autocorrelation curves of the baseline current for comparison.

three proteins, and were thus in the expected range given that the average dipole moment of proteins in the Weizmann database is 550 ± 420 . Additionally, the value of 730 Debyes for the dipole moment of GPI-AchE that we determined with this method lies in

the expected range (700 to 1000 Debyes) of GPI-AchE's highly conserved dipole moment (64, 65). Moreover, the dipole moment that we determined for the IgG₁ antibody using this method was similar to the value we determined in the previous section using the two-state Boltzmann model (i.e. 1220 compared to 996 Debyes). In additional support of this analysis, we generated temporal autocorrelation curves of $\theta(t)$ and determined the characteristic times, τ_C , of their exponential decay (Fig. 3.6), where $\tau_C = k_B T / (D_R \times k_\theta)$ and k_θ is an effective rotational spring constant approximated by $\bar{E} \bar{\mu}$ (Section 3-App.S5) (66). Using the values of D_R , \bar{E} , and $\bar{\mu}$ determined by fitting $\langle \Delta\theta^2(t) \rangle$ curves, we compared the predicted τ_C with the value of τ_C determined in the autocorrelation curves. In the case of the IgG₁ and GPI-AchE events (Fig. 3.6A and Fig. 3.6B) the predicted and measured characteristic times were identical (e.g. for IgG antibody τ_C was 130 μ s compared to the predicted value of 125 ± 20 μ s and for GPI-AchE τ_C was 101 μ s compared to the predicted value of 100 ± 10 μ s). In the case of the Fab fragment event (Fig. 3.6C), however, the measured characteristic time was a factor of ~ 1.5 shorter than the expected value (e.g. τ_C was 29 μ s compared to the predicted value of 45 ± 5 μ s). This difference could be due to rotational diffusion of the Fab fragment about more than one axis (see Fig. 3.1C), or it could be due to the limited temporal resolution of the electronic amplifiers. For instance, the autocorrelation curve in Fig. 3.6C for the Fab fragment approaches the curve due to electrical noise (blue points). These results demonstrate that long translocation events can be used to resolve the rotation of individual non-spherical proteins and thus to determine effective rotational diffusion coefficients and dipole moments of proteins in the nanopore.

To obtain a more complete picture of how much time molecules spent in a given orientation in the nanopore, we generated histograms of intra event- ΔI values from *all* translocation events. Interestingly, for the IgG₁ protein, these distributions had more than the expected two modes and instead showed approximately five local maxima (Fig. 8-App.3). Given that the regions of an IgG antibody between the Fc domain and the two Fab fragments are very flexible (58, 67), these modes may correspond to dynamic fluctuations in the shape and conformation of IgG antibodies

3.5 Conclusion.

The work presented here extends the capability of nanopores for distinguishing and characterizing proteins by adding the estimation of shape and volume of non-spherical proteins to those properties of proteins that can already be determined in nanopores such as charge and affinity for a ligand. Unlike the standard technique of determining a protein's shape via small angle x-ray scattering, this method can be used to determine the native shape of single proteins or protein complexes in aqueous environments, with relatively simple equipment, and in only a few minutes. This capability will aid structural and functional studies of proteins since for many proteins only fragments can be crystallized and knowing the general shape of proteins facilitates determining their structure.

Dynamic fluctuations in the orientations of proteins in the nanopore were reflected in the intra event ΔI signals, thereby, permitting calculation of the effective rotational diffusion coefficient and dipole moment of individual non-spherical proteins within the nanopore. Additional studies of protein dynamics with this method will benefit from low-noise electronic amplifiers with improved time resolution such as those recently described by Rosenstein (67, 68). Moreover, molecular dynamics and hydrodynamic modeling will likely advance the understanding of variations in the ΔI signals due to proteins and possibly due to fluctuations in their conformation. We expect the combination of these methods to enable direct and accurate observation of dynamic heterogeneities in protein structures, orientations, and dipole moment *in situ* without requiring chemical modification of the protein. Finally, we anticipate that anchoring proteins to amine-reactive or thiol-reactive lipid head groups will be a strategy to extend this approach to a large number of proteins.

Chapter 3 Appendix

3-App.Methods

Materials. All phospholipids were obtained from Avanti Polar Lipids. Streptavidin, monoclonal anti-biotin antibody (B7653), and GPI-anchored acetylcholinesterase purified from human erythrocytes (C0663) were purchased from Sigma Aldrich, Inc. and polyclonal anti-biotin Fab fragments (20938) from Rockland.

Methods of nanopore-based sensing experiments. To sense proteins, we first formed a supported lipid bilayer of 1-palmitoyl-2-oleoyl-*sn*-glycero-3-phosphocholine (POPC) lipids (Avanti Polar Lipids, Inc.) and a 0.15 mol% fraction of 1,2-dipalmitoyl-*sn*-glycero-3-phosphoethanolamine-N-capbiotinyl (biotin-PE) lipids on the silicon-nitride surface that contained a nanopore. We described details of the bilayer formation in Yusko *et al.* (16). The dimensions of all nanopores are shown in Fig. 5-App.3. After measuring the expected baseline ionic current and confirming the absence of irregular noise, we added solutions containing the desired protein to the top solution compartment of the fluidic setup (2 M KCl with 10 mM HEPES pH 7.4) such that the final concentration of protein ranged from 5 pM to 10 nM. In sensing GPI-anchored acetylcholinesterase, we started recording resistive pulses after incubating the bilayer-coated nanopore for 1 h with GPI-anchored acetylcholinesterase to allow time for the GPI-lipid anchor of the protein to insert into the fluid lipid bilayer coating. We recorded resistive pulses at an applied potential difference of -0.1 V with the polarity referring to the top fluid compartment relative to the bottom fluid compartment, which was connected to ground. We used Ag/AgCl pellet electrodes (Warner Instruments) to monitor ionic currents through electrolyte-filled nanopores with a patch-clamp amplifier (Axopatch 200B, Molecular Devices Inc.) in voltage-clamp mode (*i.e.*, at constant applied voltage). We set the analog low-pass filter of the amplifier to a cutoff frequency of 100 kHz. We used a digitizer (Digidata 1322) with a sampling frequency of 500 kHz in combination with a program written in LabView to acquire and store data (69). To distinguish resistive pulses reliably from the electrical noise, we first filtered the data digitally with a Gaussian low-pass filter ($f_c = 15$ kHz) in MATLAB and then used a modified form of the custom written MATLAB routine described in Pedone *et al.* (70). We calculated the

translocation time, t_d , as the width of individual resistive-pulse at half of their peak amplitude, also known as the full-width-half-maximum value (6, 16). From this analysis we obtained the ΔI and t_d values for each resistive pulse, and we only analyzed ΔI values for resistive-pulses with t_d values greater than 50 μs , since resistive pulses with translocation times faster than 50 μs have attenuated ΔI values due to the low-pass filter (16, 70).

3-App.S1. Details regarding equation (3.1).

The relationship between the magnitude of ΔI and the volume of a particle stems from Maxwell's derivation (71), and it is shown in equation (1-App.3).(4, 29, 49, 72)

$$\frac{\Delta I}{I} = -\frac{4\Lambda\gamma}{\pi d_p^2 (l_p + 0.8d_p)} S\left(\frac{d_M}{d_p}\right) \Rightarrow \Delta I = -\frac{\Lambda V_A \gamma}{\rho (l_p + 0.8d_p)^2} S\left(\frac{d_M}{d_p}\right), \quad \text{(1-App.3)}$$

where γ is the electrical shape factor (26, 27, 43, 47, 49, 51), Λ (m^3) is the excluded volume of the particle, l_p (m) is the length of the pore, d_p (m) is the diameter of the pore, ΔI (A) is the magnitude of the change in the current during translocation of a particle, I (A) is the baseline current, V_A (V) is the applied voltage, and ρ ($\Omega \text{ m}$) is the resistivity of the electrolyte. $S\left(\frac{d_M}{d_p}\right)$ is a correction factor applied when the diameter of the particle, d_M , approaches the diameter of the pore, D_p , (i.e. $d_M > 0.5 D_p$).(49, 72) Under these conditions the electric field in the pore is additionally distorted between the particle and the pore walls resulting in a non-linear increase in the resistance with increasing particle volume (49, 72). Qin *et al.* recently reviewed these correction factors and showed that the most accurate correction factor for all d_M/d_p ratios was developed by Smythe (42) and Deblois et al. (72), equation (2-App.3) (41):

$$S\left(\frac{d_M}{D_p}\right) = \frac{1}{1 - 0.8\left(\frac{d_M}{d_p}\right)^3}. \quad \text{(2-App.3)}$$

Note that in the majority of resistive-pulse sensing literature, particles and proteins have been considered spherical and consequently γ was set to a value of 1.5 and Λ was constrained to equal $\frac{1}{6} \pi d_M^3$. Substituting these values into equation (1-App.3)

simplifies it to the more commonly seen form in equation (3-App.3) (4, 29, 41, 43, 71, 72):

$$\frac{\Delta I}{I} = -\frac{d_M^3}{d_p^2(l_p + 0.8d_p)} S\left(\frac{d_M}{d_p}\right) \Rightarrow \Delta I = -\frac{\pi V_A d_M^3}{4\rho(l_p + 0.8d_p)^2} S\left(\frac{d_M}{d_p}\right), \quad (3-App.3)$$

Since in this work we analyzed resistive-pulses due to the translocation of non-spherical proteins and we expected d_M to be less than $\frac{1}{2} d_p$, we set the correction factor to a value of 1 (4, 16, 29). We used equation (1-App.3) and expressed the impeded flow of ions through the nanopore during protein translocation events as reductions in current, ΔI .

3-App.S2. Broad distributions of IgG₁ antibodies were not due to impurities, dimers, or simultaneous translocations.

To confirm that the distributions of ΔI values during experiments with monoclonal anti-biotin IgG₁ antibodies were not affected by potential impurities in the solution, we performed two control experiments. In one control experiment, we added an excess concentration of soluble biotin to the aqueous solution of an ongoing experiment (Fig. 2A-App.3) in order to inhibit competitively the binding of the IgG₁ antibodies to the biotin-PE lipids on the surface (Fig. 2B-App.3). Fifteen minutes after the addition of the soluble biotin we observed the frequency of resistive pulses decrease from 34 s⁻¹ to 1.3 s⁻¹. In the second control experiment, we generated a lipid bilayer coated nanopore that did not contain biotin-PE lipids in the coating and therefore was not specific for the translocation of IgG₁ antibodies (Fig. 2C-App.3). In this experiment, the concentration of the IgG₁ antibody was even higher (25 nM compared to 20 nM) than in the original experiment (Fig. 2A-App.3), and the frequency of translocation events was 2 s⁻¹. Since the frequency of events is proportional to concentration, we estimated that if the concentration of IgG₁ in this control experiment was 20 nM, we would expect to observe an event frequency of approximately 1.6 s⁻¹. From these two control experiments, we estimated that during experiments with biotin-PE lipids in the bilayer coating only 3.8 to 4.7 % of translocation events were due to IgG₁ or other proteins not bound to biotin-PE lipids. Furthermore, almost all of the translocation times calculated from resistive-pulses observed in control experiments (where binding to biotin-PE was not possible) were less

than 50 μ s, and we did not include resistive-pulses with translocation times less than 50 μ s in the analysis of ΔI distributions because the amplitude would be attenuated due to electronic filtering (16, 69). Consequently, we concluded that the protein we detected in the purified solution of anti-biotin IgG₁ antibodies was bound to biotin-PE lipids specifically. We also concluded that the resistive-pulses were not due to Fab fragments of the IgG₁ in solution because the translocation of Fab Fragments through the same nanopore resulted in resistive pulses with ΔI values less than those observed for the IgG₁ antibody (244-325 pA compared to 383-1085 pA, Table 1-App.3).

Since IgG antibodies can occasionally form dimers (73), we performed dynamic light scattering (DLS) experiments to characterize the hydrodynamic diameter of the IgG₁ antibodies. If dimers of IgG₁ antibodies were present in solution and contributing to the bimodal distribution of ΔI values in Fig. 3, we would expect the dimers to be reflected in DLS experiments in a significant fraction because approximately $\frac{1}{2}$ of the resistive pulses had ΔI values within the second bimodal peak of ΔI values. Consequently, if dimers were present, we would expect to observe two peaks in the distributions of estimated hydrodynamic diameters of the particles (in this case proteins) in DLS experiments (73). Fig. 3-App.3 shows that we only observed one peak corresponding to a hydrodynamic diameter of 10.5 ± 2.0 nm. This value is in good agreement with previously published hydrodynamic diameters of IgG antibodies of 10.9 -11.0 nm (73, 74). As additional evidence, we added urea to a concentration of 8 M to denature all proteins and disassociate potential aggregates. Again we only observed one peak corresponding to a hydrodynamic diameter of 12.9 ± 2.7 nm (Fig. 3-App.3). This hydrodynamic diameter is slightly larger because of the random-coil and ball-like structure of denatured IgG₁ antibodies compared to their native, oblate-shaped structures (73). These results confirm that dimers of IgG₁ antibodies were not responsible for the bimodal distribution of ΔI values.

To rule out the possibility that the widely distributed ΔI values were due to two proteins passing through the nanopore simultaneously, we compared the frequency of translocation events with the translocation times for each protein (75). In the case of streptavidin translocations, we observed approximately 45 translocation events per second and a most-probable translocation time of about 115 μ s. Consequently, on

average there was a 0.52% probability of a molecule occupying the nanopore at any time, and the probability of two streptavidin proteins occupying the nanopore at the same time would be 0.003%. In the case of the IgG₁ translocation events, the maximum frequency we observed was approximately 30 events per second and a most probable translocation time of about 55 μ s. Consequently, on average there was a 0.16% probability of an IgG₁ protein occupying the nanopore at any time, and the probability of two IgG₁ proteins occupying the nanopore at the same time would then be 0.0027%. Even if the first translocation event of an IgG antibody would be exceptionally long lived (e.g. 1000 μ s), the probability of a second antibody to enter the pore during that time would still only be around 3% at an average translocation frequency of 30 Hz. This analysis neglects steric effects, which we expect would be significant given the size of an IgG₁ antibody and the dimensions of the nanopores. For GPI-anchored acetylcholinesterase the estimated probability of a two proteins being in the nanopore at the same time was 0.0036% and for Fab fragments it was 0.0016%.

Even during the resistive-pulse sensing experiments with streptavidin in which we estimated the highest probability of observing a protein in the nanopore, we did not observe resistive-pulses with multiple current levels that might suggest the translocation of two proteins simultaneously. Consequently, we conclude that the resistive pulses due to the IgG₁, Fab fragments, and GPI-anchored acetylcholinesterase proteins were due to the translocation of one protein at a time.

3-App.S3. Electrical shape factor and distributions of shape factors.

To relate the value of ΔI to the volume and shape of non-spherical proteins, we considered the possible values of the electrical shape factor, γ , with the condition that a protein may have an oblate, prolate or spherical shape. Oblates and prolates have an axis of revolution (shown as the dashed blue line in Fig. 3.4) with length A and secondary axes with length B . Golibersuch elegantly pointed out that equation (4-App.3) describes the electrical shape factor, γ , for these ellipsoids as a function of the angle between the axis of symmetry and the electric field, θ , (Fig. 3.4) (47, 48):

$$\gamma(\theta) = \gamma_{\perp} + (\gamma_{\parallel} - \gamma_{\perp}) \cos^2(\theta) \quad (4-App.3)$$

where γ_{\parallel} and γ_{\perp} are the electrical shape factors when the axis of symmetry is parallel to the electric field (i.e. $\theta = 0, \pi, \dots$) and perpendicular to the electric field (i.e. $\theta = \pi/2, 3\pi/2, \dots$), respectively. Equation (4-App.3) implies that the shape factor for any orientation will range between the values of γ_{\parallel} and γ_{\perp} . These factors, γ_{\parallel} and γ_{\perp} , are related to the well-described depolarization factors for ellipsoids, n_{\parallel} and n_{\perp} , by equation (5-App.3) and are a function of the length to diameter ratio, $m = A/B$, of an ellipsoid (47, 51-53).

$$\gamma_{\parallel} = \frac{1}{1-n_{\parallel}} \text{ and } \gamma_{\perp} = \frac{1}{1-n_{\perp}} \quad \text{(5-App.3)}$$

where n_{\parallel} for a prolate spheroid with $m = A/B > 1$ is described by equation (6-App.3):

$$n_{\parallel} = \frac{1}{m^2-1} \left[\frac{m}{\sqrt{m^2-1}} \ln \left(m + \sqrt{m^2-1} \right) - 1 \right] \quad \text{(6-App.3)}$$

and n_{\parallel} for an oblate spheroid with $m = A/B < 1$ is described by equation (7-App.3):

$$n_{\parallel} = \frac{1}{1-m^2} \left[1 - \frac{m}{\sqrt{1-m^2}} \cos^{-1}(m) \right] \quad \text{(7-App.3)}$$

and $n_{\perp} = (1 - n_{\parallel})/2$ (43, 47, 52).

To derive the distribution of shape factors, we considered the simplest scenario that an ellipsoid protein rotates freely around the chemical linker with only one axis of rotation such that, by symmetry, values of θ ranged between 0 and $\pi/2$. We also assumed that all angles of θ were equally likely when the maximum ΔI was measured. According to Golibersuch, these assumptions enable using substitution of variables to write a probability distribution function for electrical shape factors $p(\gamma)$ based on the probability of observing a certain orientation $p(\theta(\gamma))$, where θ is a function of γ (e.g. equation (8-App.3)): (47)

$$p(\gamma)d\gamma = p[\theta(\gamma)] \frac{d\theta}{d\gamma} d\gamma \quad \text{(8-App.3)}$$

Since by symmetry, the value of θ ranges between 0 and $\pi/2$ and we assumed that all angles of θ were equally likely, we solved for $p(\theta)$ by noting that the integral of a probability distribution function equals 1:

$$\int_0^{\pi/2} p(\theta)d\theta = 1 = \int_0^{\pi/2} \frac{2}{\pi} d\theta \Rightarrow p(\theta)d\theta = \frac{2}{\pi} d\theta \quad \text{(9-App.3)}$$

Combining equation (8-App.3) with (9-App.3), we obtained:

$$p(\gamma)d\gamma = \frac{2}{\pi} \left(\frac{d\gamma}{d\theta} \right)^{-1} d\gamma. \quad \text{(10-App.3)}$$

Differentiating equation (4-App.3) with respect to θ , *i.e.* $\frac{d\gamma}{d\theta}$, and combining the result with equation (10-App.3), we obtained a probability density function for the possible shape factors (47).

$$p(\gamma)d\gamma = \frac{1}{2\pi \left[(\gamma - \gamma_{\perp})(\gamma_{\parallel} - \gamma) \right]^{1/2}} d\gamma \quad \text{(11-App.3)}$$

Fig. 3.4C of the main chapter (black line) shows this probability density function (equation 11-App.3) is bimodal and symmetric with peaks at $\gamma = \gamma_{\parallel}$ and γ_{\perp} . The bimodal character of this distribution reflects the fact that for small deviations in θ near 0 and near $\pi/2$, there is little change in the value of the shape factor compared to deviations in θ around $\pi/4$ (Fig. 3.4B).

To expand on the theories developed by Golibersuch, we considered the possible probability distribution of shape factors if the orientation of the protein were biased by the electric field in the nanopore. The electric field in the nanopore is on the order of 10^6 V m⁻¹, and consequently, we expect the orientation of a protein to be biased by alignment of its dipole moment, $\bar{\mu}$ (Debye $\approx 3.33564 \times 10^{-30}$ C m), in the electric field, \bar{E} (V m⁻¹). Taking into account the potential energy of a dipole in an electric field, $\Delta U = \bar{E} \bar{\mu} \cos(\theta)$, and using the Boltzmann distribution of energies, we derived equation (12-App.3; see 3-App.S6). Equation (12-App.3) describes a probability distribution function of shape factors for spheroid proteins when their orientation is biased by the dipole energy in an electric field.

$$p(\gamma)d\gamma = \frac{1}{A} \exp \left[\frac{\Delta U \left(\frac{\gamma - \gamma_{\perp}}{\gamma_{\parallel} - \gamma_{\perp}} \right)^{0.5}}{KT} \right] \left[\frac{1}{2\pi [(\gamma - \gamma_{\perp})(\gamma_{\parallel} - \gamma)]^{1/2}} \right] d\gamma \quad (12\text{-App.3})$$

In equation (12-App.3), A is a normalization constant described in Section 3-App.S6. Equation (12-App.3) assumes that the dipole moment is aligned with the axis of symmetry of the spheroid. Fig. 3.4C of the main chapter demonstrates that for spheroid proteins with dipoles less than approximately 1,500 D, it is theoretically possible to observe a bimodal distribution of shape factors. The average dipole moments of proteins is approximately 550 Debye (<http://bioinfo.weizmann.ac.il/dipol/indexj.html>), suggesting that many aspherical proteins may generate a skewed bimodal distribution of shape factors. Additional factors may bias the orientation of proteins in the nanopore including steric effects, hydrodynamics, and interactions with the pore wall. Therefore, equation (12-App.3) is an approximation of how the orientation, and therefore distribution of shape factors, of a protein with a dipole moment may be biased.

Since the value of ΔI is directly proportional to the electrical shape factor, γ , according to equation (1-App.3), we can also express equation (12-App.3) in terms of ΔI . In this case, this probability distribution is the expected distribution of ΔI values due only to the possible values of the shape factor – it does not include effects such as experimental or analytical errors in determining ΔI values. Since the modes of the distribution γ_{\min} and γ_{\max} correspond to either ΔI_{\min} or ΔI_{\max} (see next section), we can write equation (12-App.3) in terms of ΔI as:

$$p(\Delta I_{\gamma})d\Delta I_{\gamma} = \frac{1}{A} \exp \left[\frac{\Delta U \left(\frac{\Delta I - \Delta I_{\max}}{\Delta I_{\min} - \Delta I_{\max}} \right)^{0.5}}{KT} \right] \left[\frac{1}{2\pi [(\Delta I - \Delta I_{\max})(\Delta I_{\min} - \Delta I)]^{1/2}} \right] d\Delta I_{\gamma} \quad (13\text{-App.3})$$

3-App.S4. Using ΔI_{\min} and ΔI_{\max} to solve for the volume and shape of proteins.

Given that the probability distribution of shape factors has modes at γ_{\parallel} and γ_{\perp} corresponding to either ΔI_{\min} or ΔI_{\max} values according to equation (1-App.3), we

expected that if the value of ΔI_{\min} and ΔI_{\max} could be determined quantitatively from the empirical distribution of ΔI values then the volume and shape of a protein could also be determined. For example, the minimum shape factor for an oblate spheroid occurs at $\theta = \pi/2$ and has a value of $\gamma_{\perp}(m)$ (equation 4-App.3). Thus, according to equation (3.1), the minimum mode in the bimodal ΔI distribution, ΔI_{\min} , is a function of Λ and $\gamma_{\perp}(m)$, and the maximum mode in the bimodal ΔI distribution, ΔI_{\max} , is a function of Λ and $\gamma_{\parallel}(m)$. Since both γ_{\parallel} and γ_{\perp} are solely a function of m , we developed the system of equations (13-App.3) and (14-App.3) in which the values of m and Λ are the only two unknowns and the values of ΔI_{\min} and ΔI_{\max} are determined from fitting the empirical distributions of ΔI with the convolution model. By rearranging equation (3-App.3), we can write for oblate spheroids with $m < 1$:

$$\Lambda(m) = \begin{cases} \Lambda(\gamma_{\perp}(m), \Delta I_{\min}) \\ \Lambda(\gamma_{\parallel}(m), \Delta I_{\max}) \end{cases} \quad \text{if } m < 1, \quad (13\text{-App.3})$$

and for prolate spheroids with $m > 1$:

$$\Lambda(m) = \begin{cases} \Lambda(\gamma_{\parallel}(m), \Delta I_{\min}) \\ \Lambda(\gamma_{\perp}(m), \Delta I_{\max}) \end{cases} \quad \text{if } m > 1. \quad (14\text{-App.3})$$

Since this system of equations has a piecewise dependence on the value of m , we substituted the determined values of ΔI_{\min} and ΔI_{\max} into equations (13-App.3) and (14-App.3) and used MATLAB to solve the system numerically for the excluded volume of the protein, Λ and the value of m .

3-App.S5. Models for describing mean squared angular displacement and autocorrelation characteristic times.

The fluctuations in the orientation of the nonspherical proteins while in the nanopore can be described by a Langevin torque equation, equation (15-App.3), which includes terms for the thermal driven torque, viscous drag torque, and electric-field induced restoring torque due to the dipole moment (61).

$$I \frac{d^2\theta}{dt^2} = \tau_R - \zeta \frac{d\theta}{dt} - \bar{E} \bar{\mu} \sin(\theta) \quad (15\text{-App.3})$$

Where I is the rotational inertia, ζ ($\text{J Pa}^{-1} \text{s}^{-1} \text{m}^{-1}$) is the rotational viscous friction coefficient, \bar{E} (V m^{-1}) is the electric field, $\bar{\mu}$ (C m) is the dipole moment of the protein, and θ (rads) is the angle between the dipole moment and the electric field. To solve this equation for the mean squared angular displacement, $\langle \Delta\theta^2(\tau) \rangle$, we first neglect the inertial term by setting it equal to zero and then linearize the equation by noting the small angle approximation of $\sin(\theta) \approx \theta$. We then solve the equation for $\langle \Delta\theta^2(\tau) \rangle$ by considering the statistical ensemble of thermal fluctuations and applying the equipartition theorem according to Russel *et al.* (61, 76). Finally, by applying the Stokes-Einstein relationship, we can replace ζ with $k_B T/D_R$ to arrive at equation (16-App.3).

$$\langle \Delta\theta(\tau)^2 \rangle = \frac{2k_B T}{\bar{E} \bar{\mu}} \left[1 - e^{-\frac{\tau \bar{E} \bar{\mu} D_R}{k_B T}} \right] \quad (16\text{-App.3})$$

We used equation 16-App.3 to fit the mean squared angular displacement curves in Fig. 3.6 of the main text with the rotational diffusion coefficient, D_R , and the dipole moment of the protein, $\bar{\mu}$, as fitting parameters. This model describes the Brownian rotational motion about one axis of a particle in a harmonic energy well; it is analogous to translational motion of a Brownian, harmonically bound particle (62).

In order to predict the characteristic times, τ_C , for the exponential decay of the autocorrelation curves, we first note that τ_C is related to the rotation diffusion coefficient and the rotation spring constant, k_θ , by equation 17-App.3 (66).

$$\tau_C = \frac{k_B T}{D_R k_\theta} \quad (17\text{-App.3})$$

Second, we note that the energy well due to the dipole moment in the electric field is $\Delta U = \bar{E} \bar{\mu} \cos(\theta)$, and the energy well of a harmonic oscillator is $\Delta U = \frac{1}{2} k_\theta \theta^2$. Since $\cos(\theta)$ can be approximated by $\theta^2/2$, the effective rotational spring constant, k_θ , is approximately equal to $\bar{E} \bar{\mu}$ (61).

3-App.S6. Derivation of a shape factor distribution that includes the dipole moment of proteins

To derive a probability distribution of shape factors that takes into account a bias for a specific orientation based on the dipole moment of a protein and the electric field, we used the Boltzmann distribution of energies:

$$\frac{N_i}{N} = \frac{g_i \exp\left[-U_i/k_B T\right]}{\sum g_j \exp\left[-U_j/k_B T\right]} \quad (18\text{-App.3})$$

where g_i is the degeneracy factor or number of states that have the same energy level, U_i is the energy level of state i , N_i is the number of molecules with energy level i , N is the total number of molecules in the system, and $k_B T$ is the thermal energy. The denominator of equation (18-App.3) is the partition function, and we will label it Z . Assuming that all of the energy affecting the orientation of the protein is in the form of the potential energy of a dipole in an electric field then g_i is constant for all energy states and cancels out of equation (18-App.3). The potential energy of a dipole in an electric field is:

$$\Delta U = \vec{E} \cdot \vec{\mu} = -E\mu \cos(\phi) \quad (19\text{-App.3})$$

where E is the electric field, μ is the dipole moment, and ϕ is the angle between the moment and the electric field. Combining equations (18-App.3) and (19-App.3), the proportion of molecules at an angle, ϕ , is:

$$\frac{N_\phi}{N} = \frac{1}{Z} \exp\left[\frac{E\mu \cos(\phi)}{KT}\right] \quad (20\text{-App.3})$$

and therefore the probability of observing an angle ϕ is:

$$p_\phi = \frac{c}{Z} \exp\left[\frac{E\mu \cos(\phi)}{KT}\right] \quad (21\text{-App.3})$$

where c is a normalization constant.

To express $\cos(\phi)$ in terms of the electrical shape factor we first rearranged equation S4, which describes γ as a function of θ , to obtain:

$$\cos(\theta) = \left(\frac{\gamma - \gamma_\perp}{\gamma_\parallel - \gamma_\perp}\right)^{0.5} \quad (22\text{-App.3})$$

Considering a simple scenario in which the dipole moment is parallel with the axis of symmetry (i.e. $\phi = \theta$), we substitute equation (22-App.3) into equation (21-App.3) to obtain:

$$p_\theta = \frac{c}{Z} \exp \left[\frac{E\mu \left(\frac{\gamma - \gamma_\perp}{\gamma_\parallel - \gamma_\perp} \right)^{0.5}}{KT} \right] \quad (23\text{-App.3})$$

Equation (23-App.3) expresses the probability of observing an angle θ as a function of the shape factor, $p(\theta(\gamma))$. As in the derivation by Golibersuch, we used substitution of variables to transform $p(\theta(\gamma))$ into $p(\gamma)$:

$$p(\gamma)d\gamma = p[\theta] \frac{d\theta}{d\gamma} d\gamma = p[\theta] \left(\frac{d\gamma}{d\theta} \right)^{-1} d\gamma \quad (24\text{-App.3})$$

and differentiated equation (6-App.3) with respect to θ , $\frac{d\gamma}{d\theta}$. Substituting this result into equation (24-App.3), we obtained equation (25-App.3):

$$p(\gamma)d\gamma = P[\theta] \left(\frac{d\gamma}{d\theta} \right)^{-1} d\gamma = \frac{c}{Z} \exp \left[\frac{E\mu \left(\frac{\gamma - \gamma_\perp}{\gamma_\parallel - \gamma_\perp} \right)^{0.5}}{KT} \right] \left[\frac{1}{2\pi [(\gamma - \gamma_\perp)(\gamma_\parallel - \gamma)]^{1/2}} \right] d\gamma \quad (25\text{-App.3})$$

To solve for the normalization constants, we integrated equation (25-App.3) and set it equal to 1 (i.e. $\int_{\gamma_\parallel}^{\gamma_\perp} p(\gamma)d\gamma = 1$). This procedure cancels out the partition function Z and

$$\text{yields: } p(\gamma)d\gamma = \frac{1}{A} \exp \left[\frac{E\mu \left(\frac{\gamma - \gamma_\perp}{\gamma_\parallel - \gamma_\perp} \right)^{0.5}}{KT} \right] \left[\frac{1}{2\pi [(\gamma - \gamma_\perp)(\gamma_\parallel - \gamma)]^{1/2}} \right] d\gamma \quad (26\text{-App.3})$$

where A is described by:

$$A = \int_{\gamma_{\parallel}}^{\gamma_{\perp}} \exp \left[\frac{E\mu \left(\frac{\gamma - \gamma_{\perp}}{\gamma_{\parallel} - \gamma_{\perp}} \right)^{0.5}}{KT} \right] \left[\frac{1}{2\pi [(\gamma - \gamma_{\perp})(\gamma_{\parallel} - \gamma)]^{1/2}} \right] d\gamma \quad (27\text{-App.3})$$

Equation (27-App.3) is identical the equation (12-App.3).

If the dipole moment is perpendicular to the axis of symmetry, for instance as may be likely for an IgG antibody then $\cos(\phi) = \sin(\theta)$. Using equation (22-App.3) and the trigonometry identity, $\sin^2(\theta) = 1 - \cos^2(\theta)$, we can then follow the same procedure as above to obtain:

$$p(\gamma)d\gamma = \frac{1}{A} \exp \left[\frac{E\mu \left(1 - \frac{\gamma - \gamma_{\perp}}{\gamma_{\parallel} - \gamma_{\perp}} \right)^{0.5}}{KT} \right] \left[\frac{1}{2\pi [(\gamma - \gamma_{\perp})(\gamma_{\parallel} - \gamma)]^{1/2}} \right] d\gamma \quad (28\text{-App.3})$$

where

$$A = \int_{\gamma_{\parallel}}^{\gamma_{\perp}} \exp \left[\frac{E\mu \left(1 - \frac{\gamma - \gamma_{\perp}}{\gamma_{\parallel} - \gamma_{\perp}} \right)^{0.5}}{KT} \right] \left[\frac{1}{2\pi [(\gamma - \gamma_{\perp})(\gamma_{\parallel} - \gamma)]^{1/2}} \right] d\gamma \quad (29\text{-App.3})$$

3-App.S7. Chapter 3 appendix figures

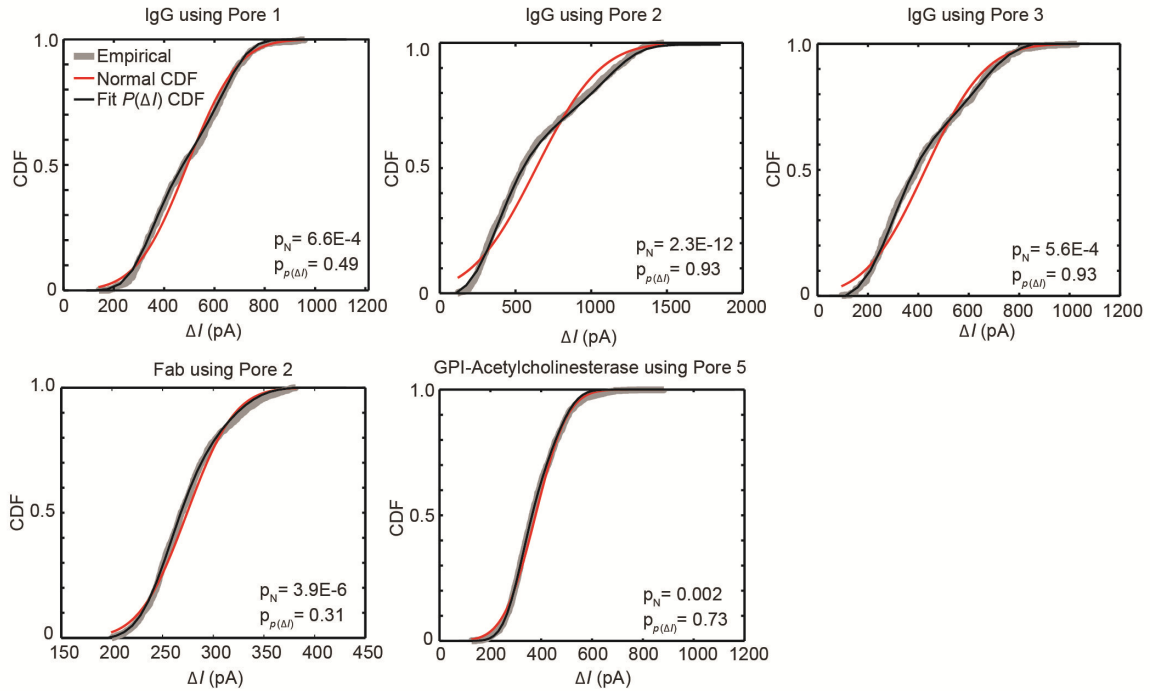


Figure 1-App.3 | Empirical cumulative distributions (grey curves) of ΔI values due to the translocation of non-spherical proteins compared to a best-fit Normal distribution (red curves) and the solution the convolution model, $p(\Delta I)$ (black curves). In each case, Kolmogorov Smirnov (KS) tests were used to determine if the empirical distribution was different than the Normal distribution and $p(\Delta I)$. Resulting p -values are shown in the figure panels. In KS-tests, the null hypothesis is that the two distributions are the same, and therefore, a p -value ≤ 0.05 indicates that the difference between two distributions is statistically significant at the $\alpha = 0.05$ level. For all of these non-spherical proteins, the distribution of ΔI values was different from a Normal distribution ($p_N < 0.002$). In contrast, the solution to the convolution model, $p(\Delta I)$, described the empirical distributions of ΔI values well ($p_{P(\Delta I)} > 0.31$).

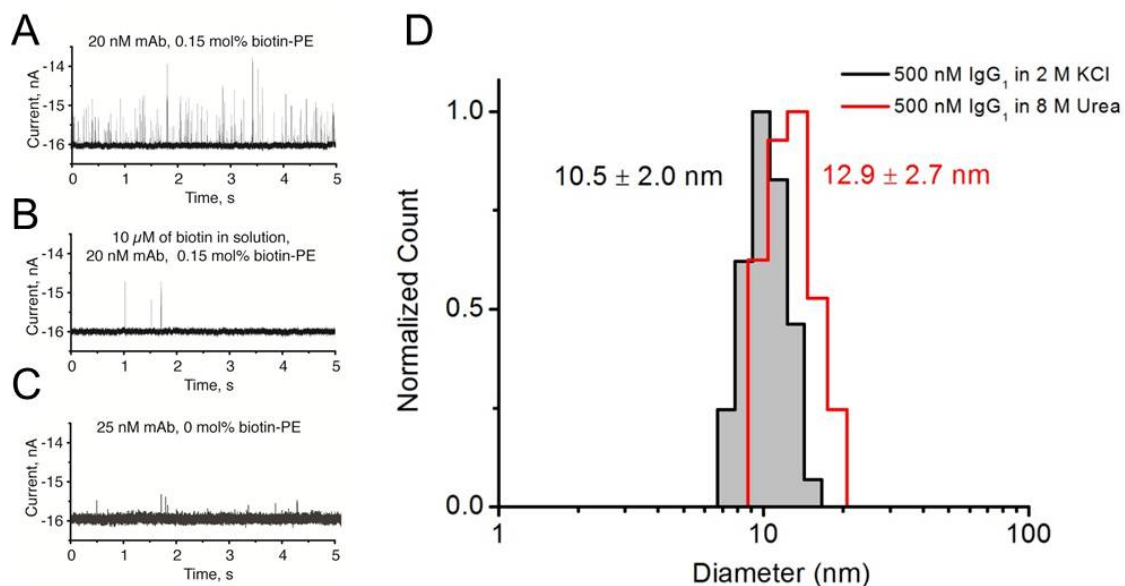


Figure 2-App.3 | Detection of monoclonal anti-biotin IgG₁ antibody with a bilayer-coated nanopore. (A) Current *versus* time trace showing resistive pulses due to translocation of IgG₁ antibodies that were bound to biotin-PE lipids in the bilayer coating. Resistive pulses occurred at a frequency of 34 s⁻¹. (B) Current *versus* time trace recorded after the addition of excess biotin (10 μM) to the solution and containing a reduced frequency of resistive pulses (1.3 s⁻¹). (C) Current *versus* time trace recorded using the same nanopore as A and B but with a bilayer coating that did not contain biotin-PE lipids. Resistive-pulses occurred at a frequency of 2 s⁻¹. The experiments were performed using nanopore 2 (Fig. 4-App.3). (D) Hydrodynamic diameter of IgG₁ antibodies determined from dynamic light scattering experiments. IgG₁ antibodies were at a concentration of 500 nM in aqueous solutions identical to the recording electrolyte (2 M KCl and 10 mM HEPES at pH = 7.4) during the dynamic light scattering experiment. Where indicated, 8 M of urea was added to the solution in order to denature all proteins. The dynamic light scattering results are the combination of 5 runs, each 60 s in duration. Results show the intensity-weighted calculation for the hydrodynamic diameter. The instrument was a Brookhaven 90Plus Particle Sizer and used a 658 nm laser at an angle of 90° to the detector. The absence of a second peak indicates that IgG₁ antibodies did not form a significant number of dimers in 2 M KCl even at concentrations 500 fold greater than in the resistive-pulse sensing experiments.

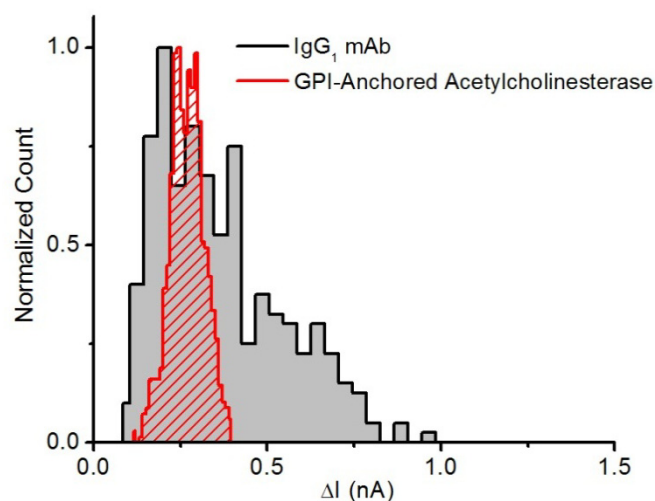


Figure 3-App.3 | Histograms of the ΔI values due to the translocation of the IgG₁ antibody (150 kDa) and GPI-anchored acetylcholinesterase (160 kDa) through the same nanopore. The experiments were performed using nanopore 3 (Fig. 4-App.3). Though both distributions are bimodal, the relatively narrow distribution of ΔI values due to GPI-anchored acetylcholinesterase compared to that of the IgG₁ antibody confirms that the large molecular weight of the IgG₁ antibody was not the reason for broadly distributed ΔI values. The recording buffer contained 2.0 M KCl and 10 mM HEPES buffered at a pH of 7.4 ± 0.1 , and currents were recorded at an applied potential difference of -0.1 V

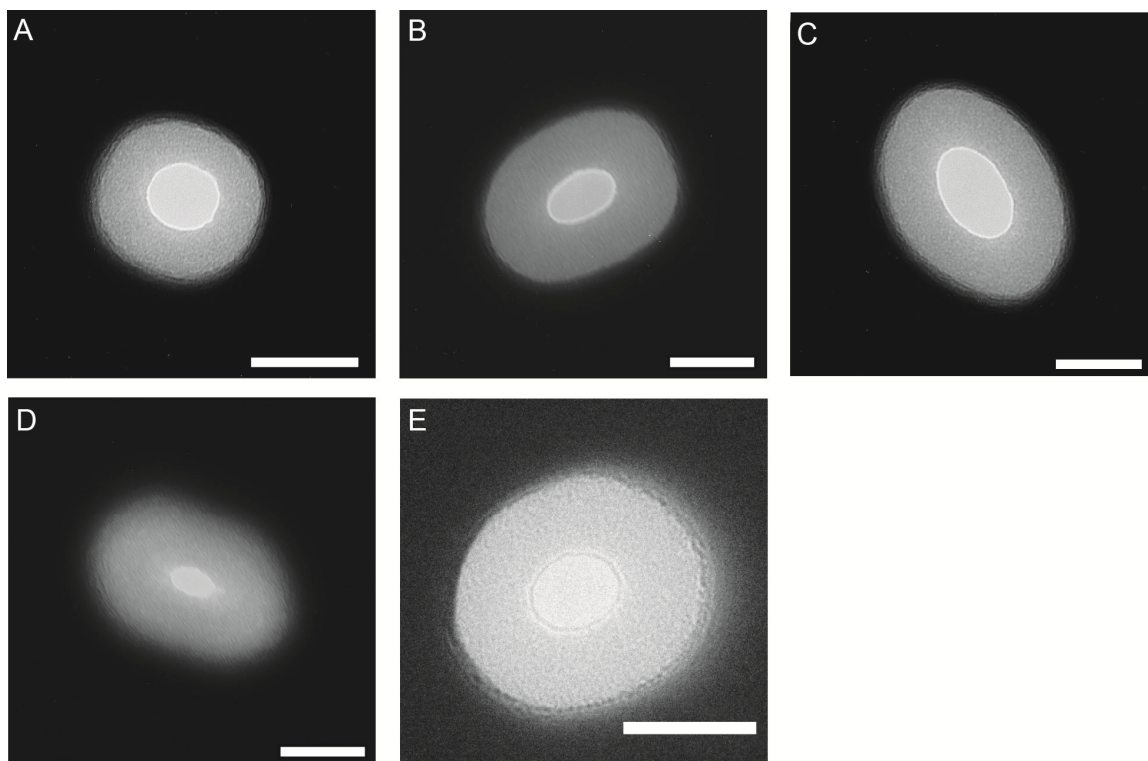


Figure 4-App.3 | Transmission electron micrographs of the nanopores used in this work. The brightest part in the center of each image depicts the shape and size of the nanopore and the surrounding circle with reduced brightness reflects the channel leading to the nanopore (16, 77). All scale bars are 50 nm. Nanopores shown are pore 1 (A), pore 2 (B), pore 3 (C), pore 4 (D), and pore 5 (E). Using Image J, we measured the area of the nanopore (bright spot in the center) to determine the corresponding radius of a perfect circle with identical area, r_p (nm), and we determined the length, l_p (nm), of the nanopore from measurements of the electrical resistance of the nanopore (16). The dimensions of the nanopores without the lipid bilayer coating were: for pore 1 $r_p = 16.1$ and $l_p = 21.3$; for pore 2 $r_p = 16.4$ and $l_p = 17.3$; for pore 3 $r_p = 22.7$ and $l_p = 16.2$; for pore 4 $r_p = 9.6$ and $l_p = 18.0$; and for pore 5 $r_p = 16.0$ and $l_p = 15.0$.

Table 1-App.3. Values of fitting parameters determined from fitting the convolution model to the empirical distributions of ΔI values (Figure 3.2 and 3.3) as well as the resulting calculations of protein volume, Λ , and shape parameter, m .

Experiment	ΔI_{\min} (pA)	ΔI_{\max} (pA)	σ (pA)	ΔU $k_B T$	R^2	Λ nm^3	m
IgG ₁ Pore 1	320	685	69	0	0.99	290	0.35
IgG ₁ Pore 2	383	1085	178	1.9	0.93	281	0.26
IgG ₁ Pore 3	259	665	94	0.2	0.92	305	0.29
Fab Fragment Pore 4	244	325	25	2.6	0.94	152 or 168	0.65 or 1.8
GPI-acetylcholinesterase Pore 3	217	323	35	0	0.99	216 or 245	0.55 or 2.3
GPI-acetylcholinesterase Pore 5	300	529	54	0.7	0.99	186 or 215	0.51 or 2.9

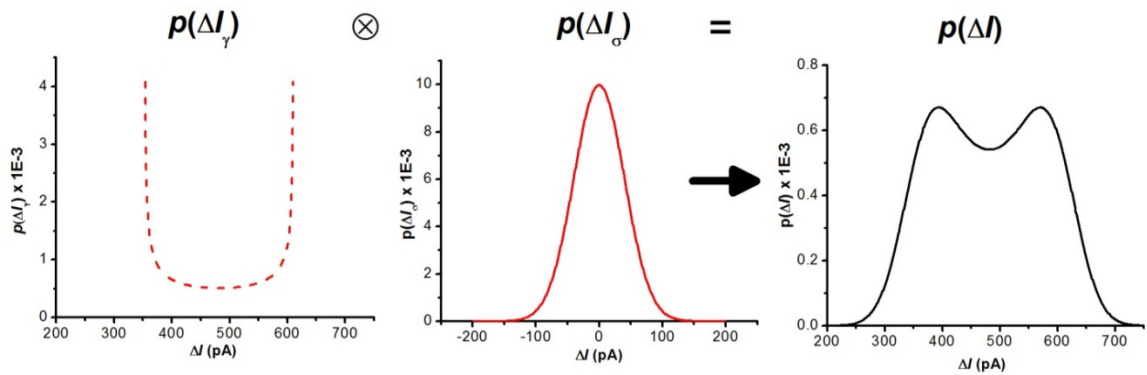


Figure 5-App.3 | Example convolution of the probability distribution of ΔI values one expects due to the distribution of shape factors, $p(\Delta I_\gamma)$ (equation (13-App.3)), and the error in determining individual ΔI values, $p(\Delta I_\sigma)$ (a Normal distribution function). The solution to the convolution is the probability distribution of ΔI values one expects to observe, $p(\Delta I)$. During the fitting procedure, $p(\Delta I)$ is compared to the empirical distribution of ΔI values, $P(\Delta I)$, and the Levenberg-Marquardt non-linear least squares fitting algorithm in OriginPro 8 software generates new values for the fitting parameters ΔI_{\min} , ΔI_{\max} , ΔU , and σ , thereby creating new iterations of $p(\Delta I_\gamma)$ and $p(\Delta I_\sigma)$. This process repeats and in all cases the fits converged after approximately 100 to 200 iterations.

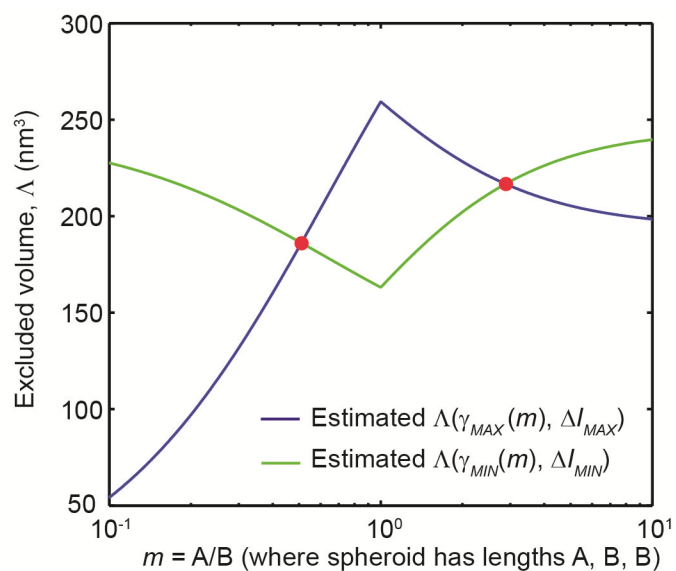


Figure 6-App.3 | Estimating the excluded volume as a function of m using ΔI_{\min} and ΔI_{\max} values illustrates that there are two solutions to equations (13-App.3) and (14-App.3) for prolate shaped proteins. This figure shows this result graphically by plotting the estimated volume of GPI-anchored acetylcholinesterase as a function of m . The two red dots indicate the two solutions to the system of equations ($m = 0.51$, $\Lambda = 186 \text{ nm}^3$ and $m = 2.9$, $\Lambda = 216 \text{ nm}^3$). In order to simplify the graph, we described the electrical shape factor with the notation γ_{MAX} or γ_{MIN} . We used this notation because for prolates ($m > 1$) $\gamma_{MAX} = \gamma_{\perp}$ and for oblates ($m < 1$) $\gamma_{MAX} = \gamma_{\parallel}$ (see equations 13-App.3 and 14-App.3). The opposite is true for γ_{MIN} .

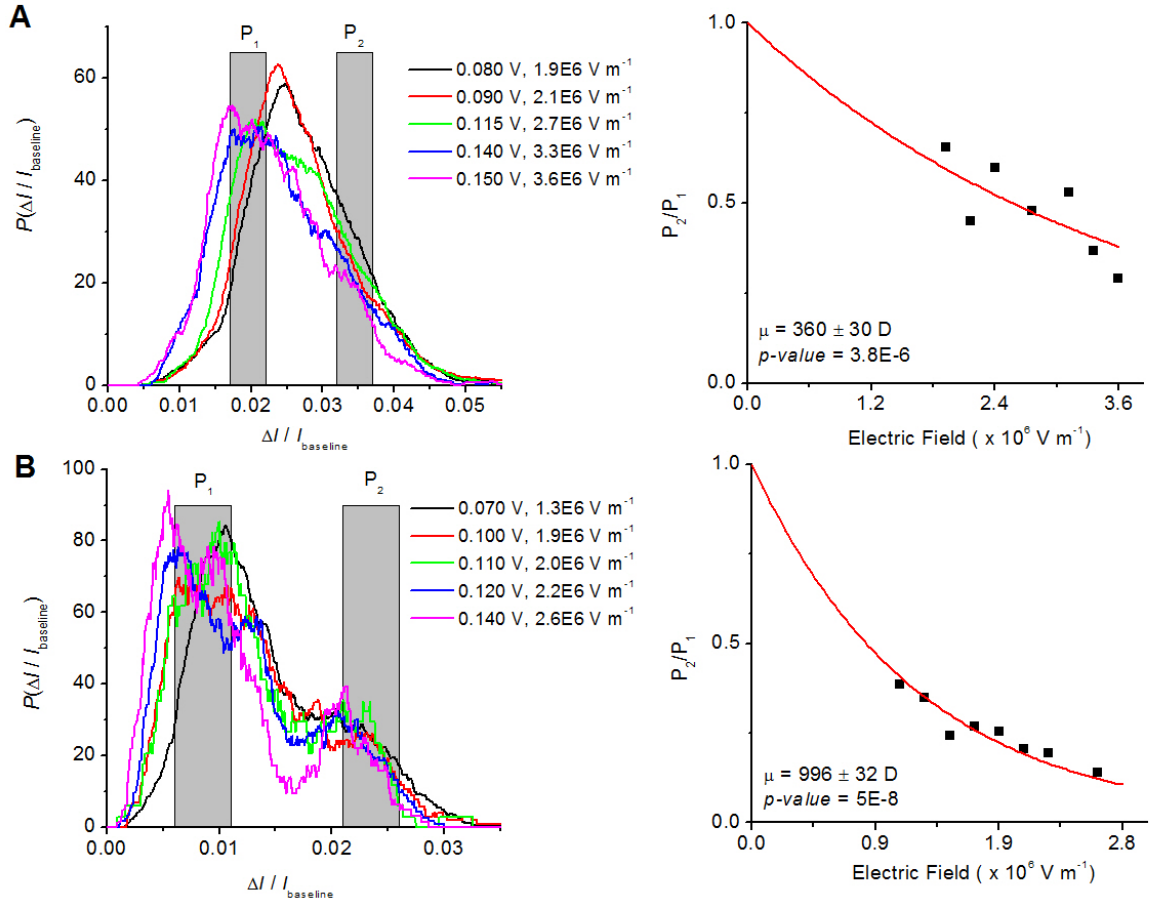


Figure 7-App.3 | Probability distributions of ΔI due to GPI-acetylcholinesterase (A) and IgG₁ antibodies (B) obtained when applying different voltages across the nanopore. The empirical probability distributions shown here were generated by creating a histogram with a bin-width of 1 pA and smoothing the histogram using a moving average (span = 75 pA); distributions were then normalized such that the total area under the curves equaled 1. To compare the distributions obtained during different applied voltages, the x-axis was normalized by dividing the ΔI value by the baseline current. The proportion of events in orientation P_2 or P_1 was determined by taking the area under the curves at $\Delta I_{\min}/I_{\text{baseline}} \pm 0.025$ and $\Delta I_{\max}/I_{\text{baseline}} \pm 0.025$, respectively. ΔI_{\min} and ΔI_{\max} for each protein were determined during the fitting procedure described in the main chapter and Fig. 5-App.3. Interestingly, the ratio of events in P_2 to P_1 (P_2/P_1) declines exponentially with increasing voltage, suggesting that the energy of each protein's dipole moment in an electric field biases the orientation of the proteins in the nanopore. Consequently, we fit the ratio P_2/P_1 with a two-state Boltzmann model: $P_2/P_1 = e^{-\bar{\mu}\bar{E}/k_B T}$ where \bar{E} is the electric field (i.e. $V/(l_P+1.6r_p)$), $\bar{\mu}$ is the dipole moment in Debyes (1 Debye $\sim 3.336\text{E-}30$ C m), and $k_B T$ is the thermal energy (4.11×10^{-21} J). This procedure returned estimates of the dipole moments of the proteins of $\bar{\mu} = 360 \pm 30$ D for GPI-AchE and $\bar{\mu} = 996 \pm 32$ D for the monoclonal IgG₁ antibodies.

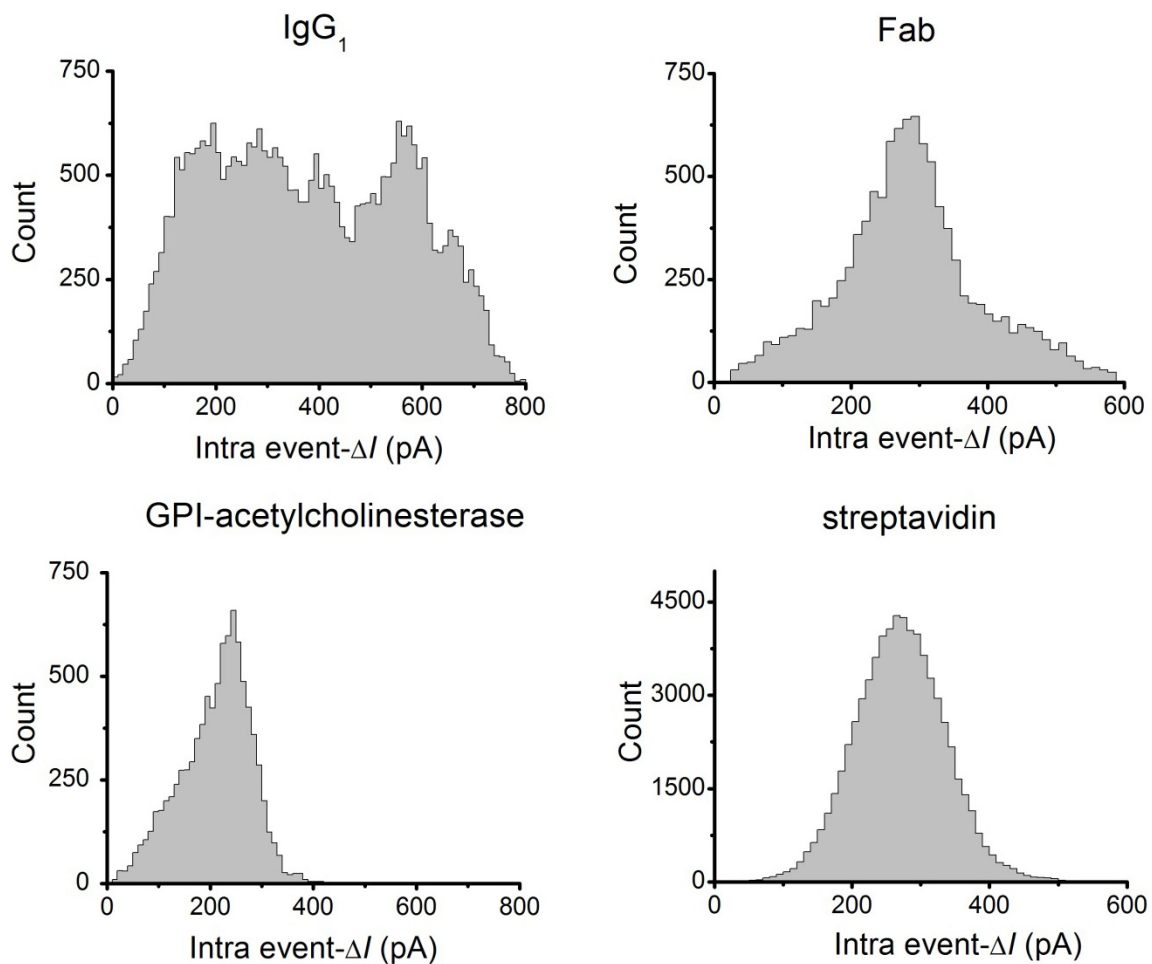


Figure 8-App.3 | Histograms of all intra event ΔI values recorded during the translocation events of IgG₁ antibodies, Fab fragments, GPI-anchored acetylcholinesterase, and streptavidin. (Note, these histograms reflect all measured values of ΔI and are not limited to the maximum ΔI values as in the analysis presented in the main text). These distributions were not Normally distributed for IgG₁ antibodies, GPI-anchored acetylcholinesterase, and Fab fragments. The intra event- ΔI values due to streptavidin translocations, however, were Normally distributed. For the IgG₁ antibody, these distributions appeared to be multimodal with more than two modes (Figure 3.6A). Given that the regions of an IgG antibody between the Fc domain and the two Fab fragments are very flexible,(58, 67) it is possible that these modes in the distribution of all intra event- ΔI values reveal dynamic fluctuations in the shape and conformation of antibodies as well as changes in their orientation relative to the electric field. Some of the shapes that the IgG₁ antibodies might sample may have been more spherical (67) than the crystal structure shown in Fig. 3.1B implies.

Chapter 3 References

1. Pandey A, Mann M (2000) Proteomics to study genes and genomes. *Nature* 405(6788):837-846.
2. Keyser UF (2011) Controlling molecular transport through nanopores. *J R Soc Interface* 8(63):1369-1378.
3. Majd S, *et al.* (2010) Applications of biological pores in nanomedicine, sensing, and nanoelectronics. *Curr Opin Biotech* 21(4):439-476.
4. Han AP, *et al.* (2008) Label-free detection of single protein molecules and protein-protein interactions using synthetic nanopores. *Anal Chem* 80(12):4651-4658.
5. Fologea D, Ledden B, David SM, Li J (2007) Electrical characterization of protein molecules by a solid-state nanopore. *Appl Phys Lett* 91(5):053901.
6. Talaga DS, Li JL (2009) Single-molecule protein unfolding in solid state nanopores. *J Am Chem Soc* 131(26):9287-9297.
7. Movileanu L (2009) Interrogating single proteins through nanopores: Challenges and opportunities. *Trends in Biotechnology* 27(6):333-341.
8. Howorka S, Siwy Z (2009) Nanopore analytics: Sensing of single molecules. *Chem Soc Rev* 38(8):2360-2384.
9. Kowalczyk SW, Blosser TR, Dekker C (2011) Biomimetic nanopores: Learning from and about nature. *Trends in Biotechnology* 29(12):607-614.
10. Dekker C (2007) Solid-state nanopores. *Nat Nanotechnol* 2(4):209-215.
11. Martin CR, Siwy ZS (2007) Learning nature's way: Biosensing with synthetic nanopores. *Science* 317(5836):331-332.
12. Sexton LT, *et al.* (2007) Resistive-pulse studies of proteins and protein/antibody complexes using a conical nanotube sensor. *J Am Chem Soc* 129(43):13144-13152.
13. Sexton LT, *et al.* (2010) An adsorption-based model for pulse duration in resistive-pulse protein sensing. *J Am Chem Soc* 132(19):6755-6763.
14. Merstorf C, *et al.* (2012) Wild type, mutant protein unfolding and phase transition detected by single-nanopore recording. *ACS Chemical Biology* 7(4):652-658.
15. Oukhaled G, *et al.* (2007) Unfolding of proteins and long transient conformations detected by single nanopore recording. *Physical Review Letters* 98(15):158101.
16. Yusko EC, *et al.* (2011) Controlling protein translocation through nanopores with bio-inspired fluid walls. *Nat Nanotechnol* 6(4):253-260.
17. Bayley H, Cremer PS (2001) Stochastic sensors inspired by biology. *Nature* 413(6852):226-230.
18. Yusko EC, *et al.* (2012) Single-particle characterization of A β oligomers in solution. *ACS Nano* 6(7):5909-5919.
19. Siwy Z, *et al.* (2005) Protein biosensors based on biofunctionalized conical gold nanotubes. *J Am Chem Soc* 127(14):5000-5001.
20. Ding S, Gao CL, Gu LQ (2009) Capturing single molecules of immunoglobulin and ricin with an aptamer-encoded glass nanopore. *Anal Chem* 81(16):6649-6655.
21. Uram JD, Ke K, Hunt AJ, Mayer M (2006) Submicrometer pore-based characterization and quantification of antibody-virus interactions. *Small* 2(8-9):967-972.

22. Clarke J, *et al.* (2009) Continuous base identification for single-molecule nanopore DNA sequencing. *Nat Nanotechnol* 4(4):265-270.
23. Branton D, *et al.* (2008) The potential and challenges of nanopore sequencing. *Nat Biotechnol* 26(10):1146-1153.
24. McDougall Z (2012) Oxford nanopore introduces DNA 'strand sequencing' on the high-throughput gridion platform and presents minion, a sequencer the size of a USB memory stick. (May 18, 2012) <http://www.nanoporetech.com/news/press-releases/view/39>
25. Kasianowicz JJ, Brandin E, Branton D, Deamer DW (1996) Characterization of individual polynucleotide molecules using a membrane channel. *Proc Natl Acad Sci U S A* 93(24):13770-13773.
26. Raillon C, *et al.* (2012) Nanopore detection of single molecule rnap-DNA transcription complex. *Nano Lett* 12(3):1157-1164.
27. Soni GV, Dekker C (2012) Detection of nucleosomal substructures using solid-state nanopores. *Nano Lett.*
28. Robertson JWF, *et al.* (2007) Single-molecule mass spectrometry in solution using a solitary nanopore. *Proc Natl Acad Sci U S A* 104(20):8207-8211.
29. Ito T, Sun L, Crooks RM (2003) Simultaneous determination of the size and surface charge of individual nanoparticles using a carbon nanotube-based Coulter counter. *Anal Chem* 75(10):2399-2406.
30. Bacri L, *et al.* (2011) Dynamics of colloids in single solid-state nanopores. *Journal of Physical Chemistry B* 115(12):2890-2898.
31. Yusko EC, Billeh YN, Yang J, Mayer M (2011) Nanopore recordings to quantify activity-related properties of proteins. *Nanopores: Sensing and fundamental biological interactions*, eds Iqbal SM & Bashir R (Springer Publishing Co., New York), pp 203-225.
32. Wei R, Gatterdam V, Wieneke R, Tampe R, Rant U (2012) Stochastic sensing of proteins with receptor-modified solid-state nanopores. *Nat Nanotechnol* 7(4):257-263.
33. Rigler R, Vogel H eds (2008) *Single molecules and nanotechnology* (Springer-Verlag, Berlin).
34. Jachimska B, Wasilewska M, Adamczyk Z (2008) Characterization of globular protein solutions by dynamic light scattering, electrophoretic mobility, and viscosity measurements. *Langmuir* 24(13):6866-6872.
35. Erickson HP (2009) Size and shape of protein molecules at the nanometer level determined by sedimentation, gel filtration, and electron microscopy. *Biol Proced Online* 11(1):32-51.
36. Wakabayashi K, *et al.* (1992) Small-angle synchrotron x-ray scattering reveals distinct shape changes of the myosin head during hydrolysis of atp. *Science* 258(5081):443-447.
37. Nierhaus KH, *et al.* (1983) Shape determinations of ribosomal proteins in situ. *Proceedings of the National Academy of Sciences* 80(10):2889-2893.
38. Gambin Y, *et al.* (2011) Visualizing a one-way protein encounter complex by ultrafast single-molecule mixing. *Nat Meth* 8(3):239-241.
39. Lipman EA, Schuler B, Bakajin O, Eaton WA (2003) Single-molecule measurement of protein folding kinetics. *Science* 301(5637):1233-1235.

40. Mathé J, Aksimentiev A, Nelson DR, Schulten K, Meller A (2005) Orientation discrimination of single-stranded DNA inside the alpha-hemolysin membrane channel. *Proc Natl Acad Sci U S A* 102(35):12377-12382.
41. Qin ZP, Zhe JA, Wang GX (2011) Effects of particle's off-axis position, shape, orientation and entry position on resistance changes of micro Coulter counting devices. *Meas Sci Technol* 22(4).
42. Smythe WR (1964) Flow around a spheroid in a circular tube. *Phys Fluids* 7(5):633-638.
43. DeBlois RW, Uzgiris EE, Cluxton DH, Mazzone HM (1978) Comparative measurements of size and polydispersity of several insect viruses. *Anal Biochem* 90(1):273-288.
44. Davenport M, *et al.* (2012) The role of pore geometry in single nanoparticle detection. *ACS Nano*.
45. Schneider SW, Larmer J, Henderson RM, Oberleithner H (1998) Molecular weights of individual proteins correlate with molecular volumes measured by atomic force microscopy. *Pflugers Arch* 435(3):362-367.
46. Goodsell D (2004) Acetylcholinesterase. June 2004 molecule of the month. (20June2012) <http://www.rcsb.org/pdb/101/motm.do?momID=54>
47. Golibersuch DC (1973) Observation of aspherical particle rotation in poiseuille flow via the resistance pulse technique. Part 1. Application to human erythrocytes. *Biophys J* 13(3):265-280.
48. Golibersuch DC (1973) Observation of aspherical particle rotation in poiseuille flow via the resistance pulse technique. Part 2. Application to fused sphere dumbbells. *J Appl Phys* 44(6):2580-2584.
49. Grover NB, Naaman J, Ben-sasson S, Doljansk F (1969) Electrical sizing of particles in suspensions. I.Theory. *Biophys J* 9(11):1398-1414.
50. Grover NB, Naaman J, Ben-sasson S, Doljansk F, Nadav E (1969) Electrical sizing of particles in suspensions. 2. Experiments with rigid spheres. *Biophys J* 9(11):1415-1425.
51. Hurley J (1970) Sizing particles with a coulter counter. *Biophys J* 10(1):74-79.
52. Osborn JA (1945) Demagnetizing factors of the general ellipsoid. *Physical Review* 67(11-1):351-357.
53. DeBlois RW, Wesley RKA (1976) Viral sizes, concentrations, and electrophoretic mobilities by nanopar analyzer. *Biophys J* 16(2):A178-A178.
54. Carbonaro A, Mohanty SK, Huang HY, Godley LA, Sohn LL (2008) Cell characterization using a protein-functionalized pore. *Lab Chip* 8(9):1478-1485.
55. Berge LI, Feder J, Jossang T (1992) A new perspective on particle sizing by the Coulter principle: Single particle dynamics. *Particle size analysis*, eds Stanley-Wood NG & Lines RW (The Royal Society of Chemistry, Cambridge), pp 374-383.
56. Woodside MT, *et al.* (2006) Direct measurement of the full, sequence-dependent folding landscape of a nucleic acid. *Science* 314(5801):1001-1004.
57. Ozinskas AJ (1994) Principles of fluorescence immunoassays. *Topics in fluorescence spectroscopy*, ed Lakowicz JR (Kluwer Academic Publishers, New York), Vol 4, p 487.

58. Carrasco B, *et al.* (2001) Crystallohydrodynamics for solving the hydration problem for multi-domain proteins: Open physiological conformations for human IgG. *Biophysical Chemistry* 93(2–3):181-196.
59. Solomentsev Y, Anderson JL (1994) Electrophoresis of slender particles. *J Fluid Mech* 279:197-215.
60. Ai Y, Qian S (2011) Direct numerical simulation of electrokinetic translocation of a cylindrical particle through a nanopore using a poisson-boltzmann approach. *Electrophoresis* 32(9):996-1005.
61. Cheng Z, Chaikin PM, Mason TG (2002) Light streak tracking of optically trapped thin microdisks. *Physical Review Letters* 89(10).
62. Mason TG, Gang H, Weitz DA (1997) Diffusing-wave-spectroscopy measurements of viscoelasticity of complex fluids. *J Opt Soc Am A* 14(1):139-149.
63. Yuan Y, Axelrod D (1995) Subnanosecond polarized fluorescence photobleaching - rotational diffusion of acetylcholine-receptors on developing muscle-cells. *Biophys J* 69(2):690-700.
64. Porschke D, *et al.* (1996) Electrooptical measurements demonstrate a large permanent dipole moment associated with acetylcholinesterase. *Biophys J* 70(4):1603-1608.
65. Antosiewicz J, Wlodek ST, McCammon JA (1996) Acetylcholinesterase: Role of the enzyme's charge distribution in steering charged ligands toward the active site. *Biopolymers* 39(1):85-94.
66. Janssen XJA, *et al.* (2012) Electromagnetic torque tweezers: A versatile approach for measurement of single-molecule twist and torque. *Nano Lett* 12(7):3634-3639.
67. Longman E, *et al.* (2003) Estimating domain orientation of two human antibody IgG₄ chimeras by crystallohydrodynamics. *Eur Biophys J Biophys Lett* 32(5):503-510.
68. Rosenstein JK, Wanunu M, Merchant CA, Drndic M, Shepard KL (2012) Integrated nanopore sensing platform with sub-microsecond temporal resolution. *Nat Meth* 9(5):487-492.
69. Uram JD, Ke K, Mayer M (2008) Noise and bandwidth of current recordings from submicrometer pores and nanopores. *ACS Nano* 2(5):857-872.
70. Pedone D, Firnkens M, Rant U (2009) Data analysis of translocation events in nanopore experiments. *Anal Chem* 81(23):9689-9694.
71. Maxwell JC (1904) *A treatise on electricity and magnetism* (Clarendon Press, Oxford) 3rd Ed.
72. Deblois RW, Bean CP (1970) Counting and sizing of submicron particles by resistive pulse technique. *Rev Sci Instrum* 41(7):909-&.
73. Bermudez O, Forciniti D (2004) Aggregation and denaturation of antibodies: A capillary electrophoresis, dynamic light scattering, and aqueous two-phase partitioning study. *J Chromatogr B* 807(1):17-24.
74. Jossang T, Feder J, Rosenqvist E (1988) Photon-correlation spectroscopy of human-IgG. *J Protein Chem* 7(2):165-171.
75. Skinner GM, van den Hout M, Broekmans O, Dekker C, Dekker NH (2009) Distinguishing single- and double-stranded nucleic acid molecules using solid-state nanopores. *Nano Lett* 9(8):2953-2960.

76. Russel WB, Saville DA, Schowalter WR (1989) *Colloidal dispersions* (Cambridge University Press, Cambridge, UK).
77. Li J, *et al.* (2001) Ion-beam sculpting at nanometre length scales. *Nature* 412(6843):166-169.

Chapter 4

Using Nanopores with Fluid Walls to Determine the Binding Affinity of Protein Ligand Interactions

Here, we demonstrate the use of lipid-bilayer coated nanopores for determining the binding affinity between a protein and a ligand that is anchored to mobile lipids in the lipid coating. This work shows that the frequency of resistive-pulses due to these proteins can be used to determine kinetic parameters of the binding interaction (*e.g.* the association rate constant, k_{on} , and dissociation rate constant, k_{off}) and equilibrium constants (*e.g.* the dissociation constant, K_d). Thus, this chapter describes methods of obtaining parameters specific to protein-ligand interactions in addition to those parameters (*e.g.* size, charge, and shape) that can already be determined by the analysis of protein translocation events through bilayer-coated nanopores. This capability is unique to nanopores with fluid walls in which the ligands are mobile in the fluid layer and is not possible with nanopores that are decorated with fixed, covalently attached ligand.

4.1 Introduction

At some point in the life of every protein, the protein will bind to a small molecule or additional protein to influence cellular processes. Consequently, numerous methods have been developed to detect association between ligands and proteins as well as to characterize the binding kinetics and affinity (1). Most techniques are average-based techniques in which the primary signal is the result of millions of binding interactions, and most techniques are limited to characterizing the binding interaction while other properties of the protein such as its size and charge are not determined during the analysis. Here, we describe a single molecule technique that uses nanopores with fluid walls for determining kinetic rate constants and equilibrium affinity constants of proteins binding to ligand; the major advantage of this nanopore-based method is that the same experiments used to characterize the binding of a protein and ligand also characterize the size, charge, and shape of the protein (2-4).

The most well-known methods of characterizing association and dissociation reactions of proteins (with ligand or other proteins) are isothermal titration calorimetry (5), surface plasmon resonance (6, 7), affinity capillary electrophoresis (ACE) (8, 9), and enzyme-linked immunosorbant assays (ELISA) (1, 10, 11). All of these techniques, however, are generally limited to characterizing the binding reaction and provide little information on the properties of the binding protein. ACE may be the exception in that the electrophoretic mobility of the analyte is typically obtained. Several other biophysical techniques are capable of characterizing binding interactions while providing additional information. For instance, dual polarization interferometry (12), fluorescence correlation spectroscopy (13, 14), and microscale thermophoresis (15-18) can all characterize binding interactions while determining the size of a protein. Microscale thermophoresis has the additional capability of being able to determine the charge and size of the hydration shell of a protein. While these techniques have proved extremely useful, they all share a limitation: since characterization of the binding parameters and additional properties of the binding-protein require measurement of millions of proteins, these techniques are not well suited for situations in which different proteins bind the same ligand.

Electrolyte-filled nanopores through an insulating membrane are an emerging technology for characterizing macromolecules such as proteins (19-30). These single-molecule experiments involve measuring the electric field-induced flow of ions through a single nanopore and the changes in this current (i.e. resistive pulses) when single protein passes through the nanopore. Measuring the magnitude and duration of these transient changes in current (ΔI and t_d) during the translocation of thousands of single proteins enables construction of distributions that can reveal dynamic heterogeneities in size (3, 21, 29, 31-36), conformation (23, 37-39), and activity of biomolecules *in situ* (2, 25, 27, 40-42). For instance, Uram *et al.* demonstrated the use of pores for determining solid-phase affinity constants based on increases in the volume of antigen-labeled beads upon binding of IgG antibodies (43). More recently Wei *et al.* and Ding *et al.* developed nanopore-based methods in which ligand were immobilized in a nanopore, and they observed the association and dissociation of single proteins to the ligand, which enabled determination of kinetic parameters (i.e. k_{on} and k_{off}) as well as equilibrium affinity constants (i.e. K_d) (41, 44). These types of nanopore-based methods benefit from an ability to determine the volume of the binding protein, and therefore, characterize the binding affinities of different proteins that bind the same ligand. Additional nanopore-based methods for characterizing activity-related properties of proteins can be found in these reviews (24, 25, 28, 40).

Recently, we used nanopores coated with lipid bilayers that contained a fraction of ligand-presenting lipids to detect and characterize the volume, charge, and shape of proteins that bound to the lipid-anchored ligand (4, 40). In those works proteins from solution bound to the mobile, lipid-anchored ligand in the supported lipid bilayer and were able to diffuse in two dimensions to the nanopore where they were electrophoretically driven through the pore (Fig. 4.1). Here, we present a model to characterize this two-dimensional mass transport problem and describe the frequency of translocation events as a function of the binding affinity of proteins to the lipid-anchored ligand that are presented on the fluid bilayer surface. We validated the model by measuring the frequency of translocation events as a function of the density of lipid-anchored proteins on the bilayer surface and applied the model to determine the

equilibrium affinity constant of a monoclonal anti-biotin IgG₁ antibody binding to biotin-PE lipids.

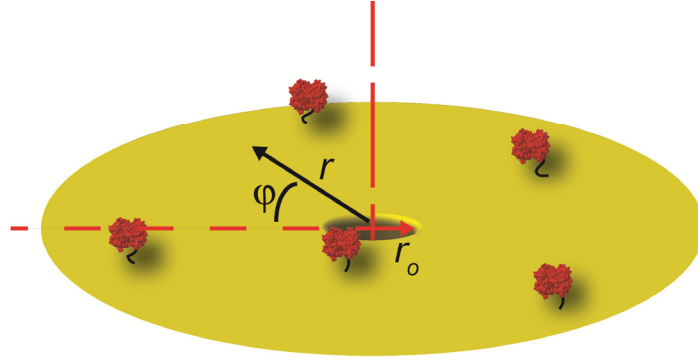


Figure 4.1 | Illustration of the cylindrical coordinate system and parameters used to describe the diffusion-limited frequency of translocation events of lipid-anchored proteins. The radius of the nanopore, r_o , is the boundary across which the flux of proteins is calculated. The density of ligand on the surface is Γ_L and the density of ligand bound proteins on the surface is Γ_{PL} . Their concentration is described in differential equation (4.5) as a function of the distance from the nanopore, r , and time, t . The angle between that vector and the azimuth is φ .

4.2 Model describing the flux of lipid-anchored proteins across the perimeter of a bilayer-coated nanopore

Supported lipid bilayers are a fluid in which diffusion occurs in a two-dimensional plane and flux occurs across a unit of length rather than through an area. In this two-dimensional environment, the concentration of an analyte on the surface (*i.e.* lipid-anchored proteins) is expressed as a surface density, Γ (# m⁻²).

To develop a model describing the frequency of the translocation events as a function of the surface density lipid-anchored proteins, we first consider that for diffusion in one direction, x , the flux of molecules across a line of length, l (m), is described by a modified form of Fick's first law of diffusion:

$$J_L = -D \frac{\partial \Gamma(x,t)}{\partial x}, \quad (4.1)$$

where J_L (# s⁻¹ m⁻¹) is the flux across a line and D (m² s⁻¹) is the diffusion coefficient of the molecules in the plane. In this case, the change in the surface density of the molecule with time is given by a modified form of Fick's second law of diffusion:

$$\frac{\partial \Gamma(x,t)}{\partial t} = D \frac{\partial^2 \Gamma(x,t)}{\partial x^2}. \quad (4.2)$$

Equations (4.1) and (4.2) are differential equations describing the flux, concentration gradient, and changes in concentration as a function of time and position for the diffusion of surface-bound analytes in one dimension. For a constant, direction-independent diffusion coefficient, equation (4.3) describes the general formulation of Fick's second law for any geometry (45):

$$\frac{\partial \Gamma}{\partial t} = D \nabla^2 \Gamma. \quad (4.3)$$

For the mass transfer of lipid-anchored proteins to the nanopore, we must consider diffusion in a two dimensional plane in which the random diffusion to the entrance of the nanopore is described by the flux of proteins across the perimeter of a circular pore. This scenario is best modeled in cylindrical coordinates in which the only variables are the radius from the origin (i.e. the center of the pore), r (m), and an angle φ (rad) from the azimuth, Fig. 4.1. The Laplacian operator for this geometry is (46):

$$\nabla^2 = \frac{\partial^2}{\partial r^2} + \left(\frac{1}{r}\right) \left(\frac{\partial}{\partial r}\right) + \frac{1}{r^2} \frac{\partial^2}{\partial \varphi^2}. \quad (4.4)$$

In these experiments, we assume the diffusion around the pore to be radially symmetric; thus, the third term in equation (4.4), $\frac{\partial^2}{\partial \varphi^2}$, equals zero. Combining equations (4.3) and (4.4) yields equation (4.5), which describes diffusion in a plane with the radius from the origin, r , and time, t , as the only parameters (45-47):

$$\frac{\partial \Gamma(r,t)}{\partial t} = D \left(\frac{\partial^2 \Gamma(r,t)}{\partial r^2} + \frac{1}{r} \frac{\partial \Gamma(r,t)}{\partial r} \right). \quad (4.5)$$

To use equations (4.1) and (4.5) for describing the flux of surface-bound analytes across the perimeter of the nanopore, we define three boundary conditions (45):

$$\Gamma(r > r_0, t = 0) = \Gamma_\infty, \quad (4.6)$$

$$\lim_{r \rightarrow \infty} \Gamma(r, t) = \Gamma_\infty, \quad (4.7)$$

$$\Gamma(r_0, t > 0) = 0, \quad (4.8)$$

where r_0 (m) is the radius of the pore and Γ_∞ ($\# \text{ m}^2$) is the density of the analyte on the surface at a far distance from the nanopore. The initial condition in equation (4.6) expresses the homogeneous distribution of analytes on the surface before the experiment starts (*i.e.* before an electric field is applied). Equation (4.7) asserts that regions distant from the pore are not affected by the flux of analytes to the pore. Equation (4.8) describes the experimental perturbation that occurs at $t \geq 0$. In the context of these experiments, the experimental perturbation that occurs at $t = 0$ is the application of an electric field across the nanopore, and we assume that in this electric field, all charged proteins arriving at the boundary r_0 are immediately driven electrophoretically through the pore to an infinite sink. This last assumption is necessary for equation (4.8) to remain valid for large values of t .

While describing the diffusion-limited current of cylindrical ultramicroelectrodes, Szabo *et al.* reported a numerical approximation to equations (4.5) – (4.8) that is valid within 1.3% (48). Equation (4.9) shows the solution presented by Szabo *et al.* in terms of flux of molecules to the boundary, r_0 , and the surface densities of the analyte, Γ :

$$J_L = \frac{D\Gamma_\infty}{r_0} \left[\frac{2e^{-0.05\sqrt{\frac{\pi 4Dt}{r_0^2}}}}{\sqrt{\frac{\pi 4Dt}{r_0^2}}} + \frac{1}{\ln\left(5.2945 + 0.74393\sqrt{\frac{4Dt}{r_0^2}}\right)} \right] \quad (4.9)$$

Note that time, t (s), remains in equation (4.9), and thus, this equation is time dependent. For long times the first term in the brackets approaches zero, and the second term in brackets dominates resulting in a quasi-steady state solution for the flux, $J_{L(qss)}$:

$$J_{L(qss)} = \frac{2D\Gamma_\infty}{r_0 \ln\left(\frac{4Dt}{r_0^2}\right)}. \quad (4.10)$$

Thus for a density of lipid-anchored proteins, Γ_{PL} ($\# \text{ m}^2$), with a diffusion coefficient, D , the frequency of translocation events, f_T ($\# \text{ s}^{-1}$), through lipid-coated nanopores can be obtained by multiplying equation (4.10) by the perimeter of the nanopore, $2\pi r_0$, to obtain equation (4.11):

$$f_T = \frac{4\pi D\Gamma_{PL}}{\ln\left(\frac{4Dt}{r_0^2}\right)}. \quad (4.11)$$

The surface density of the lipid-anchored proteins can be calculated from:

$$\Gamma_{PL} = \Gamma_L \Theta, \quad (4.12)$$

where Γ_L (# m⁻²) is the total density of ligand on the surface and Θ (unitless) is the fraction of ligand bound to a protein. Under equilibrium conditions, the Langmuir-binding isotherm describes the fraction of ligand bound to a protein as a function of the concentration of unbound protein, [P] (mol L⁻¹) and the dissociation constant K_d (mol L⁻¹) (49, 50):

$$\Theta \equiv \frac{\Gamma_{PL}}{\Gamma_L} = \frac{[P]}{[P] + K_D}. \quad (4.13)$$

The binding isotherm in equation (4.13) assumes that the binding of proteins to ligands on the surface does not deplete the concentration of unbound protein in solution, and thus, that the total protein added, [P_o], is approximately equal to the concentration of unbound protein in solution [P]. Resistive-pulse experiments, however, often take place with low concentrations of proteins (*i.e.* ~10 nM) and small reagent volumes (*i.e.* less than 100 uL), and thus, protein depletion likely occurs (*i.e.* [P_o] ≠ [P]). Equation (4.14) is the correct Langmuir binding isotherm for experimental conditions in which unbound proteins are depleted from solution by binding to a surface (49). Here, we use equation (4.14) to describe the fraction of ligand that is bound to the protein.

$$\Theta = \frac{K_d + [P_o] + [P_o]\alpha - \sqrt{K_d^2 + 2K_d[P_o] + 2K_d[P_o]\alpha + [P_o]^2 - 2[P_o]^2\alpha + [P_o]^2\alpha^2}}{2[P_o]\alpha} \quad (4.14)$$

where α is the ratio of $\frac{\text{total ligand}}{\text{total protein}} = \frac{\Gamma_L \text{ Surface Area}}{A_v [P_o] \text{ Volume}}$

In these experiments, we estimated the surface area to be 3.14×10^{-6} m² (Section 4-App.Methods) and the volume of electrolyte was always 100×10^{-9} m³. Equation (4.13) and (4.14) also assume that the binding interaction is monovalent and that the binding of a protein to the lipid-present ligand does not block additional ligand. Since in this work we employ densities of ligand on the surface that are a minimum of 6.6 times smaller than the cross-sectional area of the protein, this later assumption is reasonable. Thus by

combining equation (4.12) with either equation (4.13) or (4.14), we obtain the quasi steady state equation (4.15) that describes the frequency of translocation events as a function of the equilibrium dissociation constant, K_d , between a protein and its lipid-anchored ligand.

$$f_T = \frac{4\pi D \Gamma_L \Theta}{\ln\left(\frac{4D t}{r_0^2}\right)}. \quad (4.15)$$

4.3 Validation of equation (4.15)

To validate the model shown in equation (4.15), we performed experiments with various densities of the ligand, 1,2-dipalmitoyl-*sn*-glycero-3-phosphoethanolamine-N-capbiotinyl (biotin-PE), in the lipid bilayer coating and an excess concentration of the biotin-binding protein streptavidin in solution. Since streptavidin has a very high affinity for biotin (*e.g.* $K_d \sim 10^{-15}$ M, (51)) and since streptavidin was present in solution at an excess concentration compared to the ligand, we expected all ligand to be bound to the protein at equilibrium (*i.e.* $\Gamma_L \approx \Gamma_{PL}$). Thus, under these particular conditions, the frequency of translocation events described by equation (4.15) will be a function of the radius of the nanopore, which we determined from TEM images; the diffusion coefficient of the lipids in the membrane, which we determined from FRAP experiments (Section 4-App.S1); and the density of ligand available in the lipid bilayer coating, Γ_L , which we control during preparation of the lipid bilayer (Section 4-App.Methods). To perform these experiments, we first formed the lipid bilayer coating with mole fractions of the biotin-PE lipids ranging from 0.1×10^{-5} to 4.0×10^{-5} in a background of 1-palmitoyl-2-oleoyl-*sn*-glycero-3-phosphocholine (POPC) lipids. Since PC lipids have an average area per lipid of 68.3 \AA^2 (52), these mole fractions of biotin-PE correspond to $\Gamma_L \sim 1.46 \times 10^{12} \text{ m}^{-2}$ to $\sim 5.86 \times 10^{13} \text{ m}^{-2}$. We then added a $\sim 10,000$ fold mole excess of streptavidin (*i.e.* 100 nM) to the electrolyte on the top side of the chip (Fig 1.3B) and monitored the frequency of translocation events as a function of time (Fig. 4.2A). Fig. 4.2A shows the expected result that the frequency of translocation events at equilibrium increased with the density of the ligand. In order to determine the equilibrium frequency of

translocation events for each ligand density, we fit these curves with a pseudo-first-order rate equation (50):

$$\Gamma_{PL}(t) = \Gamma_{PL(\text{equilibrium})} [1 - e^{-k_{obs}t}] \quad (4.16)$$

where k_{obs} (h^{-1}) is the observed rate constant of the fit and described by:

$$k_{obs} = k_{on}\Gamma_L + k_{off} \quad (4.17)$$

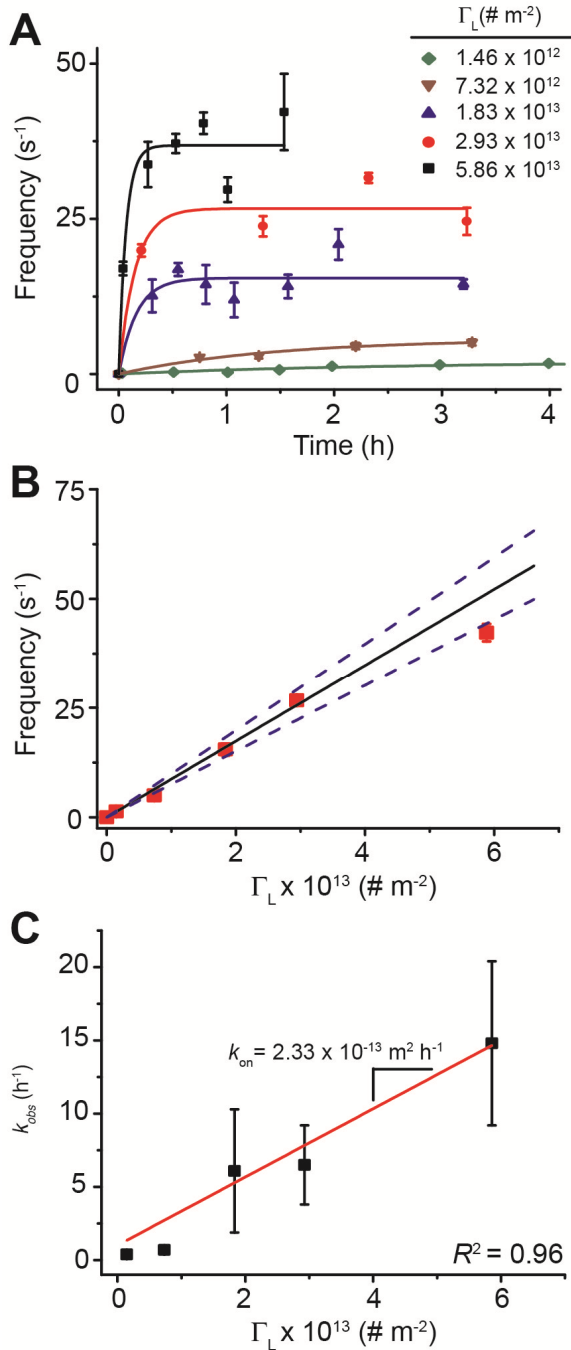


Figure 4.2 | Frequency of translocation events due to streptavidin-biotin-PE complexes with different fractions of biotin-PE lipids in the bilayer coating as well as kinetic analysis of the binding interaction. (A) Frequency of translocation events as a function of time for different densities of biotin-PE lipids in the bilayer coating. Plots were fit with equation (4.16) to estimate the equilibrium frequency of translocation events, where $f(t)$ and $f_{\text{equilibrium}}$ replaced parameters $\Gamma_{PL}(t)$ and $\Gamma_{PL(\text{equilibrium})}$, respectively. (B) Plot of the frequency of translocation events at equilibrium as determined from the best-fits in (A) as a function of the ligand density in the bilayer coating. The black line indicates the expected frequency of translocation events based on the measured diffusion coefficient of biotin-PE lipids $D = (1.14 \pm 0.16) \times 10^{-12} \text{ m}^2 \text{ s}^{-1}$ (Section 4-App.S1), the radius of the nanopore, $r_o = 7.2 \times 10^{-9} \text{ m}$, the density of ligand in the bilayer coating Γ_L , and equation (4.15). Blue dashed lines indicate the 95% confidence interval given the errors in determining the diffusion coefficient of the lipids and the diameter of the nanopore. (C) Observed rate constant, k_{obs} , from (A) as a function of the biotin-PE density in the bilayer coating.

and k_{on} ($\text{m}^2 \text{h}^{-1}$) is the association rate constant and k_{off} (h^{-1}) is the dissociation rate constant. Fig. 4.2B plots the equilibrium frequency of events as a function of the ligand density, Γ_L , and compares it to the expected frequency of translocation events based on equation (4.15) with $\Gamma_{PL} = \Gamma_L$ (black line). The excellent agreement between the expected frequency of translocation events based on the measured diffusion coefficient of the lipids in the membrane and the measured frequency of translocation events confirms that the model in equation (4.15) accurately describes the two-dimensional mass transport processes of lipid-anchored proteins to the nanopore.

To determine kinetic parameters of the binding interaction between streptavidin and biotin-PE, we plotted the value of k_{obs} determined from the best-fits in Fig. 4.2A as a function of Γ_L and fit these points with the linear model in equation (4.17) (Fig. 4.2C). As expected the value of k_{obs} increased linearly with ligand density, and the slope of line returned an estimate of k_{on} of $2.33 \times 10^{-13} \pm 0.2 \times 10^{-13} \text{ m}^2 \text{ h}^{-1}$. The *y-intercept* of the line returned the value of k_{off} equal to $1.0 \pm 1.1 \text{ h}^{-1}$. Consequently, we estimated the equilibrium dissociation constant, K_d , for these pseudo-first order conditions by using the estimates of k_{on} and k_{off} returned from the fitting procedure, $K_d = k_{on}/k_{off} = 4.3 \times 10^{12} \text{ m}^{-2}$ or $7.1 \times 10^{-12} \text{ mol m}^{-2}$. Note that this equilibrium dissociation constant has units of moles per m^2 , since the parameter varied in this experiment was the ligand density, and thus K_d here characterizes the binding affinity between streptavidin in solution and a surface-constrained biotin-PE lipid. For comparison, the equilibrium dissociation constant of streptavidin to biotin in solution is reported to be $\sim 10^{-15} \text{ M}$ or $\sim 10^{-12} \text{ mol m}^{-3}$ (51). The agreement between the expected affinity constant and the measured affinity constant provide additional evidence that this method of analyzing the frequency of the translocation is an accurate method for characterizing the binding interactions between proteins and a ligand.

Since equations (4.9)-(4.11) and (4.15) predict that the frequency of translocation events will decay to a quasi-steady state value after the electric field is first applied, we examined the frequency of streptavidin translocation events that we observed immediately after applying the electric field. Fig. 4.3 illustrates the interesting result, that immediately after turning on the electric field we did not observe a decay in the frequency of translocation events as predicted by the model. This result is likely due to

the incorrect assumption in the model that at $t \leq 0$, the surface density of the ligand-bound protein, $\Gamma_{\text{PL}}(r)$, is homogenous (equation 4.6). Since in these experiments, we added protein to the electrolyte on only one side of the chip, the lipid bilayer coating on the opposite side of the nanopore will not contain a significant fraction of ligand bound to streptavidin. In other words, on the opposite side of the nanopore, the lipid bilayer coating has a $\Gamma_{\text{PL}} \sim 0$. Thus, even before the electric field is applied, a concentration gradient near the nanopore in the density of biotin-PE lipids bound streptavidin is established. Fig. 4.3 also illustrates, however, that the quasi-steady state approximation (*i.e.* $t > 300$ s) predicts the measured frequencies of translocation events well. This result, combined, with the good agreement between the expected and measured frequencies of translocation events shown in Fig. 4.2B validates that the model in equation (4.15) accurately describes the frequency of translocation events as a function of the density of lipid-anchored proteins, Γ_{PL} .

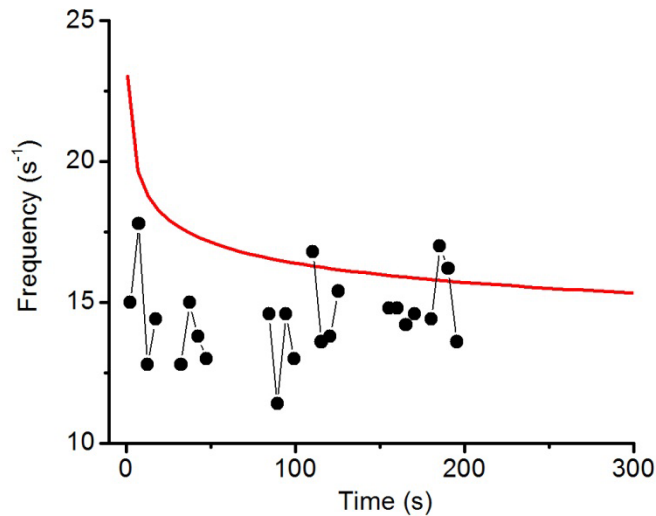


Figure 4.3 | Frequency of translocation events due to streptavidin bound to biotin-PE lipids immediately after applying the electric potential difference. The red line is the predicted frequency of the translocation events as a function of time (*i.e.* not employing the quasi-steady state approximation) and the points show the measured frequency of translocation events as determined by counting the number of translocations during 5 s intervals. The values for the parameters used to generate the red line were the same as in Fig. 4.2B with $\Gamma_{\text{L}} = 1.83 \times 10^{13} \text{ m}^{-2}$.

4.4 Affinity constant of a monoclonal anti-biotin IgG₁ antibody binding to biotin-PE lipids.

To determine the affinity constants for monoclonal IgG₁ antibodies binding to biotin-PE lipids, we coated a nanopore with a POPC lipid bilayer containing 0.0015 mol fraction ($\Gamma_L = 2.2 \times 10^{15} \text{ m}^{-2}$) of biotin-PE lipids and varied the concentration of the antibody in solution. Fig. 4.4A shows the equilibrium frequency of translocation events as a function of protein concentration. Since we expect the protein to be depleted from solution due to binding the biotin-PE lipids (*i.e.* $[P_o] \neq [P]$), we fit this data with the Langmuir binding isotherm described in equation (4.14) and the mass transport model in equation (4.15). This procedure returned a value for the equilibrium dissociation constant, K_d , the only fitting parameter, of $1000 \pm 33 \text{ nM}$. This value for the micromolar affinity is at the high end within the expected range for antibody-ligand interactions (43, 53).

To determine the affinity constant of this monoclonal IgG antibody for biotin, we performed affinity capillary electrophoresis experiments (8, 9). In these experiments, we varied the concentration of the ligand, biotin-5-fluorescein, and determined the fraction of unbound biotin-fluorescein at equilibrium. Fig. 4.4B shows an example electropherogram with peaks corresponding to the standard Rhodamine B, IgG-biotin-fluorescein complexes, and unbound biotin-fluorescein. The area under each peak is proportional to the concentration of the particular analyte. Consequently, to best estimate the area under the peak due to unbound biotin-fluorescein peak, we first subtracted the baseline signal and the signal due to the IgG-biotin-fluorescein peak (dashed red line) from the original signal (Fig. 4.4B top panel) and integrated the area under the biotin-fluorescein peak relative to the baseline as exemplified in the bottom panel of Fig. 4.4B (Section 4-App.S2). To determine the concentration of unbound biotin-fluorescein from the resulting area of the peaks, we generated a calibration curve using known concentrations of unbound biotin-fluorescein (Section 4-App.S2). Since we know the total concentration of biotin-fluorescein, $[L_o]$, in each solution, we calculated the fraction of IgG₁ that was bound to biotin fluorescein, $[PL]/[P_o]$, by $\Theta = ([L_o] - [L_{\text{unbound}}]) / [P_o]$ and plotted it against the total concentration of ligand added to the experiment, $[L_o]$, (Fig.

4.4C). A best-fit of this plot with equation (1-App.4), where K_d was the only fitting parameter, returned a value of K_d of 165 ± 11 nM. This value of K_d is 6.0-fold less than

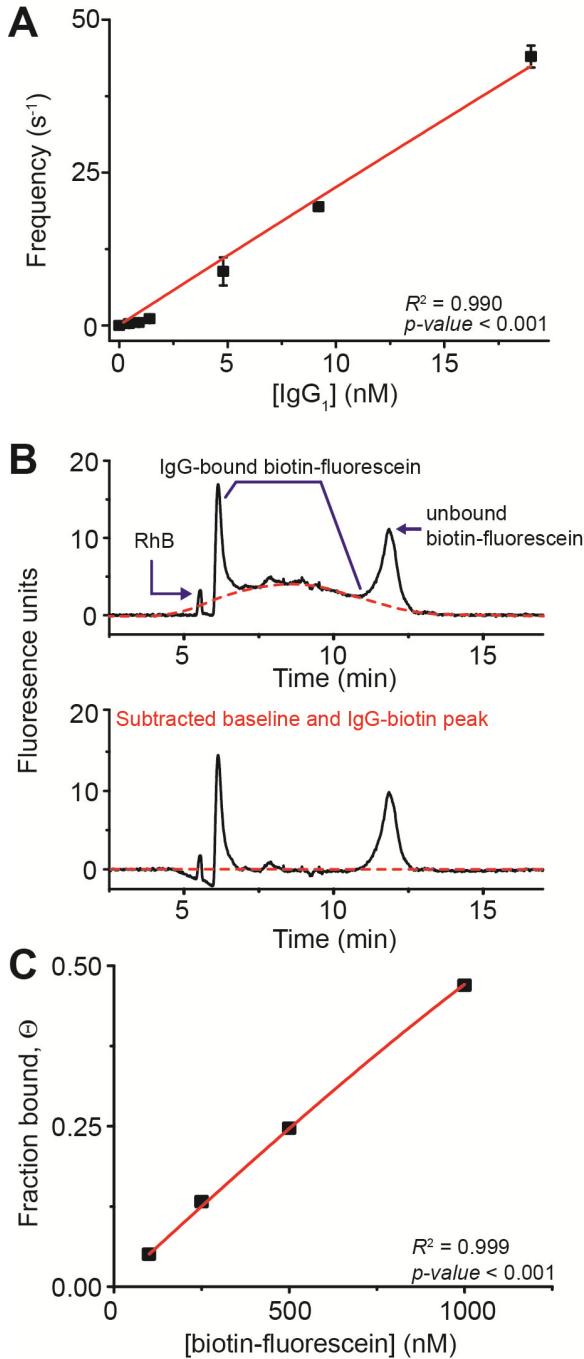


Figure 4.4 | Determination of the equilibrium dissociation constant, K_d , for the binding of monoclonal anti-biotin IgG₁ antibodies to biotin-PE and biotin-fluorescein. (A) Frequency of translocation events due to IgG₁ antibodies that are bound to biotin-PE lipids at equilibrium. Points were fit with equation (4.14) and (4.15) with K_d as the only fitting parameter. Values for other parameters were fixed at the following values: $D = 1.4 \times 10^{-12} \text{ m}^2 \text{ s}^{-1}$, $\Gamma_L = 2.19 \times 10^{15} \text{ m}^{-2}$, $r_o = 11.7 \times 10^{-9} \text{ m}$, surface area = $3.14 \times 10^{-6} \text{ m}^2$, volume = $100 \times 10^{-9} \text{ m}^3$, and $t = 600 \text{ s}$. (B) Electropherogram obtained during affinity capillary electrophoresis experiments in which fluorescence due to biotin-5-fluorescein was detected. Each experiment contained $133 \mu\text{M}$ of the standard Rhodamine B, RhB, and $1.8 \mu\text{M}$ of the IgG₁ antibody. The electropherogram on the bottom shows an example trace in which the baseline signal and the signal due to the IgG₁-bound ligand (red dashed line) was subtracted in order to calculate the area under the peak due to the unbound biotin-fluorescein ligand. (C) Fraction of IgG₁ antibodies bound to biotin-fluorescein as a function of the ligand concentration and fit with equation (1-App.4), where K_d was the only fitting parameter.

the value calculated based on the frequency of translocation events due to IgG₁ binding the biotin-PE lipid. Note that in the affinity capillary electrophoresis experiments, biotin-5-fluoresceins were in solution whereas biotin-PE lipids were part of the two-dimensional lipid bilayer surface. This result agrees well with observations made by Pisarchick and Thompson under similar conditions with lipid-anchored ligands. Pisarchick and Thompson compared the equilibrium association constant of anti-DNP Fab fragments binding to a lipid-anchored ligand, DNP-cap-DPPE (dinitrophenyl-aminocaproyldipalmitoyl phosphatidylethanolamine), and the same Fab fragments to a similar ligand (DNP-glycine) in solution, and the authors observed a ~10 fold reduction in the association constant for the binding of the Fab fragments to the lipid-anchored ligand compared to the ligand in solution (54). Pisarchick and Thompson concluded that steric hindrances significantly affected the equilibrium binding constants and suggest that the binding affinities of proteins to ligands at the lipid interface may be affected by the lipid composition and, therefore, interface properties of the bilayer surface (54, 55). Consequently, the 6.0-fold higher dissociation constant that we observed for binding of the anti-biotin IgG₁ antibodies to biotin-PE lipids is in good agreement with the dissociation constant determined during affinity capillary electrophoresis.

4.5 Conclusion

This work presented and validated a model that describes the frequency of translocation events due to lipid-anchored proteins through lipid bilayer-coated nanopores. The frequency of events was a function of the radius of the nanopore, the diffusion coefficient of the lipids, and the density of the lipid-anchored proteins in the bilayer coating. This work also demonstrated the ability of these bilayer-coated nanopores to determine kinetic parameters and equilibrium affinity constants of binding interactions by monitoring the frequency of the translocation events over time and applying the Langmuir-binding isotherm. We further validated the model by determining the affinity of a monoclonal IgG₁ antibody binding to biotin-PE lipids and observing that this value compared well to the affinity that we determined by affinity capillary electrophoresis. The strategy presented here should be applicable for determining kinetic

parameters and equilibrium affinity constants of various proteins when their ligands are lipid-anchored and incorporated into the bilayer coating at known concentrations. Since lipids can be purchased with a variety of chemically active groups, covalently linking various ligands to lipids should be straightforward. Additionally, this technique benefits from the ability to define precisely the density of ligands in the bilayer coating by varying the mole-fraction of ligand-presenting lipids in the liposome preparation. This fact also enables control of the sensitivity of the system; for instance, only 0.5 pM of a protein with a K_d of 1000 nM for biotin-PE (the same affinity constant we measured for the IgG₁ antibody) would be required to observe ~1 translocation per second if the nanopore were coated with a lipid bilayer comprised only of biotin-PE lipids. Finally, these translocation signals due to lipid anchored proteins can be used to determine the volume, charge, and shape of proteins. Therefore, this technique expands on traditional methods of characterizing protein-ligand interactions by characterizing several additional properties of the protein in addition to the affinity of the protein-ligand interaction.

Chapter 4 Appendix

4-App.Methods

Liposome preparation and formation of supported lipid bilayers. We formed supported lipid bilayers by fusion of small unilamellar vesicles (SUVs) (56-59). We prepared these SUVs as described in Yusko *et al.* (2). Briefly, we dissolved the desired lipids in 100 μ L chloroform to a lipid concentration of 10 mM. The main lipid component in each liposome preparation was 1-palmitoyl-2-oleoyl-*sn*-glycero-3-phosphocholine (POPC). Where indicated we also added the ligand lipid 1,2-dipalmitoyl-*sn*-glycero-3-phosphoethanolamine-N-(biotinyl) (biotin-PE) at mole fractions of the total lipid composition of 0.1×10^{-5} up to 1.5×10^{-3} . Each liposome preparation also contained a 0.008 mol fraction of the fluorescently-labeled lipid, 1,2-dipalmitoyl-*sn*-glycero-3-phosphoethanolamine-N-(lissamine rhodamine B sulfonyl) (Rh-PE), for measuring the fluidity of lipid bilayers by fluorescence recovery after photobleaching (FRAP, see Section 4-App.S1). We evaporated the solvent under vacuum using a rotary evaporator to form a lipid film in a round bottom glass flask with a volume of 10 mL. We resuspended this lipid film in an aqueous solution containing 150 mM KCl and 10 mM HEPES at pH 7.5 such that the lipid concentration was 2 mM. Finally, we formed SUVs via tip sonication (Branson Sonifier 150) of the solution with a power of 3 – 4 W for ~ 10 min and stored these solutions at 4 °C for up to 4 days.

To form the supported lipid bilayer on silicon nitride membranes, we filled the top compartment of the PDMS fluidic setup with 10 – 30 μ L of the aqueous solution with the SUVs and the bottom compartment with a 150 mM KCl solution without liposomes. After 5-10 min, we removed excess SUVs by immersing the entire fluidic setup for 5 – 10 min in a large (500 mL) beaker containing deionized water. Before recordings, the fluidic compartments were filled with the desired electrolyte.

Resistive-pulse experiments and detection and analysis of resistive-pulses. To sense proteins, we first formed a supported lipid bilayer of 1-palmitoyl-2-oleoyl-*sn*-glycero-3-phosphocholine (POPC) lipids (Avanti Polar Lipids, Inc.) and the indicated mole fraction of 1,2-dipalmitoyl-*sn*-glycero-3-phosphoethanolamine-N-capbiotinyl (biotin-PE) lipids on the silicon-nitride surface that contained a nanopore. The top solution compartment was created by a polydimethylsiloxane (PDMS) stamp (Fig. 1.3B)

with a 2 mm diameter hole punched in the center. Thus the surface area with available ligand was estimated as $\pi \times (0.001 \text{ m})^2 = 3.14 \times 10^{-6} \text{ m}^2$. After measuring the expected baseline ionic current and confirming the absence of irregular noise, we added solutions containing the desired protein to the top solution compartment of the fluidic setup (2 M KCl with 10 mM HEPES pH 7.4). For the experiments with streptavidin we added streptavidin to a final concentration of 100 nM in the top solution compartment, which was 100 μL in volume. This concentration of streptavidin in 100 μL of electrolyte corresponded $\sim 10,000$ fold mole excess compared to the number of available ligand on the bilayer. For the experiments with the monoclonal IgG₁ anti-biotin antibody (Clone BN-34 from Sigma), we added IgG₁ antibodies to a final concentration ranging from 0.1 nM to 40 nM in 100 μL of electrolyte on the top side of the chip.

We recorded resistive pulses at an applied potential difference of -0.1 V with the polarity referring to the top fluid compartment relative to the bottom fluid compartment, which was connected to ground. We used Ag/AgCl pellet electrodes (Warner Instruments) to monitor ionic currents through electrolyte-filled nanopores with a patch-clamp amplifier (Axopatch 200B, Molecular Devices Inc.) in voltage-clamp mode (*i.e.*, at constant applied voltage). We set the analog low-pass filter of the amplifier to a cutoff frequency of 100 kHz. We used a digitizer (Digidata 1322) with a sampling frequency of 500 kHz in combination with a program written in LabView to acquire and store data.⁽⁶⁰⁾ To distinguish resistive pulses reliably from the electrical noise, we first filtered the data digitally with a Gaussian low-pass filter ($f_c = 15 \text{ kHz}$) in MATLAB and then used a modified form of the custom written MATLAB routine described in Pedone *et al.* (2, 3, 61). To determine the frequency of translocation events and estimate an error in that measurement at each concentration or time interval, we counted the number of translocation events in 6 to 7 sequential current recordings where each recording was 20 s in duration.

4-App.S1 FRAP experiments to measure the diffusion coefficient of lipids

We used epifluorescence microscopy and the fluorescence recovery after photobleaching (FRAP) method to determine the diffusion coefficient of lipids in the bilayer coating. To visualize the lipid bilayer, we prepared all liposomes with 0.8 mol%

of lipids labeled with the fluorophore rhodamine B (1,2-dipalmitoyl-*sn*-glycero-3-phosphoethanolamine-N-(lissamine rhodamine B sulfonyl)) (Rh-PE). We used a Nikon E600FN upright microscope equipped with an Evolution MP (Media Cybernetics, Canada) camera and a 60× water-dipping objective (NA = 1.00) to image the bilayers (2). To determine the diffusion coefficient of the lipids in the bilayer, we performed fluorescence recovery after photobleaching (FRAP) experiments (Fig. 1-App.4) (2, 62). We analyzed these images by calculating the difference between the mean fluorescence intensity of the photobleached spot and a second spot on the same bilayer that was not photobleached. We normalized to the maximum difference between these two intensities and determined the diffusion coefficients by the equation, $D \text{ (m}^2 \times \text{s}^{-1}) = 0.224 \times \omega^2 \text{ (nm)}^2 / t_{1/2} \text{ (}\mu\text{s)}$, where ω is the radius of the bleached spot and $t_{1/2}$ is the half time of the fluorescence recovery (63, 64). We obtained the value of $t_{1/2}$ from an exponential curve fit through the data (Fig. 1B-App.4). On the chip used for detecting translocation events due to streptavidin, the diffusion coefficient for the bilayer containing primarily POPC lipids was $1.14 \times 10^{-12} \pm 0.16 \times 10^{-12} \text{ m}^2 \times \text{s}^{-1}$ (this error is the standard error of the mean value from 5 FRAP experiments). These values are close to the reported values of diffusion coefficients of supported bilayers, which range from $2 \times 10^{-12} \text{ m}^2 \text{ s}^{-1}$ to $5 \times 10^{-12} \text{ m}^2 \text{ s}^{-1}$, and similar to the values we obtained previously of $1 \times 10^{-12} \text{ m}^2 \text{ s}^{-1}$ to $1.5 \times 10^{-12} \text{ m}^2 \text{ s}^{-1}$ (2, 55, 65).

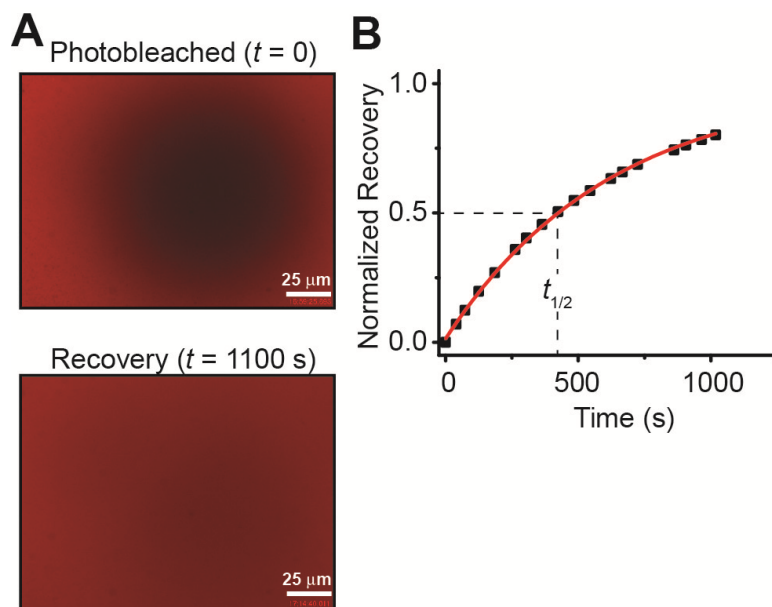


Figure 1-App.4 | Fluorescence micrographs for determining bilayer fluidity by fluorescence recovery after photobleaching (FRAP) experiments. (A) Epifluorescence micrographs indicating the recovery of fluorescence in a photobleached spot of the lipid bilayer on the Si-Si₃N₄ chip used to detect translocation events due to streptavidin. (B) Plot of mean intensity within the photobleached area *versus* time. Images in (A) were both contrast enhanced to the same extent to increase clarity. The scale bars correspond to 25 μm.

4-App.S2 Calibration curve for affinity capillary electrophoresis experiments

In order to determine the concentration of unbound biotin-fluorescein in affinity capillary electrophoresis experiments, we used a CE instrument from Beckman equipped with fluorescence detection and constructed a calibration curve. Fig. 1A-App.4 shows electropherograms, in which two different concentrations of biotin-fluorescein were injected into the capillary. Since biotin-5-fluorescein has a net charge of approximately -1 at pH 7.4, it migrates through the capillary slower than the zwitterionic, electrically neutral marker, Rhodamine B, and is detected several minutes later. In each electropherogram we determined the area of the peak due to biotin-fluorescein and normalized it to the area of the peak due to the standard, RhB. Fig. 2B-App.4 shows the resulting calibration curve that we used to calculate the concentration of unbound biotin-fluorescein in the affinity experiments. To detect binding of biotin-5-fluorescein and the anti-biotin IgG₁ antibodies, we incubated the antibodies with the ligand prior to performing the CE experiment. Fig. 4.4B in the main chapter shows the resulting

electropherograms in which biotin-5-fluorescein that is bound to the IgG antibody is detected at earlier times than the unbound biotin-5-fluorescein.

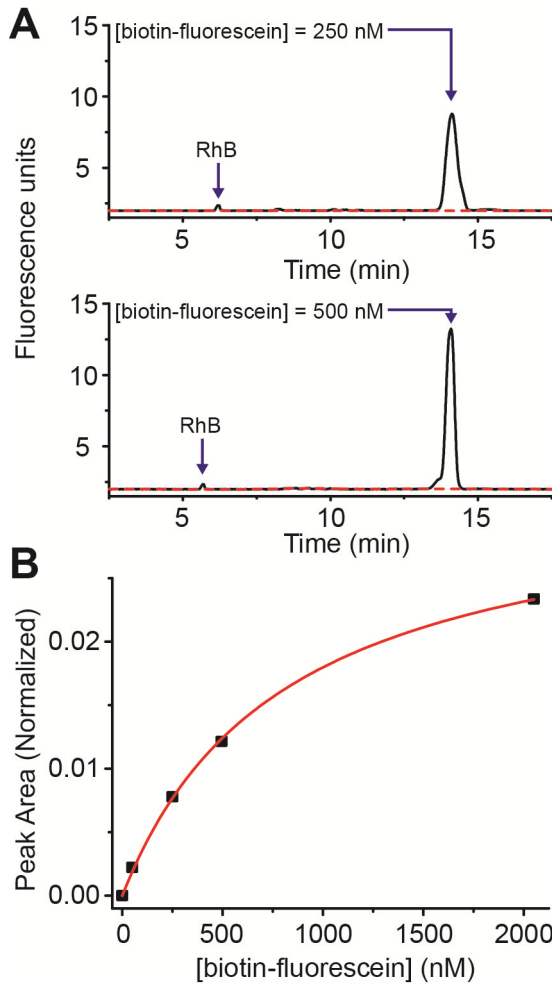


Figure 2-App.4 | Affinity capillary electrophoresis data for constructing a calibration curve that relates the peak area due to biotin-fluorescein to the concentration of biotin-fluorescein. (A)

Electropherograms obtained with a CE instrument equipped with fluorescence excitation at 490 nm and detection at 540 nm. The protein sample was prepared in PBS at pH 7.4 and included the zwitterionic fluorophore, rhodamine B (RhB), which served as the neutral fluorescent marker. Note that the peak due to RhB has a small area because the excitation and emission spectra of RhB are not well aligned with the excitation and detection wavelengths of the instrument. The two electropherograms contained 250 nM and 500 nM of biotin-5-fluorescein, with a net charge of $z = -1$. The capillary was a fused silica capillary with a total length of 30 cm and an internal diameter of 50 μm . The length of the capillary to the detector was 20 cm and the total applied voltage was 7.0 kV. The temperature of the capillary was maintained at 28 $^{\circ}\text{C}$. Note that the baseline of these electropherograms was not adjusted. **(B)** Calibration curve of the peak area due to biotin-fluorescein as a function of the concentration of biotin-fluorescein. The peak area was normalized to the area of the standard peak due to RhB to account for injection errors. The resulting calibration curve was best described by $y = \frac{0.032[\text{biotin-fluorescein}]}{808 + [\text{biotin-fluorescein}]}$ with an R^2 value of 0.999 and p -value less than 0.001.

To determine the affinity constant of the binding interaction from this data (i.e. Fig. 4.4B in the main chapter), we calculated the area under the peak due to unbound biotin-5-fluorescein. Thus, the concentration of ligand bound to the IgG₁ antibodies, [PL], is given by: $[\text{PL}] = [\text{L}_0] - [\text{L}_{\text{unbound}}]$. Since in these experiments we kept the total concentration of IgG₁ antibodies constant at 1.8 μM (i.e. $[\text{P}_0] = 1.8 \mu\text{M}$) and we expect the unbound ligand to be depleted from solution, we fit the fraction of protein bound to a ligand with a depletion model, equation (1-App.4), (50).

$$\frac{[PL]}{[P_o]} = \frac{([P_o] + [L_o] + K_d) - \sqrt{([P_o] + [L_o] + K_d)^2 - 4[P_o][L_o]}}{2 [P_o]} \quad \text{(1-App.4)}$$

In these experiments, we varied the concentration of the biotin-5-fluorescein, $[L_{total}]$, and kept $[P_o]$ constant. We measured $[PL]$, and thus, K_d , was the only fitting parameter in Fig. 4.4B.

Chapter 4 References

1. Pandey A, Mann M (2000) Proteomics to study genes and genomes. *Nature* 405(6788):837-846.
2. Yusko EC, *et al.* (2011) Controlling protein translocation through nanopores with bio-inspired fluid walls. *Nat Nanotechnol* 6(4):253-260.
3. Yusko EC, *et al.* (2012) Single-particle characterization of A β oligomers in solution. *ACS Nano* 6(7):5909-5919.
4. Yusko EC, *et al.* (2012) Determining the shape of single, native proteins. *submitted*.
5. Leavitt S, Freire E (2001) Direct measurement of protein binding energetics by isothermal titration calorimetry. *Current Opinion in Structural Biology* 11(5):560-566.
6. Homola J (2003) Present and future of surface plasmon resonance biosensors. *Analytical and Bioanalytical Chemistry* 377(3):528-539.
7. Karlsson R, Michaelsson A, Mattsson L (1991) Kinetic-analysis of monoclonal antibody-antigen interactions with a new biosensor based analytical system. *Journal of Immunological Methods* 145(1-2):229-240.
8. Chu YH, Avila LZ, Biebuyck HA, Whitesides GM (1992) Use of affinity capillary electrophoresis to measure binding constants of ligands to proteins. *Journal of Medicinal Chemistry* 35(15):2915-2917.
9. Gomez FA, Avila LZ, Chu YH, Whitesides GM (1994) Determination of binding constants of ligands to proteins by affinity capillary electrophoresis - compensation for electroosmotic flow. *Anal Chem* 66(11):1785-1791.
10. Voller A, Bartlett A, Bidwell DE (1978) Enzyme immunoassays with special reference to elisa techniques. *Journal of Clinical Pathology* 31(6):507-520.
11. MacBeath G (2002) Protein microarrays and proteomics. *Nature Genetics* 32:526-532.
12. Lin SM, *et al.* (2006) Homopolyvalent antibody-antigen interaction kinetic studies with use of a dual-polarization interferometric biosensor. *Biosens Bioelectron* 22(5):715-721.
13. Pramanik A (2004) Ligand-receptor interactions in live cells by fluorescence correlation spectroscopy. *Current Pharmaceutical Biotechnology* 5(2):205-212.
14. Lalonde S, *et al.* (2008) Molecular and cellular approaches for the detection of protein-protein interactions: Latest techniques and current limitations. *Plant Journal* 53(4):610-635.
15. Lippok S, *et al.* (2012) Direct detection of antibody concentration and affinity in human serum using microscale thermophoresis. *Anal Chem* 84(8):3523-3530.
16. Jerabek-Willemsen M, Wienken CJ, Braun D, Baaske P, Duhr S (2011) Molecular interaction studies using microscale thermophoresis. *Assay and Drug Development Technologies* 9(4):342-353.
17. Zillner K, *et al.* (2012) Microscale thermophoresis as a sensitive method to quantify protein: Nucleic acid interactions in solution. *Functional genomics: Methods and protocols, second edition*, Methods in molecular biology, eds Kaufmann M & Klinger C), Vol 815, pp 241-252.

18. Wienken CJ, Baaske P, Rothbauer U, Braun D, Duhr S (2010) Protein-binding assays in biological liquids using microscale thermophoresis. *Nature Communications* 1.
19. Keyser UF (2011) Controlling molecular transport through nanopores. *J R Soc Interface* 8(63):1369-1378.
20. Majd S, *et al.* (2010) Applications of biological pores in nanomedicine, sensing, and nanoelectronics. *Curr Opin Biotech* 21(4):439-476.
21. Han AP, *et al.* (2008) Label-free detection of single protein molecules and protein-protein interactions using synthetic nanopores. *Anal Chem* 80(12):4651-4658.
22. Fologea D, Ledden B, David SM, Li J (2007) Electrical characterization of protein molecules by a solid-state nanopore. *Appl Phys Lett* 91(5):053901.
23. Talaga DS, Li JL (2009) Single-molecule protein unfolding in solid state nanopores. *J Am Chem Soc* 131(26):9287-9297.
24. Movileanu L (2009) Interrogating single proteins through nanopores: Challenges and opportunities. *Trends in Biotechnology* 27(6):333-341.
25. Howorka S, Siwy Z (2009) Nanopore analytics: Sensing of single molecules. *Chem Soc Rev* 38(8):2360-2384.
26. Kowalczyk SW, Blosser TR, Dekker C (2011) Biomimetic nanopores: Learning from and about nature. *Trends in Biotechnology* 29(12):607-614.
27. Dekker C (2007) Solid-state nanopores. *Nat Nanotechnol* 2(4):209-215.
28. Martin CR, Siwy ZS (2007) Learning nature's way: Biosensing with synthetic nanopores. *Science* 317(5836):331-332.
29. Sexton LT, *et al.* (2007) Resistive-pulse studies of proteins and protein/antibody complexes using a conical nanotube sensor. *J Am Chem Soc* 129(43):13144-13152.
30. Sexton LT, *et al.* (2010) An adsorption-based model for pulse duration in resistive-pulse protein sensing. *J Am Chem Soc* 132(19):6755-6763.
31. Siwy Z, *et al.* (2005) Protein biosensors based on biofunctionalized conical gold nanotubes. *J Am Chem Soc* 127(14):5000-5001.
32. Uram JD, Ke K, Hunt AJ, Mayer M (2006) Submicrometer pore-based characterization and quantification of antibody-virus interactions. *Small* 2(8-9):967-972.
33. Raillon C, *et al.* (2012) Nanopore detection of single molecule map-DNA transcription complex. *Nano Lett* 12(3):1157-1164.
34. Soni GV, Dekker C (2012) Detection of nucleosomal substructures using solid-state nanopores. *Nano Lett*.
35. Robertson JWF, *et al.* (2007) Single-molecule mass spectrometry in solution using a solitary nanopore. *Proc Natl Acad Sci U S A* 104(20):8207-8211.
36. Ito T, Sun L, Crooks RM (2003) Simultaneous determination of the size and surface charge of individual nanoparticles using a carbon nanotube-based Coulter counter. *Anal Chem* 75(10):2399-2406.
37. Oukhaled G, *et al.* (2007) Unfolding of proteins and long transient conformations detected by single nanopore recording. *Physical Review Letters* 98(15):158101.
38. Merstorf C, *et al.* (2012) Wild type, mutant protein unfolding and phase transition detected by single-nanopore recording. *ACS Chemical Biology* 7(4):652-658.

39. Bacri L, *et al.* (2011) Dynamics of colloids in single solid-state nanopores. *Journal of Physical Chemistry B* 115(12):2890-2898.
40. Yusko EC, Billeh YN, Yang J, Mayer M (2011) Nanopore recordings to quantify activity-related properties of proteins. *Nanopores: Sensing and fundamental biological interactions*, eds Iqbal SM & Bashir R (Springer Publishing Co., New York), pp 203-225.
41. Wei R, Gatterdam V, Wieneke R, Tampe R, Rant U (2012) Stochastic sensing of proteins with receptor-modified solid-state nanopores. *Nat Nanotechnol* 7(4):257-263.
42. Rigler R, Vogel H eds (2008) *Single molecules and nanotechnology* (Springer-Verlag, Berlin).
43. Uram JD, Mayer M (2007) Estimation of solid phase affinity constants using resistive-pulses from functionalized nanoparticles. *Biosensors and Bioelectronics* 22(7):1556-1560.
44. Ding S, Gao CL, Gu LQ (2009) Capturing single molecules of immunoglobulin and ricin with an aptamer-encoded glass nanopore. *Anal Chem* 81(16):6649-6655.
45. Bard AJ, Faulkner LR (2001) *Electrochemical methods: Fundamentals and applications* (John Wiley & Sons, Inc., Hoboken, NJ) 2 Ed.
46. Crank J (1975) *Mathematics of diffusion* (Oxford University Press, Oxford, UK) 2 Ed.
47. Heinze J (1993) Ultramicroelectrodes in electrochemistry. *Angew Chem-Int Edit Engl* 32(9):1268-1288.
48. Szabo A, Cope DK, Tallman DE, Kovach PM, Wightman RM (1987) Chronoamperometric current at hemicylinder and band microelectrodes - theory and experiment. *J Electroanal Chem* 217(2):417-423.
49. Lauffenburger DA, Linderman JJ (1993) *Receptors: Models for binding, trafficking, and signaling* (Oxford University Press, Oxford, UK).
50. Copeland RA (2000) *Enzymes: A practical introduction to structure, mechanism, and data analysis* (Wiley-VCH, Inc., New York, NY) 2 Ed.
51. Weber PC, Ohlendorf DH, Wendoloski JJ, Salemme FR (1989) Structural origins of high-affinity biotin binding to streptavidin. *Science* 243(4887):85-88.
52. Kucerka N, Tristram-Nagle S, Nagle JF (2005) Structure of fully hydrated fluid phase lipid bilayers with monounsaturated chains. *J Membr Biol* 208(3):193-202.
53. Kumagai I, Tsumoto K (2001) Antigen-antibody binding. *Els*, (John Wiley & Sons, Ltd).
54. Pisarchick ML, Thompson NL (1990) Binding of a monoclonal-antibody and its fab fragment to supported phospholipid monolayers measured by total internal-reflection fluorescence microscopy. *Biophys J* 58(5):1235-1249.
55. Thompson NL, Poglitsch CL, Timbs MM, Pisarchick ML (1993) Dynamics of antibodies on planar model membranes. *Accounts of Chemical Research* 26(11):568-573.
56. Watts TH, Brian AA, Kappler JW, Marrack P, McConnell HM (1984) Antigen presentation by supported planar membranes containing affinity-purified i-a^d. *Proc Natl Acad Sci U S A* 81(23):7564-7568.
57. Cremer PS, Boxer SG (1999) Formation and spreading of lipid bilayers on planar glass supports. *Journal of Physical Chemistry B* 103(13):2554-2559.

58. Reimhult E, Hook F, Kasemo B (2003) Intact vesicle adsorption and supported biomembrane formation from vesicles in solution: Influence of surface chemistry, vesicle size, temperature, and osmotic pressure. *Langmuir* 19(5):1681-1691.
59. Sackmann E (1996) Supported membranes: Scientific and practical applications. *Science* 271(5245):43-48.
60. Uram JD, Ke K, Mayer M (2008) Noise and bandwidth of current recordings from submicrometer pores and nanopores. *ACS Nano* 2(5):857-872.
61. Pedone D, Firnkes M, Rant U (2009) Data analysis of translocation events in nanopore experiments. *Anal Chem* 81(23):9689-9694.
62. Majd S, Mayer M (2005) Hydrogel stamping of arrays of supported lipid bilayers with various lipid compositions for the screening of drug-membrane and protein-membrane interactions. *Angew Chem-Int Edit* 44(41):6697-6700.
63. Axelrod D, Koppel DE, Schlessinger J, Elson E, Webb WW (1976) Mobility measurement by analysis of fluorescence photobleaching recovery kinetics. *Biophys J* 16(9):1055-1069.
64. Soumpasis DM (1983) Theoretical-analysis of fluorescence photobleaching recovery experiments. *Biophys J* 41(1):95-97.
65. Starr TE, Thompson NL (2000) Formation and characterization of planar phospholipid bilayers supported on tio2 and sr tio3 single crystals. *Langmuir* 16(26):10301-10308.

Chapter 5

Single Particle Characterization of A β Oligomers in Solution

Determining the pathological role of amyloids in amyloid-associated diseases will require a method for determining the dynamic distributions in size and shape of amyloid oligomers with high resolution. Here, we explored the potential of resistive-pulse sensing through lipid bilayer-coated nanopores to measure the size of individual amyloid- β oligomers directly in solution and without chemical modification. This method classified individual amyloid- β aggregates as spherical oligomers, protofibrils, or mature fibers and made it possible to account for the large heterogeneity of amyloid- β aggregate sizes. The approach revealed the distribution of protofibrillar lengths as well as the average cross-sectional area of protofibrils and fibers.

5.1 Introduction

Irregular aggregation of amyloidogenic proteins and peptides is associated with the pathophysiology of several diseases including Alzheimer's disease, Parkinson's disease, Huntington's disease, and Type II diabetes mellitus (1-5). These amyloid aggregates are associated with many cytotoxic effects (1). The toxic form and pathogenic mechanisms of these aggregates, however, generally remain unclear (6, 7) in part because the size and shape of amyloid oligomers are typically heterogeneous and dynamic in solution.(8) Consequently, the potential toxic effects of subpopulations of oligomers in these heterogeneous preparations are difficult to discern, since these subpopulations are often masked in ensemble measurement techniques (8, 9). For example, Cabriolu *et al.* recently developed a computational model describing the size distribution of aggregates of amyloid- β , the peptide implicated with Alzheimer's disease (10), and reported the occurrence of "magic" fibril sizes – preferred aggregate sizes that appear as peaks in the distribution (11, 12). The authors could only qualitatively verify this result (13) because of a "lack of suitable experimental or simulation data for the size distribution of amyloid fibrils" (11). Here, we make a first attempt to determine the size and shape distributions of unlabeled A β aggregates in solution by analyzing resistive current pulses from hundreds of single aggregates during their passage through an electrolyte-filled nanopore. We propose that resistive pulse sensing is an enabling technique for characterizing aggregated amyloidogenic peptides, since it is the only technique that measures single particles volumetrically and is, therefore, particularly well-suited for characterizing particles with irregular shapes (14).

Increasing evidence indicates that certain sizes of A β oligomers, and possibly certain shapes of these oligomers, are more neurotoxic than others and, thus, play different roles in the pathology of Alzheimer's disease (10, 15-21). Aggregated forms of A β in the brain are thought to stem from an imbalance between the generation and clearance of A β monomers, which subsequently leads to their accumulation and aggregation (6, 22) to oligomers (15), protofibrils (17, 23), fibers (18), and amyloid plaques (6). The size of A β oligomers range from the monomer molecular weight of 4.3 kDa for the 40 amino acid peptide to ~ 43 kDa (24), whereas protofibrils have molecular weights greater than ~ 43 kDa and are approximately 5 nm in diameter and less than

~200 nm in length (24, 25). Fibers result from the assembly of protofibrils and have an average diameter of approximately 7 - 10 nm and lengths up to several micrometers (25-27), while senile plaques are dense meshes of A β fibers in the brain (6, 7).

One reason why the pathogenic role of different A β aggregates in Alzheimer's disease is not understood stems from conflicting reports and difficulties reproducing the exact conditions of previous experiments (6, 7, 21, 28). Conducting assays with reproducible distributions of A β aggregates is challenging, since temperature, concentration, pH, solvent conditions, solvent history, agitation, and air-water interfaces strongly influence nucleation and aggregation rates and the distribution of aggregate shapes and sizes (24). Consequently, methods for characterizing the distribution of aggregated species quickly, accurately, and in solution are needed to interpret functional studies as well as to determine the pathological role of amyloidogenic peptides in Alzheimer's disease and other neurodegenerative disorders (10, 24, 29).

Several techniques are currently being used to characterize the aggregation and structure of A β aggregates. Gel electrophoresis with native gels and SDS gels makes it possible to identify and separate low molecular weight A β aggregates; however, the technique can misrepresent the native aggregation state and can only accurately resolve low-molecular weight aggregates (*i.e.* less than decamers) (24, 29). Size exclusion chromatography is considered the best non-SDS-based method for identifying and separating A β aggregates; although, it is a relatively low resolution method compared to SDS-PAGE (8, 29). Electron microscopy and atomic force microscopy imaging techniques provide the highest quality information on the structure of A β aggregates; however, they require drying the sample and the results may be affected by biased adsorption of the aggregates to the TEM substrates (26, 27, 30, 31). Light scattering techniques permit *in situ* measurements, but they are ill-suited for monitoring fibrillar objects and heterogeneous populations such as those found in solutions containing A β aggregates (24, 32). Circular dichroism (23, 24), thioflavin T fluorescence assays (13), and surface enhanced Raman spectroscopy (33) monitor changes in the conformation of A β during aggregation but do not provide information on the size of aggregates (29).

Recently, the first attempts to apply single-molecule techniques toward A β aggregation and toxicology studies emerged. Knowles *et al.* combined the thioflavin T

assay with a microfluidic technique to follow amyloid aggregation from single-aggregate nuclei (34). Schierle *et al.* used a super-resolution fluorescence imaging technique to image, *in situ* and in live cells, individual aggregates of A β with sizes greater than ~20 nm (35). The technique requires covalent modification of A β monomers with a fluorophore or the binding of fluorescently labeled antibodies to A β aggregates. Wang *et al.* used the resistive-pulse sensing technique with the biological α -hemolysin pore to assess conformational changes in A $\beta_{(1-42)}$ aggregates that were induced by Congo red or β -cyclodextrin (two molecules with opposite effects on A $\beta_{(1-42)}$ aggregation) (36). Finally, Dukes *et al.*, Schauerte *et al.*, Ding *et al.* and Johnson *et al.* have used fluorescently labeled A β peptides combined with single-molecule fluorescence spectroscopy to measure the aggregation of single A $\beta_{(1-40)}$ peptides and the binding of single aggregates to model membranes and cell membranes (8, 9, 37, 38). These techniques exemplify the search for single-molecule techniques capable of detecting individual aggregates of A β *in situ* in order to determine the heterogeneous size distribution of aggregates, their kinetics of assembly, and their pathogenic function (10).

With the same goal in mind, we recently demonstrated that lipid-coated, electrolyte-filled nanopores in a resistive-pulse sensing configuration could be used to detect A β fibers in solution without drying, chemically modifying, or labeling A β samples (39). Resistive-pulse sensing (40-52) is an attractive technique to characterize heterogeneous samples since the magnitudes of transient changes in ionic current, ΔI , are due to the translocation of individual particles through the nanopore (Fig. 5.1A) and are proportional to the volume of electrolyte excluded by the aggregate (39, 53, 54). Additionally, the duration of the resistive pulse, t_d , is related to the electrophoretic mobility of the aggregate, and the frequency of translocation events is related to the concentration of the particles (39, 55-57).

Here, we extend the use of lipid-coated, synthetic nanopores from analyzing A β fibers to characterizing the smaller and clinically more relevant soluble A β oligomers. The lipid coating of the nanopore (Fig. 5.1A inset) is required for detection of A β aggregates, since synthetic nanopores without a fluid coating clogged due to adsorption of A β on the nanopore walls (see Section 5-App.S1) (39). We show that resistive-pulse sensing with lipid-coated nanopores can be used to track the time-dependent aggregation

of $A\beta_{(1-40)}$ by monitoring the size distribution of $A\beta$ aggregates in solution, and we validated this method by analyzing transmission electron microscopy micrographs of $A\beta_{(1-40)}$ aggregates from the same $A\beta$ preparations.

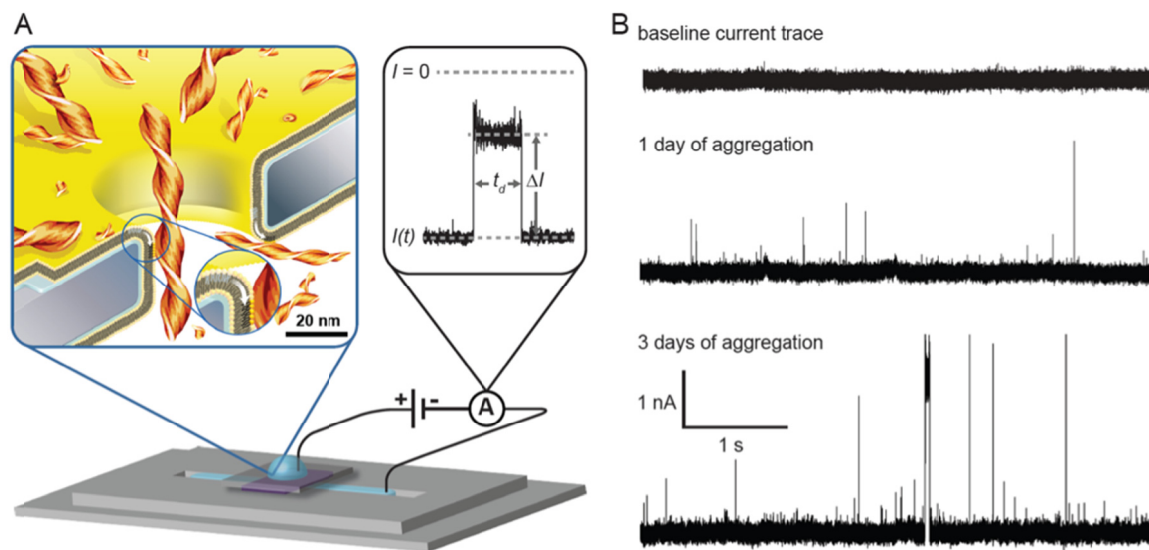


Figure 5.1 | Synthetic nanopores with fluid walls make it possible to characterize individual $A\beta$ aggregates by resistive pulse recordings. (A) Illustration of the experimental setup with fluid access channels to a nanopore embedded in a silicon nitride chip (58, 59). Silver-silver/chloride electrodes immersed in the two fluidic compartments are connected to a patch-clamp amplifier and used to measure the ionic current through the nanopore. Inset left. Cartoon showing a cross-section of a nanopore that is coated with a fluid lipid bilayer, thereby enabling the translocation of $A\beta$ aggregates without clogging the pore. Inset right. Original current trace showing a characteristic resistive pulse with the parameters ΔI and t_d . (B) Original current traces recorded before and after adding $A\beta$ that was permitted to aggregate for 1 or 3 days. The nanopore had a length of 18 nm and a diameter of 28 nm before the lipid bilayer coating (length of 28 nm and a diameter of 18 nm after the bilayer coating).

5.2 Results and discussion

To perform nanopore-based detection of $A\beta_{(1-40)}$ aggregates, we started from aqueous solutions containing mostly monomers of $A\beta_{(1-40)}$ as well as dimeric and trimeric aggregates that are thought to be in rapid equilibrium with the monomeric form (24) (Section 5-App.S2). We prepared aggregates of $A\beta_{(1-40)}$ by incubating these solutions for zero to three days under well-controlled conditions before adding 1 - 2.5 μL of these $A\beta$ preparations to the electrolyte in the top compartment of the recording setup (Fig. 5.1A) (24, 60). Gel electrophoresis confirmed that this preparation method resulted in increasing aggregate sizes over time (Section 5-App.S2) (60). Additionally, circular dichroism spectroscopy and thioflavin T binding assays showed an increase in β -sheet

content and fibril formation with increasing aggregation time (Section 5-App.S3). Cytotoxicity assays confirmed that this preparation method resulted in aggregates that were biologically active and yielded similar toxicity characteristics to those reported in literature (Section 5-App.S3) (10, 61, 62).

Fig. 5.1B shows recordings of the baseline current before and after adding $A\beta_{(1-40)}$ solutions that had been permitted to aggregate for one or three days. Consistent with time-dependent aggregation, the current trace from the three-day sample shows resistive pulses with increased frequency and larger amplitude than the current trace from the one-day sample. Fig. 5.2A shows scatter plots of ΔI versus t_d values for translocation events with a ΔI value greater than 250 pA (5 times the standard deviation of the noise) and with a t_d value greater than 35 μ s (the smallest t_d value we could measure accurately) (39, 63). As expected, the values of ΔI , and hence the sizes of aggregates, increased with increasing aggregation time. Interestingly, the amplitude of ΔI values reached a maximum at ~ 5 nA, which was only 19% of the 26 nA baseline current magnitude, despite large variations in t_d values (Fig. 5.2B, cluster (iv)). This result is consistent with translocation of cylindrical objects with similar diameters but varying lengths that are longer than the length of the nanopore, similar to the translocation of DNA strands of varying lengths (59, 64-67). Protofibrils, which have lengths up to 200 nm, and fibers, which can reach lengths of several micrometers, have these characteristics: both types of aggregates have nearly constant average diameters along their widely varying lengths (12, 25-27), and therefore, resistive pulses due to their translocation will have a maximum ΔI value and broadly distributed t_d values (12, 25).

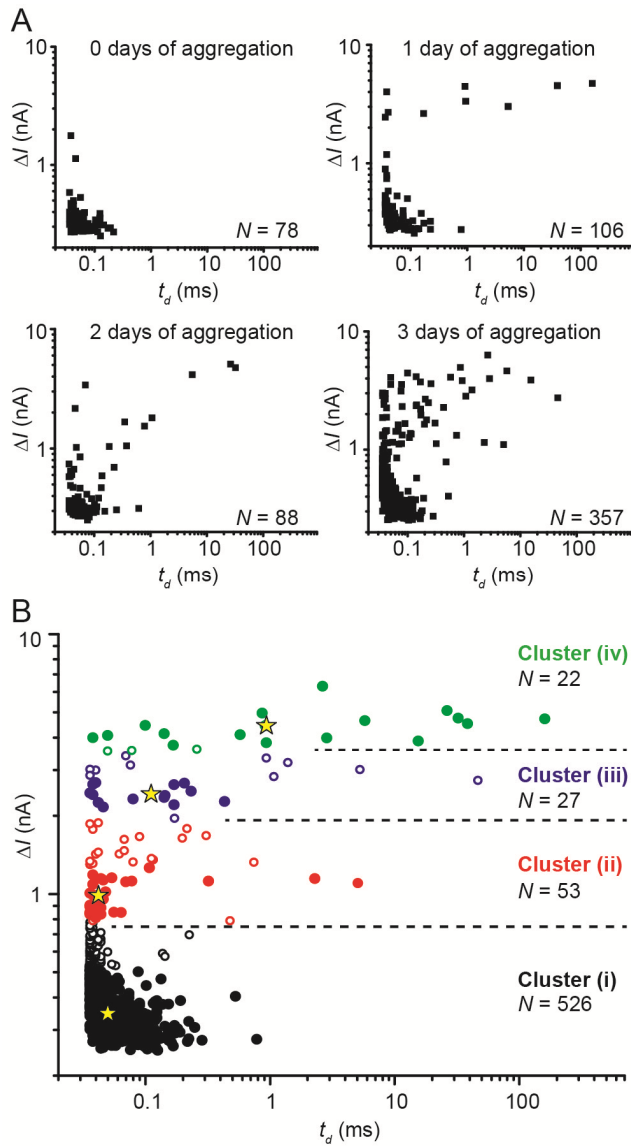


Figure 5.2 | Scatter plots of ΔI values versus t_d values from the translocation of individual $A\beta$ aggregates reveal clusters of translocation events due to spherical oligomers, protofibrils with lengths shorter than the length of the nanopore, protofibrils with lengths longer than the length of the nanopore, and mature fibers. (A) Scatter plots of $\Delta I(t_d)$ from aggregates of $A\beta_{(1-40)}$ that were analyzed after 0, 1, 2, and 3 days of incubation. (B) Scatter plot of all data combined and color coded according to the results from statistical cluster analysis (68). Open and filled symbols show the results of the cluster classification based on the original data set. Filled symbols indicate points that were classified in the same cluster in more than 90% bootstrap resamples (Section 5-App.S4). Yellow stars indicate the mean ΔI value and median t_d value based on the filled symbols in each cluster.

In order to distinguish among resistive pulses resulting from the translocation of spherical oligomers, protofibrils or fibers through the nanopore, we performed a cluster analysis on a data set from all resistive pulses (Fig. 5.2B) based on the ΔI value for each translocation event. To perform the cluster analysis, we used the *k-means* algorithm in the open-source, statistics software R (<http://www.R-project.org>) and set the number of clusters to four, since we expected four clusters of ΔI versus t_d values that represented the translocation of: (i) spherical oligomers, (ii) cylindrical protofibrils with lengths shorter than the effective length of the nanopore, (iii) cylindrical protofibrils with lengths longer than the effective length of the nanopore, or (iv) fibers with a length longer than the effective length of the nanopore. The open and filled symbols in Fig. 5.2B illustrate the resulting cluster assignment given to each recorded resistive pulse. To test the robustness of this clustering procedure, we performed bootstrap resampling combined with *k-means* clustering to track the stability of the cluster classification for each point (69). This analysis revealed that 82% of the measured ΔI values were classified into the same clusters at least 90% of the time. We re-plotted these points as filled-colored points in Fig. 5.2B (Section 5-App.S4).

Fig. 5.2B reveals that cluster (iv) contains resistive pulses with very long transit times (up to 200 ms) and ΔI values that converge to a maximum value of 4 to 5 nA. This result would be expected for fibrils of varying lengths but relatively constant diameters. Cluster (iii) also contains pulses with long transit times (up to 60 ms) whose median is three times larger than the median transit time in cluster (ii). In both, clusters (iii) and (iv), the range of t_d values is greatly distributed over 2 to 4 orders of magnitude and toward longer translocation times than those observed in clusters (i) or (ii). Broad distributions of t_d values over a full order of magnitude can be expected due to the stochastic nature of molecular diffusion combined with biased motion by electrophoresis (67, 70). Additional effects such as non-specific interactions between analytes and the pore walls with various frequencies and strengths can further increase the width of distributions of t_d such that they range several orders of magnitude even for the exact same analyte (45, 48). In the work presented here, the broadly distributed lengths of aggregates have an additional effect on t_d values; for instance protofibrils can have lengths ranging from ~ 10 to 500 nm and fibers can have lengths ranging from less than

one micrometer to several micrometers. The combination of large variations in length, stochastic elements of transit times through the pore, and potential for non-specific binding result in large variations in t_d values. Despite these effects, several groups showed that median t_d values of molecules that are longer than the length of the pore increase with aggregate length (59, 64-66). Indeed, the yellow stars in Fig. 5.2B show that median t_d values increased from cluster (ii) to cluster (iii) and cluster (iv), indicating the expected result that cluster (iv) contains longer aggregates than cluster (iii), which in turn contains longer aggregates than cluster (ii). This result, the broadly distributed t_d values in clusters (iii) and (iv), and the convergent maximal ΔI values in cluster (iv) suggest that the resistive pulses in these two cluster originated from the translocation of protofibrils and fibers of various lengths with nearly constant diameters.

To determine the size of $A\beta_{(1-40)}$ aggregates in each cluster, we used the value of ΔI from each translocation event and considered two extreme cases yielding two different equations (39, 53, 70). Equation (5.1) describes the relationship between ΔI and the excluded volume, Λ (nm^3), of spherical oligomers (71-74), whereas equation (5.2) describes the relationship between ΔI and the average cross-sectional area, A_X (nm^2), of aggregates with lengths longer than the effective length of the nanopore (67, 70).

$$\Delta I = \frac{\gamma V_A \Lambda}{\rho (l_p + 1.6r_p)^2} \text{ for } l_M < l_{eff} \quad (5.1)$$

$$\Delta I = \frac{\gamma V_A A_X}{\rho (l_p + 1.6r_p)} \text{ for } l_M > l_{eff} \quad (5.2)$$

In these equations, γ is a shape factor (with a value of 1.5 for globular spheres and a value of 1.0 for long cylinders that are aligned parallel to the electric field) (53, 54, 75-78), V_A (V) is the applied electric potential difference, ρ ($\Omega \text{ m}$) is the resistivity of the electrolyte solution, l_p (m) is the length of the nanopore, r_p (m) is the radius of the nanopore, and l_M (m) is the length of the protofibril or fiber. The effective length of the cylindrical nanopore, l_{eff} , is defined by the term $(l_p + 1.6r_p)$ in the denominator of equations (5.1) and (5.2), and it accounts for the extension of the electric field lines from the nanopore into the bulk solution (79).

Table 5.1. Average values of ΔI , excluded volumes Λ , diameters of spherical $A\beta_{(1-40)}$ aggregates \varnothing_S , and cross-sectional areas A_X as well the corresponding cylindrical diameter \varnothing_C of rod-shaped $A\beta_{(1-40)}$ aggregates in each cluster compared to equivalent values measured *via* TEM and values reported in literature.

cluster	$\langle \Delta I \rangle$	Λ	\varnothing_S	TEM values ^a	literature value
	(min, max) pA	(min, max) nm ³	(min, max) nm	nm	nm
(i): spherical oligomers	383 (250, 777)	101 (66 ^b , 205)	5.8 (5.0, 7.3)	$\varnothing_S = 6.2 \pm 1.2$	$\varnothing_S = 3-5$ Ref. (80)
(ii): protofibrils $l_M \leq l_{eff}$	1177 (787, 1874)	403 (244, 683)	–	$\varnothing_C = 6.5 \pm 2.0$	$\varnothing_C = 5$ Ref. (23, 25)
cluster	$\langle \Delta I \rangle$	A_X	\varnothing_C	TEM values	literature value
	pA	nm ²	nm	nm	nm
(iii): protofibrils $l_M > l_{eff}$	2668 (1953, 3397)	24.5 (18, 31)	5.6 (4.8, 6.3)	$\varnothing_C = 6.4 \pm 1.5$	$\varnothing_C = 5$ Ref. (23, 25)
(iv): fibers $l_M \gg l_{eff}$	4340 (3548, 9552)	40 (33, 88)	7.1 (6.4, 10.6)	^c $W_1 = 5.6 \pm 0.8$ $W_2 = 11.5 \pm 1.5$ $A_X \sim 51 \pm 10 \text{ nm}^2$	$W_1 = 6.6$ Ref. (26) $W_2 = 13.2$ Ref. (26) $A_X = 30-90 \text{ nm}^2$ Ref. (26, 27, 31)

^aErrors shown in Table 1 are standard deviations. ^bUsing the average molecular weight density of $A\beta_{(1-40)}$ aggregates of 0.81 kDa / nm³ (26, 81) and the molecular weight of an $A\beta_{(1-40)}$ monomer of 4.355 kDa, the smallest spherical oligomers detected in cluster (i), corresponding to a molecular volume of 250 nm³, contained approximately 12 $A\beta$ monomers. Completing this same calculation, ΔI values in cluster (i) correspond to aggregates ranging from approximately 12 to 38 monomers, and ΔI values in cluster (ii) correspond to aggregates ranging from 55 to 156 monomers. ^c W_1 and W_2 refer to the widths of twisting $A\beta_{(1-40)}$ fibers when the fibers are twisted or crossing over themselves, W_1 , or when the fibers are lying flat, W_2 , on the TEM grid (Fig. 5.3) (26).

Table 5.1 lists the mean value of ΔI and the range of ΔI values that we measured for each cluster as well as the values for the excluded volume that we calculated using equation (5.1) for cluster (i) and the values for the cross-sectional areas that we calculated using equation (2) for clusters (iii) and (iv). Using bootstrap resampling statistics (82, 83), we confirmed that the differences among these four mean ΔI values is statistically significant at the $\alpha = 0.05$ level, and we present confidence intervals for the mean values in Section 5-App.S4. Table 5.1 also compares the sizes of $A\beta_{(1-40)}$ aggregates determined by resistive-pulse analysis with those determined by TEM from the same samples (Fig. 5.3) as well as with literature values. For instance, the mean ΔI of the resistive pulses in cluster (i) corresponds to a spherical diameter of 5.8 nm (with a range of 5 – 7.3 nm), and we measured by TEM that the smallest spherical aggregates had an average diameter of

6.2 ± 1.2 nm ($N = 18$) (Fig. 5.3A). Similarly, the mean ΔI of the resistive pulses in cluster (iii) due to protofibrils with $l_M > l_{eff}$ corresponds to a cylindrical diameter of 5.6 nm (with a range of 4.8 to 6.3 nm). In TEM micrographs, we observed protofibrils with an average diameter of 6.4 ± 1.5 nm ($N = 117$) and with lengths ranging from ~ 6 nm to 350 nm (Fig. 5.3B & 5.3C); the reported diameter of protofibrils in literature is ~ 5 nm (23, 25). Finally, the mean ΔI of resistive pulses in cluster (iv) due to fibers corresponds to a cross-sectional-area of 40 nm² (with a range of 33 nm² to 88 nm²). From the TEM micrographs, we estimated the cross-sectional area of A $\beta_{(1-40)}$ fibers to be 51 ± 10 nm² ($N = 27$) based on the two visible widths of the twisting fibers of 5.6 ± 0.8 nm and 11.5 ± 1.5 nm (Fig. 5.3A:Day 3 and Fig. 5.3D). The literature values of the cross-sectional areas of amyloid fibers range from 30 nm² to 90 nm² (26, 27, 31). For these three forms of A $\beta_{(1-40)}$ aggregates, the general agreement among the sizes determined from resistive-pulse analysis with those determined by TEM analysis and those reported in literature demonstrates that resistive-pulse analysis makes it possible to characterize A β oligomers, protofibrils, and fibers in solution. This agreement also indicates that the cluster analysis in Fig. 5.2 produced reasonable assignments for the majority of the resistive pulses. For instance, based on values from TEM analysis, the ratio between the cross-sectional area of fibrils and protofibrils is 1.58 ± 0.8 (84). According to equation 5.2 we expect that the ratio between the mean ΔI value from the translocation of A β fibrils in cluster (iv) and the mean ΔI value from the translocation of A β protofibrils in cluster (iii) to have this same value, if the cluster assignment was accurate and if the A β aggregates in clusters (iii) and (iv) were longer than the length of the pore. Indeed, the ratio of the mean ΔI values between clusters (iv) and (iii) was 1.63 ± 0.3 and, therefore, not statistically different from the expected value of 1.58. We discuss additional evidence for the accuracy of the cluster analysis in Section 5-App. S3 and provide results from the bootstrap resampling statistics in Section 5-App.S4.

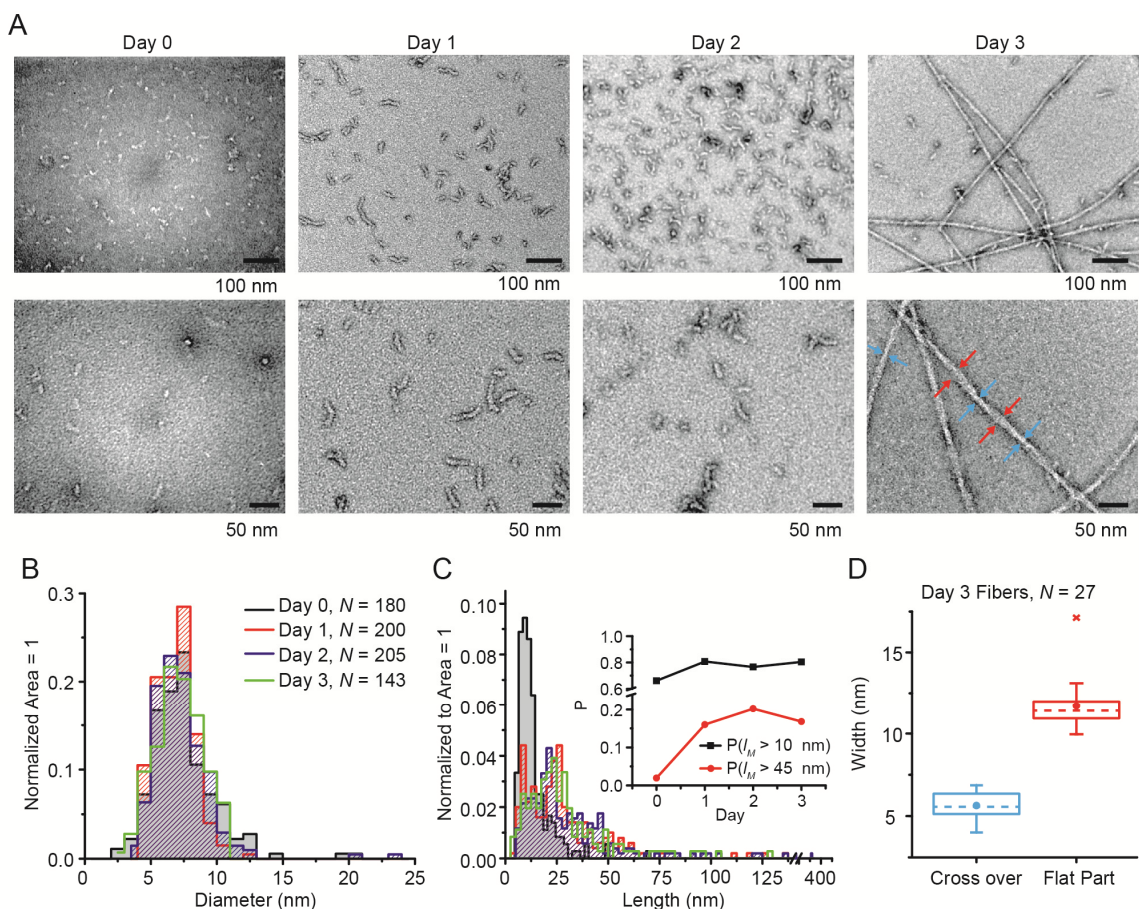


Figure 5.3 | Transmission electron microscopy (TEM) analysis of the size of $A\beta_{(1-40)}$ aggregates. (A) Micrographs showing aggregates with increasing size after incubation in water for 0, 1, 2 and 3 days. (B) & (C) Histograms of the diameters (B) and lengths (C) of all aggregates that were not mature fibers. Inset in (C). Proportion of aggregates with lengths longer than 10 nm and 45 nm. (D) Boxplots characterizing mature fibers after three days of aggregation. The fibers were characterized by their apparent widths when lying flat W_2 (red arrows in A) on the TEM grid and when twisted or crossing over themselves W_1 (blue arrows in A) on the TEM grid (26). The box represents the range between the 1st and 3rd quartiles, the dashed line represents the median, the dot is the mean, and the whiskers extend to the range of the data (minimum and maximum values) except for one outlier, which is plotted as “x”.

In order to estimate the excluded volume, Λ , of the protofibrils with $l_M < l_{eff}$ from the resistive pulses in cluster (ii), we made two assumptions. First, protofibrils pass through the nanopore with their long-axis aligned parallel to the electric field resulting in a relatively constant shape factor that can be approximated from the shape factor of a prolate aligned parallel to an electric field, γ_{\parallel} . This alignment is predicted because aggregates approaching the nanopore from the bulk solution experience a strong converging electric field gradient (55, 75-77, 85-87). Ai and Qian recently modeled the dynamics of nanorods (1 nm x 10 nm) approaching a nanopore under similar conditions

to those reported here and demonstrated that rods will completely align with their length axis parallel to the electric field prior to entering the nanopore (88). Furthermore, the distribution of translocation times in cluster (ii) was narrower than the distribution in cluster (i) (Fig. 5.2B). This result suggests reduced diffusive spreading due to accelerated motion through the pore as a result of reduced viscous drag on aggregates in cluster (ii) compared to those in cluster (i) (see Section 5-App.S6 for distributions of t_d values in clusters i and ii) (67, 70). Indeed, prolate spheroids moving parallel to their long axis experience less viscous drag than a spherical particle of similar volume (89). These effects combined with the strong electrophoretic force on an A β aggregate due to the net negative charge of each monomer of approximately -3 at pH 7.0 (19, 90) and the high electric field in the nanopore ($V_A/l_{eff} = 4.5 \times 10^6 \text{ V m}^{-1}$) likely orient protofibril aggregates with their long axis parallel to the electric field in the nanopore. The second assumption, based on results by Kellermayer *et al.*, was that the elongation of A β protofibrils occurs at a constant average diameter, \varnothing_C , for lengths greater than 6.5 nm (12). We confirmed the validity of this assumption by TEM analysis of the samples used here (see Fig. 5.3 and Section 5-App.S7). Consequently, the excluded volume of these protofibrils could be described by the equation of a cylinder, $\Lambda = \frac{1}{4} \pi \varnothing_C^2 l_M$, and a system of equations that includes the shape factor $\gamma_{||}$ as a function of the length of the aggregate, l_M , and ΔI as a function of $\gamma_{||}$ and l_M . We summarized the details of these equations, the resulting shape factors, and results of this analysis in Section 5-App.S8. Solving this system of equations while using the values of ΔI from the resistive pulses in cluster (ii) and the average diameter of protofibrils ($\varnothing_C = 5.6 \text{ nm}$, Table 5.1), this analysis returned shape factors for each translocation event that ranged from $\gamma_{||} = 1.06$ to 1.25 (average $\gamma_{||} = 1.15$) and excluded volumes that ranged from 244 nm^3 to 683 nm^3 (Table 5.1).

As a first attempt at examining the peaks in the distribution of A $\beta_{(1-40)}$ sizes reported by Cabriolu *et al.*, we determined the lengths of the protofibrils in clusters (i) and (ii) by using the equations described in Section 5-App.S8. From the resulting data, we generated an empirical cumulative distribution (Fig. 5.4 Inset) of protofibril lengths in these two clusters (91). In order to test if this cumulative distribution of protofibril lengths was multimodal, we fit it with a trimodal Gaussian cumulative distribution

function (trimodal CDF) and confirmed *via* a Kolmogorov Smirnov test that the differences between the two distributions were not statistically significant ($p = 0.28$). This result indicates that the trimodal CDF described the empirical distribution very well. In contrast, differences between the empirical cumulative distributions and best curve fits to CDFs for the normal, lognormal, extreme value, exponential, or Poisson distributions were all statistically significant ($p = 0$, $p = 3.2\text{E-}8$, $p = 0.001$, $p = 0.0007$, $p = 2\text{E-}27$, respectively), indicating that these unimodal distributions did not fit the data well.

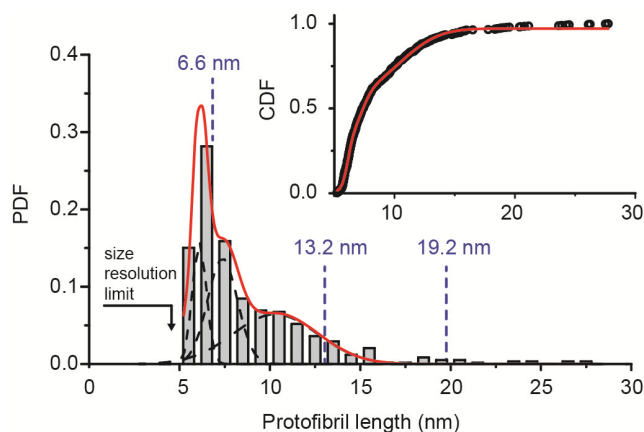


Figure 5.4 | Distributions of estimated lengths of $A\beta_{(1-40)}$ protofibrils in clusters (i) and (ii). The blue dotted lines in the probability density function (PDF) indicate the location of local maxima in the size distributions of $A\beta_{(1-40)}$ predicted by Cabriolu *et al.* (11). The trimodal Gaussian distribution was derived from fitting the empirical distribution shown as black symbols in the inset followed by differentiating the fit to the cumulative distribution. Inset: Empirical cumulative distribution of protofibril lengths (black points) and fit with a trimodal Gaussian cumulative distribution function (red curve). Bootstrap resampling and refitting procedures revealed that the mean and 95% confidence interval for the means of each peak in the PDF were located at lengths of 6.1 (6.06 – 6.13) nm, 7.4 (7.22 – 7.51) nm, and 10.3 (10.16 – 10.40) nm.

To test the robustness of the analysis of the data in Fig. 5.4, we used bootstrap resampling followed by *k-means* clustering and protofibril length estimation. In each resampling iteration, we generated an empirical cumulative distribution and fit it with the trimodal CDF. In each case the fitting procedure returned similar values for the three modes of the distributions as well as the standard deviations (Fig. 5.4).

For comparison, the dotted blue lines in Fig. 5.4 indicate the lengths of protofibrils at which Cabriolu *et al.* observed peaks in the distribution of sizes; these lengths are 6.6, 13.2, and 19.2 nm (11). Kellermayer *et al.* reported segmented growth of

A β protofibrils generated by the 25-35 amino acid portion of A $\beta_{(1-40)}$ that led to protofibril lengths of 6.5, 13.3, 23.2, 32.5, and 40 nm (12, 92). These reports together with the observation of multimodal distribution in Fig. 5.4, suggest that protofibrils of A $\beta_{(1-40)}$ occur in solution with certain preferred lengths corresponding to local minima in the work for fibril formation as reported by Cabriolu *et al.* and Kellermayer *et al.*

Since nanopore-based resistive pulse sensing detects single aggregates, the frequency of translocation events is proportional to the concentration of the aggregates in solution (73, 93-95). Therefore, monitoring the frequency and magnitude of resistive pulses due to A β aggregates has the potential to reveal information on the kinetics of aggregation. The frequency of events is, however, also a function of aggregate diffusion to the pore, and hence, the size and shape of the aggregates. Consequently, a direct comparison between frequencies observed in different clusters is not possible. For instance, for identical concentrations of A β fibers and small A β oligomers, the frequency of fiber translocations would be significantly lower than the frequency of oligomer translocations due to the reduced diffusion constant of large fibers compared to oligomers. Additionally, for long protofibrils and fibers, the frequency of events may be affected by steric and entropic effects that influence “threading” of these rod-like species into the nanopore (70, 96, 97). With these limitations in mind, Fig. 5.5 shows the frequency of translocation events as a function of the aggregation time within each cluster separately. Assuming that the diffusion constant and barriers to entering the nanopore are similar for all aggregates within a cluster, these four plots provide an indication of the changes in the concentration of aggregates in each cluster. For instance, Fig. 5.5 reveals that the frequency of events due to the translocation of large, mature fibers in cluster (iv) increased over three days while the frequency of events due to small spherical oligomers in cluster (i) decreased as expected for time-dependent aggregation of A β (98). Fig 5.5 also shows that the frequency of translocation events of short protofibrils in cluster (ii) remained relatively constant within the error of the measurement. This result is consistent with an intermediate species in a nucleation-dependent process that has reached a steady-state concentration. Combined with the decreasing frequencies observed in cluster (i) and with the increasing frequencies observed in clusters (iii) and (iv), it suggests that the number of aggregates growing large

enough to move into cluster (ii) from cluster (i) was approximately equal to the number of aggregates growing large enough to move from cluster (ii) into cluster (iii) during the three-day aggregation process examined in this work.

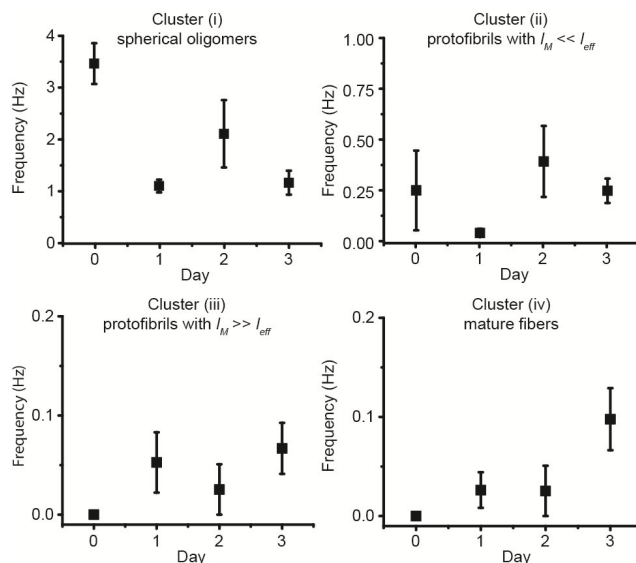


Figure 5.5 | Frequency of translocation events organized by cluster classification reveals time-dependent aggregation. Mean values and standard deviations were calculated by counting the number of translocation events within a given cluster classification during several recordings totaling 40 – 100 s in duration.

5.3 Conclusions

We report the use of nanopores with fluid walls for detecting and characterizing size distributions of unlabeled aggregates of $A\beta_{(1-40)}$ *in situ*. These distributions were obtained by measuring hundreds of single aggregates, making it possible to characterize the large range of $A\beta$ aggregate sizes and shapes. The results from this analysis agree well with those from TEM analysis of the same $A\beta$ preparations and with literature values. Several challenges remain, however, including accurately applying the shape factor, γ , to estimate the distribution of protofibril lengths in clusters (i) and (ii). To improve this analysis it would be helpful to account for possible rotation of short protofibrils with a low aspect ratio while they move through the confining pore as well as the corresponding electric field lines around the molecule (78). Another challenge involves the time and size resolution of the technique; currently, $A\beta$ aggregates smaller

than dodecamers could not be included in the analysis due to resolution limits in ΔI values and t_d values. Reducing the translocation speed of $A\beta_{(1-40)}$ aggregates should improve the determination of ΔI values, reduce the ΔI threshold, and ensure that all t_d values can be determined accurately. Inclusion of lipids in the bilayer coating that preferentially interact with aggregated forms of $A\beta$ such as phosphatidylserine (99) or the ganglioside GM_1 (100, 101) may be one strategy. Another challenge is that the high ionic strength of the recording electrolyte accelerates the aggregation of $A\beta$ (see Section 5-App.S2 and 5-App.S9). Nanopores with smaller dimensions than the pore used here combined with techniques to increase translocation times may ultimately enable the use of electrolyte solutions with physiologic ionic strength in these assays.

Despite these challenges, we show that nanopore-based resistive pulse recordings made it possible to characterize the size and shape of unlabeled aggregates of disease-relevant amyloids in solution. The particular strength of nanopore sensing lies in its ability to characterize a large number of individual aggregates. This capability for single particle analysis is required to characterize $A\beta$ aggregates with a wide-ranging, dynamic heterogeneity in size and shape as well as to correlate cytotoxicity and pathogenic mechanisms with aggregate sizes and shapes (10).

Chapter 5 Appendix

5-App.Methods

Preparation of A β aggregates. We received A β ₍₁₋₄₀₎ peptides in powder form from GL Biochem (Shanghai) Ltd with a purity above 98% as determined by HPLC. To remove aggregates of A β ₍₁₋₄₀₎ and solubilize A β ₍₁₋₄₀₎ in predominantly monomeric form (see Figure 3-App.5), we dissolved the powder in hexafluoroisopropanol (HFIP) to a concentration of 1 mM of A β ₍₁₋₄₀₎ (28). After 24 h incubation in HFIP, we diluted this solution with cold (4 °C) deionized water at a 2:1 (v/v) ratio (H₂O:HFIP). We then rapidly aliquoted the solution, immediately froze it in a liquid nitrogen bath, and lyophilized the frozen aliquots for two days. This procedure removes all HFIP to amounts that are below detectable levels of fluorine-NMR (Section 5-App.S2). To start the aggregation process of A β ₍₁₋₄₀₎ peptides, we dissolved the lyophilized powder in deionized water to a concentration of 1 mg \times mL⁻¹. We incubated these samples in 0.5 mL closed siliconized plastic microcentrifuge tubes (Fisherbrand Low-Retention Siliconized Tubes) on a temperature-controlled shaker (Thermomixer, Eppendorf) set to 750 rpm at a temperature of 22 °C for zero, one, two and three days.

Nanopore-based sensing experiments. To detect aggregates of A β ₍₁₋₄₀₎, we first formed a supported lipid bilayer of 1-palmitoyl-2-oleoyl-*sn*-glycero-3-phosphocholine (POPC) lipids (Avanti Polar Lipids, Inc.) on a nanopore that was 28 nm in diameter and had a length of 18 nm, resulting in a coated diameter of approximately 18 nm and coated length of 28 nm (39). We described details of the bilayer formation in Yusko *et al.* (39). We added solutions containing A β ₍₁₋₄₀₎ to the top solution compartment of the fluidic setup (2 M KCl with 10 mM HEPES pH 7.4) such that the final concentration of A β ₍₁₋₄₀₎ ranged from 0.007 to 0.025 mg \times mL⁻¹. We recorded resistive pulses at an applied potential difference of -0.2 V with the polarity referring to the top fluid compartment relative to the bottom fluid compartment, which was connected to ground. Recordings were completed within 10 to 15 minutes of adding A β ₍₁₋₄₀₎.

We used Ag/AgCl pellet electrodes (Warner Instruments) to monitor ionic currents through electrolyte-filled nanopores with a patch-clamp amplifier (Axopatch 200B, Molecular Devices Inc.) in voltage-clamp mode (*i.e.*, at constant applied voltage). We set the analog low-pass filter of the amplifier to a cutoff frequency of 100 kHz. We

used a digitizer (Digidata 1322) with a sampling frequency of 500 kHz in combination with a program written in LabView to acquire and store data (102). To distinguish resistive pulses reliably from the electrical noise, we first filtered the data digitally with a Gaussian low-pass filter ($f_c = 15$ kHz) in MATLAB and then used a modified form of the custom written MATLAB routine described in Pedone *et al.* (63). We modified the MATLAB routine to calculate the translocation time, t_d , as the width of individual resistive-pulse at half of their peak amplitude, also known as the full-width-half-maximum value (39, 70). From this analysis we obtained the ΔI and t_d values for each resistive pulse.

Preparation of transmission electron microscopy samples. We prepared samples for transmission electron microscopy (TEM) analysis using a negative staining method and glow-discharged, carbon-coated copper grids (Electron Microscopy Sciences, Cat no: FCF-200-Cu). We applied 5 μL of each A β sample ($1 \text{ mg} \times \text{mL}^{-1}$), which had been permitted to aggregate in pure water for zero, one, two, or three days, to the glow-discharged carbon coated copper grid. After 2 min, we wicked the fluid off the grids with filter paper and washed the grids with a 5 μL drop of deionized water for 1 min. After wicking off the fluid again, we applied a 5- μL drop of 2% uranyl acetate for 1 min, wicked off the excess fluid on the grids, and allowed the grids to dry.

5-App.S1. Nanopores without a fluid, lipid coating clog due to adsorption of $A\beta$



Figure 1-App.5 | Nanopores without a fluid, lipid coating clogged after adding $A\beta_{(1-40)}$. Plot of eight concatenated, 20 sec, current versus time traces. The time gap between current traces is not to scale. The elapsed time between adding $A\beta_{(1-40)}$ ($0.025 \text{ mg} \times \text{mL}^{-1}$ in the top solution compartment) and the last current trace is 231 s, and the average time interval between recordings was 15 s. Before adding $A\beta_{(1-40)}$, the current was -52 nA , and after adding $A\beta_{(1-40)}$ the current decreased to $\sim -25 \text{ nA}$. The gradual decrease of the current was due to adsorption of $A\beta$ on the nanopore walls while the stepwise changes in current presumably indicate the adsorption and desorption of large aggregates. Note that after a few seconds, reliable analysis of $A\beta$ aggregates cannot be performed, and after two minutes, no more resistive-pulses can be observed. This experiment proceeded under identical conditions to those reported in the main chapter with the exception that the nanopore was not coated with a lipid bilayer. The $A\beta_{(1-40)}$ sample had been permitted to aggregate in pure water for $\sim 3 \text{ h}$ prior to the experiment. The applied electric potential difference was -0.2 V .

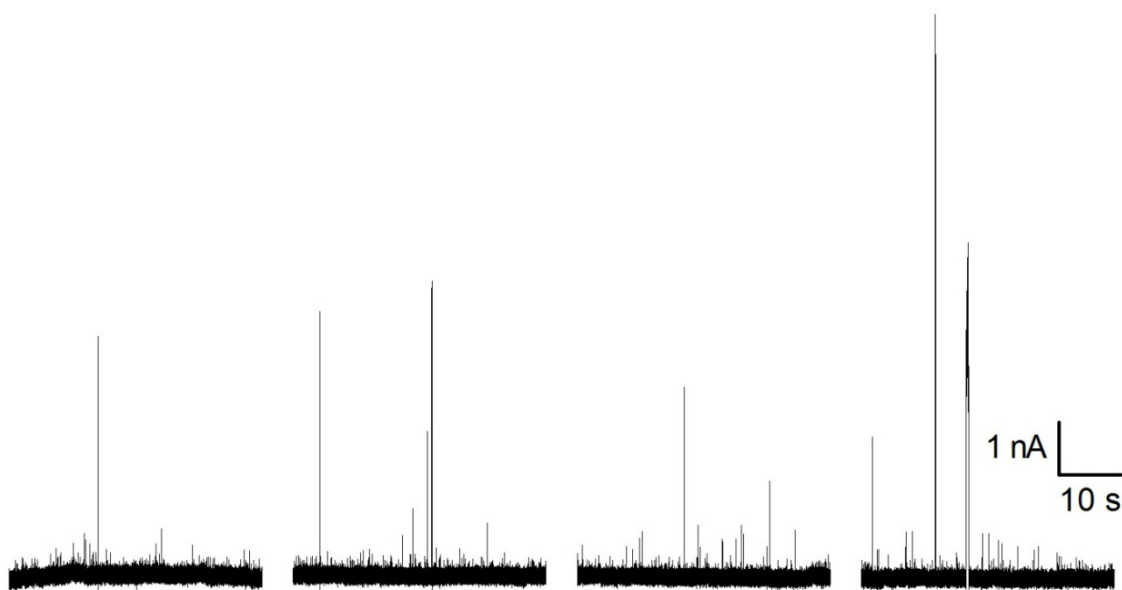


Figure 2-App.5 | Nanopores with a fluid lipid coating do not clog after adding $A\beta_{(1-40)}$, thereby permitting characterization of aggregates. Plot of four concatenated current traces that are each 20 s in duration. The time gap between current traces is not to scale. The elapsed time between adding $A\beta_{(1-40)}$ ($0.0125 \text{ mg} \times \text{mL}^{-1}$ in the top solution compartment) and the last current trace is 180 s. This $A\beta_{(1-40)}$ sample had been permitted to aggregate in pure water for one day prior to the experiment. Bilayer-coated nanopores remain usable for sensing resistive-pulses of $A\beta$ aggregates for at least 1.5 h (39).

5-App.S2. Gel electrophoresis experiments

To confirm that the $A\beta$ preparation used in this work (Section 5-App.Methods) yields starting solutions containing mostly monomeric forms of $A\beta$ as well as to confirm that the $A\beta$ peptides in this preparation aggregated over time, we performed gel electrophoresis experiments followed by Western blotting. We compared three samples of $A\beta$: i) solutions of $A\beta_{(1-40)}$ prepared directly from the powders provided by suppliers, ii) solutions of $A\beta_{(1-40)}$ after treatment with HFIP, subsequent lyophilization and rehydration, and iii) solutions of these HFIP-treated samples after rehydration and aggregation for zero to three days (39). Prior to performing the electrophoresis, we aliquoted $0.5 \text{ }\mu\text{L}$ of $1 \text{ mg} \times \text{mL}^{-1}$ $A\beta_{(1-40)}$ (in pure water) into $38 \text{ }\mu\text{L}$ of pure water or into $38 \text{ }\mu\text{L}$ of 2 M KCl, resulting in an $A\beta_{(1-40)}$ concentration of 0.13 mg mL^{-1} – the same concentration used in the nanopore-based characterization. In order to prevent rearrangements during electrophoretic separation, we immediately cross-linked these

$A\beta_{(1-40)}$ samples by adding 4 μL of 0.688% (v/v) glutaraldehyde in water. After 10 – 20 min at room temperature, we stopped the cross-linking reaction by adding 45 μL of 200 mM Tris buffer. We aliquoted 10 μL of these samples into 20 μL of Native Sample Buffer (Bio-Rad: 62.5 mM Tris-HCl pH 6.8, 40% glycerol, 0.01% Bromophenol Blue), which we modified to also contain 10% (v/v) sodium dodecyl sulfate (SDS) and 0.02 M β -mercaptoethanol. To resolve aggregates of $A\beta_{(1-40)}$ of different molecular weights, we used a polyacrylamide gel: 16.5% Tris-Tricine Ready Gel (Bio-Rad) in Tris-Tricine buffer or a 7.5% Tris-HCl Ready Gel (Bio-Rad) in Tris-Glycine Buffer following standard electrophoresis protocols (103). After running the gels, we transferred proteins to a polyvinylidene fluoride (PVDF) membrane (PerkinElmer Life Science) and blocked the membrane for 1 h with TBS buffer containing 5% (w/v) nonfat dry milk and 0.063% (w/v) Tween-20. We incubated the membrane with a primary antibody against $A\beta_{(1-40)}$ (6E10 from Covance) for 1.5 h. An IgG anti-goat antibody conjugated to horseradish peroxidase served as the secondary antibody and was incubated with the membrane for 1 h. We developed the membrane onto film using enhanced chemiluminescence (ECL, PerkinElmer Life Sciences). Fig. 3-App.5 shows the results of these gel electrophoresis experiments.

Fig. 3A-App.5 confirms that the solubilization procedure with HFIP followed by lyophilization generates aqueous solutions containing mostly monomeric aggregates of $A\beta_{(1-40)}$ as well as some dimeric and trimeric aggregates that are thought to be in rapid equilibrium with the monomeric form (24). We confirmed by Fluorine-NMR that after the two day lyophilization procedure, the solution does not contain detectable amounts of residual HFIP (Fig. 4-App.5). Fig. 3B-App.5 shows the presence of increasingly larger aggregates after one, two, or three days of aggregation time. Fig. 3B-App.5 and 3C-App.5 also show the accelerated aggregation of $A\beta_{(1-40)}$ in the presence of 2 M KCl for \sim 20 min (the shortest possible time for the gel electrophoresis procedure). Regardless of this accelerated aggregation, time-dependent aggregation to higher molecular weight aggregates is apparent by the increasingly darker bands in the wells, where fibers are retained, over time. Additionally, Fig. 3C-App.5 highlights that in the 50 – 250 kDa aggregates increasingly larger aggregates develop between 1 and 3 days of aggregation, eventually resulting in a relatively darker, larger band in the well on Day 3 compared to

Days 1 and 2. This result is important since 50 kDa is approximately the minimum molecular weight of protofibrils and marks the beginning of the transition from spherical oligomers into cylindrical protofibrils (24). We confirmed by TEM analysis that the increased aggregation rate due to the high ionic strength did not affect the morphology of the fibrils (Section 5-App.S9).

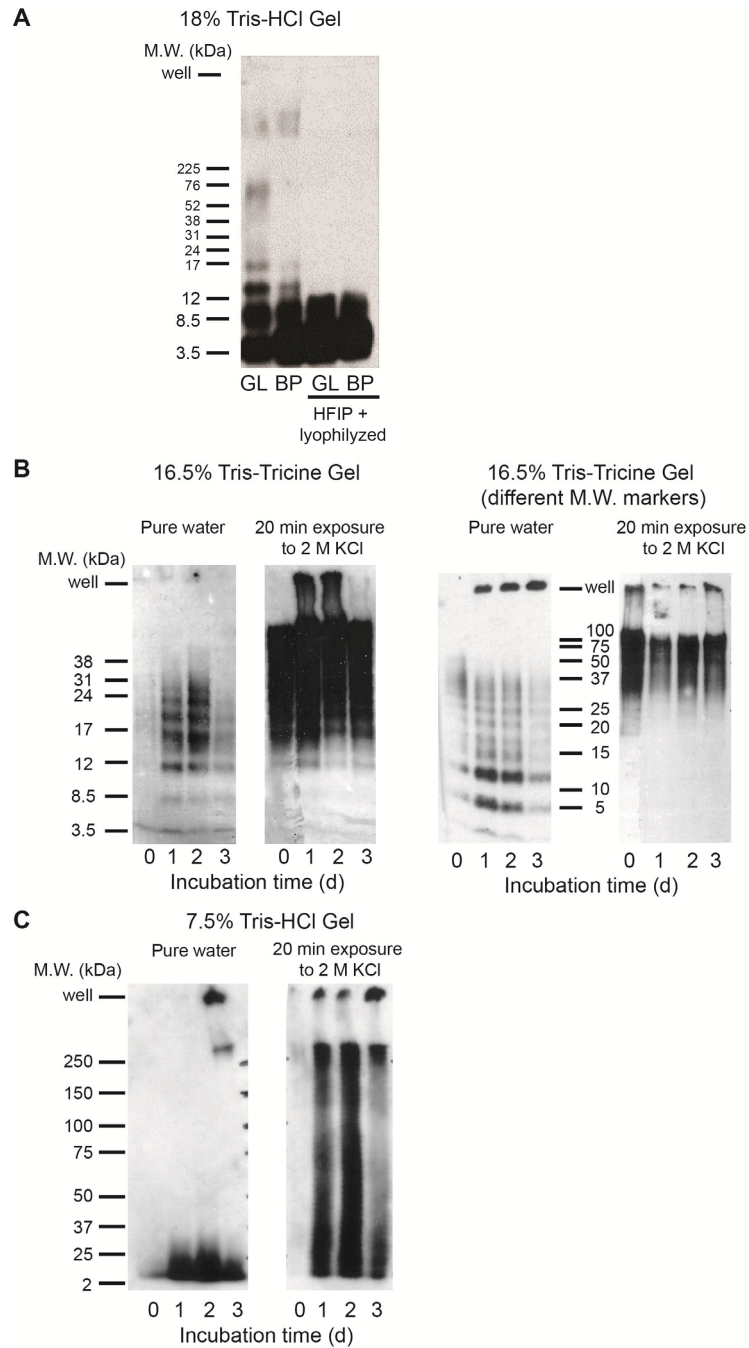


Figure 3-App.5 | SDS-PAGE/Western Blot results showing $A\beta_{(1-40)}$ aggregates in the initial preparation and after aggregation. (A) Aggregates of $A\beta_{(1-40)}$ in the samples from GL = GL Biochem and BP = Biopeptide Inc. before and after treatment with HFIP followed by lyophilization. In this work, we used $A\beta_{(1-40)}$ supplied by GL Biochem (Shanghai). (B) & (C) Aggregates of $A\beta_{(1-40)}$ after incubation times in aqueous solutions of zero, one, two, and three days.

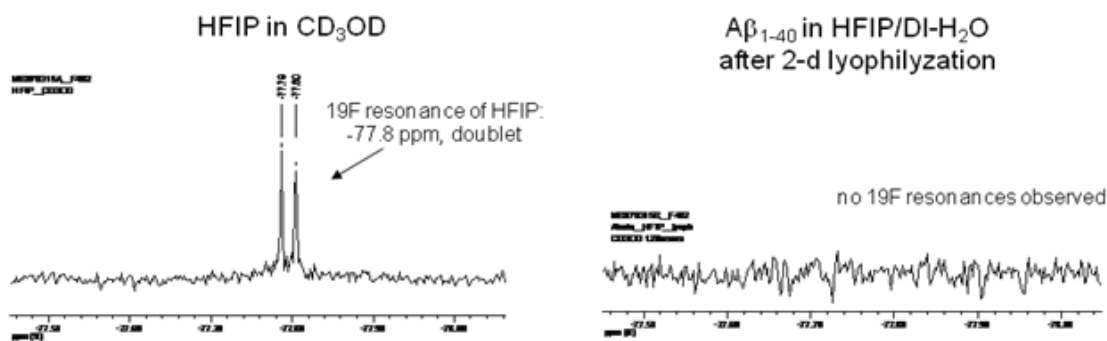


Figure 4-App.5 | ^{19}F -NMR spectroscopy of HFIP in CD_3OD (*left*) and $\text{A}\beta_{1-40}$ sample that was incubated with HFIP and then lyophilized for two days as described in Section 5-App.Methods (*right*). ^{19}F resonance of HFIP gave a doublet at -77.8 ppm, while the peak was absent after $\text{A}\beta$ was lyophilized in HFIP for 48 h.

5-App.S3. Additional characterization of $\text{A}\beta$ preparations by ThT fluorescence assays, circular dichroism spectroscopy and cytotoxicity assays.

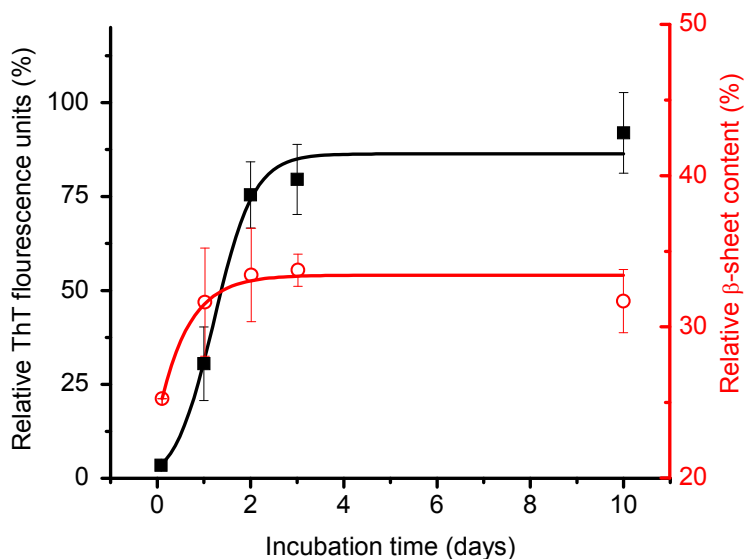


Figure 5-App.5 | Aggregation of $\text{A}\beta_{(1-40)}$ over time, determined by relative intensity of ThT fluorescence (*black*), and the relative β -sheet content as determined from circular dichroism spectra (*red*). Aggregation of $\text{A}\beta$ species is associated with an increase in ThT fluorescence and β -sheet content (10, 13, 23, 90). The solid curves are fits of ThT fluorescence intensity or β -sheet content (y) as a function

of time (t) to a sigmoidal function, $y = A_1 - \frac{A_2}{1 + \exp\left(\frac{t - t_0}{t_1}\right)}$, where A_1 , A_2 , t_0 , t_1 are fitting parameters.

Each point represents an average value from 5-20 experiments for ThT binding assays and from 3-5 experiments for CD experiments.

#

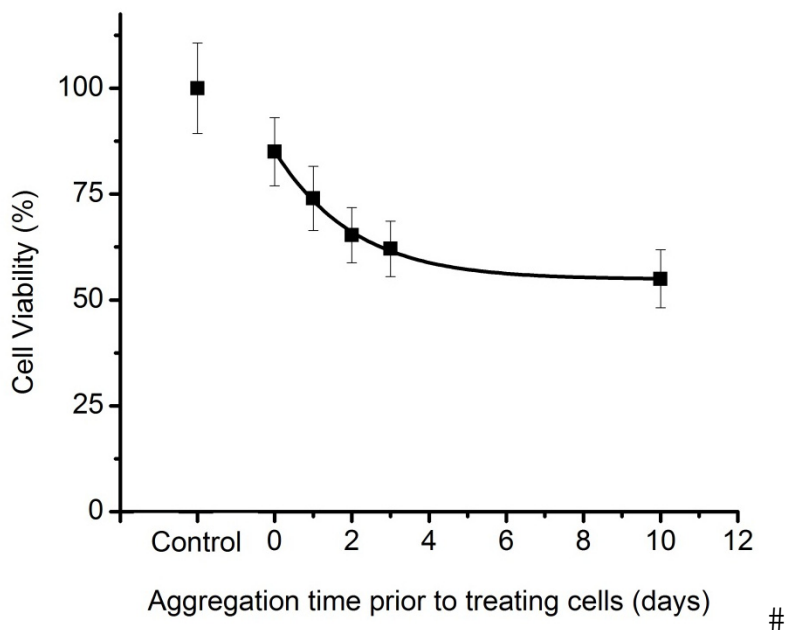


Figure 6-App.5 | Cell viability of human neuroblastoma SH-SY5Y cells after a 24 h exposure to serum-free media containing aggregates of A β that were prepared as described in the methods for various aggregation times. The total concentration of A β was 20 μ M. Cell viability (in %) was measured by MTT assays and averaged over 5 to 15 independent experiments. The curve is the best fit to the data with a standard exponential decay function. The results are in agreement with previous reports (18, 23, 61).

5-App.S4. Bootstrap resampling statistics of the clustering procedure.

To test the robustness of the clustering procedure, we performed bootstrap resampling (83), in which we resampled the original data set with replacement 1000 times. For each resampling iteration, we used the *k-means* algorithm in R (<http://www.R-project.org>) to classify individual points as belonging to one of four clusters. Similar bootstrap resampling techniques combined with cluster analysis are commonly performed in phylogenetics and gene chip experiments in order to comment on the stability of the clusters and provide statistical measures (69, 104). By keeping track of the cluster classification of each point during the 1000 iterations, we were also able to estimate the expected mean ΔI value of each cluster and estimate a 95% confidence interval for the mean values. For each ΔI value, Fig. 7-App.5 plots the probability that a point was classified into a given cluster. During the 1000 iterations, each point was either classified into one or two clusters; a point was never classified into more than two clusters. This procedure revealed that the clustering process was stable and robust: 82% of the measured ΔI values were classified into the same cluster in at least 900 of the 1000 (90%) resampling iterations (i.e. the points above the $F = 0.90$ line in Fig. 7-App.5). In each

resampling and re-clustering iteration, we also calculated the mean value of each cluster. Fig. 7-App.5 shows the distribution of these mean values as histograms and shows that during the resampling methods the mean values of each cluster were well separated and consistent. From this result, we estimated a mean ΔI value and 95% confidence interval for cluster (i) of 373 (333 – 394) pA, for cluster (ii) of 1037 (623 – 1321) pA, for cluster (iii) of 2447 (1470 – 2930), and for cluster (iv) of 4262 (3496 – 4814) pA. This result indicates that differences between mean values are statistically significant at the $\alpha = 0.05$ level. These mean values are less than 8% different from those shown in Table 5.1 of the main chapter, because Table 5.1 lists the mean value of ΔI that we calculated based on the cluster analysis of the original data set (*i.e.* before resampling).

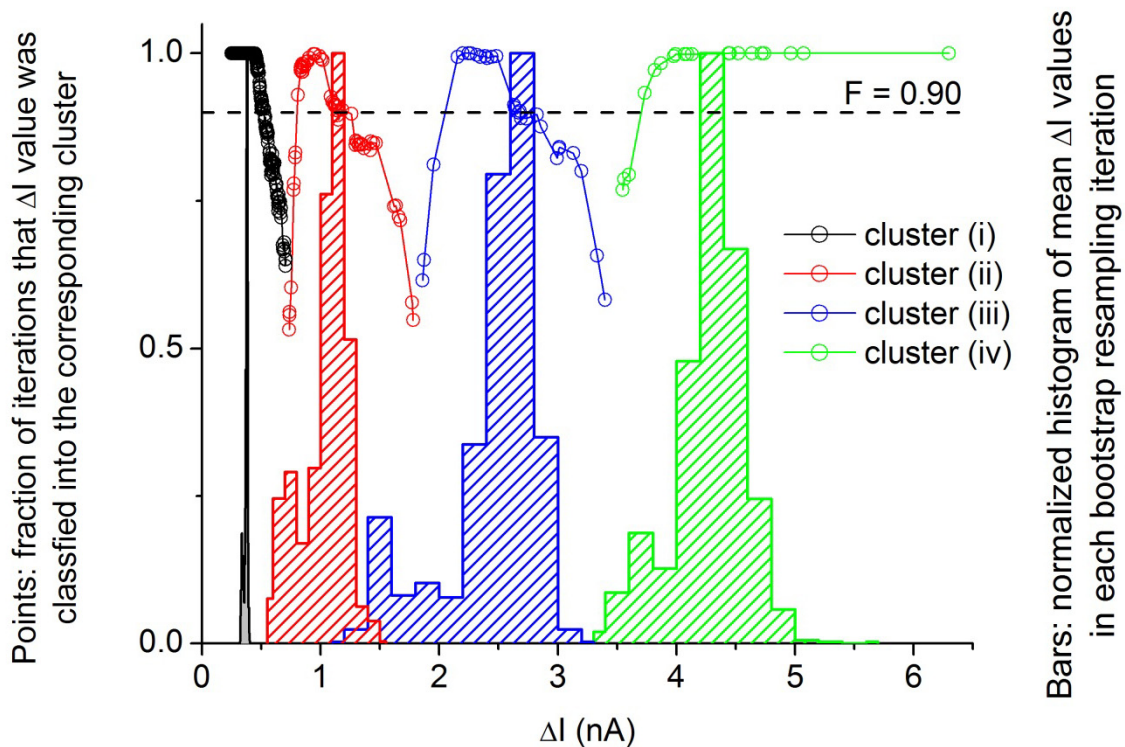


Figure 7-App.5 | Bootstrap resampling and re-clustering iterations reveal the stability of the clusters and the distributions of their mean ΔI values. Points in the plot show individual ΔI values and the corresponding fraction of iterations that the respective point was classified into the same cluster. The bars make up a normalized histogram showing the distribution of mean values of ΔI for each cluster during each bootstrap iteration. The dashed black line indicates the threshold at which a ΔI value was classified into the same cluster in 90% of the sampling iterations; 82% of all points are above this line and were thus classified consistently in at least 900 of the 1000 total sampling iterations.

5-App.S5. $A\beta$ aggregate sizes determined by nanopore-based characterization compared to sizes determined by TEM.

To cross-examine our assumptions and results from the cluster analysis, we applied equation (5.2) to ΔI values from cluster (i) to estimate a cross-sectional area of aggregates in this cluster, and we applied equation (1) to ΔI values from clusters (iii) and (iv) to estimate the excluded volumes of these aggregates; this analysis ignores the requirement for $l_M < L_{eff}$ for equation (5.1) and $l_M > L_{eff}$ for equation (5.2). Finally, we searched the TEM images (Fig. 5.3 in the main chapter and Section 5-App.S9) for aggregates with the sizes predicted by this analysis and did not find aggregates in the TEM images with these sizes or shapes. For instance, if we incorrectly apply equation (5.2) to the data in cluster (i) (i.e. if we enforce that aggregates in cluster (i) have $l_M > L_{eff}$), we obtain cylindrical diameters of 3.5 nm. We did not observe elongated aggregates of $A\beta_{(1-40)}$ with diameters this small in the TEM images, suggesting that aggregates classified in cluster (i) should indeed be approximated as spherical oligomers with equation (5.1) in the main chapter in agreement with the approach that we used. Similarly, if we incorrectly assume that the requirement of $l_M < l_p$ for equation (5.1) was satisfied by the $A\beta$ aggregates represented in clusters (iii) and (iv), we obtained spherical diameters of 11 nm and 13 nm, respectively. We typically did not observe spherical aggregates of $A\beta_{(1-40)}$ with diameters greater than 11 nm in the TEM images (i.e. only 3 out of 347 observed aggregates had spherical diameters of 11 nm or larger), suggesting that the aggregates represented in cluster (iii) are indeed protofibrils and that the aggregates represented in cluster (iv) are indeed fibers longer than the effective length of the nanopore, again in agreement with the approach we used in the main chapter.

These results show that the cluster assignment of translocation events by statistical cluster analysis of ΔI and t_d values of each event yielded diameters and lengths of $A\beta$ aggregates that are consistent with observations by TEM.

5-App.S6. Distributions of t_d values in clusters (i) and (ii)

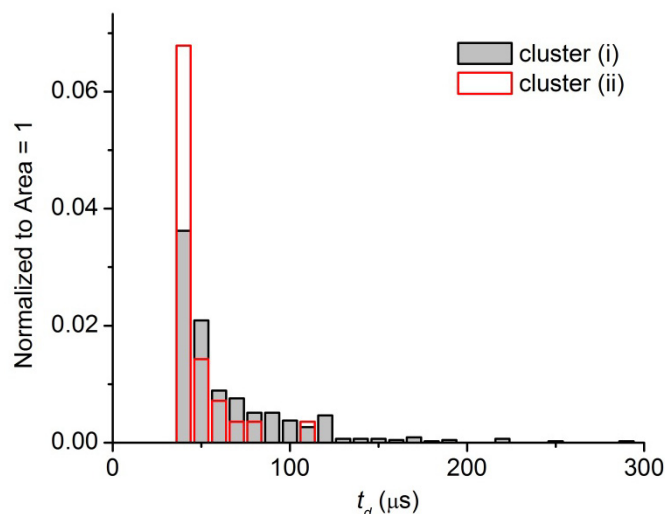


Figure 8-App.5 | Histogram of translocation times of A β aggregates that were classified into clusters (i) and (ii). The width of the bins in the histogram is 10 μs , and the first bin starts at 35 μs since that was the minimum translocation time that could be determined accurately (63). As a result, the complete distribution of translocation times could not be obtained. Using a Kolmogorov-Smirnov test, the difference between the two distributions of t_d values is statistically significantly, $p = 0.028$.

Discussion about the results in Fig. 8-App.5. The observation that almost all translocation events in cluster (ii) had a t_d value between 35 μs and 45 μs compared to the more distributed t_d values in cluster (i) suggests that the aggregates in cluster (ii) had increased electrophoretic mobility (67, 70). The resulting shorter time for translocation through the pore minimized time-dependent diffusional spreading and, therefore, led to a narrower distribution of t_d values compared to events in cluster (i). The reasons for this increased electrophoretic mobility of events in cluster (ii) could be decreased interactions with the lipid bilayer coating (39) or an orientation of the aggregate in the nanopore that reduces viscous drag, such as a prolate or cylinder moving with its long axis parallel to the direction of movement (89). As a third possibility, this result could be due to an increasing charge per aggregate from addition of charged monomers to the growing aggregate, if electrostatic charge regulation is neglected and, we assume spherical aggregates. With the latter two assumptions, the mathematical relationship between the most-probable translocation time, diffusion constant, charge, and molecular weight involves equations (1-App.5) – (3-App.5):

$$|z| = \left| \frac{-3}{4.3 \text{ kDa}} \right| \times N, \quad (1\text{-App.5})$$

$$D = \frac{k_B T}{6\pi\eta \left(\frac{3 \text{ M.W.}}{4\pi A_v \rho} \right)^{1/3}}, \quad (2\text{-App.5})^{(89)}$$

and

$$t_d = \frac{l_p^2 k_B T}{|z| e V_p D} \quad (3\text{-App.5})^{(39)}$$

where, z is the net charge valence of the aggregate, N is the number of monomers in the aggregate, D ($\text{m}^2 \text{ s}^{-1}$) is the diffusion constant of the aggregate, M.W. (kDa) is the molecular weight of the aggregate (i.e. here $4.3 \text{ kDa} \times N$), k_B (J K^{-1}) is Boltzmann's constant, T (K) is the temperature, η (Pa s) is the viscosity of the solution, A_v is Avagadro's number, ρ (kDa m^{-3}) is the molecular weight density of amino acids in a protein, l_p (nm) is the length of the nanopore, e (C) is the elementary charge of an electron, and V_p (V) is the voltage drop across the nanopore. The factor of $-3/4.3\text{kDa}$ in equation (1-App.5) is included to account for the expected net charge per $\text{A}\beta_{(1-40)}$ monomer of -3 and the molecular weight of a monomer of 4.3 kDa (19, 90). By combining equations (1-App.5) – (3-App.5), we solved for t_d as a function of the number of monomers in the aggregate, V_p , and a constant c to yield equation (4-App.5):

$$t_d = \frac{c}{N^{2/3} V_p} \quad (4\text{-App.5})$$

Fig. 9-App.5 shows a plot of equation (4-App.5) and illustrates the trend in most-probable translocation times for aggregates with increasing molecular weight, assuming a constant charge to mass ratio, a constant applied voltage, a spherical aggregate, and an aggregate with a length less than the length of the nanopore. This analysis shows that increasing the number of monomers in a low-molecular weight aggregate could conceivably increase the electrophoretic force more than the viscous drag force, resulting in decreased translocation times that are more narrowly distributed (67, 70) as the aggregates molecular weight, and hence charge, increases. This analysis does not apply to aggregates in clusters (iii) or (iv), since those aggregates have lengths longer than the length of the nanopore.

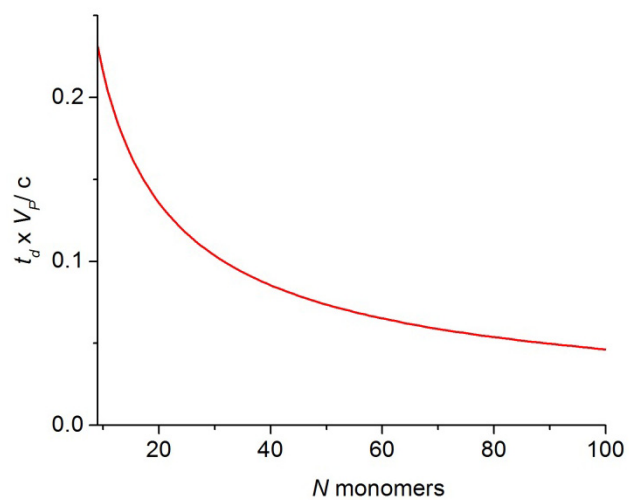


Figure 9-App.5 | Predicted trend in the most-probable translocation time for aggregates with constant charge per molecular weight ratio while neglecting electrostatic charge regulation and assuming a spherical aggregate. This plot is not valid for molecules with varying lengths that are longer than the length of the nanopore.

5-App.S7. Protofibril diameters as a function of their length determined by TEM analysis.

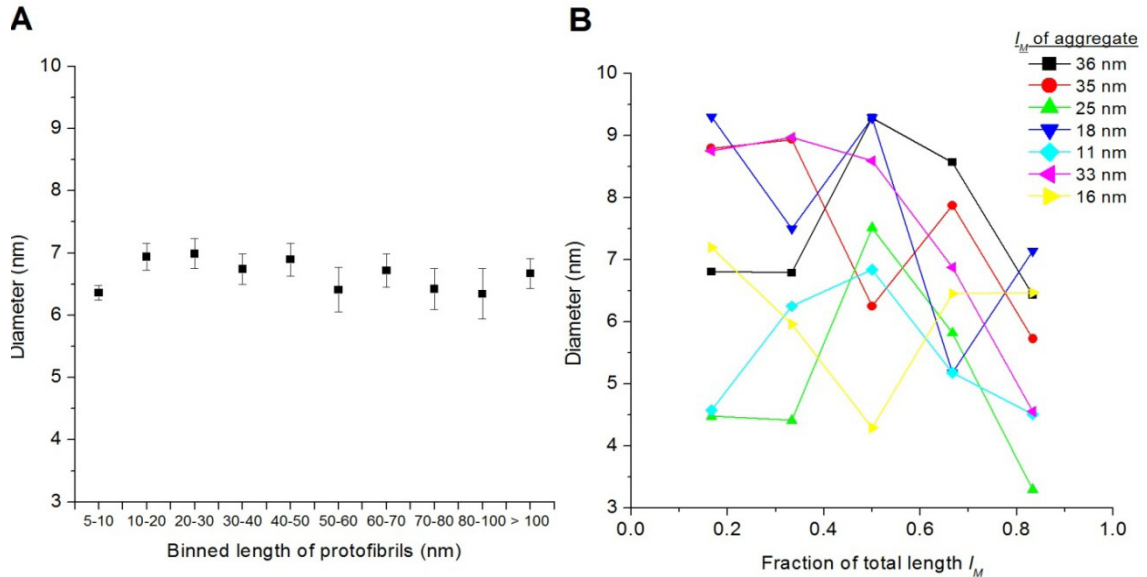


Figure 10-App.5 | Diameter of protofibrils with various lengths (A) and diameter of individual protofibrils at various positions throughout the length of the aggregate as seen in TEM micrographs (B). (A) Mean diameter of protofibrils with various total lengths, l_M , for protofibrils grouped into bins with lengths ranging from 5 nm to greater than 100 nm. Error bars are standard error of the mean. (B) The diameter of seven aggregates measured at five different locations within the length of the aggregate. Note that the diameter remains relatively constant throughout the length of the individual aggregate suggesting that the shape of these protofibrils resembles that of a cylinder more than that of a prolate. Additionally, the difference among population means at each position along an aggregate are not significantly significant at the $\alpha = 0.05$ level.

5-App.S8. Estimation of protofibril lengths

To generate histograms of the lengths of aggregates in clusters (i) and (ii) of the main chapter (Fig. 5.3), we expected that these aggregates were protofibrils elongating with a constant diameter (12) and hence had an area-equivalent cylindrical diameter, θ_c , of 4.4 nm (Table 5.1 in the main chapter). We also expected the aggregates in cluster (i) to be free to rotate in three dimensions, while the protofibrils in cluster (ii) would be oriented with their length, l_M , parallel to the length of the nanopore and hence electric field (55, 85, 88). We defined the excluded volume of an aggregate and the shape factor of an aggregate as a function of its length and solved a system of equations for γ and l_M based on the ΔI value of each translocation event.

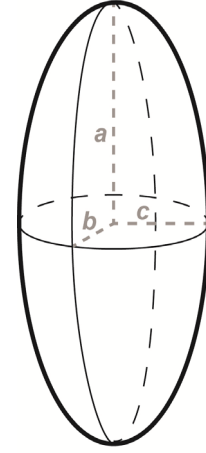


Figure 11-App.5 |
Prolate.

Since TEM analysis (Section 5-App.S5) and data in the literature (12) show that the diameter of protofibrils is constant and independent of length, we defined their excluded volume as the volume of a perfect cylinder:

$$\Lambda = \frac{1}{4} \pi \theta_c l_M \quad (5-App.5)$$

Substituting equation 5-App.5 into equation (5.1) of the main chapter yields ΔI as a function of γ and l_M :

$$\Delta I(\gamma, l_M) = \frac{\gamma V_A \pi \theta_c l_M}{4\rho(l_p + 1.6r_p)^2} \text{ for } l_M < l_{eff} \quad (6-App.5)$$

To estimate a shape factor for this analysis, we used equations derived by Fricke(53, 105) that describe the shape factor of spheroidal prolate particles. A prolate can be described by three dimensions of lengths, a , b , and c (Fig. 11-App.5). For a perfectly ellipsoidal (spheroidal) prolate, $b = c$, and in Cartesian coordinates it is described by $x^2/c^2 + y^2/b^2 + z^2/a^2 = 1$. Equations yielding the same shape factor, but through a different derivation processes that can be extended to non-symmetric spheroids, can be found in reports by Golibersuch, Deblois *et al.*, and Osborn (75-77, 106).

According to Fricke, when the longest axis, a , is parallel to the electric field, the shape factor, γ_{\parallel} , is:

$$\gamma = \left[\frac{m^2}{m^2 - 1} - \frac{m \cosh^{-1}(m)}{(m^2 - 1)^{3/2}} \right]^{-1}, \quad (7\text{-App.5})$$

Where $m = a/b = a/c$ and is greater than 1. Since we define the diameter of the aggregates in this section as $\varnothing_C = 5.6$ nm, we set $m = l_M / \varnothing_C$ and rewrite equation 7-App.5:

$$\gamma_{\parallel} = \left[\frac{(l_M / \varnothing_C)^2}{(l_M / \varnothing_C)^2 - 1} - \frac{(l_M / \varnothing_C) \cosh^{-1}(l_M / \varnothing_C)}{\left((l_M / \varnothing_C)^2 - 1\right)^{3/2}} \right]^{-1}. \quad (8\text{-App.5})$$

For the aggregates in cluster (i), which we assume can rotate in three dimensions, we need to calculate an average shape factor. By considering the shape factor of a prolate with its axis a perpendicular to the electric field:

$$\gamma_{\perp} = \frac{2\gamma_{\parallel}}{2\gamma_{\parallel} - 1}, \quad (9\text{-App.5})$$

the average shape factor for a prolate free to rotate about all axes is (77, 89):

$$\gamma_{AVG} = \frac{1}{3}\gamma_{\parallel} + \frac{2}{3}\gamma_{\perp}. \quad (10\text{-App.5})$$

Finally we solved equations (6-App.5) and (8-App.5)–(10-App.5) using MATLAB to obtain values of γ and l_M for each aggregate in clusters (i) and (ii) based on its ΔI value. The lengths obtained for the aggregates are shown in an empirical cumulative distribution and a histogram in Fig. 5.4 of the main chapter. The values of γ_{AVG} in cluster (i) ranged from 1.5 to 1.57 with an average of 1.52, and in cluster (ii), values of γ_{\parallel} ranged from 1.06 to 1.25 with an average of 1.15. Note that the value of γ_{AVG} for cluster (i) correspond to an aligned prolate with a γ_{\parallel} of 1.25, which is equal to the maximum shape factor observed for the aligned protofibrils in cluster (ii) and that γ_{AVG} is nearly identical to the shape factor of 1.5 commonly used for spherical objects (i.e. the shape factor we used to calculate the excluded volume for cluster (i) in Table 5.1 of the main chapter).

Since the density of observations at 6.1 nm in Fig. 5.4 of the main chapter is high, features of the length distribution beyond ~12-13 nm may be obscured. To overcome this limitation, we also explored empirical cumulative distributions generated only from events classified into cluster (ii) (Fig. 12-App.2). As in the main chapter, we fit the empirical cumulative distribution with a multimodal Gaussian cumulative distribution function (CDF) and confirmed via a Kolmogorov-Smirnov test that the difference between the empirical distribution and the theoretical CDF were not statistically significant ($p = 0.9917$). The empirical distribution and resulting fit to a multimodal CDF, suggest the occurrence of preferred fibril sizes; however, the difference between this empirical distribution and an exponential distribution function was not statistically significant ($p = 0.51$, Fig. 12-App.5). Therefore, although the multimodal fit described the distribution in Fig. 12-App.5 most closely, we could not assign statistical significance to this fit. The multimodal fit to data only in cluster (ii) is therefore only suggestive.

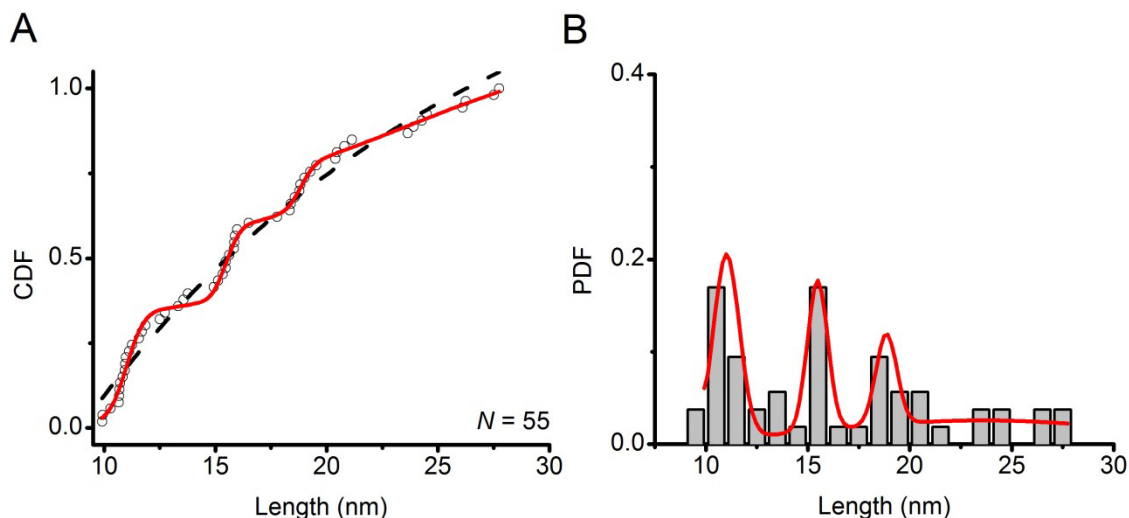


Figure 12-App.5 | Distribution of aggregate lengths in cluster (ii). (A) Empirical distribution of lengths (black circles) fit with a multimodal-Gaussian cumulative distribution function (CDF) (red curve). The multimodal CDF returned 4 modes with values of 11.0, 15.5, 18.9, and 23.6 nm. A Kolmogorov-Smirnov test confirmed that the difference between the resulting theoretical CDF and the empirical distribution was not statistically significant ($p = 0.9917$). The difference between the empirical distribution and an exponential distribution function was, however, also not significantly different from an exponential distribution (black dashed line, $p = 0.51$) while it was significantly different from the normal, extreme value, and Poisson distributions ($p = 4E-48$, $p = 0.001$, and $p = 0.035$). (B) Distribution of lengths shown as a histogram. The red line shows the probability density function (PDF) obtained from the derivative of the theoretical multimodal CDF from the fit in panel A.

We would like to point out one important limitation to the analysis presented previously in this section. The calculation of lengths involved defining the geometry of aggregates in clusters (i) and (ii) as cylindrical (since TEM images revealed that the diameter of many aggregates remained constant independent of length, Section 5-App.S5) while applying the shape factor for a prolate. An alternative approach is to define the shapes and volumes of the aggregates as spheroidal prolates rather than cylinders. The excluded volume of a perfect spheroidal prolate is:

$$\Lambda = \frac{4}{3} \pi b c a$$

or using the parameter symbols in this work

$$\Lambda = \frac{1}{6} \pi \theta_c^2 l_M \tag{11-App.5}$$

Solving the system of equations (5-App.5, 6-App.5, and 8-App.5 – 10-App.5) described above, in which equation (11-App.5) replaces (5-App.5), yields the distribution of lengths shown in Fig. 13-App.5. The value of γ_{AVG} for the aggregates in cluster (i) ranged from 1.56 – 1.64 with an average value of 1.59, and for the aggregates in cluster (ii) γ_{\parallel} ranged from 1.02 to 1.07 with an average value of 1.04. Note that the lengths in this distribution are ~1.5 times the lengths shown in Fig.5.4 of the main chapter. This result is a consequence of the fact that for a prolate and cylinder with the same volume, the prolate will have a length 1.5 times that of the length of the cylinder. The best method probably lies between estimating the volumes of aggregates based on the shape of a cylinder and the shape of a prolate.

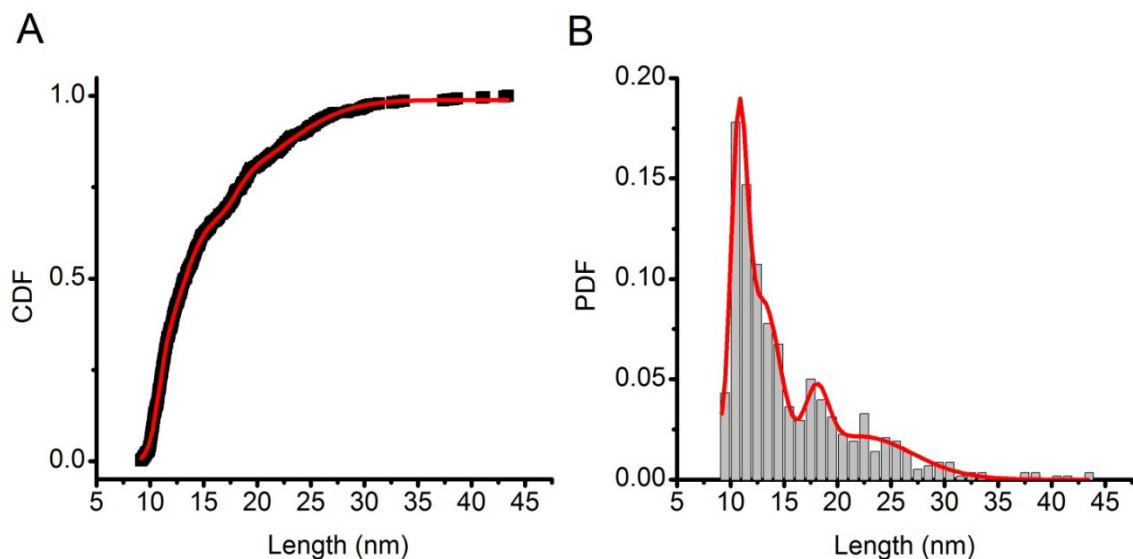


Figure 13-App.5 | Distribution of aggregate lengths in clusters (i) and (ii) when defining their shape and volume as prolate spheroids. (A) Empirical distribution of lengths fit with a multimodal-Gaussian CDF. The multimodal CDF returned 4 modes with values of 10.8, 13.1, 18, and 22.1 nm. A Kolmogorov-Smirnov test confirmed that the resulting theoretical CDF was not significantly different from the empirical distribution ($p = 0.9917$). The empirical distribution was significantly different from the normal, exponential, extreme value, and Poisson distributions ($p = 0$, $p = 0.004$, $p = 0.001$, and $p = 2.2E-32$), indicating that the multimodal fit best described the data. (B) Distribution of lengths shown as a histogram. The red line is the derivative of the theoretical CDF from the fit in panel A.

To summarize this section, we estimated the lengths of aggregates in clusters (i) and (ii) by solving a system of equations including $\gamma(l_M)$ and $\Delta I(\gamma, l_M)$. The resulting lengths and shape factors were dependent on whether the volume of the aggregate was constrained to a cylindrical shape or a prolate spheroid shape. Regardless, this technique reveals the distributions of protofibril length in solution and suggests that the distributions of lengths could have local maxima as predicted by Cabriolu *et al.* (11).

5-App.S9. Preparation of transmission electron microscopy samples

To examine the morphology of aggregates formed in 2 M KCl, we performed a slightly different procedure. We diluted the $1 \text{ mg} \times \text{mL}^{-1}$ sample of $A\beta_{(1-40)}$ to a concentration of 0.05 mg/mL in 2 M KCl. We immediately mixed this solution using a vortex shaker and applied 5 μL of the sample to the glow-discharged carbon coated grids. After 10 min, we wicked off the fluid on the grids with filter paper and washed the grids three times with 5 μL deionized water (1 min each time). After wicking off the fluid again, we applied a 5- μL drop of 2% uranyl acetate for 1 min, wicked off the excess fluid

on the grids, and allowed the grids to dry. We examined the images of negatively stained A β structures using a JEOL 3011 high resolution electron microscope (Jeol Ltd., Tokyo, Japan).

Fig. 14A-App.5 shows several TEM images of A $\beta_{(1-40)}$ aggregates that were first prepared in pure water like all samples in this work and then exposed to 2 M KCl for 10 min. We analyzed the dimensions of the aggregates in the same manner as Fig. 5.3 in the main chapter. For all parameters, the morphology of aggregates that were exposed to 2 M KCl for 10 min, as in the resistive-pulse sensing experiment, was the same as the morphology of aggregates prepared only in pure water (Fig. 5.). Table 1-App.5. summarizes the characterized parameters. For instance, the diameter of protofibrils and fibers were nearly identical between the two preparations. The range of lengths of the protofibrils were similar between the two treatment methods; however, the probability of observing long protofibrils was slightly higher in samples exposed to 2 M KCl (i.e. $P(l_M > 45 \text{ nm})$ on Day 1-2 of $\sim 0.3 - 0.4$) compared to the samples that were not exposed to KCl (i.e. $P(l_M > 45 \text{ nm})$ on Day 1-2 of $\sim 0.15 - 0.2$) (Fig. 5.3C inset in the main chapter and Fig. 14C-App.5 inset). This suggests that brief incubation in solutions with high ionic strengths accelerates the time-dependent aggregation of A β such that the number of A β aggregates increases, which enables the formation of protofibrils with longer lengths than those produced in solutions in low ionic strengths.

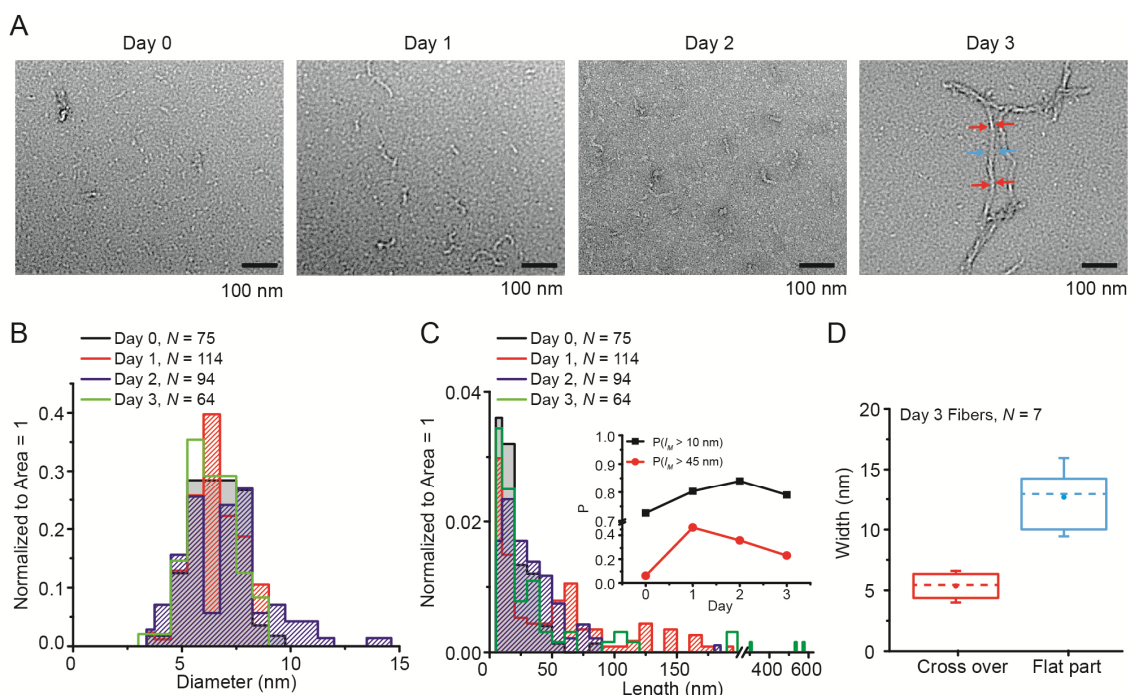


Figure 14-App.5 | Analysis of the size of $A\beta_{(1-40)}$ aggregates seen in micrographs taken with a transmission electron microscope. (A) Micrographs showing aggregates with increasing size after incubation in pure water for 0, 1, 2 and 3 days. (B) & (C) Histograms of the diameters (B) and lengths (C) of all aggregates that were not mature fibers. Inset in C, the proportion of aggregates with lengths longer than 10 nm and 45 nm, the effective length of the nanopore, as a function of aggregation time. (D) Boxplots characterizing the mature fibers that formed after three days of aggregation. The fibers were characterized by their apparent widths when lying flat (blue arrows in A) on the TEM grid and when twisted or crossing over itself (red arrows in A) on the TEM grid (26). The box represents the range between the 1st and 3rd quartiles, the dashed line represents the median, the dot is the mean, and the whiskers extend to the range of the data (minimum and maximum values).

Table 1-App.5. Morphology of $A\beta_{(1-40)}$ aggregates exposed only to pure water and aggregates that were exposed to 2 M KCl for 10 min. Errors are standard deviations from the mean value. All values are not statistically different between the two treatment methods at the $\alpha = 0.05$ level; the *p*-values are shown in the last row of the table.

Treatment	Spherical \emptyset nm	Protofibril \emptyset nm	Fiber x-over W_1 nm	Fiber flat W_2 nm	Distance between x-overs nm
Pure Water	6.2 ± 1.2 $N = 18$	6.3 ± 1.5 $N = 117$	5.6 ± 0.8 $N = 27$	11.5 ± 1.5 $N = 27$	97 ± 27 $N = 27$
10 min exposure to 2M KCl	7.2 ± 1.5 $N = 32$	6.5 ± 1.1 $N = 178$	5.4 ± 1.0 $N = 7$	12.7 ± 2.3 $N = 7$	80 ± 9 $N = 6$
	$p = 0.65$	$p = 0.91$	$p = 0.91$	$p = 0.71$	$p = 0.77$

Chapter 5 References

1. Trojanowski JQ, Mattson MP (2003) Overview of protein aggregation in single, double, and triple neurodegenerative brain amyloidoses. *Neuromol Med* 4(1-2):1-5.
2. Morgado I, Fandrich M (2011) Assembly of alzheimer's a beta peptide into nanostructured amyloid fibrils. *Curr Opin Colloid Interface Sci* 16(6):508-514.
3. Querfurth HW, LaFerla FM (2010) Mechanisms of disease alzheimer's disease. *N Engl J Med* 362(4):329-344.
4. Selkoe DJ (2001) Clearing the brain's amyloid cobwebs. *Neuron* 32(2):177-180.
5. Selkoe DJ (2011) Resolving controversies on the path to alzheimer's therapeutics. *Nat Med* 17(9):1060-1065.
6. Hardy J (2006) A hundred years of alzheimer's disease research. *Neuron* 52(1):3-13.
7. Schnabel J (2011) Little proteins, big clues. *Nature* 475:S12-S14.
8. Ding H, Wong PT, Lee EL, Gafni A, Steel DG (2009) Determination of the oligomer size of amyloidogenic protein beta-amyloid(1-40) by single-molecule spectroscopy. *Biophys J* 97(3):912-921.
9. Johnson RD, Schauerte JA, Wisser KC, Gafni A, Steel DG (2011) Direct observation of single amyloid-beta(1-40) oligomers on live cells: Binding and growth at physiological concentrations. *PLoS One* 6(8).
10. Ono K, Condon MM, Teplow DB (2009) Structure-neurotoxicity relationships of amyloid beta-protein oligomers. *Proc Natl Acad Sci U S A* 106(35):14745-14750.
11. Cabriolu R, Kashchiev D, Auer S (2011) Size distribution of amyloid nanofibrils. *Biophys J* 101(9):2232-2241.
12. Kellermayer MSZ, Karsai Á, Benke M, Soós K, Penke B (2008) Stepwise dynamics of epitaxially growing single amyloid fibrils. *Proc Natl Acad Sci U S A* 105(1):141-144.
13. Journal of Structural Biology Goldsbury CS, *et al.* (2000) Studies on the in vitro assembly of a β 1–40: Implications for the search for a β fibril formation inhibitors. *J Struct Biol* 130(2-3):217-231.
14. Lines RW (1992) The electrical sensing zone method (the Coulter principle). *Particle size analysis*, eds Stanley-Wood NG & Lines RW (The Royal Society of Chemistry, Cambridge), p 352.
15. Demuro A, *et al.* (2005) Calcium dysregulation and membrane disruption as a ubiquitous neurotoxic mechanism of soluble amyloid oligomers. *J Biol Chem* 280(17):17294-17300.
16. Giuffrida ML, *et al.* (2009) Beta-amyloid monomers are neuroprotective. *J Neurosci* 29(34):10582-10587.
17. Hartley DM, *et al.* (1999) Protofibrillar intermediates of amyloid beta-protein induce acute electrophysiological changes and progressive neurotoxicity in cortical neurons. *J Neurosci* 19(20):8876-8884.
18. Bucciantini M, *et al.* (2002) Inherent toxicity of aggregates implies a common mechanism for protein misfolding diseases. *Nature* 416(6880):507-511.
19. Hortschansky P, Schroeckh V, Christopeit T, Zandomenighi G, Fandrich M (2005) The aggregation kinetics of alzheimer's beta-amyloid peptide is controlled by stochastic nucleation. *Protein Sci* 14(7):1753-1759.

20. Zagorski MG, *et al.* (2001) Amyloid abeta-the peptide from hell. *Regulatory Peptides* 97(1):31.
21. Zagorski MG, *et al.* (1999) Methodological and chemical factors affecting amyloid beta peptide amyloidogenicity. *Methods Enzymol* 309:189 - 204.
22. Parihar MS, Hemnani T (2004) Alzheimer's disease pathogenesis and therapeutic interventions. *J Clin Neurosci* 11(5):456-467.
23. Walsh DM, *et al.* (1999) Amyloid beta-protein fibrillogenesis - structure and biological activity of protofibrillar intermediates. *J Biol Chem* 274(36):25945-25952.
24. Jan A, Hartley DM, Lashuel HA (2010) Preparation and characterization of toxic a beta aggregates for structural and functional studies in alzheimer's disease research. *Nat Protoc* 5(6):1186-1209.
25. Roychoudhuri R, Yang M, Hoshi MM, Teplow DB (2009) Amyloid beta-protein assembly and alzheimer disease. *J Biol Chem* 284(8):4749-4753.
26. Schmidt M, *et al.* (2009) Comparison of alzheimer a beta(1-40) and a beta(1-42) amyloid fibrils reveals similar protofilament structures. *Proc Natl Acad Sci U S A* 106(47):19813-19818.
27. Sachse C, Fandrich M, Grigorieff N (2008) Paired beta-sheet structure of an a beta(1-40) amyloid fibril revealed by electron microscopy. *Proc Natl Acad Sci U S A* 105(21):7462-7466.
28. Capone R, *et al.* (2009) Amyloid-beta-induced ion flux in artificial lipid bilayers and neuronal cells: Resolving a controversy. *Neurotox Res* 16(1):1-13.
29. Bitan G, Fradinger EA, Spring SM, Teplow DB (2005) Neurotoxic protein oligomers - what you see is not always what you get. *Amyloid-J Protein Fold Disord* 12(2):88-95.
30. Adamcik J, *et al.* (2010) Understanding amyloid aggregation by statistical analysis of atomic force microscopy images. *Nat Nanotechnol* 5(6):423-428.
31. Meinhardt J, Sachse C, Hortschansky P, Grigorieff N, Fandrich M (2009) A beta(1-40) fibril polymorphism implies diverse interaction patterns in amyloid fibrils. *J Mol Biol* 386(3):869-877.
32. Kremer JJ, Pallitto MM, Sklansky DJ, Murphy RM (2000) Correlation of beta-amyloid aggregate size and hydrophobicity with decreased bilayer fluidity of model membranes. *Biochemistry* 39(33):10309-10318.
33. Chou IH, *et al.* (2008) Nanofluidic biosensing for β -amyloid detection using surface enhanced raman spectroscopy. *Nano Lett* 8(6):1729-1735.
34. Knowles TPJ, *et al.* (2011) Observation of spatial propagation of amyloid assembly from single nuclei. *Proc Natl Acad Sci U S A* 108(36):14746-14751.
35. Schierle GSK, *et al.* (2011) In situ measurements of the formation and morphology of intracellular beta-amyloid fibrils by super-resolution fluorescence imaging. *J Am Chem Soc* 133(33):12902-12905.
36. Wang HY, Ying YL, Li Y, Kraatz HB, Long YT (2011) Nanopore analysis of beta-amyloid peptide aggregation transition induced by small molecules. *Anal Chem* 83(5):1746-1752.
37. Dukes KD, Rodenberg CF, Lammi RK (2008) Monitoring the earliest amyloid-beta oligomers via quantized photobleaching of dye-labeled peptides. *Anal Biochem* 382(1):29-34.

38. Schauerte JA, *et al.* (2010) Simultaneous single-molecule fluorescence and conductivity studies reveal distinct classes of a beta species on lipid bilayers. *Biochemistry* 49(14):3031-3039.
39. Yusko EC, *et al.* (2011) Controlling protein translocation through nanopores with bio-inspired fluid walls. *Nat Nanotechnol* 6(4):253-260.
40. Actis P, *et al.* (2011) Reversible thrombin detection by aptamer functionalized sting sensors. *Biosens Bioelectron* 26(11):4503-4507.
41. Coulter WH (1953) Office USP 2,656,508.
42. Dekker C (2007) Solid-state nanopores. *Nat Nanotechnol* 2(4):209-215.
43. Kowalczyk SW, Blosser TR, Dekker C (2011) Biomimetic nanopores: Learning from and about nature. *Trends in Biotechnology* 29(12):607-614.
44. Howorka S, Siwy Z (2009) Nanopore analytics: Sensing of single molecules. *Chem Soc Rev* 38(8):2360-2384.
45. Majd S, *et al.* (2010) Applications of biological pores in nanomedicine, sensing, and nanoelectronics. *Curr Opin Biotech* 21(4):439-476.
46. Yusko EC, Billeh YN, Yang J, Mayer M (2011) Nanopore recordings to quantify activity-related properties of proteins. *Nanopores: Sensing and fundamental biological interactions*, eds Iqbal SM & Bashir R (Springer Publishing Co., New York), pp 203-225.
47. Stanley-Wood NG, Lines RW (1992) *Particle size analysis* (The Royal Society of Chemistry, Cambridge) p 352.
48. Branton D, *et al.* (2008) The potential and challenges of nanopore sequencing. *Nat Biotechnol* 26(10):1146-1153.
49. Keyser UF (2011) Controlling molecular transport through nanopores. *J R Soc Interface* 8(63):1369-1378.
50. Ivanov AP, *et al.* (2011) DNA tunneling detector embedded in a nanopore. *Nano Lett* 11(1):279-285.
51. Iqbal SM, Bashir R (2009) *Nanoelectronic-based detection for biology and medicine* (Springer-Verlag Berlin, Berlin) pp 1433-1449.
52. Actis P, Jejelowo O, Pourmand N (2010) Ultrasensitive mycotoxin detection by sting sensors. *Biosens Bioelectron* 26(2):333-337.
53. Grover NB, Naaman J, Ben-sasson S, Doljansk F (1969) Electrical sizing of particles in suspensions. I. Theory. *Biophys J* 9(11):1398-1414.
54. Grover NB, Naaman J, Ben-sasson S, Doljansk F, Nadav E (1969) Electrical sizing of particles in suspensions. 2. Experiments with rigid spheres. *Biophys J* 9(11):1415-1425.
55. Solomentsev Y, Anderson JL (1994) Electrophoresis of slender particles. *J Fluid Mech* 279:197-215.
56. Han AP, *et al.* (2008) Label-free detection of single protein molecules and protein-protein interactions using synthetic nanopores. *Anal Chem* 80(12):4651-4658.
57. Sexton LT, *et al.* (2010) An adsorption-based model for pulse duration in resistive-pulse protein sensing. *J Am Chem Soc* 132(19):6755-6763.
58. Cai Q, Ledden B, Krueger E, Golovchenko JA, Li JL (2006) Nanopore sculpting with noble gas ions. *J Appl Phys* 100(2):024914.

59. Li J, *et al.* (2001) Ion-beam sculpting at nanometre length scales. *Nature* 412(6843):166-169.
60. Prangkio P (2011) Investigation of cytotoxicity and ion flux induced by various aggregation states of amyloid-beta peptides. Ph.D. (University of Michigan, Ann Arbor, MI).
61. Horiuchi M, *et al.* (2012) Amyloid beta 1-42 oligomer inhibits myelin sheet formation in vitro. *Neurobiol Aging* 33(3):499-509.
62. Brining SK (1997) Predicting the in vitro toxicity of synthetic beta-amyloid (1-40). *Neurobiol Aging* 18(6):581-589.
63. Pedone D, Firmkes M, Rant U (2009) Data analysis of translocation events in nanopore experiments. *Anal Chem* 81(23):9689-9694.
64. Fologea D, Brandin E, Uplinger J, Branton D, Li J (2007) DNA conformation and base number simultaneously determined in a nanopore. *Electrophoresis* 28(18):3186-3192.
65. Storm AJ, *et al.* (2005) Fast DNA translocation through a solid-state nanopore. *Nano Lett* 5(7):1193-1197.
66. Meller A, Nivon L, Branton D (2001) Voltage-driven DNA translocations through a nanopore. *Physical Review Letters* 86(15):3435-3438.
67. Li JL, Talaga DS (2010) The distribution of DNA translocation times in solid-state nanopores. *J Phys-Condens Matter* 22(45).
68. Rousseeuw PJ, Kaufman L (1990) *Finding groups in data: An introduction to cluster analysis* (John Wiley & Sons, Inc., New York, NY).
69. Kerr MK, Churchill GA (2001) Bootstrapping cluster analysis: Assessing the reliability of conclusions from microarray experiments. *Proceedings of the National Academy of Sciences* 98(16):8961-8965.
70. Talaga DS, Li JL (2009) Single-molecule protein unfolding in solid state nanopores. *J Am Chem Soc* 131(26):9287-9297.
71. Ito T, Sun L, Crooks RM (2003) Simultaneous determination of the size and surface charge of individual nanoparticles using a carbon nanotube-based Coulter counter. *Anal Chem* 75(10):2399-2406.
72. Fologea D, Ledden B, David SM, Li J (2007) Electrical characterization of protein molecules by a solid-state nanopore. *Appl Phys Lett* 91(5):053901.
73. Uram JD, Ke K, Hunt AJ, Mayer M (2006) Submicrometer pore-based characterization and quantification of antibody-virus interactions. *Small* 2(8-9):967-972.
74. Uram JD, Ke K, Hunt AJ, Mayer M (2006) Label-free affinity assays by rapid detection of immune complexes in submicrometer pores. *Angew Chem-Int Edit* 45:2281-2285.
75. DeBlois RW, Uzgiris EE, Cluxton DH, Mazzone HM (1978) Comparative measurements of size and polydispersity of several insect viruses. *Anal Biochem* 90(1):273-288.
76. Golibersuch DC (1973) Observation of aspherical particle rotation in poiseuille flow via the resistance pulse technique. Part 2. Application to fused sphere dumbbells. *J Appl Phys* 44(6):2580-2584.

77. Golibersuch DC (1973) Observation of aspherical particle rotation in poiseuille flow via the resistance pulse technique. Part 1. Application to human erythrocytes. *Biophys J* 13(3):265-280.
78. Kozak D, Anderson W, Vogel R, Trau M (2011) Advances in resistive pulse sensors: Devices bridging the void between molecular and microscopic detection. *Nano Today* 6:531-545.
79. Hille B (2001) *Ion channels of excitable membranes* (Sinauer Associates, Inc., Sunderland) pp 347-349.
80. Lambert MP, *et al.* (1998) Diffusible, nonfibrillar ligands derived from $\alpha\beta 1-42$ are potent central nervous system neurotoxins. *Proc Natl Acad Sci U S A* 95(11):6448-6453.
81. Matthews BW (1968) Solvent content of protein crystals. *J Mol Biol* 33(2):491-&
82. Adler J (2010) *R in a nutshell* (O'Reilly Media, Inc., Sebastopol, CA) p 333.
83. Whitlock MC, Schluter D (2009) *The analysis of biological data* (Roberts and Company Publishers, Greenwood Village, CO) pp 550 - 557.
84. Footnote (
85. Solomentsev Y, Anderson JL (1995) Electrophoretic transport of spheroidal colloids in nonhomogeneous electric fields. *Industrial & Engineering Chemistry Research* 34(10):3231-3238.
86. Wanunu M, Morrison W, Rabin Y, Grosberg AY, Meller A (2010) Electrostatic focusing of unlabelled DNA into nanoscale pores using a salt gradient. *Nat Nanotechnol* 5(2):160-165.
87. Bretherton FP (1962) The motion of rigid particles in a shear flow at low reynolds number. *J Fluid Mech* 14(2):284-304.
88. Ai Y, Qian S (2011) Direct numerical simulation of electrokinetic translocation of a cylindrical particle through a nanopore using a poisson-boltzmann approach. *Electrophoresis* 32(9):996-1005.
89. Berg HC (1993) *Random walks in biology* (Princeton University Press, Princeton, NJ).
90. Guo M, Gorman PM, Rico M, Chakrabartty A, Laurents DV (2005) Charge substitution shows that repulsive electrostatic interactions impede the oligomerization of alzheimer amyloid peptides. *FEBS Lett* 579(17):3574-3578.
91. Footnote2 (
92. Footnote3 (
93. An R, *et al.* (2008) Ultrafast laser fabrication of submicrometer pores in borosilicate glass. *Opt Lett* 33(10):1153-1155.
94. Sun L, Crooks RM (2000) Single carbon nanotube membranes: A well-defined model for studying mass transport through nanoporous materials. *J Am Chem Soc* 122(49):12340-12345.
95. Lee S, Zhang YH, White HS, Harrell CC, Martin CR (2004) Electrophoretic capture and detection of nanoparticles at the opening of a membrane pore using scanning electrochemical microscopy. *Anal Chem* 76(20):6108-6115.
96. Bikwemu R, Wolfe AJ, Xing XJ, Movileanu L (2010) Facilitated translocation of polypeptides through a single nanopore. *J Phys-Condens Matter* 22(45).
97. Bacri L, *et al.* (2011) Dynamics of colloids in single solid-state nanopores. *Journal of Physical Chemistry B* 115(12):2890-2898.

98. Harper JD, Lansbury PT (1997) Models of amyloid seeding in Alzheimer's disease and scrapie: Mechanistic truths and physiological consequences of the time-dependent solubility of amyloid proteins. *Annu Rev Biochem* 66:385-407.
99. Simakova O, Arispe NJ (2007) The cell-selective neurotoxicity of the Alzheimer's A β peptide is determined by surface phosphatidylserine and cytosolic ATP levels. Membrane binding is required for A β toxicity. *J Neurosci* 27(50):13719-13729.
100. Vestergaard M, Hamada T, Takagi M (2008) Using model membranes for the study of amyloid β : Lipid interactions and neurotoxicity. *Biotechnol Bioeng* 99(4):753-763.
101. Williams TL, Serpell LC (2011) Membrane and surface interactions of Alzheimer's A β peptide - insights into the mechanism of cytotoxicity. *FEBS J* 278(20):3905-3917.
102. Uram JD, Ke K, Mayer M (2008) Noise and bandwidth of current recordings from submicrometer pores and nanopores. *ACS Nano* 2(5):857-872.
103. Stine WB, Dahlgren KN, Krafft GA, LaDu MJ (2003) In vitro characterization of conditions for amyloid- β peptide oligomerization and fibrillogenesis. *J Biol Chem* 278(13):11612-11622.
104. Shimodaira H (2002) An approximately unbiased test of phylogenetic tree selection. *Systematic Biology* 51(3):492-508.
105. Fricke H (1953) The electric permittivity of a dilute suspension of membrane-covered ellipsoids. *J Appl Phys* 24(5):644-646.
106. Osborn JA (1945) Demagnetizing factors of the general ellipsoid. *Physical Review* 67(11-1):351-357.

Chapter 6

Determining the Activity of Membrane-Active Enzymes with Lipid-Coated Nanopores

Many lipids in cell membranes serve as chemical messengers in signaling pathways that affect cell proliferation, vesicle trafficking, and meiosis. Enzymes that process lipids in membranes regulate the formation of these lipid messengers, and irregular activity of these membrane-active enzymes is associated with a range of diseases including cancer. Here, we demonstrate the use of nanopores fabricated in silicon nitride for monitoring the activity of these enzymes *in situ*. In this method, a supported lipid bilayer formed on the silicon nitride coats the nanopore and results in a pore-shaped lipid membrane. Since most enzyme-catalyzed reactions on phospholipids change the net charge of the lipid substrate, the activity of these enzymes can change the surface charge on the walls of the bilayer-coated nanopore, and consequently, the concentration of ions in the pore. Hence, this work monitors a change in the conductance of bilayer-coated nanopores to report the activity of membrane-active enzymes. This method is advantageous since the supported lipid bilayer coating is relatively robust compared to suspended planar lipid bilayers and since the reaction proceeds on native lipid bilayers without the presence of detergents. In addition, the method does not require labeled substrates or secondary enzyme reactions.

5.1 Introduction

Various lipids in cell membranes serve as chemical messengers that are involved in regulating proliferation, meiosis, secretion, and intracellular signaling (1-4). Cells employ enzymes to regulate these lipids, including phospholipases that catalyze the hydrolysis of specific ester bonds in phospholipids (*i.e.* phospholipase D, PLD, and phospholipase C, PLC), kinases (*i.e.* diacylglycerol kinase and phosphatidylinositol-3-kinase, PI3K), and phosphatases (*i.e.* phosphate and tensin homolog protein, PTEN). Anomalous function of these membrane-active enzymes is implicated in inflammation, myocardial disease, and cancer (1-4). For instance, PI3K and PTEN are the two most frequently mutated proteins in cancer and are being explored as therapeutic targets for tissue regeneration and preventing cancer (4, 5). Overactive PLD is also thought to be associated with cancer since *in vivo* PLD hydrolyzes phosphatidylcholine lipids (PC) into phosphatidic acid lipids (PA) (Fig. 6.1A), and PA is rapidly converted to diacylglycerol (DAG), a common signaling molecule involved in cell growth (3, 6-8). Due to the role of membrane-active enzymes in diseases and their potential value as therapeutic targets, assays capable of rapidly and quantitatively assessing their activity *in situ*, in real time, and without requiring labels would be useful (9). Realizing assays with these capabilities is difficult, however, because the substrates of membrane-active enzymes are typically the hydrophilic head groups of membrane-associated amphiphilic lipids that expose only their hydrophilic head groups to the aqueous solution (10-12). These enzymes can therefore be classified as interfacial enzymes (13). Established assays for monitoring the activity of interfacial enzymes measure the absorbance, fluorescence, or radioactivity of the enzymatic products, and consequently, often require labeled substrates (3, 10, 14). Other methods employ a secondary enzyme reaction, in which the sensitivity of the assay may be limited by the experimental conditions required for the activity of both enzymes (1, 15). More recently, liquid crystals formed from lipids were used to indicate the presence of active phospholipases by observing changes in the optical properties of the liquid crystal (16-18).

Recently, we described a rapid, label-free, and quantitative method for monitoring membrane-active enzymes *in situ* (9). This method used the single-channel conductance of the pore-forming peptide gramicidin A (gA) in free standing planar lipid bilayers to

report the activity of PLD and PLC based on an enzyme-induced change in the charge of the lipid head groups in a bilayer (9). In solutions with low ionic-strength, changes in the surface charge of a lipid bilayer also change the local concentration of ions near the bilayer, which in turn affects the single-channel conductance of gA pores in the bilayer (9, 19-21). Since gA must be imbedded in a free standing lipid bilayer to measure the flux of ions through individual gA pores, this method is susceptible to the mechanical and thermodynamic instability of planar lipid bilayer experiments (22).

Here, we demonstrate the use of synthetic nanopores that are fabricated in chemically and mechanically robust silicon nitride membranes for monitoring the activity of membrane-active enzymes. The method involves coating the silicon nitride window and the walls of a nanopore in this window with a supported lipid bilayer (Fig. 6.1B) (23). The resulting bilayer-coated nanopore used a synthetic nanopore rather than a fragile biological pore, thereby solving the problem of limited mechanical stability of free standing bilayers by supporting the bilayers on a solid substrate. Enzymatic modification of the charge of the lipid headgroups close to, and inside of, the nanopore changed the concentration of counter ions in the pore and led to a measurable change in the conductance of the nanopore (Fig. 6.1C).

We demonstrate this method by monitoring the activity of phospholipase D. In this case, PLD-mediated hydrolysis of zwitterionic PC lipids to negatively charged PA lipids resulted in the accumulation of PA lipids in the lipid coating of the nanopores, and an increase in the net negative surface charge on the nanopore walls. Consequently, the local concentration of cations in the pore increased, and ultimately, led to a measurable change in the conductance of the nanopore in solutions with low ionic strength. Fig. 6.1 illustrates this concept for PLD-activity in bilayer-coated nanopores.

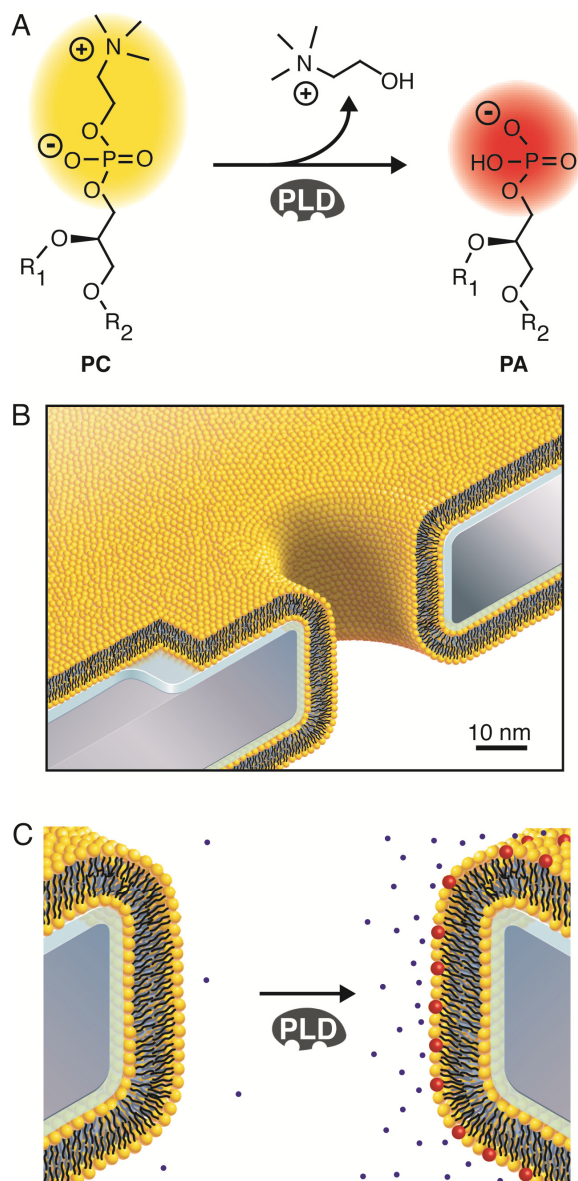


Figure 6.1 | Schematic of PLD-mediated hydrolysis of phosphatidyl choline lipids and illustration of a synthetic, bilayer-coated nanopore for monitoring the activity of phospholipase D. (A) PLD catalyzes the hydrolysis of zwitterionic and electrically neutral phosphatidyl choline lipids (PC), generating a soluble product, choline, and a negatively charged lipid product, phosphatidic acid (PA). **(B)** To scale drawing of a nanopore in a silicon nitride substrate (grey) that supports a lipid bilayer comprised of electrically neutral PC lipids (yellow and black) and an interstitial water layer (blue). **(C)** Schematic of the accumulation of negatively charged PA lipids (red) in the lipid bilayer as a consequence of the activity of PLD on PC lipids. The accumulation of negatively charged PA lipids in the bilayer is associated with the accumulation of positively charged counter ions (blue) near the bilayer and inside the nanopore, leading to a measurable increase in the ionic current through the nanopore.

While biological pores embedded in lipid bilayers have been used to monitor the activity of enzymes (9, 24-27), the work presented here is among the first reports on using synthetic nanopores for monitoring the activity of enzymes (28) and is the first time synthetic nanopores have been used to determine the activity of enzymes quantitatively. Many studies have employed mesoporous substrates to characterize the activity of enzymes in confined volumes, but in most cases the nanopores themselves were not used as a part of the sensing element (29-31). Recently, Mubarak *et al.*, created a hydrogen peroxide sensor by covalently decorating the inner walls of a single synthetic nanopore

with horseradish peroxidase (HRP) (28). In the work by Mubarak *et al.* the ionic current through the nanopore changed in response to the HRP-catalyzed redox reaction between hydrogen peroxide and 2,2'-azino-bis(3-ethylbenzothiazoline-6-sulfonate), in the presence of hydrogen peroxide at concentrations greater than 10 nM. In contrast to that work, the technique presented here uses a lipid-coated nanopore, in which the lipids in the coating are the substrate for the enzyme, while monitoring the change in current through the pore over time to characterize quantitatively and *in situ* the activity of the membrane-active enzyme Phospholipase D.

6.2 Experimental section

We fabricated nanopores in a free-standing silicon nitride membrane, which was supported by a silicon chip, as described previously (32, 33). For each chip, the silicon nitride membrane had a total thickness of 275 ± 15 nm and initially contained one cylindrical channel with a diameter of 100 ± 15 nm (32, 33). One end of the channel was partially closed with the ion-beam sculpting technique to generate a nanopore, and we determined from transmission electron microscopy micrographs that the four cylindrical nanopores used in this work had diameters of 22 – 32 nm and lengths of 14 – 20 nm (dimensions before formation of a lipid bilayer coating). For a schematic of these chips see Yusko *et al.* (34) or Section 2-App.S1. For all experiments, we mounted the silicon chip between two pieces of cured polydimethylsiloxane such that fluidic channels connected to the nanopore Fig. 1.3B (35-37).

We formed the lipid bilayer coating on the silicon nitride membranes *via* vesicle fusion and verified the formation of a fluid supported lipid bilayer by fluorescence recovery after photobleaching experiments in addition to measurements of the electrical resistance of the nanopore (23, 38-40). We prepared the vesicles from 1,2-diphytanoyl-*sn*-glycero-3-phosphocholine (DiPhyPC) or 1-palmitoyl-2-oleoyl-*sn*-glycero-3-phosphocholine lipids (POPC) as described previously (23). When indicated, these vesicles also contained 1,2-dioleoyl-*sn*-glycero-3-phosphate (PA). Since Ca^{2+} is required for the activity of PLD and since the method presented here is sensitive to the ionic strength of the solution, we used a recording electrolyte containing 0.75 mM CaCl_2 with pH ~ 7.0 for all experiments (9, 15). To determine the conductance of the pores, we

recorded ionic currents through the pores at various applied electric potential differences between ± 0.3 V using a patch-clamp amplifier (AxoPatch 200B, Molecular Devices). We averaged the current at each potential difference for 10 s and determined the conductance of each nanopore from the current-voltage relationship as a function of the mole fraction of PA lipids, X_{PA} , in the bilayer coating.

We received PLD isolated from cabbage (EC 3.1.4.4, Sigma Aldrich) as a lyophilized powder and dissolved it to a final activity of 500 units mL^{-1} in a solution containing 0.75 mM CaCl_2 , 0.25 mM KCl, and 1 mM PIPES buffer with a pH of 7.0 ± 0.1 . We aliquoted and stored this solution at -80 °C. According to Sigma Aldrich, 1 unit of PLD liberates 1.0 μmol of choline from L-R-phosphatidylcholine (egg yolk) per hour at a pH of 5.6 and a temperature of 30 °C. The specific activity of this enzyme according to Sigma Aldrich was approximately 1,670 units per milligram of protein. To report the concentration of PLD in molar concentration units, we assumed a pure enzyme and used a molecular weight for PLD of 92 kDa to calculate that a concentration of 6.5 nM corresponds to an activity of 1 unit mL^{-1} (9, 41). During experiments with PLD, we added PLD to the solution on one side of the chip such that the final enzyme concentration ranged from 24 – 95 nM. We measured the ionic current through the pore over time while switching the applied voltage between ± 0.1 V every $\sim 20 - 30$ s, and we calculated the resulting conductance of the pore as a function of time.

6.3 Results and discussion

In order to determine the activity of PLD on PC lipids *in situ*, we determined the ionic conductance of bilayer-coated nanopores as a function of the mole fraction of PA lipids (the lipid product of the PLD-catalyzed reaction) in the bilayer coating. We formed these different bilayer coatings by incorporating increasing mole fractions of PA lipids, X_{PA} , in liposome preparations containing primarily DiPhyPC lipids or POPC lipids, followed by spreading of these liposomes on the silicon nitride chips. Fig. 6.2A shows that the ionic conductance of bilayer-coated nanopores increased with increasing X_{PA} in the DiPhyPC supported bilayer. Assuming the packing density of PA lipids in the bilayer is similar to that of DiPhyPC lipids, the surface charge on the walls of the nanopore increases in a linear fashion with increasing X_{PA} (42). Consequently, we

expected to observe a linear increase in the ionic conductance of bilayer-coated nanopores with increasing X_{PA} (42). Fig. 6.2A confirmed this expectation and shows a linear increase in the conductance, κ (Ω^{-1}), of the nanopore with increasing X_{PA} . This result demonstrates the possibility to monitor changes in the ionic current or conductance through a calibrated bilayer-coated nanopore for calculating the amount of X_{PA} in a lipid bilayer *in situ*.

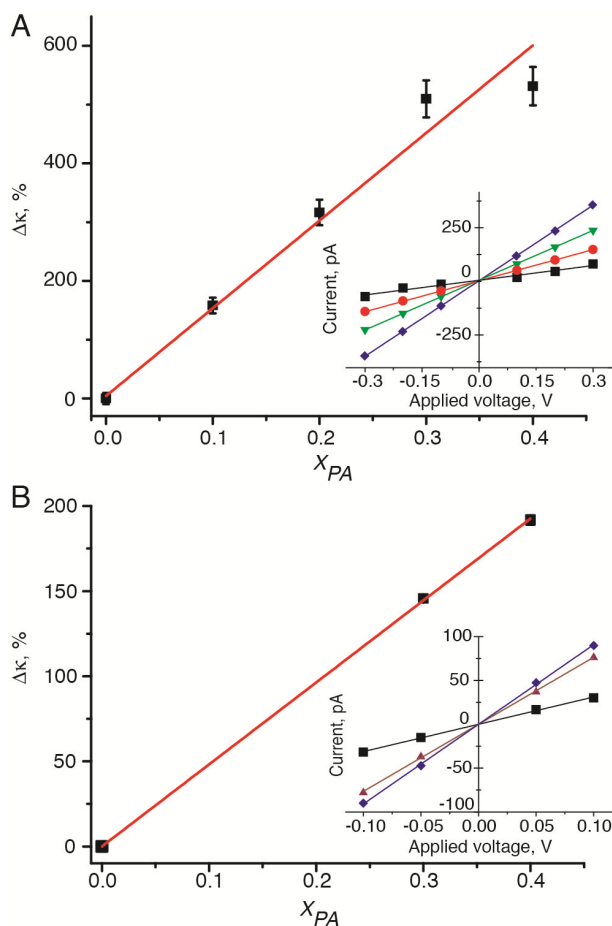


Figure 6.2 | Increase in the conductance of bilayer-coated nanopores as a function of the mole fraction of PA lipids (X_{PA}).

(A) Increase in the conductance of a bilayer-coated nanopore, $\Delta\kappa$, coated with a DiPhyPC bilayer containing increasing X_{PA} . The conductance was calculated from the inverse of the slopes in the current-voltage plots (inset) when the supported lipid bilayer contained 0% (■), 10% (●), 20% (▼), and 40% (◆) PA lipids. (B) $\Delta\kappa$ of a bilayer-coated nanopore that was coated with a POPC bilayer containing increasing X_{PA} . The κ was calculated from the inverse of the slopes in the current-voltage plots (inset) when the supported lipid bilayer contained 0% (■), 30% (▲), and 40% (◆) PA lipids. In both plots, the conductance was normalized to the conductance of the pore when the bilayer coating contained 0% PA lipids, yielding (A) $\Delta\kappa = X_{PA} \times 1510\%$ with a standard error in the slope of $\pm 80\%$ and (B) $\Delta\kappa = X_{PA} \times 482\%$ with a standard error in the slope of $\pm 2\%$.

During formation of the bilayer coating from liposomes of DiPhyPC lipids, we had difficulty washing un-fused liposomes from the surface, and the nanopores frequently clogged during the bilayer formation processes. To avoid these problems, we explored generating bilayer-coated nanopores from spreading liposomes containing POPC lipids instead of DiPhyPC lipids. Liposomes formed from POPC lipids washed away easier and

resulted in fewer clogged pores than when we used the DiPhyPC lipids; consequently, we used liposomes formed from POPC lipids in the remainder of this work. Figure 2B shows the ionic conductance as a function of X_{PA} when the bilayer coating contained primarily POPC lipids. This plot provides a second example of the expected linear increase in the conductance of a bilayer-coated nanopore with increasing X_{PA} and serves as a calibration curve for calculating the amount of X_{PA} in a lipid bilayer, *in situ*, in response to PLD activity.

To monitor the activity of PLD, we formed a supported lipid bilayer from pure POPC lipids on the chip. After determining the initial conductance values, we added PLD to the electrolyte solution on one side of the chip such that the final concentration was 48 nM and monitored the conductance of the pore over time (Fig. 6.3A). The conductance of the nanopore increased after the addition of PLD due to hydrolysis of PC lipids, the subsequent accumulation of PA lipids in the supported lipid bilayer, and the concomitant accumulation of cations near the surface of the lipid bilayer within the nanopore. To calculate X_{PA} in the bilayer as a function of time after adding PLD, we used the calibration method depicted in Fig. 6.2 and shown in equation (6.1):

$$X_{PA} = \frac{\Delta\kappa}{\left(\frac{d\kappa}{dX_{PA}}\right)}, \quad (6.1)$$

where $\Delta\kappa$ (%) is the increase in the conductance and $\frac{d\kappa}{dX_{PA}}$ ($\% \times X_{PA}^{-1}$) is the percentage increase in conductance as a function of X_{PA} (e.g. the slope of the curves shown in Fig. 6.2). For the three pores used to measure the activity of PLD, $\frac{d\kappa}{dX_{PA}}$ was $368 \pm 6 \%$, $455 \pm 14 \%$, and $482 \pm 2 \%$. Using equation (6.1), we calculated X_{PA} from the increase in conductance after addition of PLD and plotted it as a function of time (Fig. 6.3A). To confirm that the increase in the conductance through each nanopore was due to the activity of PLD, we performed a control experiment with thermally denatured PLD obtained by incubating PLD in solution at 90 °C for 1 h. Upon adding 50 nM of this denatured PLD to the electrolyte solution, we observed no increase in the conductance of the pore (Section 6-App.S1). This result proves that the increase in the conductance of

the pore upon the addition of PLD was due to PLD-mediated hydrolysis of PC lipids to PA lipids and not due to the presence of possible contaminants in the enzyme solution.

Since the hydrolysis of PC lipids by PLD activity occurs on the two-dimensional surface of the bilayer and the presence of PA lipids in the membrane increases PLD activity (9, 15, 43), we recently developed a kinetic model to describe the production of PA lipids over time, $X_{PA}(t)$, by the activity of PLD (Section 6-App.S2). This model is shown in equation (6.2) and is based on a kinetic description for catalysis on a surface developed by Verger *et al.* and includes terms to describe the increased activity of PLD with the formation of PA lipids in the bilayer (so-called product activation) (43, 44).

$$X_{PA}(t) = \frac{X_o}{1 + \alpha e^{-Q_m X_o C_{Eo} t}} \quad (6.2)$$

X_o (unitless) is the mole fraction of the product produced at equilibrium; α is an integration constant (unitless); Q_m ($\text{nM}^{-1} \text{min}^{-1}$) is an interfacial quality constant that includes an interfacial Michaelis-Menton constant, the catalytic rate constant; and the affinity of the enzyme for the surface (Section 6-App.S2); and C_{Eo} (M) is the total concentration of the enzyme. The interfacial quality constant Q_m takes into account physicochemical properties of the interface as they pertain to the overall activity of the enzyme; for instance, a higher value of Q_m would indicate a faster overall reaction velocity for a given enzyme and interface compared to a lower value of Q_m (44, 45).

To explore the possibility of measuring the activity of PLD quantitatively, we monitored the conductance of bilayer-coated nanopores after adding several concentrations of PLD and fit the $X_{PA}(t)$ curves with equation (6.2). Fig. 6.3A shows the generation of PA lipids over time for two different concentrations of PLD and the resulting fits of equation (6.1) the data with X_o , Q_m , and α as fitting parameters. Each fit returned similar values for the interfacial quality constant, Q_m , of 0.072, 0.13, 0.047, and 0.061 (mean = 0.078, standard deviation = 0.036). We obtained a similar value of $Q_m = 0.079 \pm 0.015 \text{ nM}^{-1} \text{min}^{-1}$ by fitting all of the data simultaneously in Fig 6.3B, where the x-axis was scaled by $[\text{PLD}] \times \text{time}$. This value is in excellent agreement with the value of Q_m of $0.05 \text{ nM}^{-1} \text{min}^{-1}$ that we reported for studies using lipid membranes composed of PC lipids that spanned micropores and used the conductance of gA as a reporter of X_{PA} . (43). The difference between the value we measured with this technique and gA-based

technique is not statistically significant (p -value = 0.15). Moreover, the value of $Q_m \sim$ of $0.08 \text{ nM}^{-1} \text{ min}^{-1}$ that we determined here is close the value reported for the activity of phospholipase A in a different system of $0.003 \text{ nM}^{-1} \text{ min}^{-1}$ (44, 45). This result demonstrates the quantitative ability of this robust-membrane system for characterizing the activity of membrane active enzymes without labels and relatively simple equipment.

Fig. 6.3A shows two interesting and non-intuitive results, however. The first result is that the mole fraction of PA lipids does not approach 1.0 at equilibrium; rather it reached a value of $X_o \sim 0.18 \pm 0.03$. The second puzzling result is that the highest concentration of PLD did not generate the highest mole fraction of PA lipids. These two results may be related and may indicate the sequestration of PLD enzyme from PC lipids. For instance, PA lipids are known to form lipid domains composed primarily of PA lipids in the presence of Ca^{++} (15), and since, PLD has a higher affinity for negatively charged membranes than for neutral membranes (15), the presence of PA-rich domains could sequester PLD from PC lipids, thereby reducing the reaction velocity. Moreover, according to the Adair equation (46), PLD can also catalyze the reverse reaction of PC lipids to PA lipids under certain conditions, and in these PA-rich domains the local concentration of PA lipids would be high while the local concentration of PC lipids would be low, thereby creating conditions more favorable toward the reverse reaction. We note, however, that an alternative interpretation of the X_o parameter, independent of an enzyme sequestration model, would be that the value of X_o represents the maximum density of lipid product that the lipid bilayer would support (9, 45).

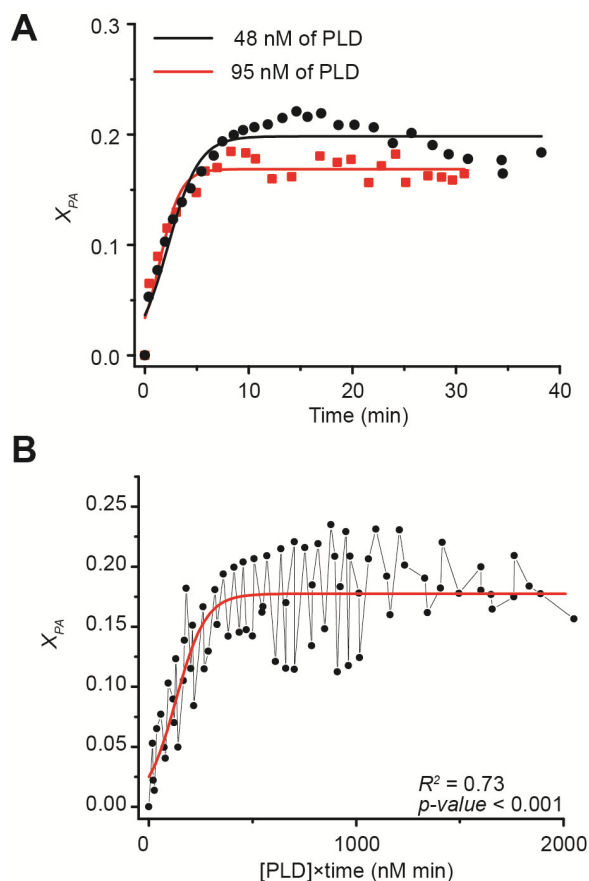


Figure 6.3 | Mole fraction of PA in the supported lipid bilayer, X_{PA} , as a function of time after addition of PLD (A) Time-dependent change in X_{PA} nanopores coated with supported lipid bilayers of PC lipids after the addition of 48 nM (●) and 95 nM (■) PLD. Data was with equation (6.2). (B) Data from all experiments with concentrations of PLD ranging from 24 nM to 95 nM plotted against an x-axis scaled by [PLD] × time.

6.4 Conclusion

The method presented here builds on a previously reported assay for monitoring the activity of membrane-active enzymes and demonstrates the first time solid-state nanopores have been used to monitor the activity of an enzyme. Here, we combined solid-state nanopores fabricated in silicon nitride with supported lipid bilayers to form pore-shaped membranes. These supported lipid membranes are more robust to thermodynamic and mechanical instabilities compared to the planar lipid bilayers used previously. Consequently, this work addresses a primary limitation of gA-based sensing of membrane-active enzymes. Furthermore, the method presented measures the steady-state ionic current through the nanopore over tens of seconds and does not require electronics with fast time resolution. Thus, it requires relatively simple electronics and, as a result, could potentially be incorporated into commercial devices for rapidly detecting and quantifying the activity of membrane-active enzymes. Finally, since this method takes advantage of a change in the net charge of a lipid upon an enzymatic reaction it should be applicable for detecting the activity of a wide range of membrane-active

enzymes. For example, all of the enzymes mentioned at the beginning of this work will yield a lipid product with a net charge different from the initial lipid substrate.

This work also presented the non-obvious result that higher enzyme concentrations did not necessarily generate more product due the possibility of product activation followed by product inhibition. Thus, a thorough and quantitative investigation of the interfacial kinetics is required to understand the activity of PLD and possibly develop models to describe the unique kinetic behavior of membrane-active enzymes.

Chapter 6 Appendix

6-App.S1 Control experiment with denatured phospholipase D

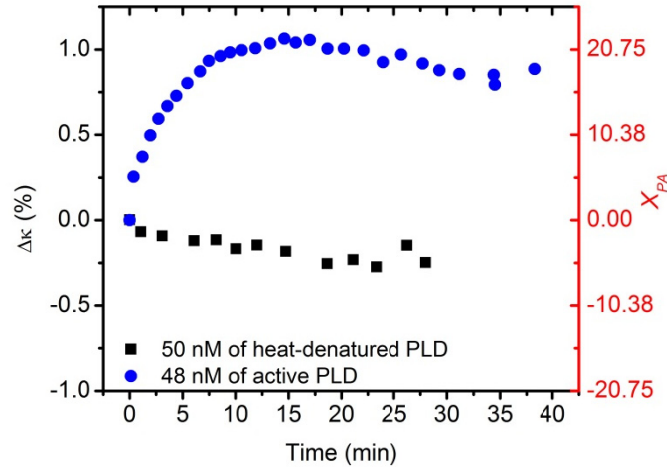


Figure 1-App.6 | Control experiment comparing the conductance of a nanopore after the addition of active PLD to the conductance of a nanopore after the addition of heat-denatured PLD. PLD was denatured by maintaining a solution containing PLD at 90 °C for 30 min. Note that when PLD was not active, there was no increase in the conductance of the nanopore, indicating that PA lipids were not produced in the membrane.

6-App.S2 Kinetic model for phospholipase D activity

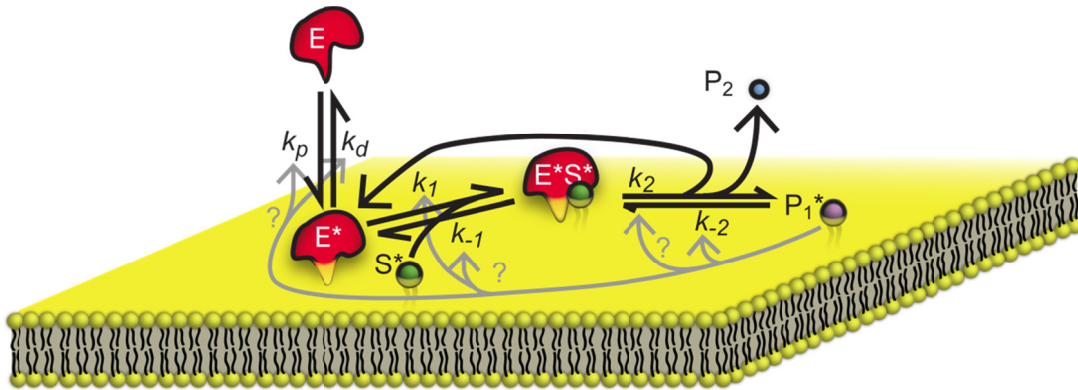


Figure 2-App.6 | Schematic of the kinetic model based on a model by Verger *et al.* with additional considerations for the effects of product activation or product inhibition.

Fig. 2-App.6 illustrates the various steps required for interfacial enzyme catalysis and their rate constants. Verger *et al.* has constructed a general model for this scenario, equation (1-App.6) (9, 43-45):

$$\frac{d\Gamma_P}{dt} = \frac{k_2 \Gamma_S C_{Eo}}{K_M^* \frac{k_d}{k_p} + (K_M^* + \Gamma_S) \frac{A}{V}} \quad \text{(1-App.6)}$$

Γ_P (# m⁻²) is the density of the product created on the surface, k_2 (min⁻¹) is the catalytic rate constant, Γ_S (# m⁻²) is the density of the available substrate on the surface, C_{Eo} (# m⁻³) is the total concentration of enzyme, K_M^* (# m⁻²) is the interfacial Michaelis-Menten constants (i.e. $K_M^* = (k_2 + k_{-1}) / k_1$ and k_1 is the association rate constant for the enzyme-substrate complex and k_{-1} is the corresponding dissociation rate constant), k_p (m min⁻¹) is the adsorption rate constant to the surface, k_d (min⁻¹) is the desorption rate constant from the surface, A (m²) is the surface area at the water-bilayer interface, and V (m³) is the volume of the aqueous phase.

Assuming that the surface area to volume ratios is negligible that the fraction of enzymes able to penetrate into the bilayer is small, we can ignore the second term in the denominator to write equation (2-App.6) (44):

$$\frac{d\Gamma_P}{dt} = \frac{k_2 \Gamma_S C_{Eo}}{K_M^* \frac{k_d}{k_p}} = Q_m \Gamma_S C_{Eo} \quad \text{(2-App.6)}$$

In equation (2-App.6) we introduced the parameter, Q_m , which is the interfacial quality

constant and equal to $\frac{k_2}{K_M^* \frac{k_d}{k_p}}$.

The models shown in (1-App.6 and 2-App.6), however, do not account for the increased activity of PLD enzymes in the presence of negative charged lipids such as PA. Therefore, we developed a simple model to account for this product activation (43):

$$\frac{d\Gamma_P}{dt} = Q_m (\Gamma_o - \Gamma_P) \Gamma_P C_{Eo} \quad \text{(3-App.6)}$$

where Γ_o (# m⁻²) is the total available substrate in the lipid bilayer and $\Gamma_o = \Gamma_S + \Gamma_P$. We can rewrite equation (3-App.6) in terms of mole fraction of lipids by assuming that the average area per lipid is not affected by the formation of the product lipid (i.e. a different mole fraction of X_{PC} vs. X_{PA}). Equation (6.1) in the main chapter shows the integrated solution to equation (3-App.6) based on these assumptions and the work outlined by Majd *et al.* (43).

Chapter 6 References

1. Brown HA, Henage LG, Preininger AM, Xiang Y, Exton JH (2007) *Lipidomics and bioactive lipids: Lipids and cell signaling*, ed Brown HA (Academic Press), Vol 434, pp 49 - 87
2. Huang P, Frohman MA (2007) The potential for phospholipase D as a new therapeutic target. *Expert Opin Ther Targets* 11(5):707-716.
3. Scott SA, *et al.* (2009) Design of isoform-selective phospholipase D inhibitors that modulate cancer cell invasiveness. *Nat Chem Biol* 5(2):108-117.
4. Chalhoub N, Baker SJ (2009) PTEN and the PI3-kinase pathway in cancer. *Annual Review of Pathology-Mechanisms of Disease* 4:127-150.
5. Liu K, *et al.* (2010) PTEN deletion enhances the regenerative ability of adult corticospinal neurons. *Nat Neurosci* 13(9):1075-1081.
6. Bocckino SB, Blackmore PF, Wilson PB, Exton JH (1987) Phosphatidate accumulation in hormone-treated hepatocytes via a phospholipase D mechanism. *J Biol Chem* 262(31):15309-15315.
7. Bocckino SB, Wilson PB, Exton JH (1987) Ca²⁺-mobilizing hormones elicit phosphatidylethanol accumulation via phospholipase D activation. *FEBS Letters* 225(1-2):201-204.
8. Hodgkin MN, *et al.* (1998) Diacylglycerols and phosphatidates: Which molecular species are intracellular messengers? *Trends in Biochemical Sciences* 23(6):200-204.
9. Majd S, Yusko EC, MacBriar AD, Yang J, Mayer M (2009) Gramicidin pores report the activity of membrane-active enzymes. *J Am Chem Soc* 131(44):16119-16126.
10. Volwerk JJ, Filthuth E, Griffith OH, Jain MK (1994) Phosphatidylinositol-specific phospholipase-c from bacillus-cereus at the lipid-water interface - interfacial binding, catalysis, and activation. *Biochemistry* 33(12):3464-3474.
11. Deems RA, Eaton BR, Dennis EA (1975) Kinetic-analysis of phospholipase-a₂ activity toward mixed micelles and its implications for study of lipolytic enzymes. *J Biol Chem* 250(23):9013-9020.
12. Jain MK, Berg OG (1989) The kinetics of interfacial catalysis by phospholipase-a₂ and regulation of interfacial activation - hopping versus scooting. *Biochimica Et Biophysica Acta* 1002(2):127-156.
13. Berg OG, Jain MK (2002) *Interfacial enzyme kinetics* (John Wiley & Sons, Ltd., West Sussex, England) p 297.
14. Bayburt T, *et al.* (1995) Continuous, vesicle-based fluorometric assays of 14- and 85-kda phospholipases a₂. *Anal Biochem* 232(1):7-23.
15. Kuppe K, Kerth A, Blume A, Ulbrich-Hofmann R (2008) Calcium-induced membrane microdomains trigger plant phospholipase d activity. *ChemBioChem* 9(17):2853-2859.
16. Brake JM, Daschner MK, Luk YY, Abbott NL (2003) Biomolecular interactions at phospholipid-decorated surfaces of liquid crystals. *Science* 302(5653):2094-2097.
17. Hartono D, Bi XY, Yang KL, Yung LYL (2008) An air-supported liquid crystal system for real-time and label-free characterization of phospholipases and their inhibitors. *Adv Funct Mater* 18(19):2938-2945.

18. Hartono D, Lai SL, Yang KL, Yung LYL (2009) A liquid crystal-based sensor for real-time and label-free identification of phospholipase-like toxins and their inhibitors. *Biosens Bioelectron* 24(7):2289-2293.
19. Capone R, Blake S, Restrepo MR, Yang J, Mayer M (2007) Designing nanosensors based on charged derivatives of gramicidin a. *Journal of the American Chemical Society* 129(31):9737-9745.
20. Apell HJ, Bamberg E, Lauger P (1979) Effects of surface-charge on the conductance of the gramicidin channel. *Biochimica Et Biophysica Acta* 552(3):369-378.
21. Andersen OS, Koeppe RE, Roux B (2005) Gramicidin channels. *IEEE Trans Nanobiosci* 4(1):10-20.
22. Majd S, *et al.* (2010) Applications of biological pores in nanomedicine, sensing, and nanoelectronics. *Curr Opin Biotech* 21(4):439-476.
23. Yusko EC, *et al.* (2011) Controlling protein translocation through nanopores with bio-inspired fluid walls. *Nature Nanotech.*
24. Deamer D (2010) Nanopore analysis of nucleic acids bound to exonucleases and polymerases. *Annual review of biophysics, vol 39*, Annual review of biophysics, (Annual Reviews, Palo Alto), Vol 39, pp 79-90.
25. Zhao QT, de Zoysa RSS, Wang DQ, Jayawardhana DA, Guan XY (2009) Real-time monitoring of peptide cleavage using a nanopore probe. *Journal of the American Chemical Society* 131(18):6324-6325.
26. Benner S, *et al.* (2007) Sequence-specific detection of individual DNA polymerase complexes in real time using a nanopore. *Nat Nanotechnol* 2(11):718-724.
27. Clarke J, *et al.* (2009) Continuous base identification for single-molecule nanopore DNA sequencing. *Nat Nanotechnol* 4(4):265-270.
28. Ali M, *et al.* (2011) Hydrogen peroxide sensing with horseradish peroxidase-modified polymer single conical nanochannels. *Analytical Chemistry:ASAP.*
29. Dai ZH, Bao HC, Yang XD, Ju HX (2008) A bienzyme channeling glucose sensor with a wide concentration range based on co-entrapment of enzymes in sba-15 mesopores. *Biosens Bioelectron* 23(7):1070-1076.
30. Matsuo T, *et al.* (2009) Meso-unsubstituted iron corrole in hemoproteins: Remarkable differences in effects on peroxidase activities between myoglobin and horseradish peroxidase. *Journal of the American Chemical Society* 131(42):15124-+.
31. Zhu AW, Tian Y, Liu HQ, Luo YP (2009) Nanoporous gold film encapsulating cytochrome c for the fabrication of a h2o2 biosensor. *Biomaterials* 30(18):3183-3188.
32. Cai Q, Ledden B, Krueger E, Golovchenko JA, Li JL (2006) Nanopore sculpting with noble gas ions. *J Appl Phys* 100(2):024914.
33. Li J, *et al.* (2001) Ion-beam sculpting at nanometre length scales. *Nature* 412(6843):166-169.
34. Yusko EC, *et al.* (2011) Controlling protein translocation through nanopores with bio-inspired fluid walls. *Nature Nanotechnology* in press.

35. Uram JD, Ke K, Hunt AJ, Mayer M (2006) Label-free affinity assays by rapid detection of immune complexes in submicrometer pores. *Angew Chem-Int Edit* 45:2281-2285.
36. Yusko EC, An R, Mayer M (2010) Electroosmotic flow can generate ion current rectification in nano- and micropores. *ACS Nano* 4(1):477-487.
37. Uram JD, Ke K, Hunt AJ, Mayer M (2006) Label-free affinity assays by rapid detection of immune complexes in submicrometer pores. *Angewandte Chemie-International Edition* 45(14):2281-2285.
38. Watts TH, Brian AA, Kappler JW, Marrack P, McConnell HM (1984) Antigen presentation by supported planar membranes containing affinity-purified i-a^d. *Proc Natl Acad Sci U S A* 81(23):7564-7568.
39. Cremer PS, Boxer SG (1999) Formation and spreading of lipid bilayers on planar glass supports. *Journal of Physical Chemistry B* 103(13):2554-2559.
40. Reimhult E, Hook F, Kasemo B (2003) Intact vesicle adsorption and supported biomembrane formation from vesicles in solution: Influence of surface chemistry, vesicle size, temperature, and osmotic pressure. *Langmuir* 19(5):1681-1691.
41. Younus H, *et al.* (2003) Proteolytic sensitivity of a recombinant phospholipase D from cabbage: Identification of loop regions and conformational changes. *J Protein Chem* 22(6):499-508.
42. Vlassioug I, Smirnov S, Siwy Z (2008) Ionic selectivity of single nanochannels. *Nano Lett* 8(7):1978-1985.
43. Majd S, Yusko EC, Yang J, Sept D, Mayer M (2012) Interfacial kinetic analysis of phospholipase d activity on long-chain lipids in planar bilayers. *Submitted*.
44. Panaiotov I, Ivanova M, Verger R (1997) Interfacial and temporal organization of enzymatic lipolysis. *Current Opinion in Colloid & Interface Science* 2(5):517-525.
45. Verger R, De Haas GH (1976) Interfacial enzyme kinetics of lipolysis. *Annual Review of Biophysics and Bioengineering* 5(1):77-117.
46. Fersht A (1999) *Structure and mechanism in protein science: A guide to enzyme catalysis and protein folding* (W. H. Freeman and Company, New York, NY).

Chapter 7

Concluding Remarks and Suggestions

The work presented in this thesis introduced the concept of nanopores with fluid walls and demonstrated their enabling properties for characterizing proteins and peptides. We realized these fluid walls by taking advantage of the self-assembly of lipids to form a supported lipid bilayer coating on the synthetic surfaces of the nanopore and surrounding substrate. These multifunctional, fluid coatings addressed in some way all of the major challenges that were preventing further development of nanopore-based devices for protein characterization (Chapter 2) and enabled new nanopore-based assays. For instance, Chapter 2 demonstrated the first time a nanopore was capable of determining the charge of a protein (by measuring thousands of translocation events); Chapter 3 demonstrated the first time that the shape of proteins were quantitatively determined with nanopores, and the first time the dipole moment and rotational diffusion coefficient could be determined by observing a *single* non-spherical protein in the pore; Chapter 4 demonstrated that the affinity of a protein for a lipid-anchored ligand could be determined in the same experiments used for determining the size, charge, and shape of proteins (Chapters 2 and 3); Chapter 5 took advantage of the non-fouling, fluid coating to characterize disease-relevant aggregates of amyloid- β peptide; and finally, Chapter 6 demonstrated the ability of lipid-bilayer coated nanopores to monitor and quantify the activity of membrane-active enzymes. Consequently, the aggregate of this work demonstrates that the addition of fluid walls to nanopores is a very promising tool for simple, portable, single-molecule assays and biophysical characterization of proteins.

The studies presented in this thesis provide an exciting glimpse into the future of nanopore-based sensors. For instance, these studies suggest it will be possible to achieve high-throughput, simultaneous, and multi-parameter characterization of *single* proteins in

complex biological solutions. This capability would be an amazing advancement because by measuring multiple biophysical properties of one protein at a time, thousands of different proteins might be characterized and identified directly from biological solutions without complex instruments or chemical modification of the proteins. In order to achieve this goal, however, several challenges need to be addressed. In the next sections, I will describe these challenges and possible solutions as well as speculate on potential embodiments of nanopore-based sensors for characterizing multi-parameters by measuring a *single* protein.

7.1 General strategies to improve the nanopore-with-fluid-walls platform

This platform needs to evolve into a general assay in which many different sizes and types of proteins can be characterized. In this work we limited our analysis to proteins that bound to a commercially available lipid (biotin-PE), and we used a protein, GPI-acetylcholinesterase, that self-associated with the fluid lipid bilayer coating *via* its GPI moiety. In order to broaden the detection and characterization capabilities that this assay provides, we must develop a general method for attaching proteins or ligands to lipid anchors in the bilayer coating. Since lipids can be purchased with a variety of chemically reactive groups, methods for covalently linking proteins *via* their cysteine residues or amine groups should be relatively straightforward. For instance, hetero-bi-functional cross-linkers with a NHS-ester moiety and a maleimide moiety, which are commonly available from companies such as Pierce, could be used to link the amine group of a protein (*via* the NHS-ester) to thiolated lipids (*via* the maleimide moiety) in the bilayer coating. For assays aimed at determining the affinity of a protein-ligand interaction or detecting a specific protein-ligand interaction, similar methods could be employed to link the desired ligand specifically to certain lipids in the bilayer coating (*e.g.* lipids exposing primary amine, thiol, or carboxyl groups to the aqueous solution). This procedure could be performed on-chip, perhaps in parallel, or on the liposomes used to form the bilayer coating. This level of flexibility is a major advantage of the fluid-bilayer coating that should permit this assay to become a general method for characterizing most proteins.

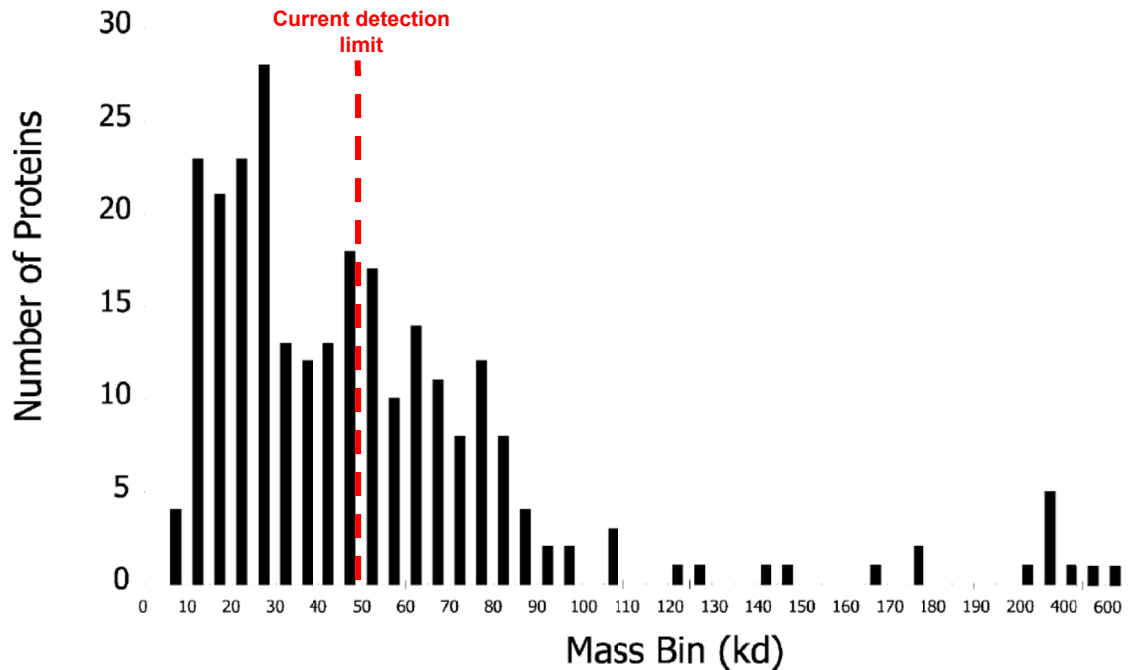


Figure 7.1 | Histogram of 289 proteins that are found in human plasma. The mass of the proteins is that of the processed form, and kd is kilo-Daltons (kDa). Dashed red line indicates the smallest proteins that can currently be detected with nanopores with fluid walls. Adopted from (1).

To detect small proteins, the diameter of the pores with a fluid bilayer coating and the electrical noise in the system (Appendix) needs to decrease. In this work, we determined that the smallest pore diameter we could achieve with a fluid lipid bilayer coating was ~ 10 nm, since lipid bilayers cannot maintain their fluid, bilayer nature at higher curvatures. With the typical baseline noise in these experiments, pores of this size cannot detect proteins that are smaller than ~ 4 to 5 nm in diameter, which corresponds to a molecular weight of ~ 50 kDa. Fig 7.1 shows, however, that a large fraction of the proteins found in human plasma are smaller than this detection limit. Thus, nanopores with fluid walls must be able to detect smaller proteins if they are to become a general and versatile platform for characterizing proteins. The most obvious strategy to decrease the detection limit is to decrease the diameter and length of the nanopores. In order to generate nanopores with fluid coatings with smaller diameters, we need to develop methods for creating fluid coatings with a high curvature (*i.e.* radius < 5 nm). One strategy would be to perform a systematic study using mixtures of lipids and detergents capable of assuming a high curvature; for instance, certain lipids and amphiphilic molecules can have various shapes conducive to membrane curvature (Fig. 7.2). Another

strategy may be to modify the substrate of the nanopore covalently with a self-assembled monolayer of alkyl silanes and form supported lipid monolayers on the surface rather than bilayers (2). Alternative strategies to obtain nanopores with fluid walls and diameters less than 10 nm may rely on using different fluid coating technologies. For instance, SLIPS (slippery liquid infused porous surfaces) technologies developed in Joanna Aizenberg’s lab employ an oil phase with a high-affinity for the underlying porous substrate (3, 4). Such technologies might not be limited by the molecular packing requirements of lipid structures and thereby, enable nanopores with diameters less than 10 nm to also have fluid walls.



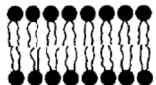

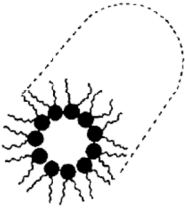

LIPID	PHASE	MOLECULAR SHAPE	CRITICAL PACKING PARAMETER (v/lS.)
Lysophospholipids Detergents	 Micellar	 Inverted Cone	$< \frac{1}{3}$ (Sphere) $\frac{1}{3}$ to $\frac{1}{2}$ (Globular Shapes; Rods)
Phosphatidylcholine Sphingomyelin Phosphatidylserine Phosphatidylinositol Phosphatidylglycerol Phosphatidic Acid Cardiolipin Digalactosyldiglyceride	 Bilayer	 Cylindrical	$\frac{1}{2}$ to 1
Phosphatidylethanolamine (Unsaturated) Cardiolipin - Ca^{2+} Phosphatidic Acid - Ca^{2+} (pH < 6.0) Phosphatidic Acid (pH < 3.0) Phosphatidylserine (pH < 4.0) Monogalactosyldiglyceride	 Hexagonal (H_{II})	 Cone	> 1

Figure 7.2 | “Polymorphic phases, molecular shapes, and the critical packing parameter for some membrane lipids.” The critical packing parameter is defined as $v / (l \times S)$, where v is the molecular volume of the hydrocarbon portion of the hydrocarbon amphiphile, l is the length of the alkyl chain, and S is the surface area of a lipid molecule. Adopted from (5).

Increasing the residence time of the proteins in the nanopore is another strategy to reduce the detection limit and improve the resolution of nanopore-based sensing assays.

For instance, if proteins could be held in the nanopore for long times (*i.e.* 500 μ s or longer), the electrical signal could be filtered at lower frequencies and, thereby, enable detection of smaller proteins compared to the same experiment where the signal is filtered at a higher frequency. While increasing the residence time of proteins in the nanopore is a simple concept to suggest; achieving this goal in practice has proved difficult because many strategies to reduce the translocation speed of proteins also reduced the mobility of ions and therefore the signal required to detect proteins (6-8). The fluid-coating concept that we developed in this work opened a unique pathway toward selectively reducing the mobility of the protein while not affecting the mobility of the ions. With this concept in mind there a few strategies one could envision to reduce the transit speed further of lipid-anchored proteins. First, increasing the viscosity of the bilayer coating by incorporating long-chain lipids or small molecules such as cholesterol would reduce the transit speed of lipid-anchored proteins. Second, linking the proteins of interest or ligand of interest to multiple lipids would selectively reduce the mobility of that lipid-anchored protein in the bilayer coating while not affecting the net viscosity of the fluid bilayer coating. These two strategies, however, suffer from the fact that the frequency of translocation events depends on the mobility of the lipid-anchored proteins in the bilayer (Chapter 4), and thus, these two strategies would reduce the frequency of translocation events to a prohibitively low frequency (*e.g.* 1 per min or less). To overcome this limitation, a third strategy would be to achieve a locally high viscosity of the bilayer coating at a defined location inside the nanopore. Figure 7.3 illustrates this concept where the locally high viscosity is achieved by covalent attachment of long-chain acyl groups to a gold layer within the nanopore structure prior to forming the lipid bilayer coating by vesicle fusion. This structure serves to create a region where the fluid lipid coating is a monolayer and, therefore, has a mobility that is approximately an order of magnitude lower compared to a lipid bilayer structure. Moreover, one could imagine developing chemically modified hydrophobic molecules that would respond to an electric field by becoming extended in a polarized state and flexible in an unpolarized state. By linking these to the gold layer and applying an electric potential difference to the gold layer, these imaginative but not entirely unrealistic molecules might enable switchable and perhaps tunable mobility of a lipid-anchored protein while in the nanopore (9).

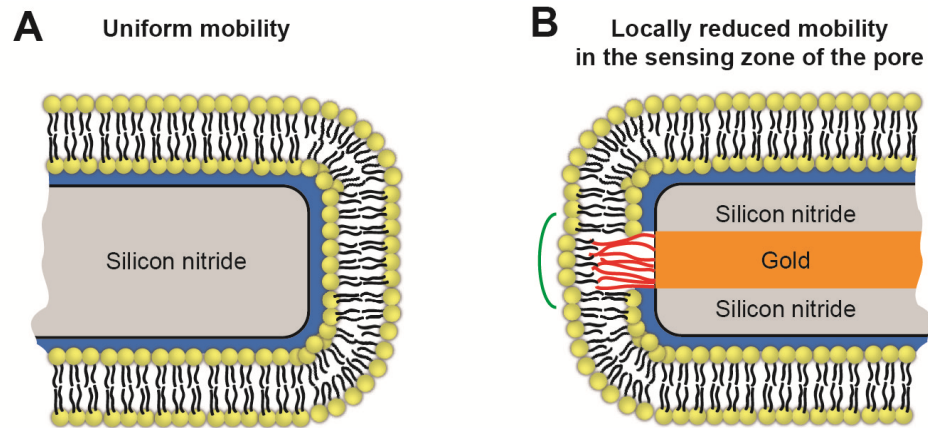


Figure 7.3 | Concept of a nanopore with fluid walls designed to increase the residence time of lipid-anchored proteins in the pore while not reducing the frequency of translocation events. (A) Original concept of a nanopore with fluid walls in a cross-sectional view of half the nanopore. The translocation speed and frequency of translocation events are both related to the viscosity of the bilayer coating. A high viscosity increases the residence time but reduces the frequency of events. (B) Concept of a nanopore with fluid walls where a region of the fluid coating has significantly increased viscosity (cross-sectional view of half the nanopore). In the example, this structure is achieved by sandwiching a gold layer between two silicon nitride layers (similar structures have been fabricated in (10-12)). The gold is modified covalently with a self-assembled monolayer of hydrophobic acyl chains (red lines). The fluid lipid layer in this region (green semi-oval) would form a monolayer with significantly reduce mobility compared to the surrounding bilayer structure. This structure would create a situation where the frequency of the translocation events is similar to that of (A), but the residence time of the lipid-anchored protein in the pore would be significantly increased.

In this work, there are two specific instances in which increased residence time would significantly improve the assay. The first instance is in the detection and characterization of amyloid- β aggregates. As stated in the conclusion of Chapter 5, ideally this assay could be used to characterize aggregates as small as trimers and detect the addition of individual monomers to aggregates of amyloid- β . For instance, we estimated that in the experiments performed in Chapter 5, addition of an individual monomer would decrease the current through the pore an additional ~ 20 pA. If the residence time of individual aggregates in the pore were sufficiently long, time-averaged currents should afford this level of resolution. The second instance in which long residence times of the proteins would have a great impact is in determining the shape of proteins and their conformational changes. We demonstrated in Chapter 3 that when non-spherical proteins resided in the nanopore for longer than ~ 400 μ s we were able to determine the size, shape, dipole moment, and rotational diffusion coefficient from a single protein. This capability would be ideal to characterize, and therefore identify,

proteins from a complex mixture based on measuring multiple properties of a single protein, one protein at a time. Consequently, if we could increase the residence time of the non-spherical proteins albeit under conditions where they still rotate, we would increase the accuracy for determining the volume, shape, dipole moment, and rotational diffusion coefficient from a single protein. Moreover, we presented evidence in Chapter 3 that suggests the ΔI value can also reflect conformational changes in flexible proteins such as an IgG₁ antibody. For instance, the histogram of *all* intraevent ΔI values in Fig. 7.4A shows several local maxima, which we hypothesize correspond to the different conformations that an IgG₁ antibody can assume (Fig. 7.4B). Fig. 7.4A was generated from thousands of translocation events; if a similar histogram could be generated by monitoring the current while a single antibody remained in the pore for a long time, it would provide strong evidence that these local maxima correspond to conformational changes.

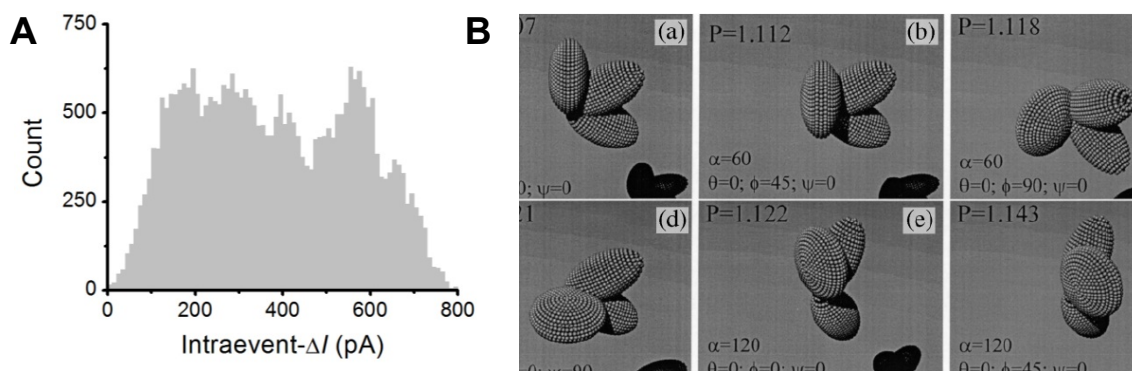


Figure 7.4 | Intraevent ΔI values due to IgG₁ antibody translocation events have several local maxima (A) and illustration of the multiple conformations of an IgG antibody (B). (B) was adopted from (13).

7.2 Proposed embodiments of the nanopores-with-fluid-walls platform for simultaneous, multi-parameter characterization of individual proteins.

In order to determine what proteins are present in a biological fluid, an ideal method would be able to characterize and identify proteins based on their biophysical properties. The classical method of identifying the presence of proteins in a complex mixture is to perform two-dimensional gel electrophoresis in which each type of protein is separated by size and isoelectric point followed by the difficult technique of mass

spectrometry on each spot (Fig. 7.5A) (Note: this is an ensemble method requiring micrograms of proteins) (14). The comparable single molecule technique would ideally be capable of measuring multiple biophysical properties of a *single* protein simultaneously such that as thousands of different proteins are characterized each protein can be distinguished. In this thesis, we demonstrated that this capability is truly a possibility by determining the dipole moment, size, and shape of *individual* non-spherical proteins. Consequently, one could envision this capability as a three-dimensional protein characterization (Fig. 7.5B). These same nanopore-based assays can also determine the rotational diffusion coefficient of non-spherical proteins; however, this value should be related to the size and shape in the absence of protein-specific interactions with the fluid coating. Further work would be required to determine if the rotational diffusion coefficient could be considered a fourth dimension for protein characterization in these types of nanopore-based assays.

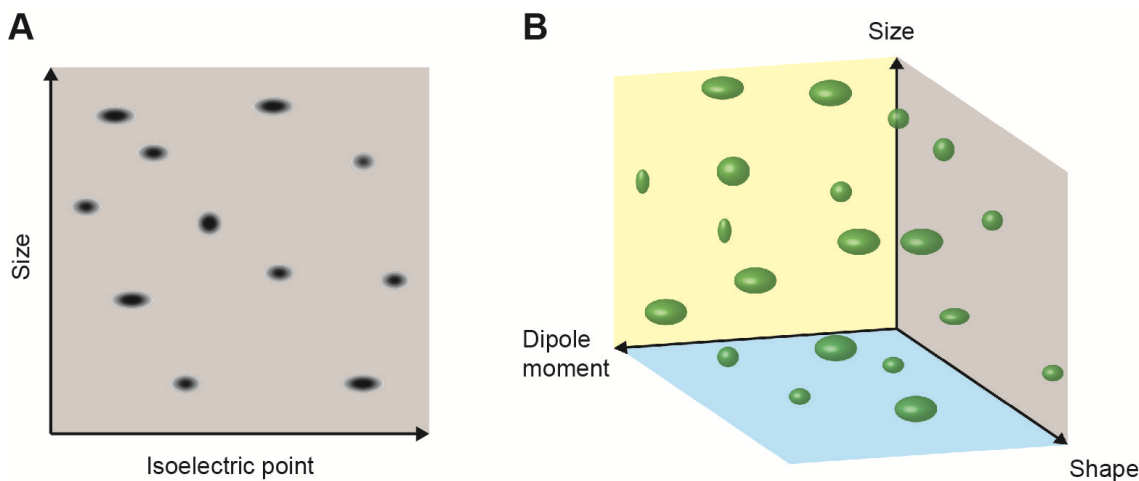


Figure 7.5 | Conceptual comparison of a two-dimensional protein characterization obtained by two-dimensional gel electrophoresis and a three-dimensional protein characterization of proteins obtained by nanopore-based single-molecule techniques. (A) Two-dimensional gel electrophoresis involves separating micrograms quantities of protein by their size and isoelectric point followed by a staining method in order to visualize the spots where there are proteins. **(B)** A nanopore-based assay with fluid walls that can measure three parameters from non-spherical proteins, however, enables a three-dimensional characterization of the proteins in solution; a hypothetical result is illustrated graphically where the “spots” indicate values of dipole moments, shapes, and sizes of the proteins as determined by measuring these properties from individual proteins as they passed through the nanopore.

In Chapters 3 and 4, we demonstrated that the charge and affinity for a ligand of a protein can be determined by measuring thousands of translocation events due to that

protein. Thus a single nanopore in use with many different of lipid-anchored proteins in the lipid coating would not enable determination of the charge or affinity of that protein since many different proteins would contribute to the signal. To overcome this limitation and thus, add these two parameters to the four discussed above, one could imagine an array of individually addressable nanopores with different sizes and with different ligand in the bilayer coating. Each nanopore in this case would be specific to a protein of interest and the translocation events from a particular pore would allow characterization of the size, charge, shape, and affinity for a ligand of that protein. This high-throughput array of nanopores is certainly reasonable considering that Oxford Nanopore Technologies has developed commercial devices with as many as 8,000 individually addressable nanopores and over 500 on-chip amplifiers (15). Such an array of nanopores would then be able to characterize and identify proteins based on four biophysical parameters (volume, shape, charge, and affinity), and for non-spherical, two additional parameters of dipole moment and rotational diffusion coefficient could also be determined.

7.3 Conclusion

In conclusion, this thesis has demonstrated the utility of nanopores with fluid walls for performing single molecule assays and biophysical characterization of proteins and peptides. We demonstrated that this platform has the potential to characterize multiple properties of a single protein while it resides in the nanopore. Nanopore-based assays have proven amenable to miniaturization due to their low-power requirements and silicon-based fabrication platform. Consequently, we suspect that with general improvements to the fluid-wall technology, nanofabrication methods, and parallelization of this technique; nanopore-based assays with fluid walls will be well-suited for simultaneous, multi-parameter characterization and identification of many proteins in complex biological mixtures. This capability will aid the search for biomarkers and the construction of personal proteomic databases.

Chapter 7 References

1. Anderson NL, Anderson NG (2002) The human plasma proteome - history, character, and diagnostic prospects. *Molecular & Cellular Proteomics* 1(11):845-867.
2. Sackmann E (1996) Supported membranes: Scientific and practical applications. *Science* 271(5245):43-48.
3. Epstein AK, Wong TS, Belisle RA, Boggs EM, Aizenberg J (2012) Liquid-infused structured surfaces with exceptional anti-biofouling performance. *Proc Natl Acad Sci U S A* 109(33):13182-13187.
4. Wong TS, *et al.* (2011) Bioinspired self-repairing slippery surfaces with pressure-stable omniphobicity. *Nature* 477(7365):443-447.
5. Gennis RB (1989) *Biomembranes: Molecular structure and function* (Springer-Verlag, New York, NY).
6. Rosenstein JK, Wanunu M, Merchant CA, Drndic M, Shepard KL (2012) Integrated nanopore sensing platform with sub-microsecond temporal resolution. *Nat Meth* 9(5):487-492.
7. Li JL, Talaga DS (2010) The distribution of DNA translocation times in solid-state nanopores. *J Phys-Condens Matter* 22(45).
8. Majd S, *et al.* (2010) Applications of biological pores in nanomedicine, sensing, and nanoelectronics. *Curr Opin Biotech* 21(4):439-476.
9. Nandivada H, Ross AM, Lahann J (2010) Stimuli-responsive monolayers for biotechnology. *Progress in Polymer Science* 35(1-2):141-154.
10. Ivanov AP, *et al.* (2011) DNA tunneling detector embedded in a nanopore. *Nano Lett* 11(1):279-285.
11. Spinney PS, Collins SD, Howitt DG, Smith RL (2012) Fabrication and characterization of a solid-state nanopore with self-aligned carbon nanoelectrodes for molecular detection. *Nanotechnology* 23(13).
12. Tsutsui M, Taniguchi M, Yokota K, Kawai T (2010) Identifying single nucleotides by tunnelling current. *Nat Nanotechnol* 5(4):286-290.
13. Carrasco B, *et al.* (2001) Crystallohydrodynamics for solving the hydration problem for multi-domain proteins: Open physiological conformations for human IgG. *Biophysical Chemistry* 93(2-3):181-196.
14. Shevchenko A, Tomas H, Havlis J, Olsen JV, Mann M (2006) In-gel digestion for mass spectrometric characterization of proteins and proteomes. *Nat Protoc* 1(6):2856-2860.
15. Oxford nanopore introduces DNA 'strand sequencing' on the high-throughput gridion platform and presents minion, a sequencer the size of a USB memory stick. (May 18, 2012) <http://www.nanoporetech.com/news/press-releases/view/39>

Appendix

A.1 Equivalent Circuit Model and Electrical Noise

Figure A.1 shows the structure of the nanopores used in this work and the corresponding equivalent circuit model. From this circuit model, we calculated the expected electrical noise in the system as a function of the signal bandwidth of the electrical recordings. In this work, the bandwidth is approximately equal to the cut-off frequency, f_c (Hz), of a low-pass filter that we digitally applied after the current recordings; we typically applied a low-pass digital filter with cut-off frequency of $f_{df} = 15$ kHz. The maximum bandwidth of recordings with these nanopores, however, was limited by the bandwidth of the head-stage amplifier of $f_{hs} = 57$ kHz (1). Equations A.1 – A.6 describe well-known sources of electrical noise in the system, and Table A.1 lists typical values for the parameters in these equations that describe the noise. Equation A.6 lists the total noise expected in these experiments; however, silicon chips that are coated with silicon nitride can exhibit a strong noise at low frequencies that follows a $1/f$ behavior, I_F (1-4). The most reported, and perhaps the best, strategies to reduce the total noise in these experiments due to $1/f$ noise and stray capacitance involve minimizing the area of the silicon nitride that is contact with solution by coating the chip with a thick layer (*i.e.* greater than 1 μm) of PDMS or applying short high voltage pulses across the pores (4, 5). Additionally, the fluid-bilayer coating adds additional noise at frequencies below ~ 2 kHz (Figure A.2) (6). Consequently, the total noise of a nanopore and therefore, its expected performance as a resistive-pulse sensor, is currently best determined experimentally by obtaining a power-spectrum of the electrical signal (Figure A.2) and integrating from 0 to f_c . From this experimental observation, the RMS-noise of the nanopore under the desired experimental conditions can be obtained, and therefore, the expected detection limits of the nanopore can be determined (Appendix B).

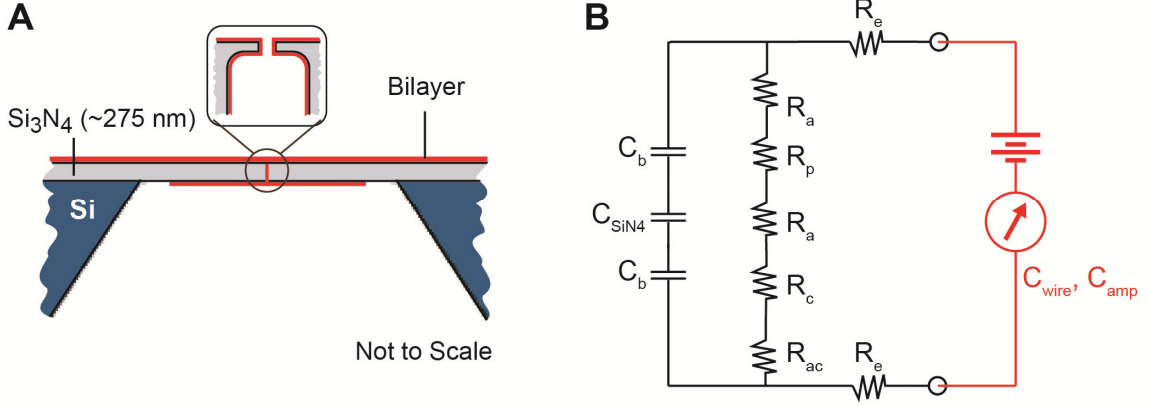


Figure A.1 | Close up cross sectional view of the nanopores used in this work and the equivalent, simplified circuit diagram. (A) Shows a close-up cross-sectional view of a typical nanopore chip. (B) Shows a simplified equivalent circuit model. For the equations below we considered the stray capacitances due to the bilayer and silicon nitride area that was in contact with the aqueous solution in the top solution compartment (5). This area was limited by the size of the hole punch used to create the fluid well and was $\sim \pi \times (0.001 \text{ m})^2$.

Intrinsic bandwidth of the pore, equation A.1 (1):

$$f_{\text{pore}} \leq \frac{1}{2\pi R_e C_m} \quad (\text{A.1})$$

Noise due to the amplifier, equation A.2:

$$I_A = \sqrt{2eI_{\text{fet}}c_1f_c + \frac{4ak_B Tc_1f_c}{R_f} + e_n^2 \left(\frac{c_1f_c}{R_f^2} + \frac{4}{3}c_3\pi^2 C_{\text{tot}}^2 f_c^3 \right)} \quad (\text{A.2})$$

Thermal noise or Johnson noise, equation A.3:

$$I_T = \sqrt{\frac{4k_B Tc_1f_c}{R_p} + \frac{4k_B Tc_1}{R_a + R_{ac}} \left(f_c - \frac{\tan^{-1}(2\pi(R_a + R_{ac})C_{\text{chip}}f_c)}{2\pi(R_a + R_{ac})C_{\text{chip}}} \right)} \quad (\text{A.3})$$

Noise due to dielectric materials, equation A.4:

$$I_D = \sqrt{4\pi k_B TDC_m c_2 f_c^2} \quad (\text{A.4})$$

Shot noise may also play a role, equation A.5:

$$I_S = \sqrt{\frac{2ef_c V_a}{R_{\text{tot}}}} \quad (\text{A.5})$$

Total noise, equation A.6:

$$I_{\text{RMS}} = \sqrt{I_A^2 + I_T^2 + I_D^2 + I_S^2 + I_F^2} \quad (\text{A.6})$$

Table A.1. Parameters affecting the noise and their typical values in this work.

Parameter	Equation	Typical value	Details
f_c	$\sqrt{\frac{1}{f_{pore}^{-2} + f_{hs}^{-2} + f_{df}^{-2}}}$	14.5-15 kHz	Effective cutoff frequency
R_e		~250 - 500 Ω	Electrolyte resistance to pore
R_p	$\frac{\rho l_p}{\pi r_p^2}$	~1-2 M Ω	Chapter 2
R_a	$\frac{\rho}{4r_p}$	~1 M Ω	Chapter 2
R_{ac}	$\frac{\rho}{4r_c}$	~1 M Ω	Chapter 2
R_{tot}	$R_p+2R_a+R_c+R_{ca}$	~3 - 5 M Ω	Chapter 2
C_b	$0.02 \text{ F m}^{-2} \times \pi 0.001 \text{ m}^2$	63 nF	Capacitance of the bilayer in contact with solution.
C_{SiN_4}	$\frac{\epsilon_o \epsilon_r \pi (0.001)^2}{d}$ where $\epsilon_r \sim 7$	101 pF	Capacitance of the silicon nitride layer.
C_m	$\sim \left(\frac{2}{C_b} + \frac{1}{C_{SiN_4}} \right)^{-1}$	~100 pF	Total capacitance of the chip.
$C_{wire} + C_{amp}$		$\beta = 1$; 30 pF $\beta = 0.1$; 98 pF	Uram <i>et al.</i> (1)
C_{tot}	$C_{chip}+C_{wire}+C_{amp}$	$\beta = 1$; 130 pF $\beta = 0.1$; 198 pF	
c_1		1.04	Correction coefficients for filtering (1)
c_2		1.3	Correction coefficients for filtering (1)
c_3		1.9	Correction coefficients for filtering (1)
a		~1.9	Extra noise in the system (1)
I_{fet}		0.2 pA	Gate leakage current (1)
R_f		$\beta = 1$; 500 M Ω $\beta = 0.1$; 50 M Ω	Feedback resistor in the amplifier
e_n		3-4 nV Hz ^{-1/2}	Voltage noise density (1, 2)
D		~0.001- 0.01	Dielectric loss tangent (1, 7)

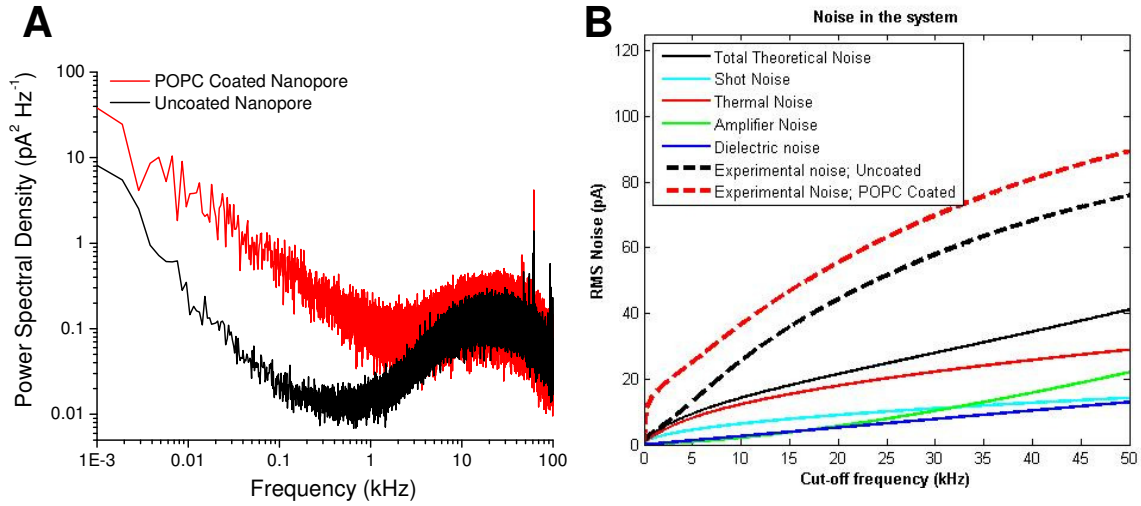


Figure A.2 | Comparison of the noise in nanopores before and after a lipid bilayer coating. (A) Power spectral densities of the electrical noise in a nanopore with and without lipid bilayer coating. The spectra were taken using an electrolyte of 2 M KCl, 10 mM HEPES (pH = 7.4, $\rho = 0.046 \Omega \text{ m}$) and at an applied voltage of 0.1 V. The nanopore had an $r_p = 15 \text{ nm}$ and an $l_p = 15 \text{ nm}$ without the bilayer coating. (B) Theoretical RMS noise compared to the actual RMS noise. Total RMS noise was predicted from equation A.6. The experimental RMS noise was obtained by taking the integral of power spectral densities in (A).

The disagreement between the theoretical noise and the experimentally observed noise in uncoated nanopores could be due to a number of factors that we briefly highlight here (Figure A.2). For the uncoated nanopores, the experimentally determined noise appears to first deviate from the predicted noise at a frequency of $\sim 2.5 \text{ kHz}$. In the range of $\sim 100 - 10 \text{ kHz}$, the noise is dominated by energy dissipation in non-ideal dielectric materials and thermal noise of the pore and measurement electronics (2). At frequencies greater than 10 kHz, noise due to the interaction of the amplifier's voltage noise (*i.e.* e_n) with the total capacitance of the system increases and may become dominant (2). The strong difference between the theoretical noise and the noise determined in experiment thus seems to stem from stray capacitance in the system and the presence of non-ideal dielectric materials. Minimizing the contribution of these two parameters should improve the noise of these experiments and lead to decreased detection limits. Figure A.2 also shows the expected result that bilayer coated nanopores exhibit a significant (*i.e.* $\sim 15\text{-}20 \text{ pA RMS}$) noise with $1/f$ behavior due to low-frequency fluctuations of the bilayer coating (6).

Another possible reason for the high electrical noise observed in experiments compared to the theoretical predications may be that the equivalent circuit model is inaccurate. For instance, in estimating the intrinsic bandwidth of the nanopore device typically only the electrolyte resistance to the pore structure is considered to be in series with the capacitance of the chip, and the access resistance to the nanometer opening of the pore is often neglected (1). One might think that the access resistance to the pore should also be considered to be in series with the capacitance of the chip; however, if that were an accurate model, the intrinsic bandwidth of the nanopore would be ~1 kHz, and we know that the actual bandwidth is actually much higher than the 57 kHz bandwidth of the head-stage amplifier (Equation A.1). This discrepancy and the complicated structure of the nanopores suggest that the simple equivalent circuit model in Figure A.1 is not entirely accurate, but provides a good first approximation to the minimum noise one might expect in these experiments.

A.2 Governing Equations

This section lists the equations that describe these nanopore-based resistive-pulse sensing experiments as a function of experimental conditions, the properties of the bilayer coating, and the properties of the protein of interest. These equations are listed below and have been combined in a MATLAB program in order to plot certain parameters of interest against multiple variables.

Change in current as a function of particle volume and shape (Chapters 2, 3, and 5):

$$\frac{\Delta I}{I} = -\frac{4\Lambda\gamma}{\pi d_p^2 (l_p + 0.8d_p)} S\left(\frac{d_M}{d_p}\right) \Rightarrow \Delta I = -\frac{\Lambda V_A \gamma}{\rho (l_p + 0.8d_p)^2} S\left(\frac{d_M}{d_p}\right) \quad (\text{A.7})$$

where

$$S\left(\frac{d_M}{D_p}\right) = \frac{1}{1 - 0.8\left(\frac{d_M}{d_p}\right)^3} \quad (\text{A.8})$$

Detection limit for spherical and slender particles:

$$\text{Spherical particles: } \Lambda_{\text{small-limit}} = \frac{\rho (l_p + 0.8d_p)^2 5I_{\text{RMS-noise}}}{V_A 1.5} \quad (\text{A.9})$$

Slender particles where $\gamma \rightarrow 1$: $\Lambda_{\text{small-limit}} = \frac{\rho(l_p + 0.8d_p)^2 5I_{\text{RMS-noise}}}{V_A}$ (A.10)

Electrical shape factor (Chapter 3 and 5):

$$\gamma_{\parallel} = \frac{1}{1-n_{\parallel}} \text{ and } \gamma_{\perp} = \frac{1}{1-n_{\perp}} \quad (\text{A.11})$$

where n_{\parallel} for a prolate spheroid with $m = A/B > 1$ is:

$$n_{\parallel} = \frac{1}{m^2 - 1} \left[\frac{m}{\sqrt{m^2 - 1}} \ln \left(m + \sqrt{m^2 - 1} \right) - 1 \right] \quad (\text{A.12})$$

and n_{\parallel} for an oblate spheroid with $m = A/B < 1$ is:

$$n_{\parallel} = \frac{1}{1 - m^2} \left[1 - \frac{m}{\sqrt{1 - m^2}} \cos^{-1}(m) \right] \quad (\text{A.13})$$

and $n_{\perp} = (1 - n_{\parallel})/2$

Distribution of translocation times and average translocation time (Chapter 2):

$$p(t_d) = \frac{(vt_d + l_p) \times e^{-\frac{[l_p - vt_d]^2}{4Dt_d}}}{2t_d \times \sqrt{4Dt_d} \pi} \quad (\text{A.14})$$

where $v = \frac{|z|eV_p D}{l_p k_B T}$

$$\langle t_d \rangle = \frac{l_p^2 k_B T}{|z|e(V_A R_p / R_{tot}) D_L} \text{ while } \langle t_d \rangle < MSD_{t_d} = \frac{l_p^2}{2D_L} \quad (\text{A.15})$$

Frequency of translocation events (Chapter 4):

$$f_T = \frac{4\pi D \Gamma_{PL}}{\ln \left(\frac{4D t}{r_p^2} \right)} \text{ for a known density of lipid-anchored protein.} \quad (\text{A.16})$$

$$f_T = \frac{4\pi D \Gamma_L \Theta}{\ln \left(\frac{4D t}{r_p^2} \right)} \text{ for the binding of a protein to a lipid-anchored ligand where} \quad (\text{A.17})$$

$$\Theta \equiv \frac{\Gamma_{PL}}{\Gamma_L} = \frac{[P]}{[P] + K_D} \quad (\text{A.18})$$

To account for depletion of the protein from solution (*i.e.* $[P] \neq [P_o]$) use equation A.19:

$$\Theta = \frac{K_d + [P_o] + [P_o]\alpha - \sqrt{K_d^2 + 2K_d[P_o] + 2K_d[P_o]\alpha + [P_o]^2 - 2[P_o]^2\alpha + [P_o]^2\alpha^2}}{2[P_o]\alpha} \quad (\text{A.19})$$

where α is the ratio of $\frac{\text{total ligand}}{\text{total protein}} = \frac{\Gamma_L \text{ Surface Area}}{A_v [P_o] \text{ Volume}}$

For all equations, if a lipid bilayer coating is used replace, l_p with $l_p + 2l_b + 2l_w$, and replace d_p with $d_p - 2l_b - 2l_w$ ($r_p = d_p / 2$), where l_b is the thickness of the lipid bilayer and l_w is the thickness of the interstitial water layer (see Chapter 2).

A.3 Plots of significant parameters:

Basic Input Parameters

Radius of the nanopore	15 (nm)
Length of the nanopore	15 (nm)
Radius of the channel	50 (nm)
Thickness of the SiN4	275 (nm) Calculated Ic: 260 (nm)
Bilayer thickness	3.7 (nm)
Water layer thickness	1.1 (nm)
Electrolyte resistivity	0.046 (Ohm m)
Applied Voltage	-0.1 (V)
Volume of Electrolyte	100 (micro-L)

Parameters for Noise

If possible use the power spectrum (more accurate)

Have Power Spectrum File path for power spectrum

Width of square SiN4 window (micro-m)

Fitting parameters for a/f^c noise (a, c). Enter 0 in each box if you have the Power Spectrum file.

(pA²) (unitless)

Properties of the Protein and Bilayer

Estimated Volume	150 (nm ³)
Estimated Charge	-3 (z -unitless)
Concentration of protein ([P])	1 (nM)
Dissociation Constant (Kd)	500 (nM)
Diffusion Constant of Lipid-Anchored Protein (DL)	1.2 (nm ² per micro-s)
Mol Fraction of Ligand (XL)	0.2 (%)

Output Parameters of Interest

Total resistance:	7.904 (M-ohm)
Baseline current:	-12.652 (nA)
Intrinsic bandwidth of the pore:	3148 (kHz)
Expected Threshold @ fc = 15kHz	179 (pA)
Expected DI	322 (pA)
Expected Average Td	98 (micro-s)
Expected freq. of events	5.164 (Hz)

Select Plots that You Want to See

- RMS Noise (fc)
- Detection Limit (fc)
- Detection Limit (rho,fc)
- Td_avg (charge)
- Td_avg (charge, diffusion coefficient)
- Td_avg (charge, applied voltage)
- Td_avg (diffusion coefficient, applied voltage)
- Distribution of T_d
- Freq (DL, XL)
- Freq (XL, [P])
- Freq (XL, Kd)

Simulate Results

Figure A.3 | MATLAB graphical user interface with typical values for all parameters entered as an example. These values were used to construct the plots below unless the corresponding parameters are varied on the x and y axis.

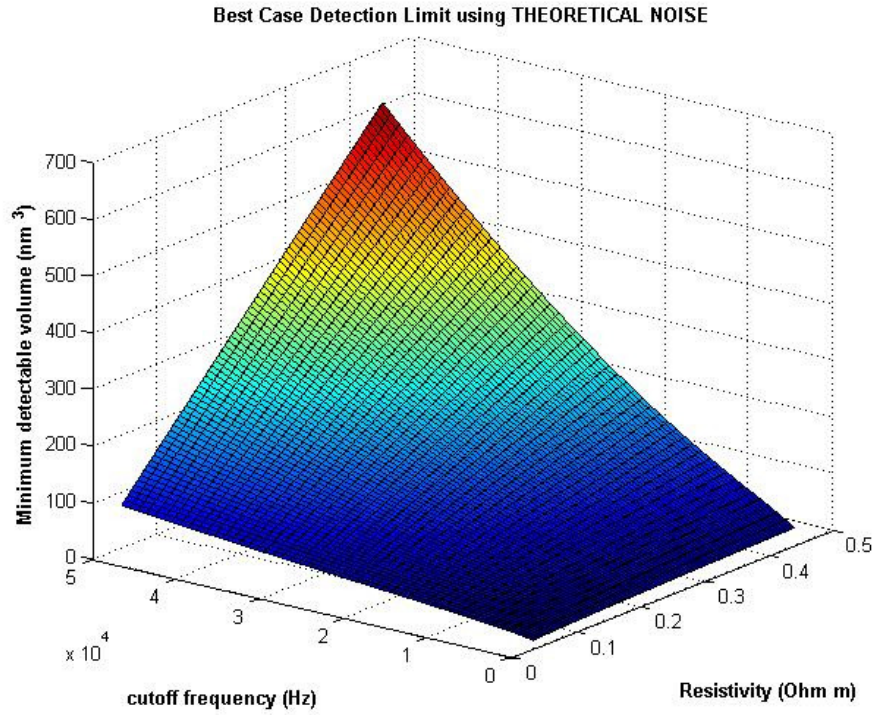


Figure A.4 | Detection limit as a function of the resistivity of the solution (corresponding roughly to 2 M to 0.2 M KCl) and cutoff frequency.

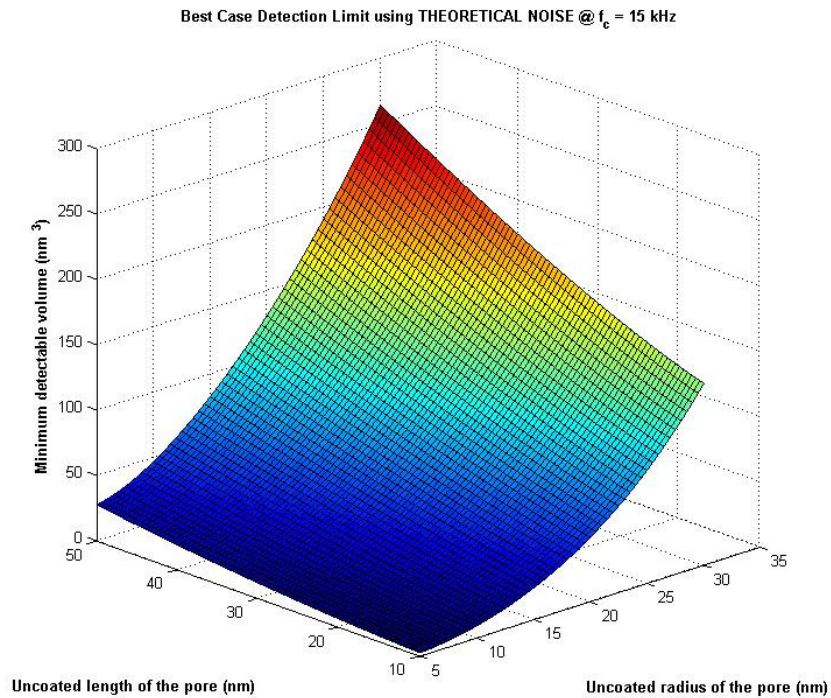


Figure A.5 | Detection limit as a function of the uncoated length and radius of the nanopore. This plot assumes a bilayer coating will be added (see Figure B.1).

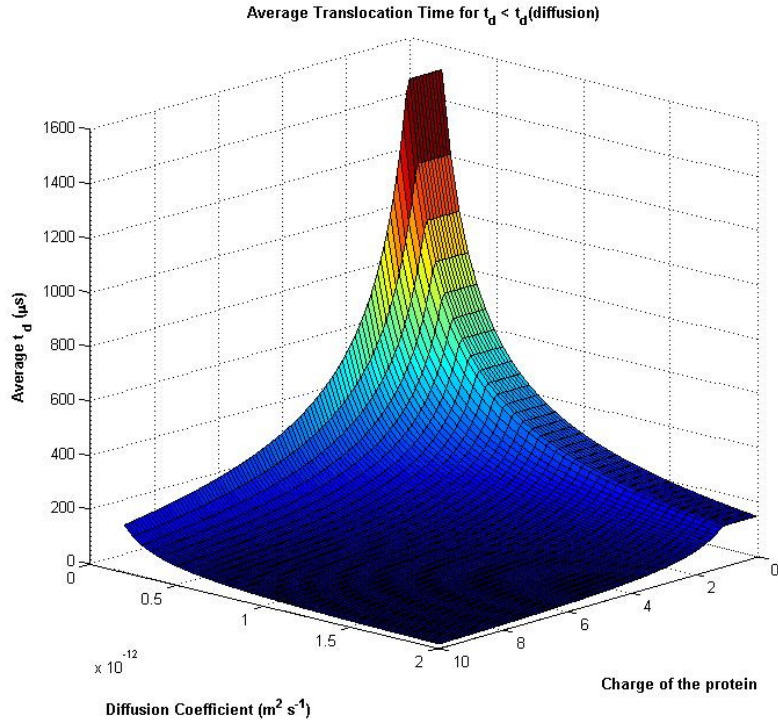


Figure A.6 | Average translocation time as a function of the diffusion coefficient of the protein-ligand complex in the bilayer coating and the net charge of the protein. The plot becomes independent of charge at the mean-squared-diffusion time for a protein to pass through a pore of length l_p .

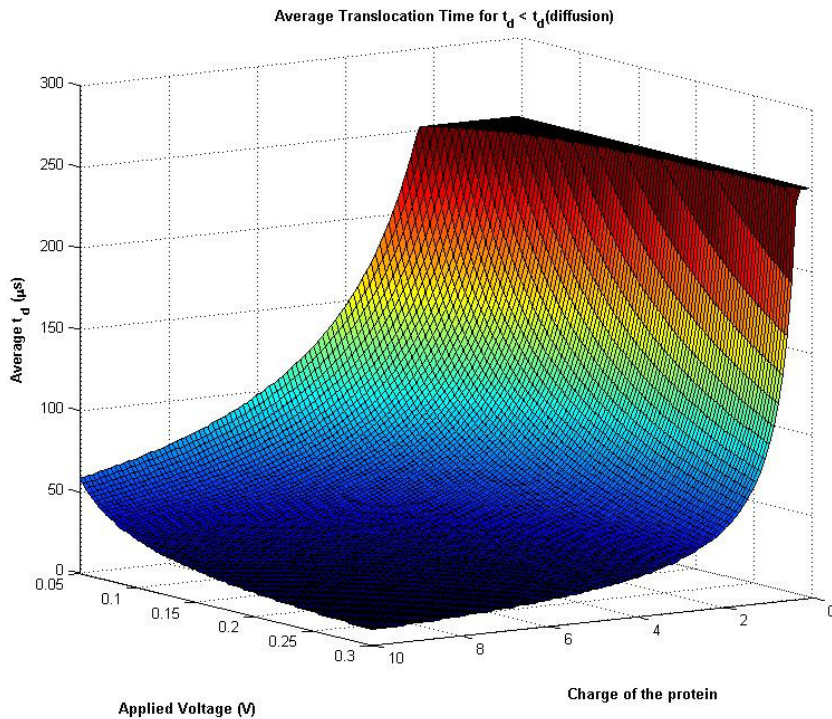


Figure A.7 | Average translocation time as a function of the applied voltage and the net charge of the protein. The plot becomes independent of charge and voltage at the mean-squared-diffusion time for a protein to pass through a pore of length l_p .

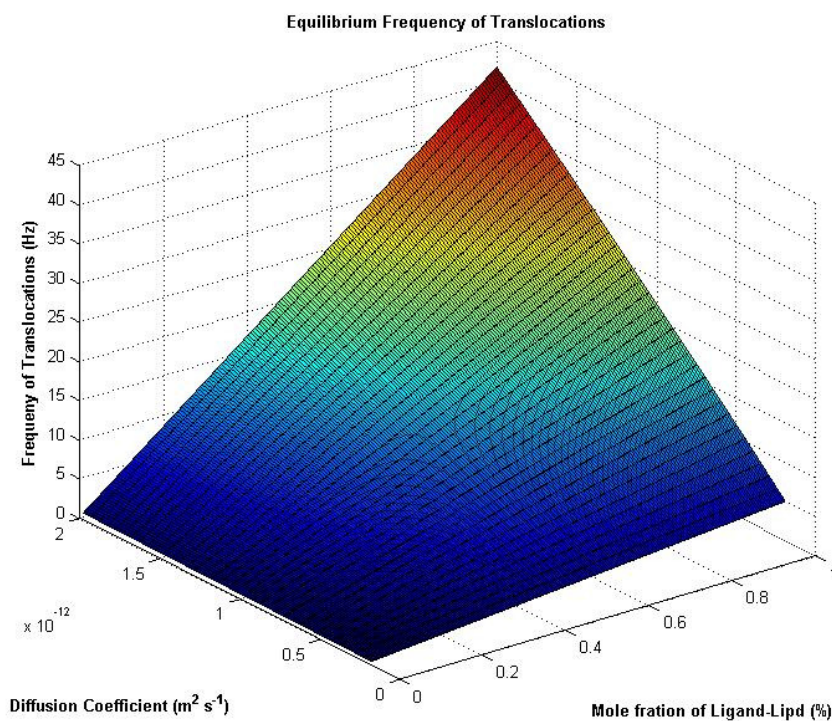


Figure A.8 | Frequency of translocation events at equilibrium as a function of the diffusion coefficient of the protein-lipid complex and the mole fraction of lipid-anchored ligand.

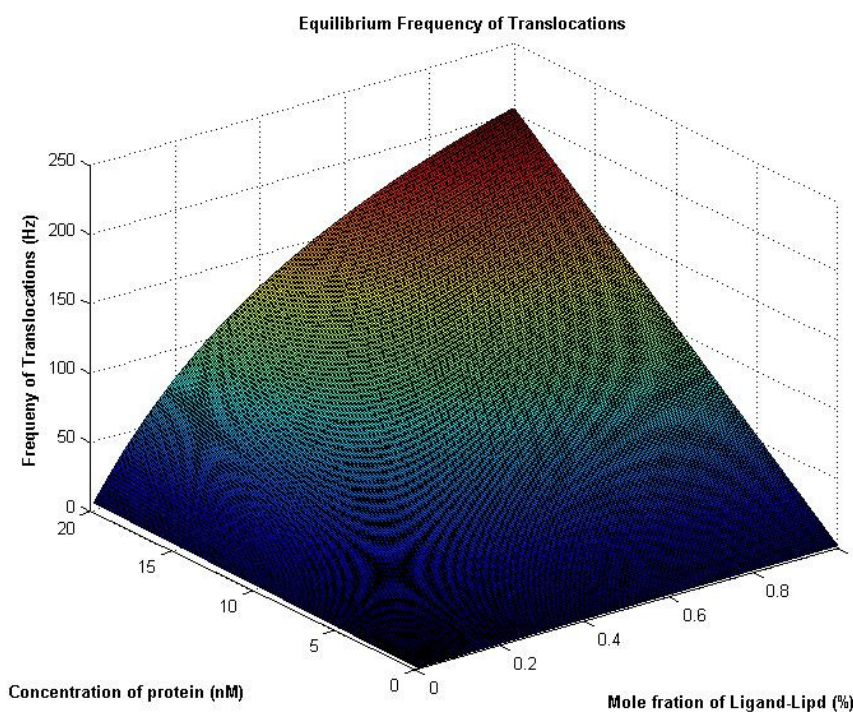


Figure A.9 | Frequency of translocation events at equilibrium as a function of the concentration of the protein and the mole fraction of lipid-anchored ligand.

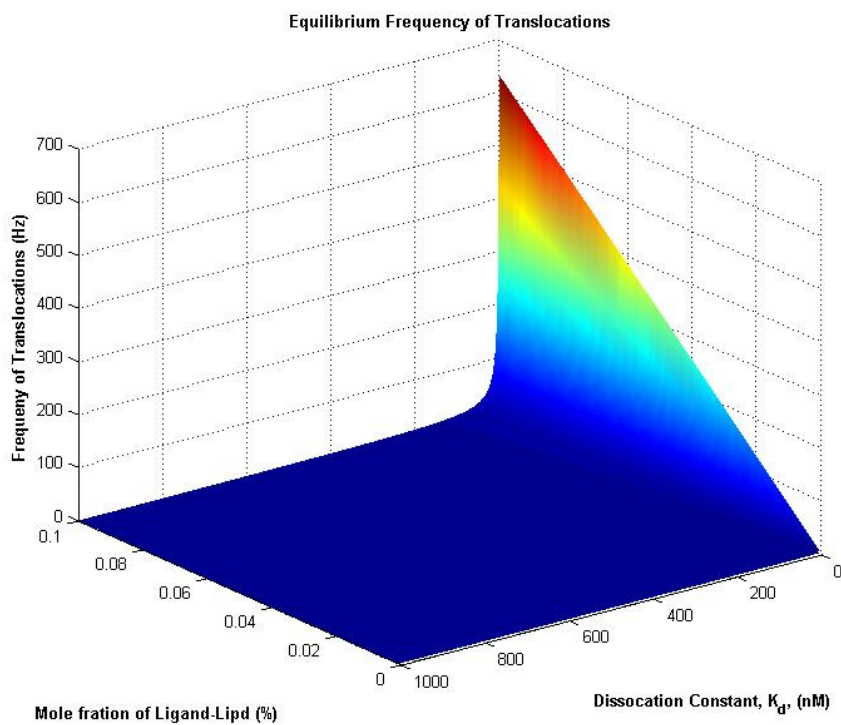


Figure A.10 | Frequency of translocation events at equilibrium as a function of the equilibrium dissociation constant and the mole fraction of lipid-anchored ligand.

Appendix References

1. Uram JD, Ke K, Mayer M (2008) Noise and bandwidth of current recordings from submicrometer pores and nanopores. *ACS Nano* 2(5):857-872.
2. Rosenstein JK, Wanunu M, Merchant CA, Drndic M, Shepard KL (2012) Integrated nanopore sensing platform with sub-microsecond temporal resolution. *Nat Meth* 9(5):487-492.
3. Smeets RMM, Keyser UF, Dekker NH, Dekker C (2008) Noise in solid-state nanopores. *Proc Natl Acad Sci U S A* 105(2):417-421.
4. Beamish E, Kwok H, Tabard-Cossa V, Godin M (2012) Precise control of the size and noise of solid-state nanopores using high electric fields. *Nanotechnology* 23(40).
5. Tabard-Cossa V, Trivedi D, Wiggin M, Jetha NN, Marziali A (2007) Noise analysis and reduction in solid-state nanopores. *Nanotechnology* 18(30).
6. Yusko EC, *et al.* (2011) Controlling protein translocation through nanopores with bio-inspired fluid walls. *Nat Nanotechnol* 6(4):253-260.
7. Mayer M, Kriebel JK, Tosteson MT, Whitesides GM (2003) Microfabricated teflon membranes for low-noise recordings of ion channels in planar lipid bilayers. *Biophys J* 85(4):2684-2695.